



Tribological study of novel metal-doped carbon-based coatings with enhanced thermal stability.

MANDAL, Paranjayee.

Available from the Sheffield Hallam University Research Archive (SHURA) at:

<http://shura.shu.ac.uk/20012/>

A Sheffield Hallam University thesis

This thesis is protected by copyright which belongs to the author.

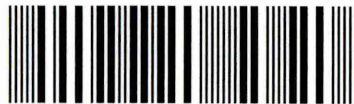
The content must not be changed in any way or sold commercially in any format or medium without the formal permission of the author.

When referring to this work, full bibliographic details including the author, title, awarding institution and date of the thesis must be given.

Please visit <http://shura.shu.ac.uk/20012/> and <http://shura.shu.ac.uk/information.html> for further details about copyright and re-use permissions.

280 10
Sheffield Hallam University
Learning and Information Services
Adsetts Centre, City Campus
Sheffield S1 1WD

102 141 950 8



Sheffield Hallam University
Learning and Information Services
Adsetts Centre, City Campus
Sheffield S1 1WD

REFERENCE

ProQuest Number: 10697319

All rights reserved

INFORMATION TO ALL USERS

The quality of this reproduction is dependent upon the quality of the copy submitted.

In the unlikely event that the author did not send a complete manuscript and there are missing pages, these will be noted. Also, if material had to be removed, a note will indicate the deletion.



ProQuest 10697319

Published by ProQuest LLC (2017). Copyright of the Dissertation is held by the Author.

All rights reserved.

This work is protected against unauthorized copying under Title 17, United States Code
Microform Edition © ProQuest LLC.

ProQuest LLC.
789 East Eisenhower Parkway
P.O. Box 1346
Ann Arbor, MI 48106 – 1346

TRIBOLOGICAL STUDY OF NOVEL METAL-DOPED CARBON-BASED COATINGS WITH ENHANCED THERMAL STABILITY

PARANJAYEE MANDAL

A thesis submitted in fulfilment of the requirements of
Sheffield Hallam University
for the degree of Doctor of Philosophy

Collaborating Organisation:

Hauzer Techno Coating

May 2015

Declaration

I hereby declare that this thesis is my own work and effort and that it has not been submitted anywhere for any award apart from that of Doctor of Philosophy at Sheffield Hallam University. Where other sources of information have been used, they have been acknowledged.

Paranjayee Mandal

Date: 27.05.2015

Contents

Abstract	vii
Acknowledgements	viii
Advanced Studies.....	ix
Publications	x
Acronyms	xi
List of Figures	xii
List of Tables.....	xvii
CHAPTER 1. Introduction.....	1
1.1. Background	1
1.2. Problem definition	4
1.3. Methodology	5
1.4. Aim and objectives of this research	7
1.5. Thesis layout	8
CHAPTER 2. Literature review	9
2.1. Introduction to the tribology of Diamond-like-carbon (DLC) coating	9
2.1.1. Review of friction and wear during sliding	9
2.1.2. Tribological coatings: DLC and metal-doped DLC	11
2.1.3. Factors affecting the friction and wear of the DLC coating	18
I. Surface roughness	18
II. Adhesive interactions	18
III. Third-body abrasion	19
IV. Tribochemical interactions	19
V. High working temperature	20
2.1.4. Engine oil as lubricant	20
2.1.5. Tribological performance of DLC and metal-doped DLC coatings	23
I. Metal-free DLC coating	23
II. Cr-doped DLC coating	23
III. Si-doped DLC coating	26
IV. Ti-doped DLC coating	27
V. Mo-doped DLC coating	28
VI. W-doped DLC coating	28
2.2. Thermal stability of DLC and metal-doped DLC coatings	29

I. DLC coating.....	29
II. Cr-doped DLC coating	30
III. Si-doped DLC coating	31
IV. Ti-doped DLC coating	31
V. Mo-doped DLC and W-doped DLC coatings.....	32
2.3. Coating deposition techniques	32
2.3.1. Unbalanced Magnetron Sputtering (UBM)	32
2.3.2. High Power Impulse Magnetron Sputtering (HIPIMS).....	36
2.3.3. Microstructure of thin films.....	37
2.4. Discussion.....	40
 CHAPTER 3. Deposition and characterisation of molybdenum and tungsten doped carbon-based (Mo–W–C) coating	42
3.1. Introduction.....	42
3.2. Sample preparation techniques and coating deposition procedure	42
3.3. Characterisation techniques	45
3.3.1. Scratch test	45
3.3.2. Rockwell hardness test	45
3.3.3. Nanoindentation	46
3.3.4. Pin-on-disc test.....	46
3.3.5. Thermo-gravimetric analysis (TGA).....	47
3.3.6. Isothermal oxidation test	47
3.3.7. Scanning electron microscopy (SEM).....	47
3.3.8. X-ray Diffraction (XRD).....	48
3.3.9. Raman spectroscopy	48
 CHAPTER 4. Results and Discussion	50
 4.1. Structural properties of molybdenum and tungsten doped carbon-based (Mo–W–C) coatings.....	50
4.1.1. Introduction.....	50
4.1.2. Coating microstructure and phase composition.....	50
4.1.3. Nanohardness and elastic properties.....	62
4.1.4. Adhesion strength	64
4.1.5. Concluding remarks	69

4.2. Tribological behaviour of Mo–W–C coatings in dry and boundary lubricated conditions at ambient temperature	70
4.2.1. Introduction	70
4.2.2. Tribological behaviour of Mo–W–C coatings during dry sliding at ambient temperature	71
I. Experimental details	71
II. Friction behaviour of Mo–W–C coatings during dry sliding	71
III. Wear behaviour of the steel counterparts during dry sliding.....	75
IV. Wear behaviour of Mo–W–C coatings during dry sliding.....	83
V. Wear mechanism during dry sliding at ambient temperature	89
4.2.3. Tribological behaviour of Mo–W–C coatings during boundary lubricated sliding condition at ambient temperature.....	91
I. Experimental details	91
II. Tribological behaviour of Mo–W–C coatings during lubricated sliding against steel counterparts	92
III. Tribological behaviour of C4 during lubricated sliding against Al ₂ O ₃ ball...	101
IV. Tribo-chemically reactive wear mechanism during lubricated sliding at ambient temperature	102
4.2.4. Influence of metal dopants on tribological behaviour of carbon-based coatings at ambient temperature	104
I. Introduction	104
II. Tribological performance of Cr-doped carbon-based coating (Cr/C) at ambient temperature	104
III. Comparison of tribological performance of Cr/C and Mo–W–C coatings ...	111
IV. Comparison of tribological performance of state-of-the-art DLC coatings and C4 at ambient temperature	114
A. <i>Dry and lubricated sliding against 100Cr6 steel balls</i>	114
B. <i>Dry and lubricated sliding against Al₂O₃ balls</i>	119
4.2.5. Concluding remarks	122
4.3. Oxidation behaviour of Mo–W–C coatings.....	123
4.3.1. Introduction	123
4.3.2. Experimental details.....	123
4.3.3. Isothermal oxidation behaviour of Mo–W–C coatings	124
I. Surface morphology and coating microstructure.....	124
II. Phase composition using X-ray diffraction.....	131
III. Phase composition using Raman spectroscopy	137
IV. Nanohardness.....	144

4.3.4. Dynamic oxidation behaviour of Mo–W–C coatings	146
I. Thermo-gravimetric analysis (TGA).....	146
II. Phase composition using XRD and Raman spectroscopy	148
4.3.5. Comparison of oxidation resistance of C4 and state-of-the-art DLC (Cr/Cr-WC/W:C-H/a:C-H) coatings.....	151
4.3.6. Concluding remarks	157
4.4. Tribological behaviour of Mo–W–C coatings in dry and boundary lubricated conditions at elevated temperature	159
4.4.1. Introduction	159
4.4.2. Tribological behaviour of Mo–W–C coatings during dry sliding at elevated temperature	160
I. Experimental details.....	160
II. Friction behaviour at elevated temperature.....	160
III. Wear behaviour at elevated temperature	165
IV. Wear mechanism during dry sliding at elevated temperature	176
4.4.3. Tribological behaviour of Mo–W–C coatings during boundary lubricated sliding at elevated temperature (200°C).....	177
I. Experimental details.....	177
II. Friction behaviour of Mo–W–C coatings during lubricated sliding	177
III. Wear behaviour of steel counterparts during lubricated sliding	178
IV. Wear behaviour of Mo–W–C coatings during lubricated sliding	188
V. Tribo-chemically reactive wear mechanism during lubricated sliding at elevated temperature	192
4.4.4. Comparison of tribological performance of C4 and DLC (Cr/Cr-WC/W:C-H/a:C-H) coatings at elevated temperature.....	193
A. Dry sliding against Al ₂ O ₃ counterparts	193
B. Lubricated sliding against Al ₂ O ₃ counterparts.....	197
C. Lubricated sliding against steel counterparts.....	200
4.4.5. Concluding remarks	203
5. Conclusions	204
5.1. Summary	204
5.2. Contributions and achievements	205
5.3. Further scope.....	208
References	209
APPENDIX - A	224

Abstract

Low friction and high temperature wear resistant PVD coatings are in high demand for use on engine components, which operate in extreme environment. Diamond-like-carbon (DLC) coatings are extensively used for this purpose due to their excellent tribological properties. However, DLC degrades at high temperature and pressure conditions leading to significant increase in friction and wear rate even in the presence of lubricant. To withstand high working temperature and simultaneously maintain improved tribological properties in lubricated condition at ambient and at high temperature, both the transitional metals Mo and W are simultaneously introduced in a carbon-based coating (Mo–W–C) for the first time utilising the benefits of smart material combination and High Power Impulse Magnetron Sputtering (HIPIMS).

This research includes development of Mo–W–C coating and investigation of thermal stability and tribological properties at ambient and high temperatures. The as-deposited Mo–W–C coating contains nanocrystalline almost X-ray amorphous structure and show dense microstructure, good adhesion with substrate ($L_c \sim 80$ N) and high hardness (~ 17 GPa). During boundary lubricated sliding (commercially available engine oil without friction modifier used as lubricant) at ambient temperature, Mo–W–C coating outperforms commercially available state-of-the-art DLC coatings by providing significantly low friction ($\mu \sim 0.03 - 0.05$) and excellent wear resistance (no measurable wear). When lubricated sliding tests are carried out at 200°C , Mo–W–C coating provides low friction similar to ambient temperature, whereas degradation of DLC coating properties fails to maintain low friction coefficient.

A range of surface analyses techniques reveal "in-situ" formation of solid lubricants (WS_2 and MoS_2) at the tribo-contacts due to *tribochemically reactive* wear mechanism at ambient and high temperature. Mo–W–C coating reacts with EP additives present in the engine oil during sliding to form WS_2 and MoS_2 . This mechanism is believed to be the key-factor for low friction properties of Mo–W–C coating and presence of graphitic carbon particles further benefits the friction behaviour. It is observed that low friction is achieved mostly due to formation of WS_2 at ambient temperature, whereas formation of both WS_2 and MoS_2 significantly decreases the friction of Mo–W–C coating at high temperature. This further indicates importance of combined Mo and W doping over single-metal doping into carbon-based coatings.

Isothermal oxidation tests indicate that Mo–W–C coating preserves its as-deposited graphitic nature up to 500°C , whereas local delamination of DLC coating leads to substrate exposure and loss of its diamond-like structure at the same temperature. Further, thermo-gravimetric tests confirm excellent thermal stability of Mo–W–C coating compared to DLC. Mo–W–C coating resists oxidation up to $\sim 800^\circ\text{C}$ and no coating delamination is observed due to retained coating integrity and its strong adhesion with substrate. On the other hand, state-of-the-art DLC coating starts to delaminate beyond $\sim 380^\circ\text{C}$.

The test results confirm that Mo–W–C coating sustains high working temperature and simultaneously maintains improved tribological properties during boundary lubricated condition at ambient and high temperature. Thus Mo–W–C coating is a suitable candidate for low friction and high temperature wear resistant applications compared to commercially available state-of-the-art DLC coatings.

Acknowledgements

I express my sincere gratitude to my PhD supervisor Prof. Papken Hovsepian and my co-supervisor Prof. Arutiun Ehiasarian for their encouragement and continuous guidance during this research. Their methods of conducting research, presenting results and writing journal articles motivated me to build my research portfolio. Further I would like to thank Mr. Roel Tietema, my co-supervisor from IHI Hauzer Techno Coating BV for the fruitful discussions and providing financial support.

A strong support from Dr. Yashodhan Purandare deserves special mention. He helped me with my experiments and tutored me on instruments in spite of his busy schedule. A special thanks to Mr. Stuart Creasy, who taught me scanning electron microscopy. I would also like to acknowledge the co-operation and the support I got from my colleagues Mr. Daniel Loch, Miss Anna Oniszczyk, Mr. Tom Morton, Mr. Gary Robinson and Dr. A. Sugumaran during this tenure. Further I would express my warm gratitude for the care and concern of Nilanjan-da, Debajyoti-da, Avishek-da, Arnab-da and Barnali during this time.

I am grateful to MERI (Materials and Engineering Research Institute) staffs and administrators, particularly Corrie, Rachel, Gail and Gillian for their help and support throughout my doctoral tenure. I am further grateful to MERI, Sheffield Hallam University and Hauzer Techno Coating for awarding me a three-year scholarship without which this research would not be feasible.

And I profoundly express my heartfelt reverence to my parents whose day-night good wishes and blessings have constantly inspired me.

Paranjayee Mandal

Advanced Studies

The following conferences and courses were attended and the presentations were given during the course of study:

1. 3rd International Conference on Fundamentals and Applications of HIPIMS, Sheffield, UK (2012)
2. Cost action on highly ionised pulsed plasma processes: MP0804, tutorial courses attended at Sheffield Hallam University, United Kingdom (December, 2012)
3. MERI Research Symposium (May, 2013) (poster)
4. 4th International Conference on Fundamentals and Applications of HIPIMS, Braunschweig, Germany (2013) (poster)
5. MERI Research Symposium (May, 2014) (oral)
6. SVC tutorial courses C-323, C-333 and C-338 attended (2013 and 2014)
7. 5th International Conference on Fundamentals and Applications of HIPIMS, Sheffield, UK (2014) (poster)
8. 14th International Conference on Plasma Surface Engineering, Garmisch-Partenkirchen, Germany (2014) (poster)
9. 58th SVC Annual Technical Conference (TechCon), Santa Clara, USA (2015) (oral)

Publications

Journal publications:

1. P. Mandal, A.P. Ehasarian, P. Eh. Hovsepian, "Lubricated sliding wear mechanism of chromium-doped graphite-like carbon coating", *Tribology International*, 77 (2014) 186–195
2. P. Mandal, A.P. Ehasarian, P. Eh. Hovsepian, "Tribological behaviour of Mo – W doped carbon-based coating at ambient condition", *Tribology International*, 90 (2015) 135–147
3. P. Mandal, A.P. Ehasarian, P. Eh. Hovsepian, "Isothermal and dynamic oxidation behaviour of Mo – W doped carbon-based coating", *Applied Surface Science*, 353 (2015) 1291–1309
4. P. Mandal, A.P. Ehasarian, P. Eh. Hovsepian, "Wear mechanism of Mo–W doped carbon-based coating during boundary lubricated sliding", manuscript to be communicated to *Carbon*

Conference publication:

5. P. Mandal, A.P. Ehasarian, P. Eh. Hovsepian, "Wear mechanism of Mo–W doped carbon-based coating during boundary lubricated sliding", manuscript submitted to *58th SVC Annual Technical Conference Proceedings*, 2015

Publication not directly related to this thesis:

6. A.A. Sugumaran, Y. Purandare, P. Mandal, A.P. Ehasarian, I. Khan, P.Eh. Hovsepian, "Effect of the Degree of High Power Impulse Magnetron Sputtering (HIPIMS) Utilisation on the Corrosion Properties of TiN Films", *56th Annual Technical Conference Proceedings, Providence, RI; 04/2013*

Acronyms

DLC	Diamond-like carbon
μ	Friction coefficient
K_c	Wear coefficient
Mo-DTC	Molybdenum dithiocarbamate
ZDDP	Zinc dialkyl dithiophosphate
Ti-DLC	Titanium-doped DLC
Mo-DLC	Molybdenum-doped DLC
W-DLC	Tungsten-doped DLC
Cr-DLC	Chromium-doped DLC
Fe-DLC	Ferrous-doped DLC
a-C	Amorphous carbon
ta-C	Tetrahedral amorphous carbon
a:C-H	Hydrogenated DLC
W:C-H	Tungsten-doped hydrogenated DLC
WC:C-H	Tungsten carbide-doped hydrogenated DLC
a:C-H-Si	Silicon-doped hydrogenated DLC
Me-DLC	Metal-doped DLC
PVD	Physical vapour deposition
CVD	Chemical vapour deposition
PACVD/PECVD	Plasma activated/enhanced CVD
RF	Radio frequency
UBM	Unbalanced magnetron sputtering
CFUBMS	Closed field UBM
HIPIMS	High power impulse magnetron sputtering
SZM	Structure zone model
Mo-W-C	Mo – W doped carbon-based coating
C2	Mo-W-C coating deposited at 2 kW target power
C4	Mo-W-C coating deposited at 4 kW target power
C6	Mo-W-C coating deposited at 6 kW target power
PAO	Polyalphaolefins
AW	Anti-wear
EP	Extreme-pressure
SEM	Scanning electron microscopy
EDX	Energy dispersive X-ray
XRD	X-ray diffraction
TGA	Thermo-gravimetric analysis
XPS	X-ray photoelectron spectroscopy
AES	Auger electron spectroscopy

List of Figures

Figure 2-1: Schematic images of four major wear modes	11
Figure 2-2: Hybridised orbitals of Carbon atoms (a) sp^1 , (b) sp^2 and (c) sp^3	12
Figure 2-3: Crystal structure of (a) graphite and (b) diamond	13
Figure 2-4: Schematic diagrams of various processes used to deposit DLC coating [3]	16
Figure 2-5: Schematic diagram of the mechanism of sputter deposition.....	33
Figure 2-6: Schematic representation of the plasma confinement observed in balanced and unbalanced magnetrons [135]	34
Figure 2-7: Schematic representation of dual unbalanced magnetron system [135]	35
Figure 2-8: schematic representation of (a) DC magnetron sputtering and (b) HIPIMS process.....	37
Figure 2-9: Structure zone model of thick films by Movchan and Demchishin in 1969	38
Figure 2-10: Structure zone model of sputtered films by Thornton in 1974	39
Figure 2-11: Structure zone model of ion beam assisted sputtered films by Messier in 1984.....	39
Figure 3-1: Schematic of the cathode configuration in HTC 1000-4 PVD coating machine during Mo–W–C coating deposition	44
Figure 3-2: Classification of levels of interfacial adhesion of thin films based on typical indentation results according to the VDI standard of acceptability [156]	45
Figure 4.1-1: (a – c) Surface morphology and (d – f) cross-sectional SEM image of as-deposited Mo–W–C coatings.....	52
Figure 4.1-2: Average surface roughness and surface profile (in the inset) of as-deposited Mo–W–C coatings	53
Figure 4.1-3: X-ray mapping of elements on the fracture cross-section of as-deposited C2	54
Figure 4.1-4: X-ray mapping of elements on the fracture cross-section of as-deposited C4	55
Figure 4.1-5: X-ray mapping of elements on the fracture cross-section of as-deposited C6	56
Figure 4.1-6: XRD patterns of as-deposited Mo–W–C coatings collected using Bragg-Brentano geometry	57
Figure 4.1-7: XRD patterns of as-deposited Mo–W–C coatings collected using glancing angle ($\omega = 2^\circ$) geometry	58
Figure 4.1-8: (a – c) Low angle XRD patterns and (d) the bilayer thickness of as-deposited Mo–W–C coatings	59
Figure 4.1-9: (a – c) Raman spectra collected from as-deposited Mo–W–C coatings ...	61
Figure 4.1-10: (a – c) Characteristic loading-unloading curves of as-deposited Mo–W–C coatings	63
Figure 4.1-11: Nanohardness and elastic modulus of as-deposited Mo–W–C coatings	64
Figure 4.1-12: Adhesive strength of as-deposited Mo–W–C coatings showing (a – c) critical loads and (d – f) SEM images of the respective scratch track ends at 100 N applied load.....	65
Figure 4.1-13 : Optical images of the indents indicating interfacial adhesion strength of as-deposited Mo–W–C coatings	66
Figure 4.1-14: EDX analysis of the indent on as-deposited C2.....	67
Figure 4.1-15: EDX analysis of the indent on as-deposited C4.....	68
Figure 4.1-16: EDX analysis of the indent on as-deposited C6.....	68

Figure 4.2-1: Friction behaviour of Mo–W–C coatings against steel counterparts.....	73
Figure 4.2-2: (a – c) Transfer layer formed on the steel counterparts and (d – f) debris strongly adhered to the counterpart surfaces after dry sliding	74
Figure 4.2-3: X-ray mapping of the debris adhered to the counterpart surfaces (steel ball) after dry sliding against Mo–W–C coatings	77
Figure 4.2-4: Raman spectra collected from the (a) uncoated steel ball and (b – d) wear scar on the steel balls after dry sliding against Mo–W–C coatings.....	79
Figure 4.2-5: (a – c) Raman spectrum collected from the debris adhered to the steel counterparts after dry sliding against Mo–W–C coatings	82
Figure 4.2-6: (a – c) SEM images of the wear track on the Mo–W–C coatings after dry sliding against steel ball	84
Figure 4.2-7: Wear track profile of Mo–W–C coatings after dry sliding against steel ball	85
Figure 4.2-8: (a – c) Raman spectra collected within the wear tracks of Mo–W–C coatings after dry sliding against steel balls	88
Figure 4.2-9: (a – c) Friction behaviour of Mo–W–C coatings in lubricated condition against steel counterparts	94
Figure 4.2-10: Wear track profiles of the Mo–W–C coatings after lubricated sliding against steel balls.....	95
Figure 4.2-11: Friction behaviour of coating C4 in lubricated sliding condition against steel counterpart for a sliding distance of 15 km	96
Figure 4.2-12: Raman spectrum collected from the thin lubricant film (Mobil1 Extended life™ 10W-60) placed on a glass slide.....	97
Figure 4.2-13: (a – c) Raman spectra collected within the wear tracks of Mo–W–C coatings after lubricated sliding against steel balls	99
Figure 4.2-14: Raman spectra collected from (a) WS ₂ and (b) MoS ₂ powder.....	100
Figure 4.2-15: Friction behaviour of C4 during lubricated sliding against Al ₂ O ₃ ball.	101
Figure 4.2-16: Raman spectra collected within the wear track of C4 after lubricated sliding against Al ₂ O ₃ ball.....	102
Figure 4.2-17: Friction behaviour and wear track profiles of C/Cr coating against steel ball in dry and lubricated sliding conditions	105
Figure 4.2-18: Raman spectra collected from the (a) as-deposited Cr/C coating and the wear track after (b) dry and (c) lubricated sliding against steel balls	109
Figure 4.2-19: Raman spectrum collected from Cr ₂ S ₃ powder sample	110
Figure 4.2-20: (a) Atomic structure of CrCl ₃ [197] and (b) stacking of layers in CrCl ₃ crystal structure [198]	110
Figure 4.2-21: Friction behaviour of Cr/C and Mo–W–C coatings against steel balls	112
Figure 4.2-22: Wear track profiles and wear coefficients of Cr/C and Mo–W–C coatings after dry sliding against steel balls.....	112
Figure 4.2-23: Friction behaviour of Cr/C and Mo–W–C coatings in lubricated condition against steel counterparts	113
Figure 4.2-24: Wear track profiles of Cr/C and Mo–W–C coatings after lubricated sliding against steel balls.....	113
Figure 4.2-25: Friction behaviour of C4 and state-of-the-art DLC coatings	114
Figure 4.2-26: Wear track profile of state-of-the-art DLC coatings after dry sliding against steel balls.....	115
Figure 4.2-27: Friction behaviour of state-of-the-art DLC coatings and coating C4 against steel balls during lubricated sliding	116
Figure 4.2-28: Wear track profiles of $DLC(Cr/Cr-WC/W:C-H/a:C-H)$ and C4 against steel ball after lubricated sliding	116

Figure 4.2-29: Raman spectra collected from the (a) as-deposited $DLC(Cr/Cr-WC/W:C-H/a:C-H)$ coating and the wear track after (b) dry and (c) lubricated sliding against steel balls	118
Figure 4.2-30: Raman spectrum collected from the debris beside the wear track of $DLC(Cr/Cr-WC/W:C-H/a:C-H)$ coating after dry sliding.....	119
Figure 4.2-31: Friction behaviour and wear track profiles of C4 and $DLC(Cr/Cr-WC/W:C-H/a:C-H)$ after dry sliding against Al_2O_3 balls	120
Figure 4.2-32: Friction behaviour and wear track profiles of C4 and $DLC(Cr/Cr-WC/W:C-H/a:C-H)$ after lubricated sliding against Al_2O_3 balls	120
Figure 4.2-33: Raman spectra collected from the wear track of $DLC(Cr/Cr-WC/W:C-H/a:C-H)$ after (a) dry and (b) lubricated sliding against Al_2O_3 balls.....	121
Figure 4.3-1: Surface morphology of heat-treated Mo-W-C coatings (400°C – 800°C)	125
Figure 4.3-2: Average surface roughness of isothermally oxidised Mo-W-C coatings	126
Figure 4.3-3: X-ray mapping on the cross-sections of C4 after heat-treated at (a) 400°C, (b) 500°C, (c) 600°C, (d) 700°C and (e) 800°C.....	130
Figure 4.3-4: (a – c) XRD patterns of as-deposited and isothermally oxidised Mo-W-C coatings collected using Bragg-Brentano geometry	133
Figure 4.3-5: (a – c) Glancing angle XRD patterns of as-deposited and isothermally oxidised (400°C – 600°C) Mo-W-C coatings.....	137
Figure 4.3-6: Raman spectra of C2 (a) as-deposited – heat-treated at 500°C and (b) heat-treated at 600°C – 800°C	141
Figure 4.3-7: Raman spectra of C4 (a) as-deposited – heat-treated at 500°C and (b) heat-treated at 600°C – 800°C	142
Figure 4.3-8: Raman spectra of C6 (a) as-deposited – heat-treated at 500°C and (b) heat-treated at 600°C – 800°C	143
Figure 4.3-9: (a – c) Nanohardness of Mo-W-C coatings in as-deposited condition and after isothermal oxidation	145
Figure 4.3-10: Thermo-gravimetric results obtained for Mo-W-C coatings.....	146
Figure 4.3-11: (a – c) SEM images showing the surface morphology of Mo-W-C coated samples after thermo-gravimetric tests	147
Figure 4.3-12: XRD patterns collected from Mo-W-C coatings after thermo-gravimetric tests using (a) Bragg-Brentano and (b) glancing angle geometry.....	149
Figure 4.3-13: Raman spectra collected from Mo-W-C coatings after thermo-gravimetric tests	150
Figure 4.3-14: Nanohardness of Mo-W-C coatings in as-deposited condition and after thermo-gravimetric tests.....	150
Figure 4.3-15: (a) Surface morphology and (b) X-ray mapping on the cross-section of $DLC(Cr/Cr-WC/W:C-H/a:C-H)$ coated sample isothermally heated to 400°C	152
Figure 4.3-16: (a) Surface morphology and (b) X-ray mapping on the cross-section of $DLC(Cr/Cr-WC/W:C-H/a:C-H)$ coated sample isothermally heated to 500°C	152

Figure 4.3-17: XRD patterns (using Bragg-Brentano geometry) of as-deposited and isothermally heat-treated $DLC(Cr/Cr-WC/W:C-H/a:C-H)$ coating	153
Figure 4.3-18: Raman spectra of as-deposited and isothermally heat-treated $DLC(Cr/Cr-WC/W:C-H/a:C-H)$ coating	154
Figure 4.3-19: Nanohardness of C4 and $DLC(Cr/Cr-WC/W:C-H/a:C-H)$ coatings in as-deposited condition and after isothermal oxidation	156
Figure 4.3-20: Dynamic oxidation behaviour of C4 and $DLC(Cr/Cr-WC/W:C-H/a:C-H)$	157
Figure 4.4-1: Friction behaviour of Mo-W-C coatings after dry sliding against Al_2O_3 balls at (a) ambient temperature, (b) 200°C, (c) 400°C and (d) 500°C.....	162
Figure 4.4-2: Transfer layer formed on the Al_2O_3 counterparts after dry sliding against Mo-W-C coatings at (a) ambient temperature, (b) 200°C, (c) 400°C and (d) 500°C ..	163
Figure 4.4-3: Raman spectra collected from the debris adhered to the Al_2O_3 balls after sliding against C2 at (a) 200°C, (b) 400°C and (c) 500°C	164
Figure 4.4-4: Wear coefficient of Al_2O_3 balls after dry sliding against Mo-W-C coatings at ambient and elevated temperature.....	165
Figure 4.4-5: SEM images of the wear tracks of C2 after dry sliding against Al_2O_3 balls at (a) ambient temperature, (b) 200°C, (c) 400°C and (d) 500°C	167
Figure 4.4-6: SEM images of the wear tracks of C4 after dry sliding against Al_2O_3 balls at (a) ambient temperature, (b) 200°C, (c) 400°C and (d) 500°C	168
Figure 4.4-7: SEM images of the wear tracks of C6 after dry sliding against Al_2O_3 balls at (a) ambient temperature, (b) 200°C, (c) 400°C and (d) 500°C	169
Figure 4.4-8: Wear track profiles of Mo-W-C coatings after dry sliding against Al_2O_3 balls at (a) ambient temperature, (b) 200°C, (c) 400°C and (d) 500°C.....	170
Figure 4.4-9: Wear coefficient of Mo-W-C coatings after dry sliding against Al_2O_3 balls at ambient and elevated temperature.....	170
Figure 4.4-10: (a – e) Raman spectra collected from the wear tracks of Mo-W-C coatings after sliding against Al_2O_3 balls at ambient temperature	172
Figure 4.4-11: (a – f) Raman spectra collected from the wear tracks of Mo-W-C coatings after sliding against Al_2O_3 balls at 200°C	173
Figure 4.4-12: (a – f) Raman spectra collected from the wear tracks of Mo-W-C coatings after sliding against Al_2O_3 balls at 400°C	174
Figure 4.4-13: (a – c) Raman spectra collected from the wear tracks of Mo-W-C coatings after sliding against Al_2O_3 balls at 500°C	175
Figure 4.4-14: Friction behaviour of Mo-W-C coatings at 200°C in lubricated condition against steel counterparts	178
Figure 4.4-15: (a – c) Transfer layer formed on the steel counterparts and (d – f) debris strongly adhered to the steel counterparts after lubricated sliding at 200°C.....	179
Figure 4.4-16: (a – c) X-ray mapping of the debris adhered to the steel counterpart after lubricated sliding against Mo-W-C coatings at 200°C	180
Figure 4.4-17: (a – c) SEM images and EDX analysis of the debris adhered to the steel counterpart after lubricated sliding against Mo-W-C coatings at 200°C	183
Figure 4.4-18: Raman spectra collected from the debris adhered to the steel counterpart after lubricated sliding against C2 at 200°C.....	185
Figure 4.4-19: Raman spectra collected from the debris adhered to the steel counterpart after lubricated sliding against C4 at 200°C.....	186

Figure 4.4-20: Raman spectra collected from the debris adhered to the steel counterpart after lubricated sliding against C6 at 200°C.....	187
Figure 4.4-21: (a – c) SEM images of the wear tracks of Mo–W–C coatings after lubricated sliding against steel balls at 200°C.....	189
Figure 4.4-22: Wear track profile of Mo–W–C coatings after lubricated sliding against steel balls at 200°C.....	190
Figure 4.4-23: (a – c) Raman spectra collected within the wear track of Mo–W–C coatings after lubricated sliding against steel balls at 200°C	191
Figure 4.4-24: Friction behaviour of $DLC(Cr/Cr-WC/W:C-H/a:C-H)$ coating after dry sliding against Al_2O_3 balls at ambient and elevated temperature.....	193
Figure 4.4-25: Wear track profile of $DLC(Cr/Cr-WC/W:C-H/a:C-H)$ coating after dry sliding against Al_2O_3 balls at ambient and elevated temperature.....	195
Figure 4.4-26: Raman spectra collected from the wear track of $DLC(Cr/Cr-WC/W:C-H/a:C-H)$ coating (a) ambient temperature, (b) 200°C, (c) 400°C and (d) 500°C	196
Figure 4.4-27: Friction behaviour of C4 and $DLC(Cr/Cr-WC/W:C-H/a:C-H)$ coatings after lubricated sliding against Al_2O_3 counterparts at 200°C.....	198
Figure 4.4-28: Wear track profiles of $DLC(Cr/Cr-WC/W:C-H/a:C-H)$ and C4 after lubricated sliding against Al_2O_3 counterparts at 200°C	198
Figure 4.4-29: Raman spectra collected from the wear track of C4 after lubricated sliding against Al_2O_3 balls at 200°C.....	199
Figure 4.4-30: Raman spectrum collected from the wear track of DLC coating after lubricated sliding against Al_2O_3 balls at 200°C.....	199
Figure 4.4-31: Friction behaviour of C4 and $DLC(Cr/Cr-WC/W:C-H/a:C-H)$ coatings after lubricated sliding against steel counterparts at 200°C.....	200
Figure 4.4-32: Wear track profile of $DLC(Cr/Cr-WC/W:C-H/a:C-H)$ coating after lubricated sliding at 200°C.....	201
Figure 4.4-33: Raman spectra collected from (a) debris adhered to the steel ball and the (b) wear track of $DLC(Cr/Cr-WC/W:C-H/a:C-H)$ coating after lubricated sliding at 200°C	202

List of Tables

Table 2-1: Influence of doping elements on the properties of DLC coating	17
Table 2-2: Properties of the base oil according to API [125]	21
Table 3-1: Sputtering yield of materials at different sputtering angles in argon atmosphere (for acceleration energy of 500 eV)	42
Table 3-2: Principal process steps of combined HIPIMS + UBM deposition procedure for Mo–W–C coatings	44
Table 4.1-1: Structural properties of as-deposited Mo–W–C coatings	69
Table 4.2-1: Typical properties of Mobil1 Extended life™ 10W-60 engine oil [186] ...	92
Table A-1: Raman peaks of the spectra collected from as-deposited Mo–W–C coatings	224
Table A-2: Raman peaks of the spectra collected from the uncoated steel ball and the wear scar on the steel balls after dry sliding against Mo–W–C coatings.....	225
Table A-3: Raman peaks of the spectra collected from the debris adhered to the steel counterpart after dry sliding against Mo–W–C coatings.....	226
Table A-4: Raman peaks of the spectra collected within the wear track of Mo–W–C coatings after dry sliding against steel balls.....	227
Table A-5: Raman peaks of the spectra collected within the wear track of Mo–W–C coatings after lubricated sliding against steel balls	228
Table A-6: Raman peaks of the spectrum collected within the wear track of C4 after lubricated sliding against Al ₂ O ₃ ball.....	229
Table A-7: Raman peaks of the spectra collected from the (a) as-deposited Cr/C coating and the wear track after (b) dry and (c) lubricated sliding against steel balls.....	229
Table A-8: Raman peaks of the metal carbides present in C4 after heat-treated to 400°C	230
Table A-9: Raman peaks of the metal carbides and metal oxides present in C4 after heat- treated to 500°C	231
Table A-10: Raman peaks of the metal oxides present in C4 after heat-treated to 600°C	231
Table A-11: Raman peaks of the metal oxides present in C4 after heat-treated to 700°C	232
Table A-12: Raman peaks of the metal oxides present in C4 after heat-treated to 800°C	232
Table A-13: Raman peaks of the metal carbides and metal oxides present in Mo–W–C coatings after dynamic oxidation	233
Table A-14: Raman peaks of the debris adhered to the Al ₂ O ₃ balls after sliding against C2 at elevated temperature.....	234

Table A-15: Raman peaks of the spectra collected within the wear track of Mo–W–C coatings after sliding against Al ₂ O ₃ balls at ambient temperature.....	234
Table A-16: Raman peaks of the spectra collected within the wear track of Mo–W–C coatings after sliding against Al ₂ O ₃ balls at 200°C.....	236
Table A-17: Raman peaks of the spectra collected within the wear track of Mo–W–C coatings after sliding against Al ₂ O ₃ balls at 400°C.....	238
Table A-18: Raman peaks of the spectra collected within the wear track of Mo–W–C coatings after sliding against Al ₂ O ₃ balls at 500°C.....	239
Table A-19: Raman peaks of the spectra collected from the adhered debris on the steel ball after lubricated sliding against Mo–W–C coatings at 200°C.....	241
Table A-20: Raman peaks of the spectra collected from the wear track of the Mo–W–C coatings after lubricated sliding against steel balls at 200°C.....	242
Table A-21: Raman peaks of the spectra collected from the wear track of C4 after lubricated sliding against Al ₂ O ₃ ball at 200°C.....	243

1. Introduction

1.1. Background

Mating components in an automotive industry such as piston-cylinder assembly of an engine often undergo high-cycle fatigue during operation, which results in wear and corrosion of the components and higher consumption of fuel leading to non-eco-friendly vehicle health. Wear can be minimised by modifying the atomistic structure of the exposed surfaces using different surface modification processes such as hardening, carburizing, nitriding and ion implantation. For example, surface layer with high ductility reduces wear due to delamination yet fails to prevent abrasive wear. A hard surface layer reduces abrasive wear but experiences brittle fracture. On the other hand, deposition of protective coatings on the surface by physical vapour deposition, electroplating, cladding, galvanisation and chemical processes significantly decreases friction and wear. The performance of protective coatings depends on their microstructure and deposition procedures, which in turn determine hardness, chemical and thermal stability and sometimes provide good tribological properties. Typically *hard coatings* possess high hardness, good wear resistance, better thermal stability and anti-sticking properties whereas *soft coatings* provide low friction coefficient but in turn, they suffer from low hardness, high wear rates and poor thermal stability. Therefore new generation coatings come into practice when the components operate in extreme environment and experience high friction and wear. These coatings tend to exhibit low friction, improved wear resistance and higher thermal stability in order to protect the components and decrease the total energy consumption.

Use of coated engine parts enhances engine performance (in terms of low friction and better wear resistance) compared to uncoated components made of cast iron and steel. Wear and temperature resistant coatings such as TiN, CrN, TiAlN, AlCrN, WC/C are applied on the components, which experience high mechanical and thermal loads, whereas metal-free (and in some cases, metal-doped) diamond-like-carbon (DLC) coatings are extensively used as tribological coatings because of their excellent combination of low friction and improved wear resistance properties. Engine parts such as piston rings, piston pins, cam followers, cam shafts, rockers, gears and tappets are often

coated with DLC and involve interfacial contacts with either steel or DLC coated surfaces in the presence of lubricant (mostly engine oil).

Amorphous carbon coatings possess an excellent combination of friction and wear properties ($\mu < 0.1$ and $K_c < 10^{-17} \text{ m}^3\text{N}^{-1}\text{m}^{-1}$) [1], high hardness ($> 20 \text{ GPa}$) [1, 2] and chemical inertness, which make them suitable for tribological applications. Depending on the ratio of sp^2 (graphite-like) to sp^3 (diamond-like) bonded carbon atoms, amorphous carbon coatings can adapt either graphite-like or diamond-like properties or a combination of properties within this range [3, 4]. Graphitic carbon coatings (with higher sp^2 content) provide lower friction and wear coefficients ($\mu < 0.1$ and $K_c \sim 10^{-17} \text{ m}^3\text{N}^{-1}\text{m}^{-1}$ respectively) compared to diamond-like-carbon (DLC) coatings in humid air or in water lubricated condition [2]. Depending on the deposition procedure and test conditions, DLC coatings provide high wear resistance ($K_c < 10^{-16} \text{ m}^3\text{N}^{-1}\text{m}^{-1}$) [2] and a wide range of friction coefficients ($\mu = 0.05 - 1.0$ at ambient air with 20% – 60% relative humidity and $\mu = 0.007 - 0.4$ in vacuum under low pressure below 10^{-4} Pa) [4] along with varying hardness values (10 – 80 GPa) [2, 4, 5].

Commercial use of standard DLC coating is often compromised due to low adhesion strength and poor thermal stability. The adhesion is deteriorated because of accumulation of high compressive residual stress (up to 13 GPa [4]) and formation porous and weak interface between coating and substrate [6]. On the other hand, graphitisation (i.e. transformation of diamond-like structure into graphite-like structure) of DLC coating starts at $\sim 350^\circ\text{C}$ [7 – 9] and further rise in temperature up to $\sim 450^\circ\text{C}$ results in complete transformation of DLC coating into nanocrystalline graphite [9] ultimately leading to drastic failure.

Excellent tribological properties of DLC coating are significantly affected at high working temperature. In ambient air or in inert atmosphere, DLC coating shows steady-state low friction and high wear resistance due to formation of graphitic tribolayer at the asperity contacts [10, 11]. For hydrogenated DLC coating, the rate of graphitisation decreases with increase in humidity level [12 – 14] leading to higher friction and wear. It was reported that the tribological behaviour started to change at $\sim 100^\circ\text{C}$ and low friction was observed up to $\sim 300^\circ\text{C}$ depending on the test conditions ($\sim 30\%$ relative humidity) [15, 16]. However at higher temperature ($> 300^\circ\text{C}$), graphitisation of DLC coating

degraded the coating properties [7 – 9] leading to substantial increase in both the friction and wear [17]. Incorporation of metal and non-metal doping elements into the DLC coating is a standard technique to delay the graphitisation process and to increase adhesion strength. For example, addition of tungsten (W) into the DLC coating improves coating-substrate adhesion [18 – 20] as well as thermal stability [21]. Depending on test conditions, metal-doped DLC coatings maintain low friction and wear under severe operating conditions [22 – 24].

The presence of lubricant (engine oil) benefits the tribological properties of DLC coating at high working temperature. The lubricant isolates the coating from the hostile environment of the surroundings and acts as a coolant. Further the polymer additives present in the engine oil react with DLC coating and form an in-situ low friction tribofilm at the asperity contacts. A research showed that no stable tribofilm was formed on the DLC coated surface when engine oil with additives was used lubricant [25], however other studies reported the formation of tribofilm on DLC coating in boundary lubricated condition [26, 27].

When engine oil contains friction modifier such as Molybdenum dithiocarbamate (Mo-DTC), a tribolayer containing both MoS_2 and MoO_3 is formed during sliding. At high working temperature, thermal decomposition of Mo-DTC results in formation of MoO_3 layer over the surface. The rubbing action between the coating and the steel counterpart mechanically removes the oxide layer and exposes the iron surface, which initiate the formation of MoS_2 at asperity contacts due to high flash temperature [28 – 31]. The friction is significantly reduced due to formation of this MoS_2 ; however MoO_3 acts as a third-body abrasive media and deteriorates wear resistance properties of DLC coating [32]. The phosphorus-based additive such as Zinc dialkyl dithiophosphate (ZDDP), present in the engine oil, promotes formation of MoS_2 [27, 33] over MoO_3 [27] but generates some harmful reaction products, which affect the tribolayer formation and eventually contaminate the oil [34]. In addition, metal-doped DLC coatings show enhanced tribological performance in boundary lubricated condition due to formation of high strength metal carbides in the defective parts of the carbon network. For example, Ti-DLC, Mo-DLC and Fe-DLC coatings deposited using RF magnetron sputtering outperform metal-free DLC coating in boundary lubricated condition, where engine oil containing both ZDDP and Mo-DTC was used as lubricant [26].

Sputtered DLC (a-C), hydrogen-free DLC (ta-C), metal-free hydrogenated DLC (a:C-H), W, WC and Si doped hydrogenated DLC (W:C-H, WC:C-H and a:C-H-Si) coatings are commercially available tribological coatings to coat various engine components, which experience high mechanical loads and wear during sliding at high temperature. Most of them provide friction coefficient in the range of 0.05 – 0.2 in dry sliding (i.e. no lubricant used) against steel counterpart depending on applications and test conditions [35 – 42] and the maximum working temperature of these coatings is mostly found in the range of 300°C – 350°C [35 – 39, 41, 42].

1.2. Problem definition

It is quite challenging to use DLC coating on the engine components such as piston-cylinder and valve-train assembly, which are operated at relatively high temperature and pressure conditions and at high sliding velocity. The maximum operating temperature for these components are 300°C and 150°C respectively [43]. DLC coating easily survives this temperature in the presence of lubricant, however the tribological behaviour depends on the counterpart material (mostly steel and sometimes DLC coated surfaces) and the reactivity of lubricant with the counterfaces. The a-C/steel tribo-pair combination provides low friction coefficient compared to steel/steel and a-C:H/steel combinations in lubricated condition [12, 44], whereas a-C:H/steel combination improves the wear resistance compared to steel/steel and a-C/steel combinations [12, 27, 44]. In addition, applied force and sliding velocity directly influence the wear of DLC coatings. Higher the force and sliding velocity, wear becomes significant [44, 45].

The friction and wear coefficients of the DLC/steel, DLC/DLC and Me-DLC/Me-DLC tribo-pair combinations are observed in the range of $\sim 0.04 - 0.13$ and $\sim 10^{-9} - 10^{-19} \text{ m}^3 \text{N}^{-1} \text{m}^{-1}$ respectively under different test parameters (including test setup, normal force, contact pressure, sliding velocity, lubricant etc.) at ambient condition [11]. Both the metal-free DLC (ta-C, a-C, a-C:H) and metal-doped (such as Si, Ti and W) DLC coatings produce low friction tribolayer under different lubricated conditions in the range of 50°C – 100°C [27, 32, 46 – 53]. However in some cases no tribolayer is formed for metal-free DLC (ta-C, a-C, DLC:H) coating even when the working temperature is in the range of 100°C – 110°C [54 – 56]. Irrespective of tribolayer formation, the friction and wear

coefficients of these coatings are documented in the range of $\sim 0.02 - 0.14$ and $\sim 10^{-17} - 10^{-18} \text{ m}^3\text{N}^{-1}\text{m}^{-1}$ respectively under different test parameters (including test temperature in the range of $50^\circ\text{C} - 110^\circ\text{C}$) [57]. This indicates that the metal-free and metal-doped DLC coatings maintain almost similar tribological properties from ambient temperature up to 110°C . When lubricated sliding tests are conducted at 150°C with different additive combinations, the friction coefficients of DLC/DLC contact are observed fairly high ($\mu \sim 0.1 - 0.3$) [58]. Similar friction behaviour ($\mu \sim 0.1 - 0.3$) is observed for DLC/steel and W-DLC/steel contacts at 200°C and absence of tribolayer during sliding simultaneously increases the wear coefficients ($K_c \sim 10^{-15} \text{ m}^3\text{N}^{-1}\text{m}^{-1}$) when tested under different lubricant combinations [46, 59].

It is important to note that the available literatures report the excellent tribological properties of metal-free and metal-doped DLC coatings in lubricated condition are maintained up to 110°C . In high temperature ($150^\circ\text{C} - 200^\circ\text{C}$) lubricated sliding tests, degradation of coating properties leads to significant increase in friction and wear rate. Therefore, these metal-free and metal-doped DLC coatings might not be suitable for components used in piston-cylinder and valve-train assembly as they are operated at much higher temperature (maximum 150°C and 300°C respectively). On the other hand, no information is available on the tribological behaviour of the commercially available DLC coatings in high temperature lubricated condition. Thus tribological behaviour of a commercially available state-of-the-art DLC coating is tested at ambient temperature and at 200°C under boundary lubricated condition. Compared to ambient temperature, poor performance is observed at 200°C due to degradation of coating properties. However, this coating performs better than the coatings reported in the literatures. Hence it is concluded that the currently available tribological coatings are unable to maintain their excellent tribological properties in high temperature lubricated conditions. This provides the idea of developing a new generation metal-doped carbon-based coating, which will be able to withstand high operating temperature and maintain improved tribological properties in lubricated condition at ambient and high temperature ($150^\circ\text{C} - 300^\circ\text{C}$).

1.3. Methodology

Good tribological performance (i.e. low friction and high wear resistance) depends on dense coating microstructure and strong coating-substrate interfacial adhesion. Dense

microstructure helps the coating to withstand wear during sliding whereas strong adhesion prevents coating delamination. The choice of doping elements further influences the friction behaviour and thermal stability.

After a comprehensive review of currently available literatures, it has been observed that the thermal stability of the DLC coating is significantly increased up to $\sim 500^{\circ}\text{C}$ with addition of Si, Mo or W [21, 60 – 62], whereas tribological properties in lubricated condition are promoted when Ti, Mo or W is used as a dopant [26, 63, 64]. Particularly during lubricated sliding of W-DLC coating, a significant reduction in friction value ($\mu < 0.1$) is observed due to formation of WS_2 in the transfer layer when pure and low additive base oil [63] and base oil with extreme-pressure additives [64] are used as lubricants. Moreover, formation of low friction tribolayer is well documented for W-DLC coatings in lubricated condition at $\sim 100^{\circ}\text{C}$ [46, 47, 50, 51]. Similar reduction in friction ($\mu \sim 0.05$) is observed for Mo-DLC coating compared to metal-free DLC coating at ambient temperature when phosphorus-based additives and friction modifiers are present in the engine oil [26]. This information provides the idea of synergizing the benefits of simultaneous doping of carbon-based coating with Mo and W atoms, which has been adopted in the present work. It is expected that this Mo – W doped carbon-based coating (Mo–W–C) would be able to resist oxidation at high temperature and maintain similar tribological properties in lubricated condition at both ambient and high temperature.

Both the coating microstructure and the adhesion strength are governed by coating deposition procedure. In this research, the combined unbalanced magnetron sputtering (UBM) and high power impulse magnetron sputtering (HIPIMS) technique is selected to deposit Mo–W–C coatings. The high power impulse magnetron sputtering (HIPIMS) is a renowned technique that provides dense coating microstructure and high adhesion with substrate [6, 65, 66]. Most of the sputtering processes suffer from occurrence of arc during film deposition, but the use of short pulses in HIPIMS technology results in almost stable and arc-free deposition. In addition, high ionisation degree of the plasma particles achieved by this technology leads to better adhesion and less lattice defects compared to other PVD techniques such as magnetron sputtering. However, low deposition rate is one of its drawbacks, which is compensated by using combining HIPIMS and UBM techniques during deposition of Mo–W–C coatings.

The analyses of coating microstructure and composition were carried out using scanning electron microscopy (SEM), energy dispersive X-ray (EDX) analysis, X-ray diffraction (XRD) using both Bragg-Brentano, glancing angle and low angle geometry, and Raman spectroscopy. The adhesion and hardness of the coatings were evaluated by the scratch test, Rockwell hardness test and nanoindentation. The coatings were subjected to a series of isothermal oxidation tests and thermo-gravimetric test at elevated temperature in order to investigate the thermal stability. The tribological performance of the coatings was studied by pin-on-disc tests at ambient and elevated temperature condition. The sliding tests were conducted in dry and lubricated (engine oil) conditions against steel and alumina counterparts. A special attention was paid to study the friction behaviour, the formation of wear debris present in the transfer layer, the wear mechanism during dry and lubricated sliding tests and the change in coating properties with increase in temperature. The tribological performance and thermal stability of Mo–W–C coatings are further compared with the commercially available state-of-the-art DLC coatings in order to establish uniqueness of this coating.

1.4. Aim and objectives of this research

This research aims to develop a low friction and high temperature wear resistance Mo – W doped carbon-based (Mo–W–C) coating, which is able to withstand high operating temperature and maintain low friction in lubricated condition at ambient and elevated temperature. The objectives of this research work are:

- (i) To characterise the microstructural and mechanical properties of Mo–W–C coating.
- (ii) To investigate the tribological properties of Mo–W–C coating with and without presence of lubricant at ambient temperature.
- (iii) To compare the tribological performance of Mo–W–C coating with Cr-doped carbon-based coating and state-of-the-art DLC coatings at ambient temperature.
- (iv) To investigate the oxidation resistance of Mo–W–C coating in isothermal and dynamic condition and to compare the performance with the state-of-the-art DLC coating.
- (v) To study the tribological properties of Mo–W–C coating with and without presence of lubricant at elevated temperature and to compare the performance with the state-of-the-art DLC coating.

1.5. Thesis layout

Based on the objectives of this research, certain strategies are adopted to address the defined problems and they are discussed accordingly in the thesis.

Chapter 2: Apart from this introductory chapter, the thesis begins with a comprehensive review of literatures discussing tribological and oxidation resistance properties of DLC and metal-doped DLC coatings, the relevant coating deposition methods and the microstructure of deposited films. The findings of earlier researches are documented in order to find their research limitations while tackling of the defined problems.

Chapter 3: The design of the Mo–WC compound target used for coating deposition, the deposition procedure of Mo–W–C coatings and the relevant characterisation tests for investigation of coating properties are explained in this chapter.

Chapter 4: This chapter includes results of the experiments and their explanations and related discussions. It has four subchapters, which focusses on the structural properties of the as-deposited coatings (*section 4.1*), tribological behaviour of the Mo–W–C coatings at ambient temperature (*section 4.2*) and elevated temperature (*section 4.4*) and oxidation resistance at high temperature (*section 4.3*). The performance of Mo–W–C coatings is compared with commercially available state-of-the-art DLC coatings and the novelty of Mo–W–C coatings is also looked at as they outperform the state-of-the-art DLC coatings during lubricated sliding and oxidation tests.

Chapter 5: The summary of the current work and the derived conclusions are discussed in this chapter directing scope for the future work.

2. Literature review

2.1. Introduction to the tribology of Diamond-like-carbon (DLC) coating

2.1.1. Review of friction and wear during sliding

In 1964, the word ‘Tribology’ was coined by David Tabor, a British physicist. ‘Tribology’ means study or knowledge of rubbing action. When one surface is rubbed against another, the friction force generated from the mechanical interlocking between two surfaces is increased to prevent any relative motion up to some limit and then the motion occurs. According to Amonton’s first law, the ratio of friction force (f) to normal force (N) at the threshold of motion is known as coefficient of static friction (μ_s) and once the motion starts, it indicates the coefficient of kinetic friction (μ_k). A pair of surfaces in dynamic contact experience the coefficient of kinetic friction (μ_k), which is less than the coefficient of static friction (μ_s). The relationships are shown in equation set (1). Surface roughness plays an important role in defining the coefficient of friction. A difference between μ_s and μ_k values is observed when surface roughness is high, however both values are found similar with decrease in surface roughness. When the surfaces become very smooth and free of contaminants, then they actually adhere to each other (cold-welding phenomena) leading to an increase in coefficient of friction.

$$\begin{aligned} f_{static} &= \mu_s \cdot N \\ f_{kinetic} &= \mu_k \cdot N \end{aligned} \tag{1}$$

The friction between sliding surfaces is governed by three different phenomena namely abrasion, shearing and adhesion [67]. Abrasion is dominant when one counterface is harder than another leading to formation of scratches and possible loss of material from the softer surface. Shearing is attributed to the viscous flow of a soft matter (such as a thin coating, a contamination layer, a tribolayer or trapped wear debris particles) confined between the hard and stiff counterfaces. Finally roughness, mechanical properties and chemical reactivity of the sliding surfaces control the adhesion during sliding. Therefore

the friction coefficient between two rubbing surfaces is defined as $\mu = \frac{F_T}{F_N} = \frac{A_r \cdot \tau}{F_N}$, where

tangential force $F_T = F_{\text{abrasion}} + F_{\text{shearing}} + F_{\text{adhesion}}$, A_r is the real contact area, τ is the shear strength of softer material and F_N is the normal force. When both counterfaces are hard and stiff, then A_r will be small and τ will be high leading to an increase in μ value. Similarly, when one or both counterfaces are soft, then τ will be small but A_r will be large enough leading to an increase in μ value. However a reduction in μ value is observed when hard and stiff counterfaces are separated by a thin soft metal film. The thin film reduces abrasion and promotes easy shear in between sliding surfaces leading to smaller A_r and τ , thus μ value is decreased.

The friction between two mating surfaces results in material removal from one or both surfaces, the phenomenon is called wear. It depends on sliding conditions, environmental and material parameters of a tribo-system. Any changes in a tribo-system affects the wear, thus it is a system response. Generally wear is evaluated by the amount of volume lost and the state of worn surface. Wear rate and wear coefficient are used to measure the degree of wear. The wear rate is defined as wear volume per unit distance and the wear coefficient (K_c) is defined as wear volume per unit distance per unit load.

The wear in any tribological contact can be categorised into four major modes such as – adhesive wear, abrasive wear, fatigue wear and corrosive wear [68]. Adhesive wear is generated under plastic contact between similar counterfaces. The fracture is observed at the contact interface due to the strong adhesive bonding between the surfaces and the resultant wear is called adhesive wear (figure 2-1a). Abrasive wear is generated under plastic contact between a hard and a relatively soft counterface. The softer surface is fractured due to the penetration of harder material leading to abrasive wear (figure 2-1b). Both the fatigue and corrosive wear can be generated under elastic and plastic contacts. The repeated friction cycles during run-in period result in fatigue fracture of the surface and the associated wear is called fatigue wear (figure 2-1c). The corrosive wear is observed when the material is removed due to the tribochemical reactions occurred at the contact interface in a corrosive medium (figure 2-1d). The most corrosive medium in air is oxygen, thus the wear of metals due to tribochemical reactions in air is called as oxidative wear.

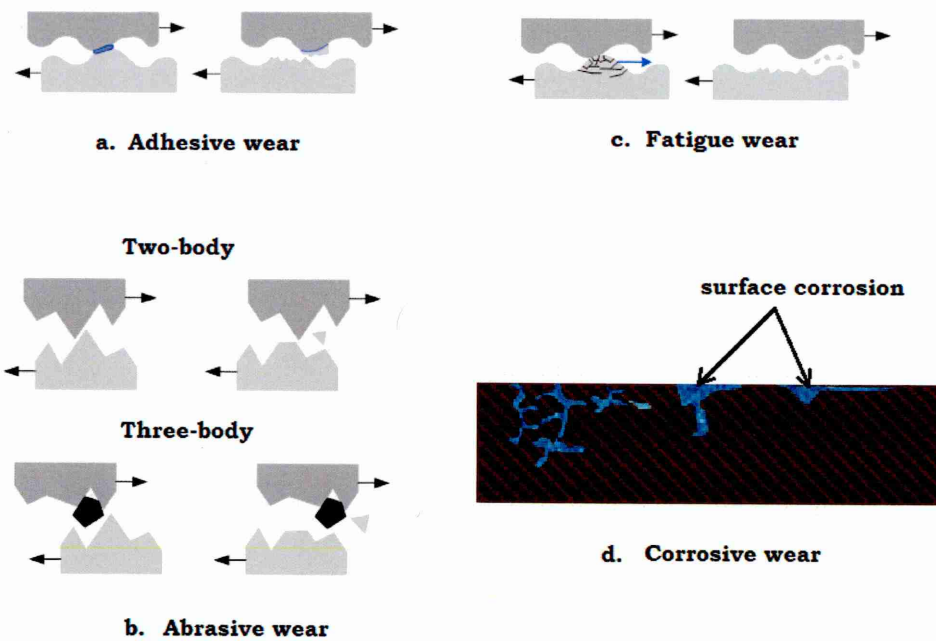


Figure 2-1: Schematic images of four major wear modes

The material removal in case of adhesive, abrasive and fatigue wear depends on the deformation and fracture in the contact region. The deformation is caused by the mechanically induced stresses and strains, which lead to brittle, ductile and fatigue fracture modes. Therefore these three types of wear are described as mechanical wear. On the other hand, material removal in corrosive wear is influenced by the deformation due to friction, micro-fracture, test environment, working temperature and successive removal of the reaction products. Thus corrosive wear is often described as chemical wear or tribochemical wear. In some processes, high working temperature results in surface cracking caused by thermal stress and frictional heating and melting of the surface, which governs the material removal. The resultant wear is called thermal wear.

2.1.2. Tribological coatings: DLC and metal-doped DLC

Tribological coatings are widely used to reduce the friction and wear of the moving parts in any sliding conditions (with or without presence of lubricant) by preventing direct contact between them. Typically these coatings are categorised as *hard coatings* (such as metal nitrides, carbides, borides and oxides) and *soft coatings* (such as polymers, soft metals, graphite and lamellar solids like MoS_2 and WS_2). *Hard coatings* (hardness >10

GPa) exhibit good wear resistance but high friction coefficient (>0.3), whereas *soft coatings* (hardness <10 GPa) provide low friction coefficient (<0.3) and high wear rate. When both low friction and good wear resistance (i.e. low wear rate) are required in the tribological contacts, it is difficult to obtain by using these conventional *hard* and *soft* coatings. Composite and multilayer coatings provide some balance between these two properties by combining both soft and hard materials, however they require complex deposition procedure and optimisation of the deposition parameters. The amorphous carbon-based coatings provide an excellent combination high hardness, low friction coefficients and good wear resistance. Three different bonding configurations namely sp^1 , sp^2 and sp^3 are observed in the atomic structure of the carbon. The carbon atoms form linear strings in sp^1 configuration, whereas two dimensional layered and three-dimensional tetrahedral lattice structures are observed in sp^2 and sp^3 configuration respectively [69]. Each carbon atom contains six electrons of which two are strongly bonded with atomic nucleus (orbital $1s$) and rest are poorly bonded valence electrons (orbitals $2s$ and $2p$). These four electrons can easily mix with each other and fill up the orbitals $2s$ and $2p$ ($2p_x$, $2p_y$, $2p_z$) due to the lower energy difference between levels $2p$ and $2s$ rather than the energy of chemical bonds. The mixing of atoms results in sp^1 , sp^2 and sp^3 hybridisations in the carbon atom as shown in figure 2-2.

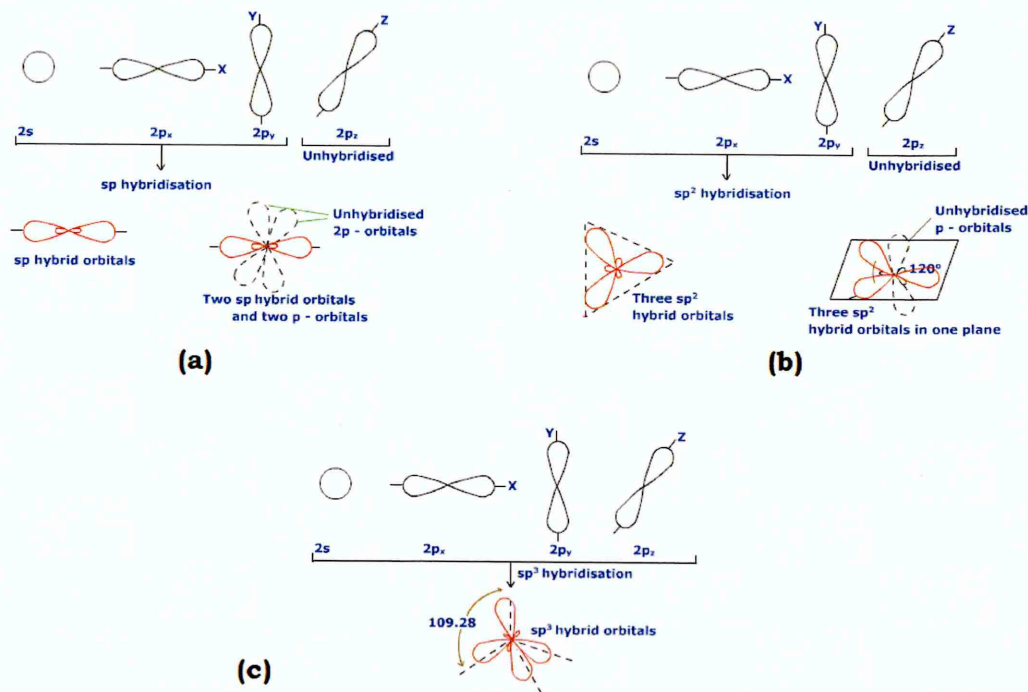
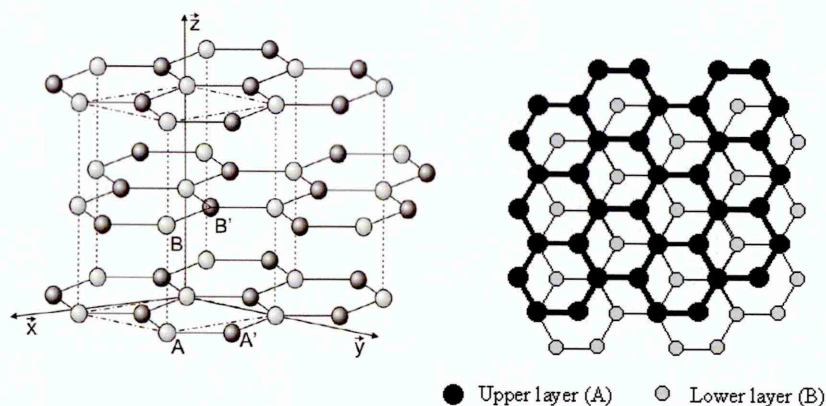


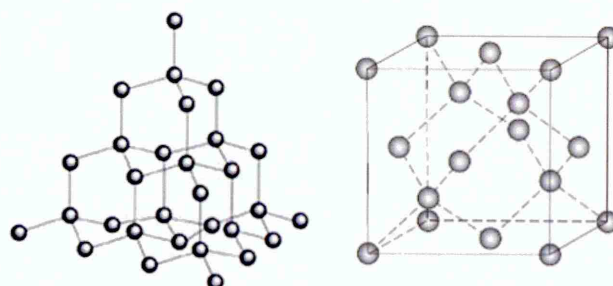
Figure 2-2: Hybridised orbitals of Carbon atoms (a) sp^1 , (b) sp^2 and (c) sp^3

The most known allotropes of carbon are graphite and diamond. Graphite is black and grey in colour and the most stable form of carbon under standard conditions. A perfect graphite crystal consists of graphene layers, in which covalently bonded carbon atoms are arranged in a two-dimensional honeycomb lattice along the xy plane. These layers are connected by the weak Van der Waals forces in the vertical z -direction (figure 2-3a), which allows easy sliding between the layers [70]. The carbon atoms are in sp^2 hybridisation and the distance between neighbouring atoms in a layer is ~ 0.142 nm, whereas the distance between the planes in the z -direction is ~ 0.335 nm [71]. This layered-structure of graphite provides low coefficient of friction during sliding [72].

In diamond, each carbon atom is covalently bonded with four other atoms arranged at the corners of a regular tetrahedron as shown in figure 2-3b. All carbon atoms are in sp^3 hybridization and the bonding length is ~ 0.155 nm [71]. Unlike graphite, diamond is well known for its highest hardness and extreme wear resistance. Diamond has a hardness of 10 in Mohs scale of mineral hardness, where hardness is defined as resistance to scratching and is graded between 1 (softest) and 10 (hardest).



(a) crystal structure of graphite



(b) crystal structure of diamond

Figure 2-3: Crystal structure of (a) graphite and (b) diamond

The soft forms of carbon such as graphite, graphite fluoride, carbon–carbon composites and glassy carbons are widely used as low-friction engineering materials in the industry. They are often used as solid lubricants to reduce friction and combat wear, where use of liquid lubricants is neither possible nor desirable [72 – 76]. On the other hand, carbon is used in the synthesis of several hard coatings including diamond-like carbon (DLC), carbon nitride, transition metal carbides and boron carbide. Some of these coatings provide high hardness, high thermal conductivity and very low friction, which have attracted tremendous interest of the researchers from both the industry and the academia. In particular, DLC coatings provide a wide range of hardness (10 – 80 GPa) [2, 4, 5] and friction coefficient ($\mu = 0.05 - 1.0$ at ambient atmosphere with 20% – 60% relative humidity and $\mu = 0.007 - 0.4$ under low pressure below 10^{-4} Pa) [2, 4] along with high wear resistance ($K_c < 10^{-16} \text{ m}^3\text{N}^{-1}\text{m}^{-1}$) [2] depending on the deposition procedure and the working environment. This combination of high wear resistance and low friction characteristics of DLC coating makes it most suitable tribological coating, which is extensively used in various automotive engine parts such as piston, piston rings, piston pins, ball and journal bearings, face seals, cylinders and brakes, gearbox and valve train components. In addition, the DLC coatings are widely used as a wear and corrosion-protective coating on cutting tools, precision parts, different bio-medical implants such as articulated hip and knee joints, commercial commodities such as razor blades, sunglasses and computer hard disc storage devices.

The earliest research on DLC films was found on 1953, when Schmellenmeier produced the carbon films [77]. However, Eisenberg and Chabot are often considered as the true pioneers of the DLC technology because of their comprehensive studies in the early 1970s [78]. They realised that the DLC films were chemically inert, very hard and scratch-resistant. Weissental and his co-workers first revealed that the DLC films were made of amorphous carbon as understood by the extensive electron microscopy and electron energy loss spectroscopy studies [79]. Most of the systematic studies on the tribological behaviour of DLC films were carried out during the 1990s and now they are considered as the most important tribological coating in various application fields.

DLC coatings can be deposited using CVD, PVD (ion plating, ion beam assisted deposition, cathodic arc deposition, activated reactive evaporation, RF sputtering, magnetron sputtering) and laser ablation processes (laser cladding, pulsed laser deposition) with a high degree of flexibility in deposition parameters [3]. The schematic

diagrams of some of the deposition process are shown in figure 2-4. DLC coatings are predominantly made of sp^2 and sp^3 bonded carbons and trace amount of sp^1 bonds can be present depending on the deposition procedure [80]. DLC coatings with more amounts of sp^2 bonded carbons are relatively soft and behave like graphite during tribological tests. Alternatively, DLC coatings with more amount of sp^3 bonded carbons are hard like diamond, thus provide excellent tribological properties. When hydrocarbon gas such as methane or acetylene is used as a precursor for carbon during deposition, the microstructure of DLC coating contains carbon and a considerable amount of hydrogen. The amounts of sp^3 bonded carbons and hydrogen in the DLC coating are affected by the average impact energy of the impinging atoms. The low impact energy results in insufficient decomposition of gaseous precursor leading to formation of polymer-like carbon film with mostly $=CH_2$ groups. At medium impact energies, the sp^3 bonding is preferred and the hydrogen content is reduced leading to formation of 'diamond-like' coating. When the impact energies are high enough, the 'graphite-like' coating with high amount of disordered sp^2 bonded carbons is obtained. A transition from 'diamond-like' to 'graphite-like' properties is observed above $\sim 250^\circ C$ and this temperature decreases with increase in ion energy during film deposition [3]. The hydrogenated DLC coatings are relatively soft and possess low residual stress [81], whereas hydrogen-free DLC coatings are very hard and contains large amount of residual stress.

The commercial use of standard DLC coating is mostly compromised due to its low adhesion strength with the substrate. Most of the state-of-the-art technologies utilise Argon ion etching as a surface pre-treatment method, which leads to amorphous interface and large amount of implanted gas in the interface. As a result, the adhesion strength decreases due to formation of porous and weak interface [6]. The compressive residual stress generated during coating deposition further deteriorates the coating-substrate adhesion. The compressive residual stress in the DLC coatings is observed in the range of $\sim 0.5 - 7$ GPa but sometimes it reaches up to 13 GPa [4]. Several approaches are introduced to improve the adhesion strength of the DLC coating. One way to ensure strong adhesion between the DLC coating and the substrate is to deposit an in-situ carbon interlayer before the coating deposition. This can be achieved by pulsed laser deposition (PLD) process in which very low pulses (of the order of femto-seconds) are used along with a high power density (up to 10^{13} W/cm²). The process provides high kinetic energy (up to 1 keV) to the impinging carbon atoms, which finally embed into the substrate. The firm embedding of the carbon atoms increases the adhesion strength of the DLC coating

with the substrate [3]. Similarly, deposition of metal interlayers (such as Ti, Ni, Cr) reduces the compressive residual stress and thus the adhesion strength is enhanced. The DLC coating without metal interlayer shows a residual stress of 1.5 GPa, whereas introduction of Cr interlayer significantly decreases the residual stress to 0.11 GPa [18], [82]. Another approach to overcome the aspects of low adhesion and high compressive stress is to incorporate W into the DLC coating. The W – doping significantly reduces the internal residual stress of the coating, thus the coating-substrate adhesion is improved [18 – 20]. Moreover, the graded design in both coating's microstructure and composition significantly improve the coating-substrate adhesion. The second major problem of standard DLC coatings is its poor thermal stability, which affects the tribological applications at higher working temperature ($>300^{\circ}\text{C}$). Incorporation of different doping elements such as Ti, Si, Cr, Mo, W improves the thermal stability [7, 8, 21, 60 – 62, 83 – 85], which is discussed in detail in the next section.

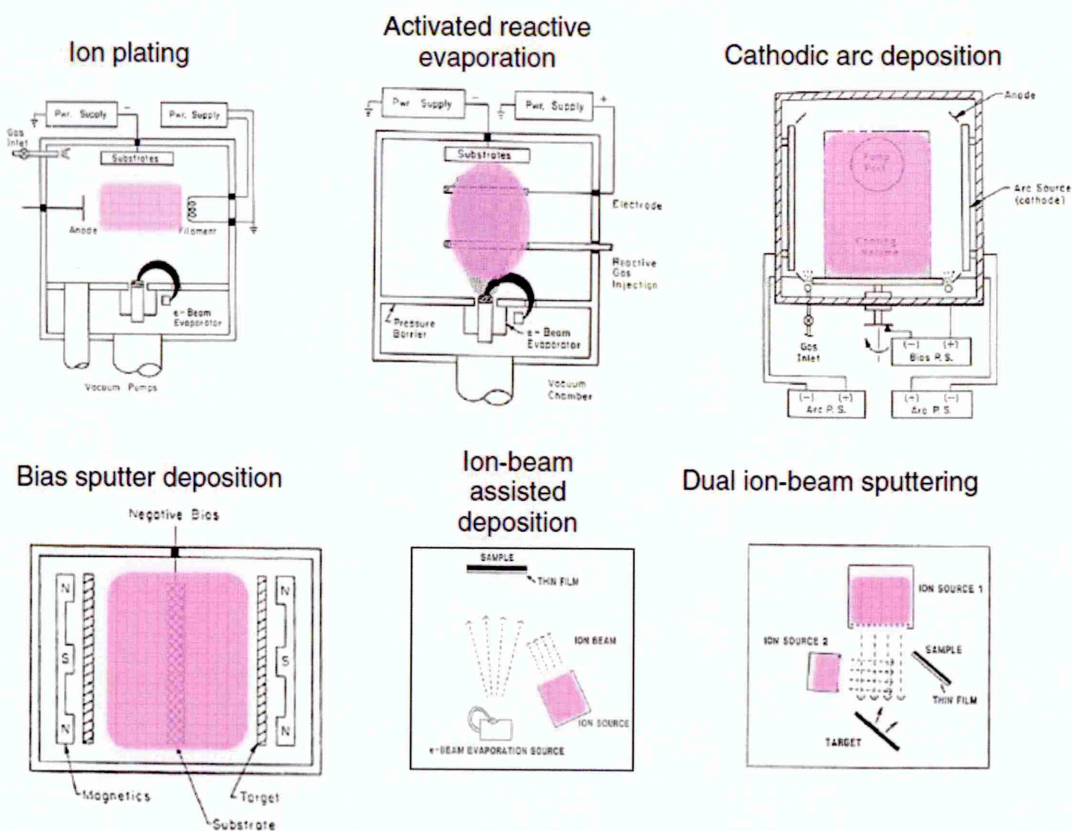


Figure 2-4: Schematic diagrams of various processes used to deposit DLC coating [3]

Several researches were done in order to understand the influence of different doping elements and subsequent changes in the properties of DLC coatings. It was observed that addition of metal and non-metal dopants into the DLC coating increased the adhesion strength and delayed the graphitisation process at high temperature compared to metal-free DLC coating. Table 2-1 lists some typical dopants used to improve the characteristics of DLC coating. It can be summarised that thermal stability of the DLC coating is significantly increased (up to $\sim 500^{\circ}\text{C}$) with addition of Si, Mo or W [21, 60 – 62]. On the other hand, doping with Ti, Mo or W benefits the tribological properties particularly in the case of lubricated sliding, where engine oil with friction modifier is used as lubricant. Very low friction coefficient was reported for lubricated sliding of Ti-DLC ($\mu \sim 0.03$) [26], Mo-DLC ($\mu \sim 0.05$) [26] and W-DLC ($\mu \sim 0.055$) [64] coatings in the presence of engine oil.

Table 2-1: Influence of doping elements on the properties of DLC coating

Dopant	Influence of dopants on properties of DLC coating	
	<i>Increase in</i>	<i>Decrease in</i>
Ag	toughness [86]	residual stress [87]
B	—	friction coefficient [3]
Cr	load bearing capacity and adhesion [88]	friction coefficient, wear coefficient and residual stress [88]
Cu	ductility, adhesion [89] and toughness [86]	residual stress [89], [90] and hardness [89]
Si	hardness [91], thermal stability [61], [92] and wear rate [92]	residual stress [93], friction coefficient [91], [92] and wear coefficient [91]
Ti	hardness, adhesion, abrasion resistance and thermal stability [7]	friction [94], [95], [12] and wear coefficient [7]
Al	toughness [86]	friction coefficient [86]
Ti-Al	tool life [96] and thermal stability [83]	friction coefficient [97]
N	Adhesion and electrical conductivity [98]	residual stress and corrosion resistance [98]
Nb	—	residual stress [99]
Ni	thermal stability and toughness [100]	corrosion resistance [101]
W	hardness [102], [103], friction coefficient [18], [104]	residual stress [102], friction and wear coefficient [20]
Mo	adhesion [105]	residual stress, hardness [105] and friction coefficient [105], [106]

2.1.3. Factors affecting the friction and wear of the DLC coating

The intrinsic factors affecting the friction and wear behaviour of DLC coating are coating microstructure and alloying elements (like hydrogen or other dopants), whereas extrinsic factors include the mechanical, chemical and physical interactions between the sliding surfaces and the surroundings, the test environment and the working temperature [3]. The influences of these factors on the friction and wear behaviour are discussed below:

I. Surface roughness

Typically friction and wear increases with increase in surface roughness. When rough surfaces slide against each other, a high level of mechanical interlocking takes place at the asperity contacts leading to high friction and severe wear. Due to the amorphous structure, the surface roughness of DLC film is observed close to the surface roughness of substrate material. When DLC film is deposited on a highly polished surface like Si wafer, the surface roughness is found extremely low. On the other hand, deposition of DLC film using PLD and arc-PVD processes or on a rough ground surface results in high surface roughness. For a fixed set of sliding test parameters, the smoother is the DLC film surface, lower is the friction and wear especially during run-in period.

II. Adhesive interactions

Covalent bonding between unoccupied or dangling σ -bonds of the sliding DLC interfaces results in severe adhesion leading to a high friction value. In humid test environment, the oxygen and water molecules are adsorbed on the DLC coated surface and passivate the σ -bonds during sliding. As a result, the adhesive interactions between the sliding surfaces are reduced leading to a decrease in friction value. This is found true for hydrogen-free DLC (both ta-C and a-C), crystalline graphite and graphitic carbon coatings, however an opposite trend is observed for hydrogenated DLC coating. At high temperature or in ultra-high vacuum conditions or in dry N₂ environment, these surface adsorbates are either absent or mechanically or thermally removed from the sliding surfaces. Thus σ -bonds become free to interact with each other eventually increasing the friction coefficient [107 – 109].

III. Third-body abrasion

Third-bodies or debris particles are produced due to wear of the sliding surfaces and trapped at the contact interfaces. These particles are severely deformed by the grinding action and chemical reaction with the counterpart surface and the surroundings. As a result, they form a thin carbon-rich transfer layer on one or both the counterfaces. The debris particles produced from most DLC films have a disordered graphite-like microstructure as indicated by the Raman spectra and electron diffraction patterns [110 – 114]. Variation in test conditions such as normal load, sliding velocity, relative humidity and working temperature influence the formation and composition of a transfer layer. A continuous transfer layer with similar composition of DLC coating is formed when normal load and sliding velocity are high. On the contrary, fibre-like debris particles of graphitic nature are generated when both normal load and sliding velocity are low [115]. The debris particles show lower rate of graphitisation with decrease in working temperature and increase in humidity level. In vacuum, very low friction coefficient (10^{-2} range) is observed between two DLC coated surfaces at lowest partial pressure of water vapour and with increase in water vapour pressure, the friction value increases [116 – 117].

IV. Tribochemical interactions

The friction is significantly influenced by the tribochemical interactions occurred between sliding surfaces and the surroundings (gas or liquid). It has been reported that highly hydrogenated DLC coatings show $\mu < 0.01$ in inert gas or vacuum environment [116, 118 – 120], however the water molecules present in the humid test environment substantially increase the friction coefficient. These highly polar water molecules physically interact with the carbon atoms of the DLC coated surfaces and form a layer of physisorbed species. This layer is mechanically removed during sliding and then reformed leading to a continuous fluctuation in the friction value. In liquid medium, the frictional behaviour of DLC coating depends on viscosity, chemical affinity, polarity and molecular size of the liquid. For certain types of DLC coatings, very low friction coefficient is observed due to formation of solid lubricants (such as MoS_x and WS_x) via tribochemical interactions occurred between sliding surfaces and the oil additives [27], [63]. Hydrogen-free DLC coatings show low friction coefficient due to termination of σ -bonds of the surface by the OH bonds when combined poly-alpha olefin base oil with glycerol monooleate (PAO + GMO) is used as lubricant [121]. Further variation in

tribochemical reaction mechanisms is observed for doped DLC coatings. For example, sliding of Si-doped DLC coating in humid air leads to formation of silicon hydroxides, which increases the chemical inertness of the coating. Thus the friction coefficient becomes less sensitive to the relative humidity of the surroundings [92, 122, 123]. Similar behaviour is noticed when small amount of F, B and S is incorporated into the DLC coating [73, 124].

V. High working temperature

A gradual transformation of DLC coating from an amorphous (highly disordered) to graphitic (ordered) structure is observed when it is exposed to high working temperature. The thermal energy rearranges the thermodynamically unstable structure of DLC coatings and forms more stable bonding configuration such as graphite. This transformation occurs at ~500°C for ta-C coatings, however friction increases with rise in test temperature due to adhesive interactions between the sliding surfaces as described before. For hydrogenated DLC coating, the hydrogen atoms (which are not bonded with carbon atoms) are diffused out when temperature reaches to ~300°C and the gradual transformation of the coating structure results in a relatively porous thin graphitic layer at the end. This soft graphitic layer wears out quickly leading to an increase in friction and wear coefficient values.

2.1.4. Engine oil as lubricant

Engine oils are mainly used to reduce friction and wear of the moving parts of an internal combustion engine. In addition, they prevent corrosion of the engine parts and act as cooling agent. Commercial engine oils contain petroleum-based or synthetic-based base oil and different additives, which react with the sliding surfaces in high pressure and temperature condition and form a continuous anti-wear tribofilm in between the surfaces. The in-situ formation and adherence of this tribofilm to the sliding surfaces is strongly dependant on the operating temperature, type of additives and additive concentration in the base oil [33]. The tribofilm is repeatedly worn away due to sliding and then reformed leading to a significant reduction in friction and wear of the sliding surfaces.

According to the American Petroleum Institute (API), the base oils are categorised into five groups (API 1509, Appendix E). Groups I, II and III are originally mineral oils and refined from petroleum crude oil. Groups IV and V are synthetic-base oils among which group IV is reserved for polyalphaolefins (PAOs) and all other base oils (such as silicone, phosphate ester, polyalkylene glycol (PAG), polyolester etc.) are included in group V. One of the most important factors to evaluate the base oils is Viscosity Index (VI), which indicates change of viscosity as a function of temperature. VI is calculated based on the difference in viscosity at 100°C and 40°C (ASTM D-2270) and oil having a high VI shows less change of viscosity with change in temperature. The flash point is another important characteristic, which indicates the lowest temperature at which enough flammable air-vapour mixture is formed near the oil surface (ASTM D-92). The most common properties of the different base oils are listed in table 2-2 [125].

Table 2-2: Properties of the base oil according to API [125]

Base oil category	Viscosity Index	Sulphur (%)	Saturation of hydrocarbon molecules (%)	Flash point (°C)
Group I (solvent refined)	80 – 120	>0.03	<90	100
Group II (hydrocracked)	80 – 120	<0.03	>90	170
Group III (severely hydrocracked)	≥120	<0.03	>90	190
Group IV	135 – 140	polyalphaolefins (PAOs)		270
Group V	all other base oils			260

The additives of the engine oils are mainly categorised into anti-wear (AW) additives and extreme pressure (EP) additives. AW additives are mainly zinc and phosphorus-based compounds and are used to decrease wear under application of lighter loads. Zinc dithiophosphate (ZDP), Zinc dialkyl dithiophosphate (ZDDP), tricresyl phosphate (TCP) are typical AW additives, among which ZDDP is widely used in formulated engine oils because of its corrosion-resistant and anti-oxidant nature. EP additives contain sulphur, phosphorus and chlorine-based compounds, which chemically react with the metal surfaces under extreme pressure condition and minimise wear by forming a thin tribofilm. Some of the EP additives, known as friction modifiers, reduce the friction significantly at elevated temperature where performance of AW additives generally degrades [34].

Molybdenum dithiocarbamate (Mo-DTC) is a widely used friction modifier, which decomposes under high pressure and forms an in-situ MoS₂ layer in between sliding surfaces.

Most of the commercial engine oils contain ZDDP and Mo-DTC in order to reduce friction and wear of the sliding engine parts. ZDDP protects the surface by forming a very thin tribolayer of amorphous polyphosphate over it (approximately 100 – 1000 nm) [11], however some phosphorus-based compounds end up being deposited on the surface and contaminating the oil. Thus reduced amount of ZDDP should be used in the engine oil to protect the surface [34], [126]. On the other hand, the concentration of Mo-DTC in the base oil must be high to produce sufficient amount of MoS₂ for friction reduction [33]. When both Mo-DTC and ZDDP are present in the base oil (PAO), Mo-DTC reacts with oxygen and sulphur contents of ZDDP and forms a tribolayer containing MoS₂, MoO₃ and ZnS. The formation of MoS₂ directly depends upon the ZDDP concentration, i.e. higher the ZDDP concentration, higher is the amount of MoS₂ formed in the tribolayer [27]. Thus base oil with an optimised amount of ZDDP and Mo-DTC provides best tribological performance compared to base oil + ZDDP or base oil + Mo-DTC combinations.

The effect of API group III base oil + Mo-DTC combination on the wear rate of DLC/DLC contacts was found insignificant but it increased the wear rate of DLC/steel contacts ($\sim 10^{-17} \text{ m}^3 \text{ N}^{-1} \text{ m}^{-1}$) due to the formation of MoO₃ at the asperity contacts [50]. Similar fact was reported in another study, where high wear rate of DLC/steel contact was observed in base oil + Mo-DTC combination. Addition of ZDDP in the oil reduced the wear rate due to the formation of MoS₂ [54]. With increase in working temperature, the formation of MoS₂ was promoted under pure sliding condition rather than sliding/rolling conditions [33]. Further, both the DLC/DLC and DLC/steel contacts showed low friction and wear in combined lubrication of PAO + Mo-DTC + ZDDP rather than combination of PAO + Mo-DTC [27].

It can be summarised that the formation of solid lubricants like MoS₂ in between sliding surfaces during boundary lubrication condition is the key factor to reduce friction and wear irrespective of the tribo-pairs used. The thermal decomposition of friction modifier (Mo-DTC) used in engine oil produces MoS₂ during sliding and its amount depends on

ZDDP concentration. Thus use of Mo-DTC containing engine oil is important in order to produce MoS₂ during lubricated sliding.

2.1.5. Tribological performance of DLC and metal-doped DLC coatings

I. Metal-free DLC coating

The tribological behaviour of a hybrid PVD/CVD deposited amorphous DLC (a-C:H) coating was tested under 10 N normal load and different lubricant combinations (mineral oil, mineral oil + AW/EP additives, mineral oil + EP additives) at three different temperatures 20°C, 80°C and 150°C. The tests conducted at 20°C and 80°C showed similar friction coefficients ($\mu \sim 0.2 - 0.3$) for DLC/DLC contacts irrespective of lubricant used, whereas a significant reduction was observed at 150°C due to tribolayer formation as detected by AES and XPS analyses. The reduction in friction was ~50% for mineral oil and mineral oil + AW/EP additives and ~20% for mineral oil + EP additives combinations. The wear coefficient was linearly increased with increase in test temperature for mineral oil and mineral oil + AW/EP additives combinations, whereas almost similar wear rate was observed for mineral oil + EP additives combinations irrespective of test temperature [58]. In another study, amorphous DLC (a-C:H) coating deposited using commercial PACVD process showed friction and wear coefficients in the range of $\mu \sim 0.1 - 0.3$ and $K_c \sim 10^{-15} \text{ m}^3\text{N}^{-1}\text{m}^{-1}$ respectively after 72 m of sliding against steel counterparts under maximum 1.5 GPa contact pressure. The friction and wear coefficients were found almost independent of test temperature (20°C – 200°C) under different lubricant combinations (PAO, PAO + AW additives and PAO + EP additives) [59].

II. Cr-doped DLC coating

The Cr-doped DLC and Cr-doped graphitic carbon coatings provide a wide range of friction coefficient ($\mu \sim 0.06 - 0.4$) and wear coefficient ($10^{-16} - 10^{-18} \text{ m}^3\text{N}^{-1}\text{m}^{-1}$) during dry sliding depending on the test parameters [2, 127 – 133]. The Cr-DLC film deposited using a hybrid sputtering ion beam system (DC magnetron sputtering and linear ion source) showed $\mu > 0.2$ after 500 m of sliding against steel ball (HRC60) and the wear coefficient ($\sim 3 \times 10^{-17} \text{ m}^3\text{N}^{-1}\text{m}^{-1}$) was found slightly higher compared to the metal-free DLC film ($\sim 2.6 \times 10^{-17} \text{ m}^3\text{N}^{-1}\text{m}^{-1}$) [129]. The Cr-DLC film deposited using hybrid PVD

and PECVD process, showed lower friction and wear coefficients ($\mu < 0.14$ and $K_c \sim 10^{-16} \text{ m}^3\text{N}^{-1}\text{m}^{-1}$ respectively) compared to the metal-free DLC film after 1000 m of sliding against 440C SS and alumina (Al_2O_3) balls under 2.5 N applied load [130].

In another study, different Cr-DLC films were deposited using a hybrid ion beam (DC magnetron sputtering and linear ion source) deposition system and the friction coefficients were reported to increase from 0.15 to 0.3 depending on Cr content present in the film after sliding against steel ball (HRC60) for 300 m distance and under 3 N applied load. A drastic rise in wear rate ($\sim 8.9 \times 10^{-18} \text{ m}^3\text{N}^{-1}\text{m}^{-1}$ to $\sim 1.4 \times 10^{-16} \text{ m}^3\text{N}^{-1}\text{m}^{-1}$) was observed with increasing Cr content in the film, which was attributed to the abrasive wear caused by the hard Chromium carbide particles present in the transfer layer during sliding [131]. This fact was further supported in another study, where both the metal-free DLC and Cr-DLC coatings were deposited using reactive magnetron sputtering in an intensified plasma-assisted coating system. The friction and wear coefficients of metal-free DLC coating ($\mu \sim 0.09$ and $K_c \sim 0.93 \times 10^{-16} \text{ m}^3\text{N}^{-1}\text{m}^{-1}$ respectively) were observed lower than the Cr-DLC coating ($\mu \sim 0.11$ and $K_c \sim 1.37 \times 10^{-16} \text{ m}^3\text{N}^{-1}\text{m}^{-1}$ respectively) after 1000 m of dry sliding against 440C SS ball. The Cr-rich nanoparticles interrupted the formation of transfer layer during sliding, thus higher friction and wear coefficients were obtained [128].

The tribological behaviour of Cr-DLC coatings deposited using a hybrid technique (vacuum arc evaporation and magnetron sputtering for Cr/C intermediate layers and RF PACVD for depositing outer DLC layer) was found very much dependent on the tribo-pairs used in dry sliding conditions [133]. Three different counterparts such as alumina (Al_2O_3), uncoated 100Cr6 and Cr-DLC coated 100Cr6 balls were tested during sliding in open-air condition under two different parametric settings (setting I: 10 km sliding distance and 20 N normal loads and setting II: 1 km sliding distance and 80 N normal loads). Irrespective of the parametric settings, the friction coefficient was reported highest ($\mu \sim 0.1 - 0.4$) for Cr-DLC/uncoated 100Cr6 tribo-pair compared to others. For parameter set I, steady state friction coefficients of ~ 0.12 and ~ 0.1 were reported for Cr-DLC/Cr-DLC coated 100Cr6 and Cr-DLC/ Al_2O_3 tribo-pairs respectively after 2000 m of sliding. On the other hand, friction coefficients were reduced to ~ 0.06 and ~ 0.08 for Cr-DLC/Cr-DLC coated 100Cr6 and Cr-DLC/ Al_2O_3 tribo-pairs respectively under parameter set II. The wear rate of coating ($K_{vc} = 3.2 - 3.8 \times 10^{-17} \text{ m}^3\text{N}^{-1}\text{m}^{-1}$) was found similar for all three

counterparts; however with increase in hardness, the wear rate of the counterparts was decreased [133].

The tribological properties of C/Cr film deposited using DC unbalanced magnetron sputtering were reported against WC-6%Co ball for 720 m sliding distance and varying normal load of 10 – 80 N. The friction and wear coefficients were dependant on coating hardness and observed in the range of 0.08 – 0.16 and $10^{-18} - 10^{-16} \text{ m}^3\text{N}^{-1}\text{m}^{-1}$ respectively [2]. The same C/Cr coating was tested further with a different parametric setting of varying normal load (20 – 80 N) and sliding distance (400 – 1000 m), in which a linear decrease in friction coefficient ($\mu \sim 0.09 - 0.06$) was observed with increasing applied load from 20 N to 80 N, however the wear coefficient ($K_c \sim 10^{-17} \text{ m}^3\text{N}^{-1}\text{m}^{-1}$) was found almost unaffected. The wear mechanism during dry sliding was influenced by the combined effect of moisture present in the test environment and the third-body abrasion. The low friction coefficient was attributed to the reorientation of graphite nanocrystalline clusters to preferable (002) planes [127].

C/Cr coating, deposited using combined steered cathodic arc and unbalanced magnetron sputtering, showed $\mu \sim 0.21 - 0.23$ in open air ($\sim 30\%$ humidity) and $\mu \sim 0.7 - 0.8$ in dry nitrogen environment (almost $\sim 0\%$ humidity) after 500 m of dry sliding against 100Cr6 ball under 5 N applied load. The moisture in the test environment reduced the adhesive interactions between sliding surfaces by forming a transfer layer during sliding, which lowered the friction coefficient in open air. However, in dry nitrogen environment, formation of such transfer layer was not possible; therefore high friction and rapid wear was observed [132].

Cr-DLC coatings with varying Cr content (0% – 23.3%) was deposited using hybrid technique (a combination of magnetron sputtering, vacuum cathodic arc sources and linear anodic layer ion sources) by controlling the Cr target current [134]. The lubricated sliding tests were carried out against Si_3N_4 ball for a sliding distance of 2300 m under applied load of 9.8 N. PAO-IV and paraffin-based mineral oil (150SN) were chosen as base lubricants, in which friction modifier (Mo-DTC) and extreme pressure (EP) additive (amine sulphuric-phosphate diester or T307) were added to enhance the performance. In base oil and base oil + T307 combinations, Cr-DLC coating showed no significant change in friction coefficient, however it is lowered with the addition of Mo-DTC in the base oil

($\mu \sim 0.05 - 0.15$). The lowest wear coefficient ($< 1 \times 10^{-16} \text{ m}^3\text{N}^{-1}\text{m}^{-1}$) was found for Cr-DLC with 0.2% Cr content, whereas other Cr-DLC coatings showed wear coefficient in the range of $\sim 10^{-16} \text{ m}^3\text{N}^{-1}\text{m}^{-1}$. The high wear resistance was attributed to the high hardness ($> 15 \text{ GPa}$) of coating because of Cr doping at an optimal level (0.2%). The friction coefficient of C/Cr multilayer coating, deposited by magnetron sputtering, was found $\mu \sim 0.1 - 0.33$ after only 273 m of sliding against polished Al_2O_3 ball under applied load of 5 N in water-lubricated environment [14]. The generated debris was adhered to the pin surface forming a thick layer, which increased the wear coefficient in the range of $\sim 10^{-15} \text{ m}^3\text{N}^{-1}\text{m}^{-1}$.

III. Si-doped DLC coating

The friction behaviour of magnetron sputtered DLC and Si-DLC coatings was investigated from room temperature to 400°C against Al_2O_3 ball under 2 N applied load. The friction coefficients of DLC, Si-DLC with 16% Si and Si-DLC coating with 26% Si were observed as 0.15, 0.17 and 0.12 respectively at room temperature. At 200°C , the friction coefficients were decreased to 0.06, 0.09 and 0.10 respectively due to partial transformation of amorphous structure into graphite-like structure. An abrupt change was observed at 400°C , where friction coefficient is increased to 0.3 for DLC coating but decreased to < 0.2 for Si-DLC coatings. Thus it was concluded that the addition of Si improved the thermal stability thus it showed little change in friction coefficient with increase in temperature [60]. Friction behaviour of RF-PACVD deposited Si-DLC coating was tested at ambient condition ($25 - 30^\circ\text{C}$ and 50 – 60% relative humidity) against steel ball under a varying normal load from 1.96 to 9.8 N. Little addition of Si decreased the friction coefficient compared to non-doped DLC coating and minimum friction value ($\mu \sim 0.06$) was observed for 9.5% Si content [135]. In another study, parallel-plate conductively coupled RF plasma system deposited DLC coating showed a friction coefficient of 0.1 at ambient condition (27°C and 30 – 50% relative humidity) against steel ball under a normal load of 40 N. Little addition of Si (5.4%) decreased the friction coefficient to 0.01 and low wear rate possibly due to formation of SiO_2 . However further addition of Si generated crack during sliding leading to higher friction coefficient ($\mu \sim 0.13 - 0.14$) and significant wear damage [92].

IV. Ti-doped DLC coating

The friction behaviour of non-doped DLC and Ti-DLC coatings, deposited using hybrid RF-PECVD and unbalanced magnetron sputtering (UMS) system, was studied at ambient air and dry nitrogen environment against under normal loads of 10 N and 20 N. Incorporation of Ti reduced and stabilised the friction coefficient at room temperature compared to non-doped DLC coating and improved load-carrying capacity due to its high hardness. At applied normal load of 20 N, non-doped DLC coating quickly failed leading to a higher friction coefficient ($\mu \sim 0.02\text{--}0.03$), whereas Ti-DLC coating showed an ultralow friction coefficient ($\mu \sim 0.008$) after 20,000 laps without any failure. Tests carried out in humid environment (10 – 100% RH) showed friction coefficient of Ti-DLC coating in the range of 0.008 – 0.03, which was reported much higher ($\mu \sim 0.02\text{--}0.5$) for both doped and non-doped DLC coatings. This excellent friction behaviour was attributed to physical properties, friction-induced structural change and formation of transfer layer during sliding [94]. In another study, Ti-DLC film deposited using cathodic arc plasma deposition showed lower friction coefficient ($\mu \sim 0.2$) compared to Ti-free DLC film ($\mu \sim 0.3$). Ti-free DLC film was delaminated from the interface with the substrate during sliding, whereas Ti-DLC film was well adhered to the substrate and Ti particles were flattened by the ball leading to lower friction coefficient [95].

The friction behaviour of RF magnetron sputtered Ti-DLC and metal-free DLC coatings were investigated in atmosphere ($\sim 50\% - 60\%$ RH) and in the presence of SAE 5W-20 oil (PAO + ZDDP + Mo-DTC) under 5 N normal load. The friction coefficients of Ti-DLC coating were found as ~ 0.2 and ~ 0.03 respectively for dry and lubricated sliding conditions. Comparatively, metal-free DLC coating exhibited high friction coefficient in dry ($\mu \sim 0.4 - 0.6$) and lubricated sliding ($\mu \sim 0.2$). The formation of low friction tribolayer due to thermal decomposition of Mo-DTC led to friction reduction in lubricated condition [26]. In another study, Ti-DLC coating deposited using hybrid magnetron sputtering and PACVD techniques showed friction and wear coefficients in the range of $\sim 0.05 - 0.1$ and $\sim 10^{-17} \text{ m}^3\text{N}^{-1}\text{m}^{-1}$ respectively against AISI 52100 steel counterpart under maximum 0.6 GPa contact pressure and different lubricant combination (PAO and PAO + Mo-DTC + ZnDTP) at 100°C . Similar friction coefficient was observed for Ti-DLC/Ti-DLC contacts, however the wear coefficient was reduced in the range of $\sim 10^{-18} \text{ m}^3\text{N}^{-1}\text{m}^{-1}$. Doping with Ti improved the tribological properties irrespective of counterpart and

lubricant combinations when compared to a-C:H coating deposited using same technology [27].

V. Mo-doped DLC coating

The friction behaviour of Mo-DLC coating, deposited using reactive RF sputtering was investigated during dry sliding against WC ball under 2 N normal load. The Mo-free DLC and Mo-DLC coatings with 3% and 15% Mo content shows friction coefficient in the range of 0.1 – 0.15, whereas Mo-DLC coating with 11% Mo content showed $\mu < 0.1$ [106]. The friction behaviour of RF magnetron sputtered Mo-DLC and metal-free DLC coatings were investigated in atmosphere (~50% – 60% RH) and in the presence of SAE 5W-20 oil (PAO + ZDDP + Mo-DTC) under 5 N normal load. In dry condition, the friction coefficients of Mo-DLC and metal-free DLC coatings were found in the range of $\mu \sim 0.2$ – 0.6 and $\mu \sim 0.4$ – 0.6 respectively. It was observed that addition of Mo not only increased hardness and micro-wear resistance, but also damaged the coating and increased friction coefficient. In lubricated condition, low friction tribolayer was formed due to thermal decomposition of Mo-DTC and addition of Mo improved the friction coefficient ($\mu \sim 0.05$ – 0.1) compared to metal-free DLC coating ($\mu \sim 0.2$) [26].

VI. W-doped DLC coating

RF magnetron sputtered W-DLC coatings showed lower friction ($\mu \sim 0.09$ – 0.12) compared to DLC coating ($\mu > 0.2$) when tested at ambient condition (25°C and 55% RH) against steel ball under applied load of 5 N. The low friction coefficient was attributed to the presence of moisture and the passivation of dangling bonds due to the addition of tungsten. The wear coefficients were observed in the range of $\sim 10^{-15}$ – 10^{-16} m³N⁻¹m⁻¹ after 1000 m of sliding distance [20]. Slightly higher friction coefficients ($\mu \sim 0.2$ – 0.3) were observed for DC magnetron sputtered W-DLC coatings at ambient condition (23°C and 55% RH) against steel ball under applied load of 30 N [18]. Similar friction value ($\mu \sim 0.2$) of W-DLC coating was documented when sliding against Al pin under 5 N applied load, however very high friction coefficient ($\mu \sim 0.6$) was observed with increase in temperature up to 300°C. With further rise in temperature at 400°C – 500°C, the reduction in friction value ($\mu \sim 0.12$ – 0.18) is observed due to formation of tungsten oxide. The

wear coefficients were observed at ambient and elevated temperature in the range of $\sim 10^{-16} \text{ m}^3\text{N}^{-1}\text{m}^{-1}$ and $\sim 10^{-14} \text{ m}^3\text{N}^{-1}\text{m}^{-1}$ respectively [104].

The W-DLC coating deposited using reactive sputtering were subjected to lubricated sliding test against steel ball at 50°C under applied load of 33 N. The pure and low additive (0.01% – 10%) PAO base oils were used as lubricant. The friction coefficient was decreased up to 50% for W-DLC coating compared to metal-free DLC coating due to formation of WS_2 in the tribolayer. This reduction in friction led to wear coefficient as low as $\sim 10^{-7} \text{ mm}^3\text{N}^{-1}\text{m}^{-1}$. Further almost instantaneous formation of WS_2 - containing tribolayer was observed when EP additive concentration was 2% – 5% [63]. Similar tribological behaviour was observed for WC-doped hydrogenated DLC coating deposited using reactive sputtering. The wear mechanism of the DLC coating was local decohesion, which was changed to chemo-mechanical polishing type after addition of EP additives. A new type of tribofilm, composed of coating material (W and C) and sulphur from the additive, was formed on steel surface leading to a friction value as low as 0.055. The formation of WS_2 in the transfer layer was confirmed by XPS analysis of the wear track [64].

W-DLC coating deposited using reactive sputtering showed almost similar friction and wear coefficients ($\mu \sim 0.1 - 0.3$ and $K_c \sim 10^{-15} \text{ m}^3\text{N}^{-1}\text{m}^{-1}$ respectively) in the temperature range of 20°C – 150°C when tested against steel counterparts and under different lubricant combinations (PAO, PAO + AW additives and PAO + EP additives). However, higher wear coefficient is observed at 200°C for due to initial coating decomposition. The increase in wear rate is significant for PAO + EP additives combination compared to others [59].

2.2. Thermal stability of DLC and metal-doped DLC coatings

I. DLC coating

Poor thermal stability is one of the major problem of standard DLC coatings, which compromises the tribological applications in automotive industry due to degradation of the coating properties at higher working temperature ($>300^\circ\text{C}$). Both the hydrogenated and non-hydrogenated DLC coatings have metastable structure, which transforms into

the stable graphite-like structure typically at $\sim 350^{\circ}\text{C}$ [7, 8]. Significant amount of sp^3 bonded carbon present in the DLC coating results in diamond-like structure, which is found stable up to $\sim 300^{\circ}\text{C}$. As the temperature reaches to $\sim 350^{\circ}\text{C}$, the sp^3 bonded carbon is converted into sp^2 bonded carbon indicating initiation of graphitisation (i.e. transformation of diamond-like structure into graphite-like structure) and further rise in temperature results in complete graphitisation of the DLC coating. Raman spectroscopy is a popular non-destructive technique to study the bonding properties of the DLC coating. Raman frequencies of sp^3 and sp^2 sites in the crystalline diamond and graphite are found $\sim 1330\text{ cm}^{-1}$ and $\sim 1550\text{ cm}^{-1}$ respectively, thus this technique shows a notable distinction between sp^3 and sp^2 bonded carbon present in the DLC coating. The Raman spectrum of DLC coating is dominated by the G (sp^2 bonded graphitic carbon) peak from ambient condition to 300°C and a D (disordered) peak is appeared in the spectrum $\sim 350^{\circ}\text{C}$ showing start of graphitisation. The distinct and dominant D and G peaks are observed in the spectrum at $\sim 450^{\circ}\text{C}$ indicating complete transformation of the DLC coating into nanocrystalline graphite [9]. The nanocrystalline graphite does not possess the superior mechanical and tribological characteristics of the DLC coating leading to its failure at elevated temperature. In brief, the transformation of diamond-like structure into the graphite-like structure at $\sim 350^{\circ}\text{C}$ degrades the properties of DLC coating [7, 8, 9]. Addition of dopants such as Ti, Si, Cr, Mo and W delays the graphitisation process and improves thermal stability [7, 8, 21, 60 – 62, 83 – 85], however it depends on the deposition procedures and test conditions as discussed in the following paragraphs.

II. Cr-doped DLC coating

The thermal stability of Cr-DLC coating deposited using CAE technique was investigated using TGA with a heating rate of $10^{\circ}\text{C}/\text{min}$ in the temperature range of $25^{\circ}\text{C} - 800^{\circ}\text{C}$ [84]. The graphitisation started below 290°C and a significant weight loss was observed due to CO_2 formation in between $290^{\circ}\text{C} - 342^{\circ}\text{C}$. The oxidation of CrN and CrC_xN_y interlayers led to weight gain in the temperature range of $400^{\circ}\text{C} - 800^{\circ}\text{C}$. The annealing tests were carried out in the range of $200^{\circ}\text{C} - 500^{\circ}\text{C}$ for 30 minutes. The graphitisation started only at 200°C and the groove formation was observed on the surface indicating the relaxation of internal residual stresses at 300°C . In another study, thermal stability of $\sim 400^{\circ}\text{C}$ was reported for Cr-doped graphite-like carbon coating (C/Cr), which was deposited using combined steered cathodic arc and unbalanced magnetron sputtering

[85]. The TGA analysis carried out with a heating rate of 1°C/min demonstrated two stages of oxidation at ~400°C and ~660°C respectively. The first stage of oxidation at ~400°C was indicated by the weight loss due to rapid evaporation of carbon and the second stage at ~660°C was indicated by the weight gain due to chromium oxide formation. Annealing tests were carried out for 1 hour in the temperature range 350°C – 700°C. Depending on the bias voltages used during deposition of the C/Cr coatings, the oxidation took place in the temperature range of 410°C – 700°C.

III. Si-doped DLC coating

Further research was carried out on the mid-frequency magnetron sputtered Si-DLC films, which was thermally stable up to 500°C after 30 minutes of annealing at ambient air [60]. The formation of silicon oxide was considered as a key factor to prevent diffusion of oxygen into the DLC coating. Another study reported that the graphitisation of RF sputtered Si-DLC film was started at ~400°C and significant oxidation was observed at ~500°C when annealing was done for 1 hour at ambient air [61]. The change in coating structure was confirmed by the rapid increase in the I_D/I_G ratio at ~500°C. The addition of Si stabilised the coating structure by forming more sp^3 bonded carbon, thus the graphitisation was delayed. Similar thermal stability was documented for conventional RF sputtered $a-C_{1-x}Si_x:H$ coating in another research [62]. The graphitisation took place ~500°C for samples with silicon content less than 15%. When silicon content was more than 15%, the structural change was delayed.

IV. Ti-doped DLC coating

The electron cyclotron resonance chemical vapour deposition (ECR-CVD) with magnetron sputtering was used to deposit Ti-DLC coating, which was found thermally stable up to ~450°C after annealing of 30 minutes at ambient condition [7]. The formation of hard TiC phases during heat-treatment delayed the graphitisation of the coating. In another study, a multilayer Ti-DLC coating (Ti/TiN/TiC_xN_y/DLC) was deposited using combined UBM and PECVD techniques and thermal stability of this coating was tested by thermo-gravimetric analyser (TGA) with a heating rate of 15°C/min from room temperature to 800°C. The top DLC layer was graphitised below 350°C leading to a sudden decrease in hardness of the coating. In the temperature range 350°C – 450°C, a rapid weight loss was occurred due to formation of CO₂. Thus the Ti-containing

intermediate layers were exposed and formation of TiO_2 led to gradual increase in the sample weight after 450°C [8]. When DLC coating was doped with both Ti and Al [nc-TiC/a-C(Al)] and deposited using UBM, a significant structural modification took place after 400°C as indicated by the sudden rise in the I_D/I_G ratio. The amorphous carbon matrix became almost graphite-like with a large cluster size as the temperature reached to 500°C . However, the presence of hard TiC phases retained the coating hardness almost similar even after the structural change [83] .

V. Mo-doped DLC and W-doped DLC coatings

The thermal stability of Mo-DLC and W-DLC coatings deposited using filtered metal cathodic arc vacuum discharge technique were investigated in the temperature range of $200^\circ\text{C} - 500^\circ\text{C}$ in Argon atmosphere. The Raman spectroscopy showed that the D and G peaks were disappeared at 400°C for DLC coating but they were present up to $\sim 500^\circ\text{C}$ for both the Mo-DLC and W-DLC coatings. The slower graphitisation rate of Mo-DLC and W-DLC coatings was attributed to the presence of metal carbide phases, which were thermally stable and continued to coalesce below 500°C [21].

2.3. Coating deposition techniques

2.3.1. Unbalanced Magnetron Sputtering (UBM)

Physical vapour deposition (PVD) is a widely used technique in the domain of thin films involving transfer of material from target to substrate in atomic level. The atoms of target material are vaporised by either thermal evaporation or sputtering (in vacuum) process and finally condensed onto the substrate forming a thin solid film. In thermal evaporation, the atoms are vaporised from target material by heating until its vapour pressure exceeds ambient pressure, whereas the high-energy gas ions strike the target surface and create the vapour by dislodging the neutral atoms during sputtering. The most common PVD processes include cathodic arc evaporation, ion beam assisted deposition, RF sputtering, closed-field and pulsed DC unbalanced magnetron sputtering.

In basic sputtering, atoms of target material (cathode) are ejected by bombardment of energetic particles in glow discharge plasma positioned in front of the target. Secondary electrons emitted from the target surface as a result of ion bombardment maintain the plasma during sputtering. Positively charged gas ions (typically Argon ions) generated in the plasma are attracted to the negatively biased target material at a very high speed. The collision creates a momentum transfer and ejects atoms from the target. These atoms are deposited as a thin film on the surface of the substrates. The schematic diagram of the mechanism of sputter deposition is shown in figure 2-5. Low deposition rate, low ionization efficiency and high substrate heating effect limits the basic sputtering process [136]. These limitations are overcome by introduction of magnetron sputtering and more precisely unbalanced magnetron sputtering. In magnetron, a magnetic field parallel to the target surface is configured and it constrains the motion of secondary electrons to the vicinity of target. The one pole of the magnets is positioned at the central axis of the target and a ring of magnets around the outer edge of the target forms the second pole. Thus the electrons are trapped in a way which increases the ionisation efficiency and therefore dense plasma in the target region is formed. As a result, ion bombardment of the target and the sputtering rate increases leading to higher deposition rates on the substrate. The increased ionisation efficiency of magnetron mode allows the discharge to be maintained at lower operating pressure and voltage (typically 10^{-3} mbar and -500V) compared to the basic sputtering mode (typically 10^{-2} mbar and -2 – -3 kV) [136].

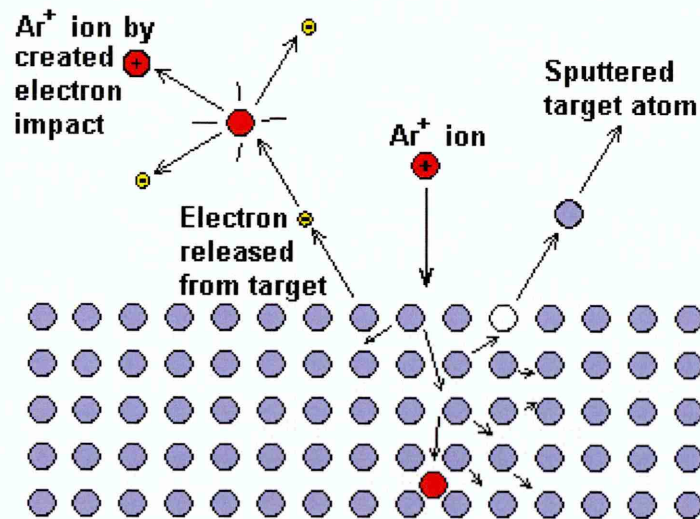


Figure 2-5: Schematic diagram of the mechanism of sputter deposition

Depending on the strengths of central and outer magnets used in the magnetron sputtering system, it can be categorised as balanced and unbalanced magnetron sputtering. A schematic representation of both the magnetrons is shown in figure 2-6. The conventional/balanced magnetron has both poles of equal strength, thus the dense plasma is strongly confined to the target region (within 60 mm from the target surface) and very low current density (typically 1 mA/cm²) is drawn to the substrate placed outside the plasma. The unbalanced magnetron of type I and type II overcomes this limitation. Type I unbalanced magnetron has much stronger central pole than outer one, thus the field lines that do not close on themselves, are directed towards the chamber wall resulting in very low ion current density ($\ll 1$ mA/cm²). Low deposition rate, high residual stress and defective film structure limits the use of type I unbalanced magnetron sputtering. In type II, stronger outer pole directs some of the field lines towards the substrate and few secondary electrons are able to follow that. As a result, plasma is allowed to flow to the substrate side resulting in high ion current density (typically 2–10 mA/cm²) without any external high bias voltage [136].

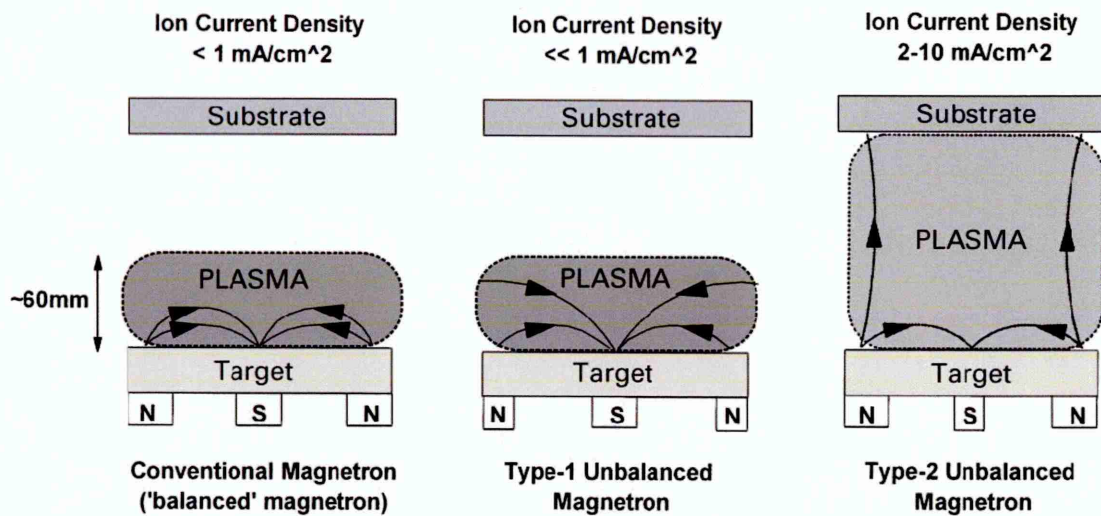


Figure 2-6: Schematic representation of the plasma confinement observed in balanced and unbalanced magnetrons [136]

During coating of the components having complex geometry, the deposition rate of unbalanced magnetron system with a single cathode source is found below the acceptable range. Thus a multiple magnetron system is introduced to use this technology commercially. In this system, magnetic arrays in the adjacent magnetrons can be

configured with identical or opposite magnetic polarities. For identical polarities, the field lines are directed towards the chamber walls resulting in the loss of secondary electrons and low plasma density near the substrate. Alternatively, the field lines are linked between the magnetrons (i.e. they are closed) for opposite magnetic polarities, thus the losses to the chamber walls are low and the plasma density becomes high near the substrate. The former one is known as mirror-field configuration, whereas the later one is known as closed-field unbalanced magnetron (CFUBMS) as schematically represented in figure 2-7. Closing of the fields forms a magnetic trap, which very effectively confines the electrons in between the cathodes leading to high levels of ion bombardment. Thus dense coating with low residual stresses is formed [136].

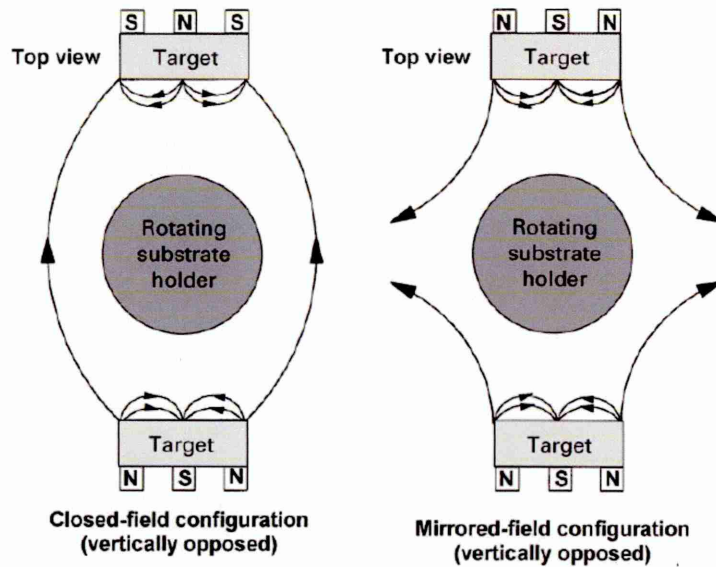


Figure 2-7: Schematic representation of dual unbalanced magnetron system [136]

Multiple cathode unbalanced magnetron system is advantageous for deposition of coatings with any desired alloy composition and graded design of the coating properties. This can be obtained by sputtering the targets at different rates or by varying the flow of reactive gas during deposition. In this way, both the interfacial adhesion between the coating and the substrate and the functional properties of the coating surface can be optimised. These features of CFUBMS lead to successful deposition of DLC coatings with low residual stress and improved adhesion strength with the substrate. This process allows depositing a number of intermediate layers to achieve strong adhesion and a gradual enhancement of the coating properties before deposition of DLC layer (typical coating architecture includes Ti/TiN/TiCN/TiC/DLC) lowers the residual stress [136].

2.3.2. High Power Impulse Magnetron Sputtering (HIPIMS)

High power impulse magnetron sputtering (HIPIMS) is a relatively new PVD technology that combines magnetron sputtering with pulsed power technology [137, 138, 139]. In conventional DC magnetron sputtering, the plasma density is observed in the order of up to 10^{17} m^{-3} in a close vicinity of the target with typical average electron energy of a few electron volts (eV) [140]. The low plasma density results in ion-to-neutral ratios of sputtered material only a few percent [141]. An increase in cathode power increases the ion to neutral ratio, however high power rises the cathode temperature sometimes leading to melting or vaporisation of the cathode. The high temperature often causes detachment of small droplets from the cathode and deposition on the substrate resulting in poor coating quality. Thus this technique is limited to a relatively small power density. By applying high power in pulses with a low duty factor (pulse on time in comparison to the cycle time) can generate high plasma density without overheating the target. The peak power of the cathode can reach up to several kW/cm^2 , which is almost two orders of magnitude higher compared to the time-averaged power [142]. This method is called high power impulse magnetron sputtering as first reported by Kouznetsov in 1999 [137]. Since then, HIPIMS has been widely investigated, both in terms of properties of the plasma and the produced coatings. The typical pulse lengths used in this technique are of $\sim 50 - 500 \mu\text{s}$ with pulse frequencies of $\sim 1 - 100 \text{ Hz}$ and the plasma density is observed in the order of $\sim 10^{19} \text{ m}^{-3}$ [143]. The advantages of HIPIMS technology are as follows:

- (i) High ratio of metal neutrals and ions to gas ions [144]
- (ii) High ratio of metal ions to metal neutrals [144]
- (iii) High Ionization degree (+2, +3) of metal atoms [145, 146]

Figure 2-8 shows the schematic representation of DC magnetron sputtering and HIPIMS process. The plasma generated in DC magnetron sputtering contains mostly Ar ions, reactive gas ions, metal neutrals and fewer metal ions (figure 2-8a), whereas the plasma generated in HIPIMS process is metal-rich (figure 2-8b). The highly ionized sputtered atoms generated in this metal-rich plasma penetrate the substrate material and gradually loss their energy by colliding with substrate atoms. In this way, sputtered atoms are implanted into the substrate surface leading to elimination of voids and subsequent changes of initial surface microstructure. This substrate etching step (prior to the coating deposition) significantly improves the coating-substrate adhesion and grows coatings

with dense microstructure and other desirable properties such as less columnar structure, high corrosion and wear protection compared to the DC magnetron sputtering [144, 147, 148]. However, this technology suffers from arcing on the cathode surface and lower deposition rate compared to DC magnetron sputtering at the same average power [149].

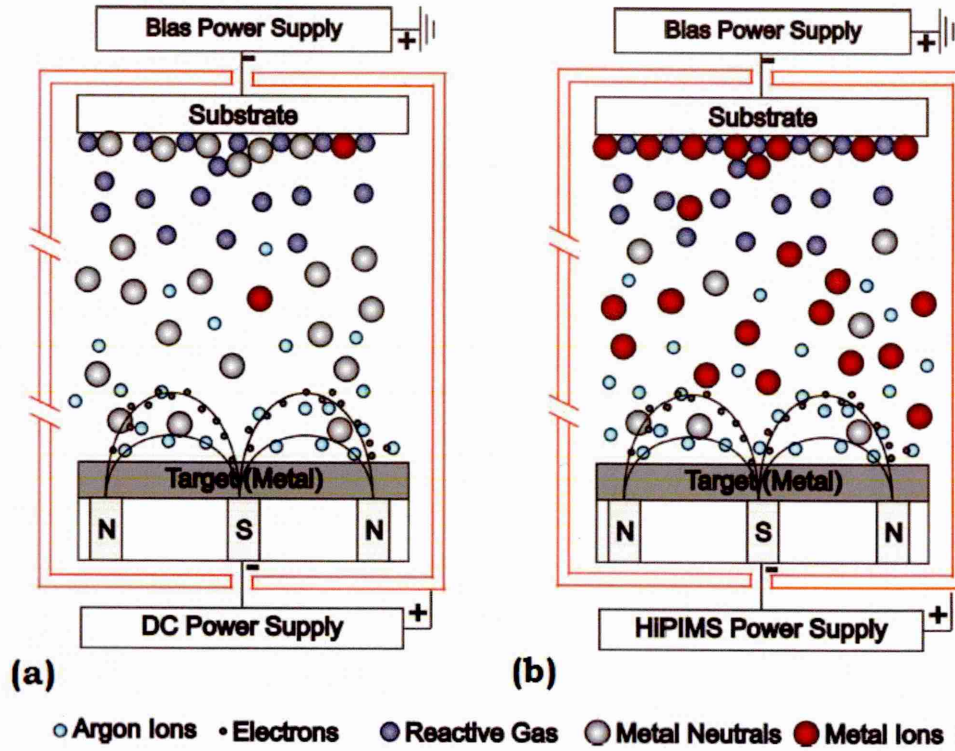


Figure 2-8: schematic representation of (a) DC magnetron sputtering and (b) HIPIMS process

2.3.3. Microstructure of thin films

Depending on the deposition processes and process parameters, thin films exhibit different microstructures, which are characterised by grain size, crystallographic texture, phase and chemical composition. The functional properties of the thin film are very much influenced by the coating microstructure, thus extensive studies have been done to understand the relationship between coating microstructure and process parameters. Movchan and Demchishin [150] introduced the idea of structure zone model (SZM) in 1969 for very thick films made by evaporation. They defined homologous temperature

$$T_h = \frac{T}{T_m}, \text{ where } T \text{ is the film growth temperature in K (often used as substrate temperature) and } T_m \text{ is the melting temperature of the deposited film material in K. Figure}$$

2-9 shows three zones of Movchan and Demchishin's SZM. Zone 1 (where $T_h < 0.3$) contains fine-grained structure ending with domed tops, however lots of lattice imperfections and pores are observed at the grain boundaries. Uniform columnar grains are observed in zone 2 (where $0.3 < T_h < 0.5$) due to the development of surface diffusion processes, which lead to formation of faceted surface with larger grains. In zone 3 (where $T_h > 0.5$), fully dense and equiaxed film structure with large grains is observed due to bulk diffusion and recrystallization.

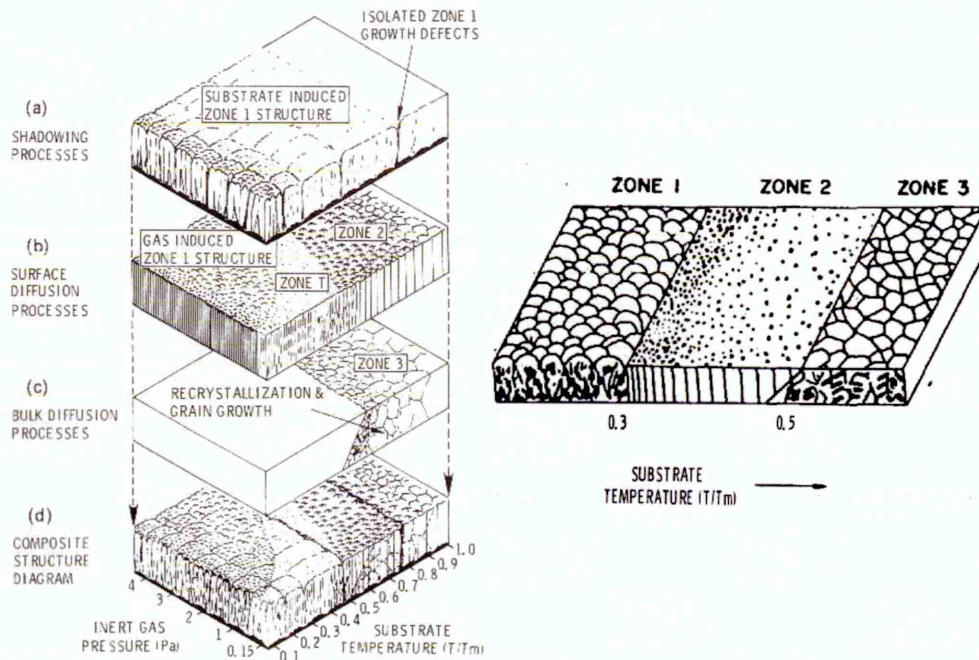


Figure 2-9: Structure zone model of thick films by Movchan and Demchishin in 1969

With development of magnetron sputtering, the SZM was needed to be revised as the film structure was dependent on both the deposition temperature and pressure. In 1974, Thornton published another SZM showing the film structure was governed by both the homologous temperature and the pressure [151] as shown in figure 2-10. Porous film structure is observed in zone 1, which changed to dense columnar grain structure in zone 2 and recrystallized grain structure in zone 3. A transition zone namely zone T containing densely packed grains is observed in between zones 1 and 2. This SZM shows that the zone T film structure can be achieved only at $T_h \sim 0.1$ when Argon pressure is as low as ~ 1 mTorr. Therefore the desired zone 2 film structure can easily be formed at much lower

temperature ($T_h < 0.5$) with low Argon pressure during film deposition. The model is best known among all the SZM models.

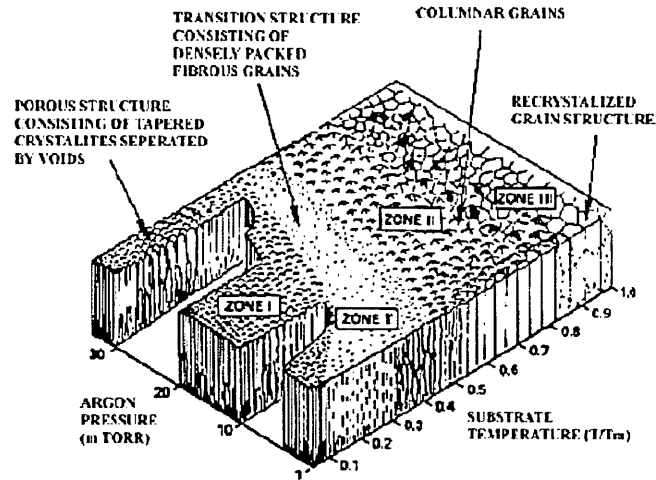


Figure 2-10: Structure zone model of sputtered films by Thornton in 1974

Further revision of SZM was required when ion beam assistance was added to magnetron sputtering processes for film deposition. Messier proposed a modified SZM in 1984 [152] as shown in figure 2-11. The model contained four zone structures such as 1, T, 2 and 3 and the pressure axis in Thornton's model was replaced by the substrate bias voltage. In this model, zone T is observed wider than zone 1 at high bias voltage due to increase in ion bombardment, which in turn rises the substrate temperature. Zones 2 and 3 are found comparable to that of Thornton's model. However, Messier's model did not consider the effect of different arrival ion-to-atom ratios or the energy of the ions during ion bombardment, which in turn influence the film growth.

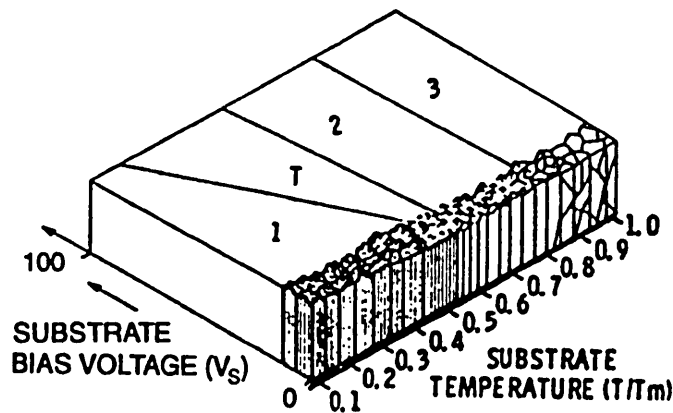


Figure 2-11: Structure zone model of ion beam assisted sputtered films by Messier in 1984

2.4. Discussion

Use of DLC and metal-doped DLC coatings in coated engine parts are widespread due to their excellent combination of mechanical and tribological properties. In dry sliding, most of the metal-doped DLCs show improved friction and wear behaviour compared to metal-free DLC coatings. Incorporation of dopants like Ti, Mo and W into the DLC coating significantly decreases the friction coefficient in lubricated sliding depending on the test conditions. Till now, the low friction in lubricated sliding has been attributed to the formation of MoS₂-containing tribolayer due to thermal decomposition of Mo-DTC present in the engine oil. Further proof has been found that the tribolayer contains WS₂ particularly during lubricated sliding of W-DLC coating, where W comes from the coating and S comes from EP additives present in the engine oil leading to very low friction. The usefulness of metal-doping is further realised for high temperature lubricated sliding tests. High friction coefficients are obtained for metal-free DLC coatings due to coating decomposition at ~150°C, however W-doping can maintain similar friction value up to ~200°C. Further combination of base oil (PAO) with an optimised amount of ZDDP and Mo-DTC provides better tribological performance compared to base oil + ZDDP or base oil + Mo-DTC combinations.

Depending on the deposition conditions, the thermal stability of metal-free DLC coating is observed ~300°C. The formation of metal carbide phases during annealing is an important factor that increases the thermal stability of the metal-doped DLC coating when compared to the metal-free DLC coating. The metal carbide phases stabilise the diamond-like structure at elevated temperature and thus the graphitisation is delayed. As found from the literature, the graphitisation can be delayed up to ~500°C if Mo, W or Si is used as doping element.

This information indicates that both the Mo-DLC and W-DLC coatings are capable to provide low friction in lubricated sliding as well as withstand elevated temperature. However, Mo-DLC coating suffers from low hardness [105] and the hardness of W-DLC coating depends on deposition process, concentration of W and bias voltage [102, 153]. Thus Mo-DLC coating provides high wear rate during sliding, whereas wear rate of W-DLC coating depends on its hardness. This research aims to develop a high temperature wear resistant coating, which maintains its tribological properties during lubricated

sliding in ambient and high temperature. Thus the idea adopted in the present work is to combine the benefits of simultaneous doping of carbon-based coating with Mo and W atoms, where the coating itself can provide elements to form lubricious compounds during sliding. This Mo – W doped carbon-based coating (Mo–W–C) is expected to provide high thermal stability and to maintain its improved tribological performance at ambient and elevated temperature condition.

As discussed, the adhesion and hardness of the coating are two important factors that influence the coating delamination and the wear rate during sliding. Strong adhesion with substrate depends on metallurgical bonds between the coating and the substrate, whereas high hardness is attributed to the dense coating microstructure. HIPIMS is a popular technique, which offers both – strong adhesion and dense coating structure. The use of metal ion etching before coating deposition ensures strong coating-substrate adhesion, whereas high ionisation degree of plasma particles leads to dense coating microstructure with less lattice defects as understood from the structure zone models explained before. The HIPIMS technique suffers from lower deposition rate, which can be compensated by the use of DC unbalanced magnetron sputtering during coating deposition. Thus, combined HIPIMS + UBM techniques is used to deposit Mo–W–C coating in order to obtain desirable coating properties for the first time. Deposition procedure and the characterisation tests used to evaluate the coating performance are described in the next chapter.

3. Deposition and characterisation of molybdenum and tungsten doped carbon-based (Mo–W–C) coating

3.1. Introduction

This chapter describes the deposition procedure of Mo–W–C coatings and the different characterisation techniques used for understanding of the coating properties. The sample preparation techniques before coating deposition and the deposition procedure with principal process steps are discussed in section 3.2. Section 3.3 includes description of the characterisation techniques used to evaluate the coating properties and relevant test parameters. The data obtained from tribological study were used for optimisation of technology of Mo–W–C coatings.

3.2. Sample preparation techniques and coating deposition procedure

The industrial sized Hauzer HTC 1000-4 PVD coating machine equipped with four targets is used to deposit Mo–W–C coatings. The target materials needed to deposit this coating are Mo, W and graphite (C). Table 3-1 lists the sputtering yields of Mo, W and graphite at different incident angle. The sputtering yield of graphite is found low compared to that of Mo and W, which indicates three graphite targets are essential in order to deposit metal-doped carbon-based coatings. In that case, both the Mo and W should be incorporated in the fourth target and it should be a compound target made of molybdenum and tungsten. Pure molybdenum (~99.9% Mo), pure tungsten (~99.9% W) and tungsten carbide (WC) targets are readily available in the market. Pure molybdenum [105, 106] and pure tungsten [103, 153 – 155] targets are often used to deposit Mo-DLC and W-DLC coatings. Some researchers have also used the pure WC targets [18, 156] as well as WC targets with Ni binder [18] for depositing W-DLC coating on steel substrates at around 290°C – 340°C.

Table 3-1: Sputtering yield of materials at different sputtering angles in argon atmosphere (for acceleration energy of 500 eV)

Sputtering yield at incident angle	Target material			
	Graphite	Molybdenum	Tungsten	Tungsten carbide
0°	0.197	0.861	0.664	Not found in literature
45°	0.528	1.377	1.001	

Prior to coating deposition, the M2 grade HSS and 304 SS disc samples (\varnothing 30 mm \times 6 mm) were polished with emery papers from rough to fine grades (P180 – P4000, where P grade indicates FEPA standard), followed by 6 μ m and 1 μ m diamond pastes resulting in mirror polish (average $R_a \sim 0.01 \mu$ m) of the surface. These polished samples – the polished 304 SS coupons (15 mm \times 50 mm \times 0.8 mm with a through hole of \varnothing 1.5 mm at one end) and the Si wafers were cleaned in an industrial sized automated ultrasonic cleaning line to remove surface impurities (such as oils, hydrocarbons, oxides etc.) and then dried in a vacuum drier before loading into the coating chamber. The HSS and SS disc samples were used for measurement of adhesion and hardness, microstructural study and pin-on-disc tests carried out at ambient and elevated temperatures. The Si wafers were used for measurement of coating thickness (from the cross-section of the coating using SEM) and surface roughness. The SS coupons were used for thermo-gravimetric tests and isothermal oxidation tests.

Clean samples were then loaded to an industrial sized HTC 1000-4 PVD coating machine, which has an octagonal cross-section and a volume of 1 m³. The coating unit is equipped with a turntable located at the centre of the machine, three heaters (two are positioned on the chamber doors and one under the turntable or substrate holder) and four rectangular cathodes. Each cathode is connected to the unbalanced magnetron power supply and additionally two of them can be operated in HIPIMS mode. Figure 3-1 shows the schematic diagram of the cathode configuration with operating modes during Mo–W–C coating deposition. Three graphite targets were operated in UBM mode and the compound Mo–WC target was operated in HIPIMS mode. All the samples experienced three-fold rotation in order to achieve homogeneity in the direction of coating growth. Prior to the coating deposition, the targets were sputter-cleaned and the sample surfaces were further pre-treated by HIPIMS ion etching. A Mo–W–N base layer was deposited in reactive Ar + N₂ atmosphere in order to enhance the coating – substrate adhesion, which is followed by the deposition of the Mo–W–C coating in Ar atmosphere. Table 3-2 lists the principal process steps of combined HIPIMS + UBM deposition procedure for Mo–W–C coatings.

The Mo–W–C coatings were deposited using combined HIPIMS + UBM techniques at a temperature of 250°C and a substrate bias voltage of –65 V. The average power of the graphite targets were fixed to 5 kW during deposition. Three different Mo–W–C coatings

named as C2, C4 and C6 were deposited by varying the average power of the compound Mo–WC target to 2 kW, 4 kW and 6 kW respectively.

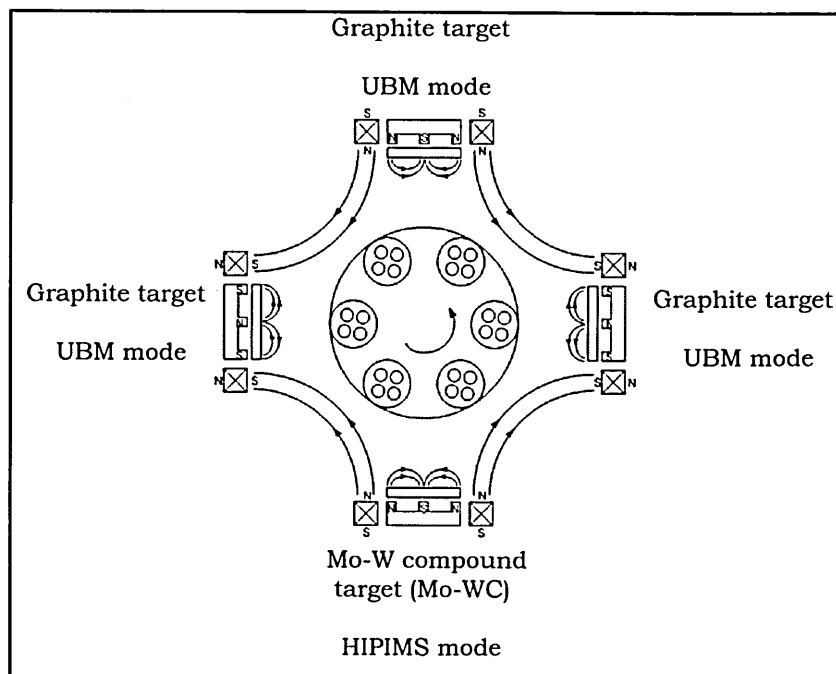


Figure 3-1: Schematic of the cathode configuration in HTC 1000-4 PVD coating machine during Mo–W–C coating deposition

Table 3-2: Principal process steps of combined HIPIMS + UBM deposition procedure for Mo–W–C coatings

Steps	Objective of the steps
1. Pumping down	Evacuating the coating chamber by rough pumping ($\sim 10^{-2}$ mbar) and fine pumping ($\sim 3 \times 10^{-5}$ mbar) in order to minimise the contamination during deposition
2. Heating	Producing suitable temperature for coating deposition
3. Target Cleaning (UBM mode)	Removing contamination on target surface
4. Metal ion etching (HIPIMS mode)	Cleaning the substrate surface by highly energetic positive metal ions
5. Base layer (HIPIMS+UBM mode)	Improving adhesion between the coating and the substrate
6. Coating (HIPIMS+UBM mode)	Deposition of Mo–W–C coatings
7. Cooling down	Cooling of the system before unloading

3.3. Characterisation techniques

3.3.1. Scratch test

An automatic scratch tester (REKETEST developed by CSM instruments) was used to evaluate the critical load (L_c) for coating delamination, which measured the adhesion strength of the coating. The scratch tester was equipped with a cone shaped (120°) Rockwell type diamond indenter and a pre-set load of 10 N was used at the start of scratching. The normal load was gradually increased with the forward movement of the indenter and the finishing load was fixed at 100 N. The scratch track was observed with the help of an optical microscope, attached to the scratch tester. The magnitude of critical load was determined by measuring the length of scratch track from the start of scratch to the first exposure of the substrate.

3.3.2. Rockwell hardness test

The interfacial adhesion strength of Mo–W–C coatings was measured by a Rockwell hardness tester (Rockwell C scale), which consisted of a 120° diamond cone indenter with 1500 N load. The indentation was observed through an optical microscope and adhesion strength was categorised according to the six grades of indentations outlined by the VDI criteria as shown in figure 3-4 [157]. The indentation grades were dependent on the cracking and/or spallation of the coating around the indentation. The strong interfacial bond between coating and substrate was guaranteed by the grades HF1 – HF4 whereas grades HF5 and HF6 indicated delamination of the coating from the substrate due to poor adhesion strength. This test was performed on the coated HSS discs.

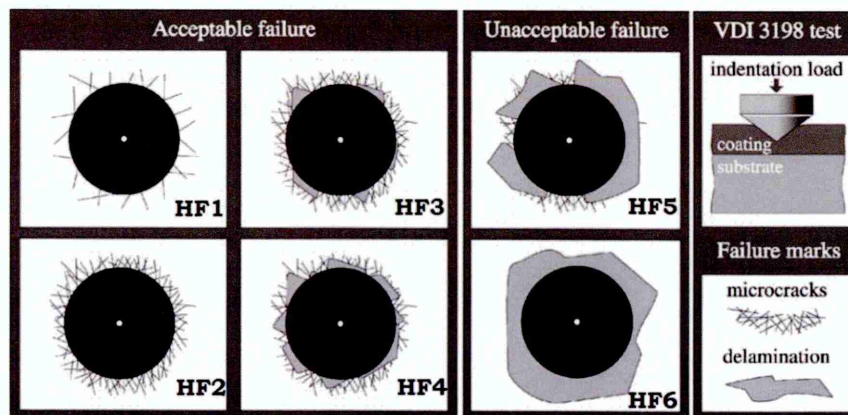


Figure 3-2: Classification of levels of interfacial adhesion of thin films based on typical indentation results according to the VDI standard of acceptability [157]

3.3.3. Nanoindentation

The nanohardness and the elastic modulus of the as-deposited and the oxidised Mo–W–C and state-of-the-art DLC coatings were measured using the CSM nanoindentation tester. The Berkovich diamond indenter was driven normal to the coated surface by applying load up to a pre-set value and then the load was gradually retracted until partial or complete relaxation of the material occurred. To avoid substrate contribution during hardness measurement, the indentation depth should be <10% of the total coating thickness. Therefore, the pre-set load was set to 10 mN and indentations were repeated for 20 – 30 times to find out the average nanohardness. The nanohardness and the elastic modulus were calculated using Oliver and Pharr method from the resultant load-displacement curves, which was an in-built module of the software.

3.3.4. Pin-on-disc test

The CSM room temperature and high temperature pin-on-disc tribometers were used to study the friction behaviour of the Mo–W–C and state-of-the-art DLC coatings in dry (i.e. no lubricant) and boundary lubricated sliding (Mobil1 Extended life™ 10W-60 engine oil used as lubricant) condition at ambient (~30°C and ~30% relative humidity) and elevated (200°C – 500°C) temperature respectively. Both the tribometers contained sample holder, which rotate against a stationary ball (used as a counterpart) under the influence of a static load. In this work, uncoated 100Cr6 steel balls and Al₂O₃ balls of 6 mm diameter were used as counterparts during sliding against coated HSS disc samples. The static load was fixed to 5 N for all the experiments and the sliding distance was varied in the range of 600 m – 15000 m (i.e. 0.6 km – 15 km) depending on the nature of the tests. The large sliding distance was selected to study the effect of metal dopants (Mo and W) on friction behaviour with time. The friction force and motor speed were included in the system calibration procedure. The coefficient of friction $\mu = F_T / F_N$ was calculated during the experiment using a measured value for the tangential force F_T and a normal force F_N exerted by a calibrated weight.

The wear coefficient was calculated using Archard's equation as $K_c = \frac{V}{F_N \times d}$ where V

is wear volume in m³, F_N is the normal load in N and d is the sliding distance in meter.

The volume of wear track (V) on the coated disc is calculated as $V = 2\pi RA$, where R is

the wear track radius and A is the cross sectional area of the wear track. The wear track profile was scanned by the surface profilometer (DEKTAK 150) and the area of the scanned profile was calculated by the associated software. The scanning was repeated for 8 – 10 times on different sections of the wear track and their average was calculated. This average area A was used in the equation mentioned above. The wear coefficient of the counterparts was also calculated using the Archard's equation.

3.3.5. Thermo-gravimetric analysis (TGA)

A high performance modular Thermo-Gravimetric Analyser (TGA) from SETARAM instrumentation was used to investigate the dynamic oxidation behaviour of Mo–W–C and state-of-the-art DLC coatings. The coated stainless steel coupons were suspended from the microbalance and heated from room temperature (20°C) to a pre-set value (1000°C) at a heating rate of 1°C per minute. Slow heating rate was preferred to monitor any distinguishable changes in sample weight during oxidation. The total duration of the test was 18 hours including the cooling phase after reaching the maximum test temperature of 1000°C. The resultant curve showing the mass change against the furnace temperature was plotted with the help of SETSYS software associated with the instrument.

3.3.6. Isothermal oxidation test

The isothermal oxidation tests were performed in the furnace (Lenton Thermal Designs Ltd). The Mo–W–C coated samples were heated from room temperature (~25°C) to the pre-set temperatures ranging from 400°C – 800°C with a step of 100°C at ambient atmosphere. Once the pre-set temperature was reached, the samples were heated at that temperature for 2 hours in order to achieve proper oxidation and then cooled slowly in air. Same heat-treatment was carried out for the state-of-the-art DLC coated samples up to 500°C and no tests were continued at higher temperatures due to local delamination of the DLC coating at 500°C.

3.3.7. Scanning electron microscopy (SEM)

FEI NOVA NANOSEM 200 coupled with Energy Dispersive X-ray (EDX) analysis module (Oxford instruments X-max detector with INCA analysis software) was used for studying microstructural, tribological and oxidation resistance properties of Mo–W–C

and state-of-the-art DLC coatings. The secondary electron detector (SE) and the thermoluminescence detector (TLD) were used for the topographical imaging and measurement of the coating thickness respectively. The X-ray mapping was done on the fractured cross-section of the as-deposited and oxidised coated samples and on the wear scar of the counterparts after sliding in order to identify the distribution of elements.

3.3.8. X-ray Diffraction (XRD)

The X-ray diffraction (XRD) was used to carry out the microstructural characterisation of the as-deposited and oxidised Mo–W–C and state-of-the-art DLC coatings with the help of a PANalytical Empyrean PIXcel 3D automated diffractometer. The microstructure and the phase composition of the as-deposited and oxidized surfaces were determined using Bragg-Brentano and glancing angle geometry. The continuous scanning was done from $2\theta = 20^\circ - 130^\circ$ with a step size of 0.026° for Bragg-Brentano geometry. The scanning range for glancing angle geometry was selected as $2\theta = 20^\circ - 120^\circ$ with an incident angle of 2° . The low angle ($2^\circ - 10^\circ$) XRD was carried out for better understanding of the multilayer structure of the as-deposited coatings. The Miller indices for all the phases present in the XRD patterns were calculated and shown in the respective figures. The X-ray source was Cu-K α radiation with a wavelength of 1.54 nm and the voltage and current of X-ray generation tube was 45 kV and 40 mA respectively.

3.3.9. Raman spectroscopy

The Raman spectroscopy was used to investigate the oxidation resistance of the Mo–W–C and state-of-the-art DLC coatings at elevated temperature and their wear behaviour during dry and lubricated sliding at ambient and elevated temperature. The Raman spectra were collected from the random positions on the as-deposited and oxidised surfaces, debris adhered to the wear scar on the counterpart surfaces and within the wear tracks after sliding. A Horiba-Jobin-Yvon LabRam HR800 integrated Raman spectrometer fitted with a green laser of wavelength 532 nm was used to collect the spectra. A 10% transmission filter was used to reduce the intensity of the incident beam so that the damage due to irradiation could be avoided. The exposure time for spectrum collection was varied in the range of 60 – 240 seconds in order to achieve better signal-to-noise ratio depending of the sample. The collected spectra were averaged over 5 acquisitions in the wavelength range of $50 - 2250 \text{ cm}^{-1}$ for each test conditions. The same parameter settings were used to accumulate the spectra from pure MoS₂, WS₂ and Cr₂S₃

powders. The powders were analysed as no data on Raman scattering from these compounds was available to us. During analysis, the background of spectrum was corrected using a 2nd order polynomial whereas a multi-peak (8 – 10) Gaussian-fitting function was used to deconvolute the spectrum and identify the Raman peaks.

The Raman spectrum of lubricant film placed on a glass slide was collected using the same acquisition settings but the exposure time and the wavelength range was set different. The lubricant film was exposed to green laser for 10s in order to avoid the chance of burning the oil. The Raman spectrum was acquired for 5 times in the wavelength range of 100 – 2200 cm⁻¹ and their average was plotted. The background of the spectrum was corrected using straight line during analyses. However, peaks could not be identified as the exact chemical compounds present in the lubricant are unknown.

The two-peak [84, 158 – 166] or three peak [167 – 170] Gaussian-fitting functions are widely used to analyse the Raman spectra. It is observed that the two-peak Gaussian-fitting functions often show higher I_D/I_G ratio, whereas three-peak models provide inconsistent I_D/I_G ratio depending on the peak positions (D1, D2, G and D, G1, G2) [171]. An alternative to the Gaussian-fitting function is a Breit-Wigner-Fano (BWF) line for G peak and a Lorentzian (L) line for D peak fitting [172]. But a four-peak Gaussian-fitting function is found similar to that of combined BWF (for G peak) and L (for D peak) fitting as both the methods give similar I_D/I_G ratio [171]. Based on the applicability of the deconvolution of techniques, the multi-peak Gaussian-fitting function is chosen for the current study.

4. Results and Discussion

4.1. Structural properties of molybdenum and tungsten doped carbon-based (Mo–W–C) coatings

4.1.1. Introduction

This chapter describes the structural properties of as-deposited Mo–W–C coatings (C2, C4 and C6). Coating microstructure, surface morphology, phase compositions and surface roughness are discussed in section 4.1.2. Surface morphology and coating microstructure are investigated with the help of scanning electron microscopy (SEM) coupled with energy dispersive X-ray (EDX) analysis module, X-ray diffraction (XRD) using Bragg-Brentano, glancing angle and low angle geometry and Raman spectroscopy. The phase compositions and the roughness measurement of as-deposited coatings are studied using XRD analyses and surface profilometry (Veeco DEKTAK 150) respectively. Sections 4.1.3 and 4.1.4 describe the hardness, elastic modulus and adhesion of the as-deposited coatings. The hardness and elastic modulus is measured using nanohardness tester. The adhesive strength between the coatings and the substrate is quantified using a scratch tester, whereas the cohesive strength of the coatings is evaluated using a Rockwell hardness tester. The concluding remarks are summarised in section 4.1.5.

4.1.2. Coating microstructure and phase composition

Figure 4.1-1 shows the surface morphology and the fracture cross-section of the as-deposited Mo–W–C coatings. The morphology of the grains indicates typical zone 2 microstructure of PVD films (according to the Thornton's structure zone model) for all three coatings (C2, C4 and C6). The nucleation during coating growth results in small spherical grains with a diameter of a few tens of nm. Large grains are formed due to

competitive growth of the small grains as observed from the micrographs of Mo–W–C coated surfaces (figures 4.1-1a – 4.1-1c).

The cross-sectional micrographs in figures 4.1-1d – 4.1-1f clearly reveal that the architecture of Mo–W–C coatings consists of a thin Mo – W – N base layer ($\sim 107 - 151$ nm) adjacent to the Si substrate, which is followed by a thick and dense Mo – W – C layer on the top. The metal content in the coatings depends on the average Mo–WC target power used during deposition. With increase in metal content, the total coating thickness increases and a significant change is observed in the coating microstructure.

The total coating thickness is observed as ~ 1.9 μm , ~ 2.2 μm and ~ 2.8 μm for coatings C2, C4 and C6 respectively. Both C2 and C4 show dense and columnar microstructure with flat column tops. The column boundaries are clearly delineated and the column diameters are found as ~ 130 nm and ~ 170 nm respectively. On the other hand, C6 possesses a dense and completely granular microstructure.

The average surface roughness (R_a) of as-deposited Mo–W–C coatings is shown in figure 4.1-2 and the corresponding surface profiles are provided in the inset. All three coatings show smooth surface finish. Lowest average surface roughness (R_a) of ~ 0.053 μm is observed for C2, whereas C4 and C6 show slightly higher roughness values (~ 0.073 μm and ~ 0.074 μm respectively).

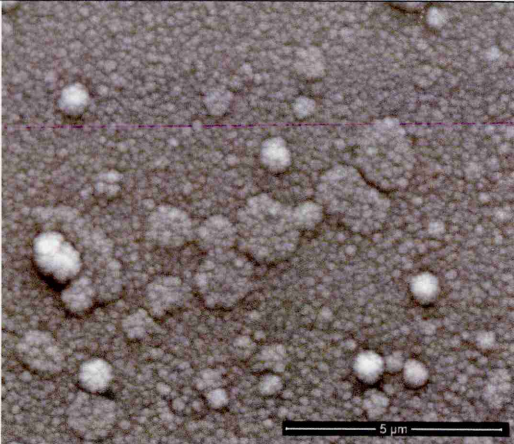
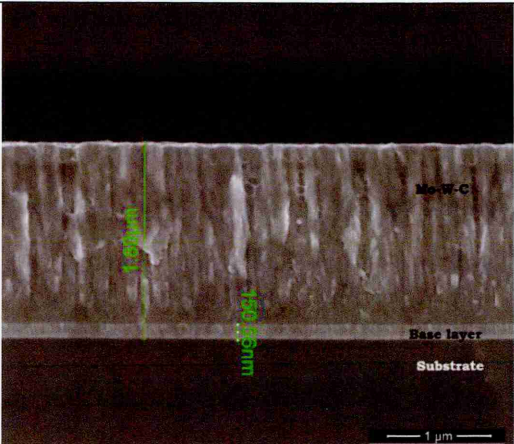
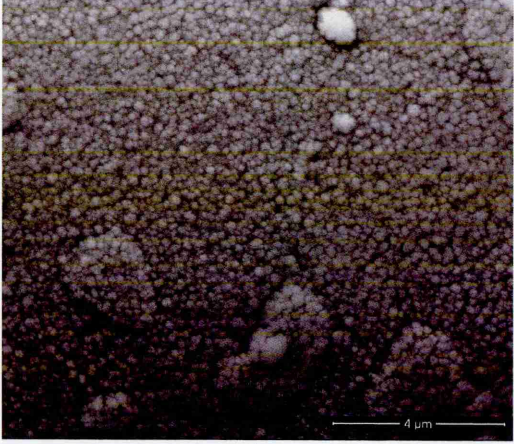
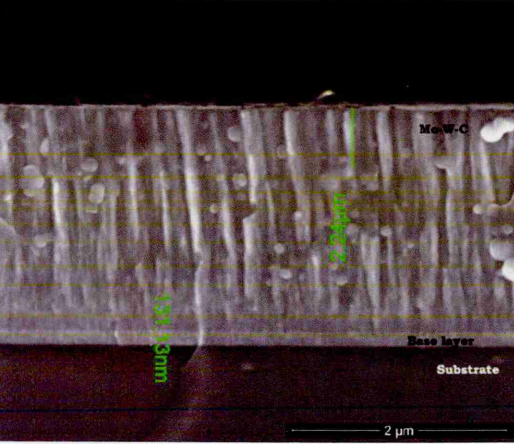
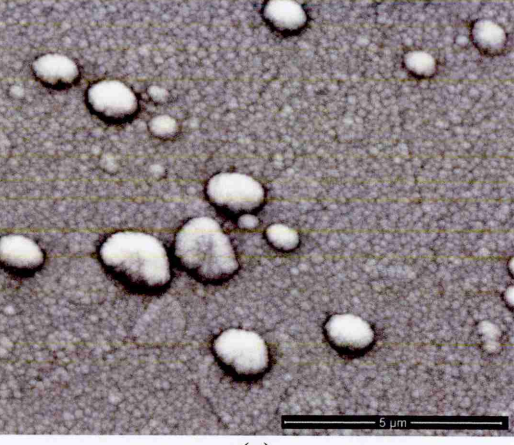
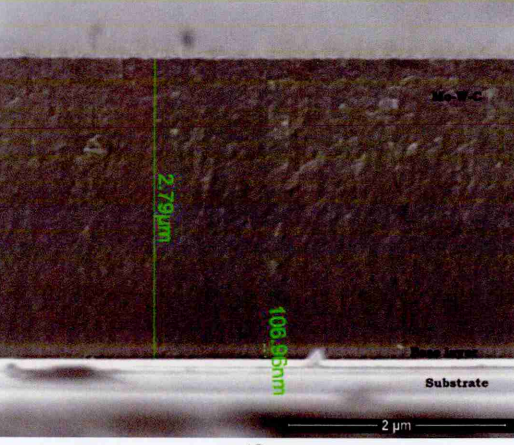
Coating	Surface morphology	Cross-section
C2	 <p>(a)</p>	 <p>(d)</p>
C4	 <p>(b)</p>	 <p>(e)</p>
C6	 <p>(c)</p>	 <p>(f)</p>

Figure 4.1-1: (a – c) Surface morphology and (d – f) cross-sectional SEM image of as-deposited Mo–W–C coatings

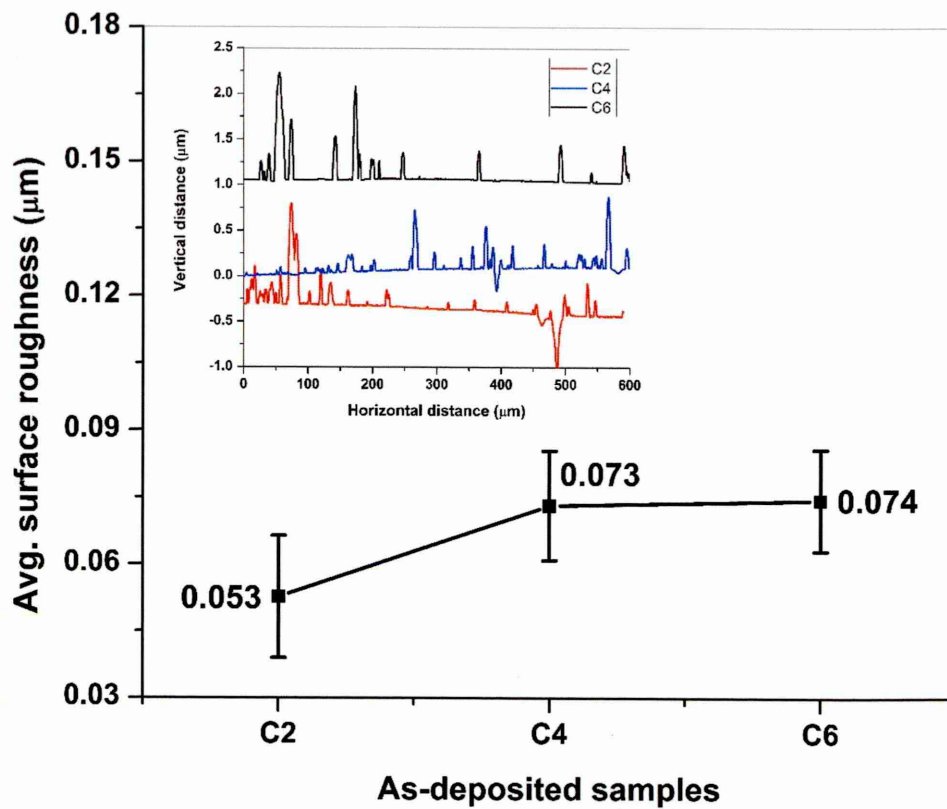


Figure 4.1-2: Average surface roughness and surface profile (in the inset) of as-deposited Mo-W-C coatings

X-ray mapping is carried out on the fracture cross-section of as-deposited Mo-W-C coatings in order to understand the elemental distribution across the coating thickness. Figures 4.1-3 – 4.1-5 indicate the presence of carbon (C), molybdenum (Mo), tungsten (W) and nitrogen (N) in Mo-W-C coatings. Higher concentration of C is observed at the top coating layer compared to the doping elements (Mo and W) for all three coatings. Mo and W are uniformly distributed throughout the entire coating thickness, however their presence as expected is found higher in the base layer. The base layer contains mostly Mo, W and N and lower amount of C. Maximum concentration of Mo and W is observed for C6 (figure 4.1-5) due to the highest average Mo-W-C target power during coating deposition. Similarly, lowest Mo-W-C target power during deposition of C2 results in highest amount of C (figure 4.1-3) compared to other coatings.

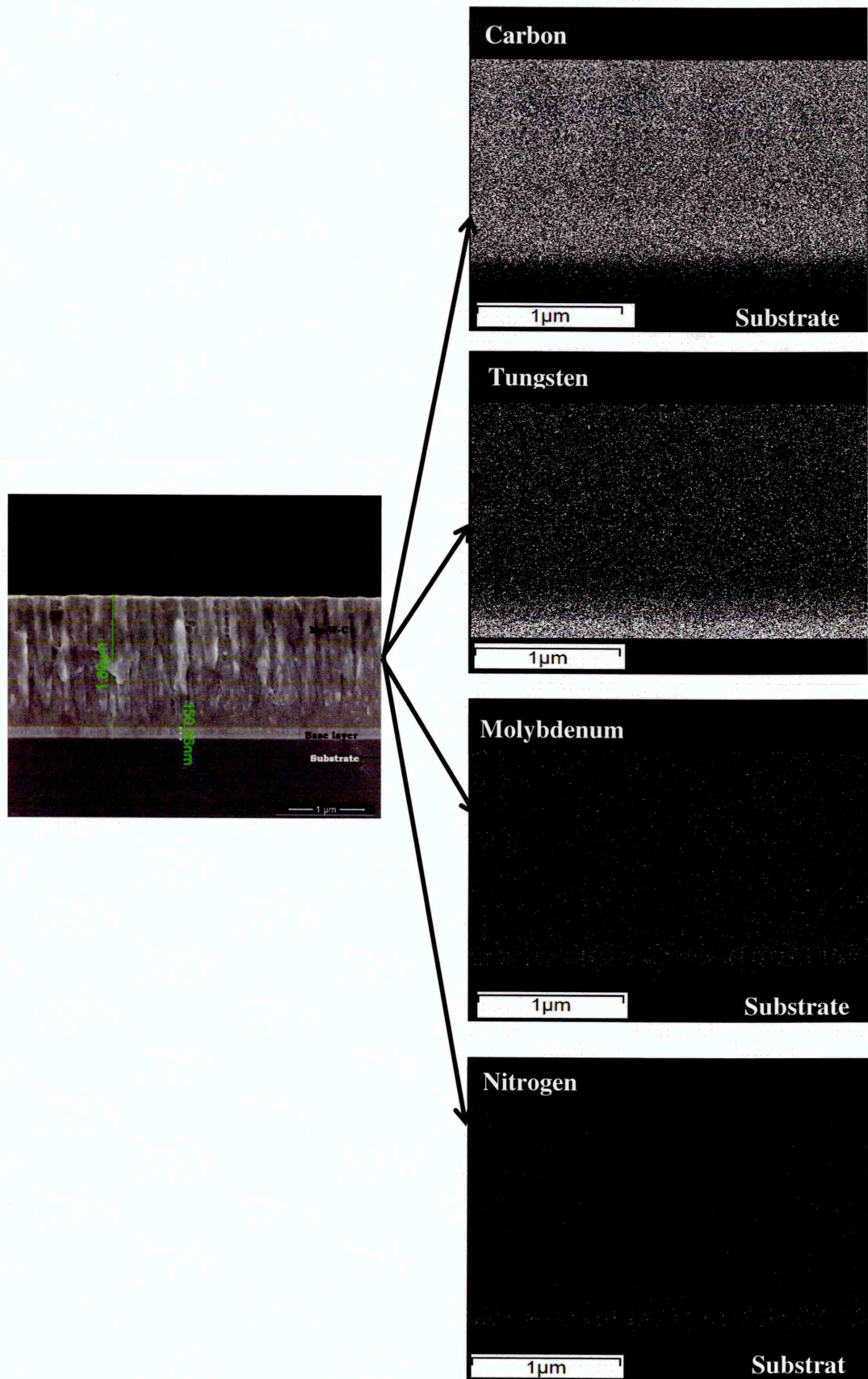


Figure 4.1-3: X-ray mapping of elements on the fracture cross-section of as-deposited C2

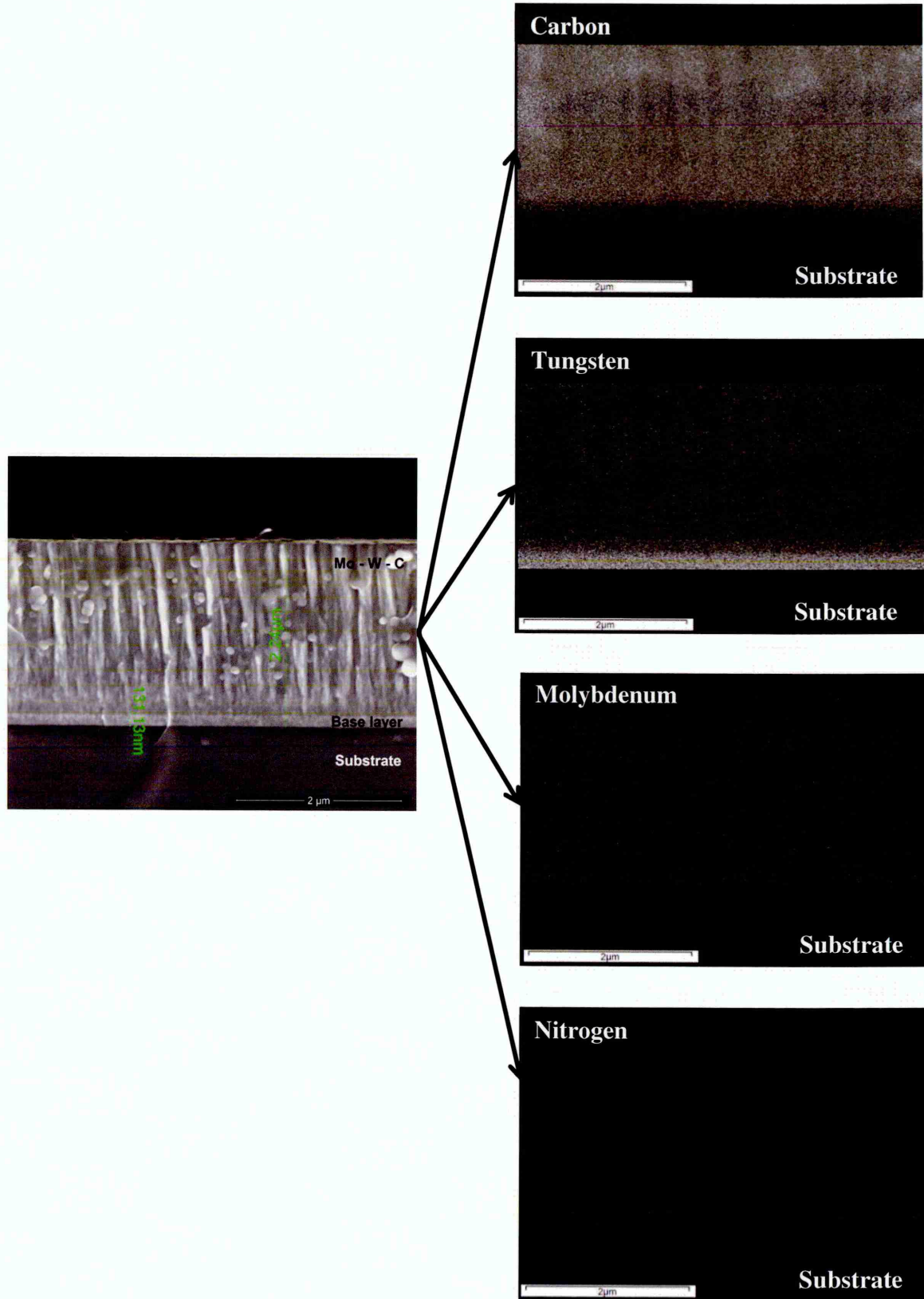


Figure 4.1-4: X-ray mapping of elements on the fracture cross-section of as-deposited C4

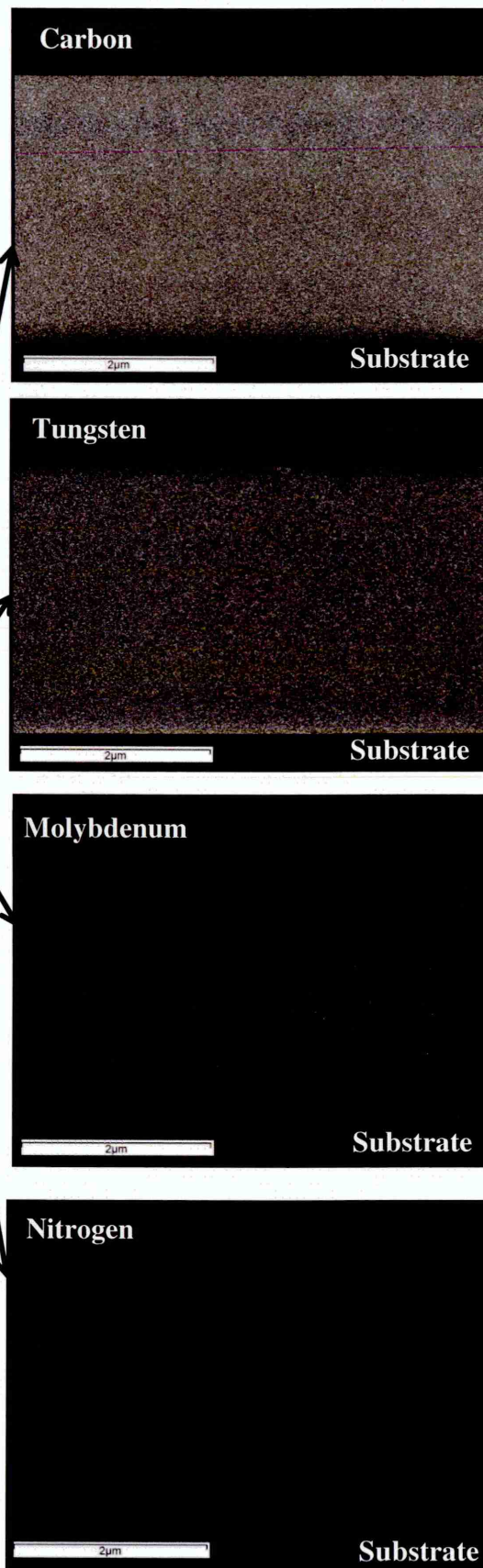
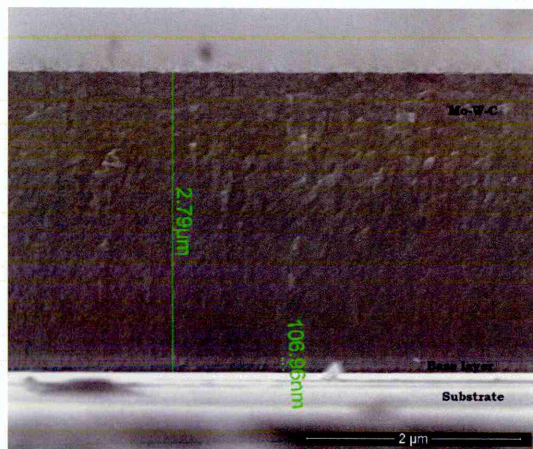


Figure 4.1-5: X-ray mapping of elements on the fracture cross-section of as-deposited C6

Figure 4.1-6 shows the XRD patterns of the as-deposited Mo–W–C coatings collected using Bragg-Brentano geometry. A sharp peak located at $\sim 35.3^\circ$ is observed for C2 indicating presence of hexagonal WC [100] and WN [100] phases. The broadening of this peak is observed with further increase in metal content and simultaneously it slightly shifts to the right. C4 shows two peaks at $\sim 35.8^\circ$ and $\sim 38^\circ$. Hexagonal WC [100] and WN [100] phases are present in the peak located at $\sim 35.8^\circ$ whereas the peak at $\sim 38^\circ$ is assigned to hexagonal W_2C [002] and Mo_2C [002] phases. Unlike C2 and C4, a wide peak ranging from $\sim 35.2^\circ - 38^\circ$ is observed for C6. Within this broad peak, WC [100] and WN [100] phases are identified at $\sim 35.8^\circ$ and W_2C [100], W_2C [002] and Mo_2C [002] phases are identified at $\sim 38^\circ$. Thus it is concluded that the top surface of all three coatings consists of metal carbide phases (WC, W_2C and Mo_2C) whereas the base layer contains metal nitride (WN) phases. Rest of the peaks are from stainless steel substrate.

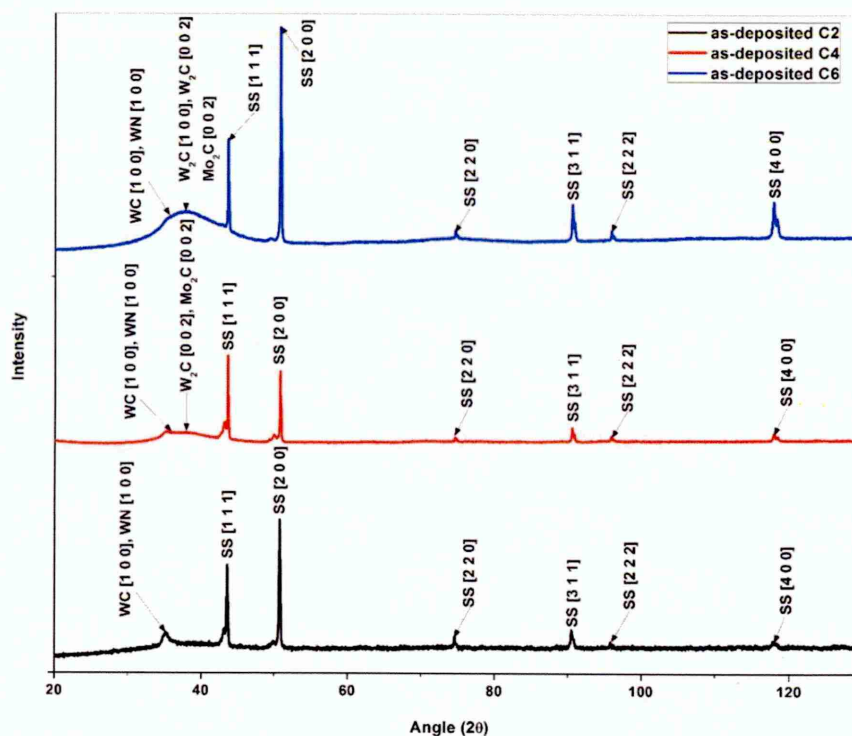


Figure 4.1-6: XRD patterns of as-deposited Mo–W–C coatings collected using Bragg-Brentano geometry

The microstructure and the phase composition of as-deposited Mo–W–C coatings are further studied using glancing angle XRD (GAXRD) with an incident angle (ω) of 2° as shown in figure 4.1-7. The GAXRD patterns of as-deposited coatings are dominated by a single broad peak located in the range of $\sim 34.5^\circ - 38^\circ$ indicating their nanocrystalline

almost X-ray amorphous nature. For C2, the broad peak ($\sim 35^\circ - 38^\circ$) is attributed to hexagonal W_2C [002] and Mo_2C [002] phases. This peak is slightly shifted towards higher angles ($\sim 35.8^\circ - 38^\circ$) in C4 indicating presence of hexagonal WC [100] phase at $\sim 35.8^\circ$ and a mixture of hexagonal W_2C [002] and Mo_2C [002] phases at $\sim 38^\circ$. The peak becomes wider ($\sim 34.5^\circ - 38^\circ$) in C6 showing a mixture of hexagonal W_2C [001] (located at $\sim 34.7^\circ$), W_2C [002] and Mo_2C [002] (located at $\sim 38^\circ$) phases. These findings support the XRD patterns obtained through Bragg-Brentano geometry as shown in figure 4.1-6.

Figure 4.1-7 shows an increase in the peak intensity with the increase in metal content of Mo–W–C coatings. The lowest peak intensity of C2 indicates presence of minimum amount of metal carbide phases. As the metal content increases, the peak becomes sharp and the intensity is significantly increased due to formation of more metal carbide phases. This is clearly observed in the GAXRD patterns of C4 and C6. Together the micrographs of the Mo–W–C coated surfaces (see figure 4.1-1) and the GAXRD patterns (see figure 4.1-7) indicate a process of surface segregation of two phases during the coating growth. The majority phase is carbon-rich and has nanocrystalline almost X-ray amorphous structure. A minority phase, probably metal-rich, may be segregated to column boundaries.

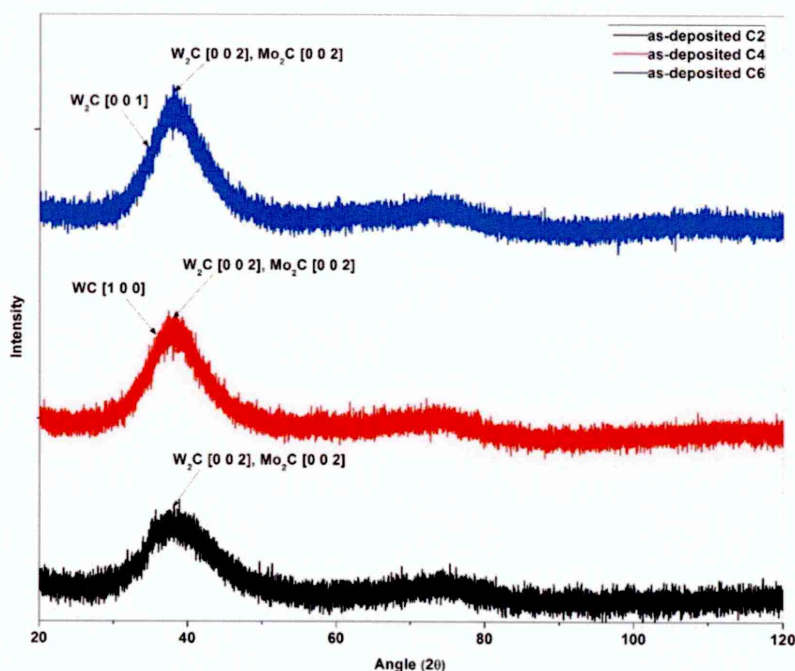


Figure 4.1-7: XRD patterns of as-deposited Mo–W–C coatings collected using glancing angle ($\omega = 2^\circ$) geometry

For better understanding of the coating microstructure, the as-deposited surfaces are further characterised using low angle XRD as shown in figure 4.1-8. A single reflection at 2.842° is found for C2 (figure 4.1-8a), whereas multiple peaks due to second order reflections are observed for C4 (at 2.456° and 4.203°) and C6 (at 2.792° and 3.013°) indicating existence of sharp interfaces in these coatings (figures 4.1-8b and 4.1-8c). Therefore, as-deposited Mo–W–C coatings have multilayer structure. The distance between the individual layers of the multilayer structure is known as the bilayer thickness (Δ) and it is calculated using Bragg's law (considering $n = 1$). Figure 4.1-8d shows that the bilayer thickness of C2 is ~ 3.1 nm, which increases to ~ 3.6 nm and ~ 4.2 nm for C4 and C6 respectively. Thus linear increase in bilayer thickness is observed with the increase in metal content of Mo–W–C coatings.

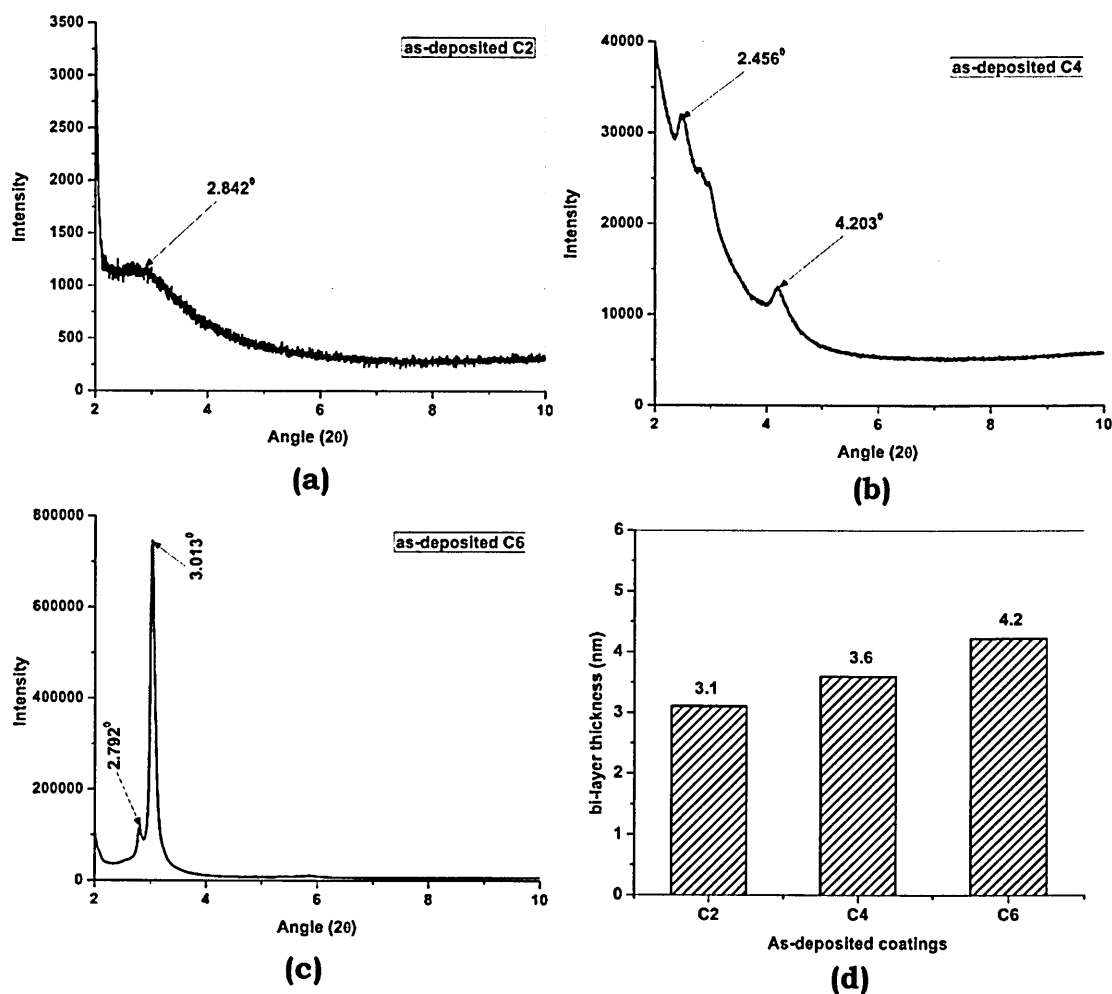


Figure 4.1-8: (a – c) Low angle XRD patterns and (d) the bilayer thickness of as-deposited Mo–W–C coatings

The as-deposited Mo–W–C coatings are further studied using Raman spectroscopy. The Raman spectra collected from the as-deposited surfaces are shown in figure 4.1-9. After deconvolution of the spectra, the distinct and dominant disordered and sp^2 bonded graphitic carbon peaks (corresponds to D and G bands respectively) are observed for C2 and C4. C2 shows an I_D/I_G ratio of 2.51 with D1, D2 and G peak positions located at 1119.6 cm^{-1} , 1393.05 cm^{-1} and 1576.52 cm^{-1} respectively (figure 4.1-9a). Similarly, C4 shows an I_D/I_G ratio of 1.96 with D and G peak positions located at 1387.04 cm^{-1} and 1574.32 cm^{-1} respectively (figure 4.1-9b). The spectrum collected from C6 shows less pronounced graphitic peaks (figure 4.1-9c) indicating less amount of free carbon present in this coating compared to others. The D and G peak positions are found at 1406.7 cm^{-1} and 1579.37 cm^{-1} respectively and the I_D/I_G ratio is calculated as 1.85. The I_D/I_G ratio is an important parameter in Raman analysis to understand the bonding characteristics and to estimate the disorder in the carbon network. The I_D indicates the intensity of D peak due to the A_{1g} breathing mode of carbon atoms in six fold rings. D peak is active only in presence of disorder and therefore this mode is absent in perfect graphite. On the other hand, the I_G indicates the intensity of graphitic (G) peak resulting from the E_{2g} stretching motion for all pairs of sp^2 bonded carbon atoms [172, 173]. The high I_D/I_G ratio indicates the graphitic nature of as-deposited Mo–W–C coatings.

Except the graphitic peaks, all other deconvoluted peaks of as-deposited Mo–W–C coatings are listed in table A-1 (see appendix A). Peaks A4 and A5 of C2 (centred at $\sim 353\text{ cm}^{-1}$ and $\sim 634\text{ cm}^{-1}$ respectively) are found at two consecutive shoulders of the spectrum and the corresponding peak widths are found as $\sim 216\text{ cm}^{-1}$ and $\sim 271\text{ cm}^{-1}$ respectively (figure 4.1-9a). Similarly, peaks B4 and B5 of C4 (centred at $\sim 342\text{ cm}^{-1}$ and $\sim 652\text{ cm}^{-1}$ respectively) are found at two consecutive shoulders of the spectrum and the corresponding peak widths are found as $\sim 213\text{ cm}^{-1}$ and $\sim 330\text{ cm}^{-1}$ respectively (figure 4.1-9b). All these four peaks belong to Mo_2C . It is found from the literature that the dominant Raman peaks of commercial Mo_2C sample are observed at $\sim 334\text{ cm}^{-1}$, $\sim 376\text{ cm}^{-1}$ and $\sim 666\text{ cm}^{-1}$ [174]. The XRD analyses obtained through Bragg-Brentano (see figure 4.1-6) and glancing angle (see figure 4.1-7) geometry indicates that the as-deposited coatings contain both molybdenum and tungsten carbide (Mo_2C , WC and W_2C) phases; however no tungsten carbide phases are detected in the Raman spectra. Unlike C2 and C4, no significant presence of molybdenum and tungsten carbide peaks is observed in C6.

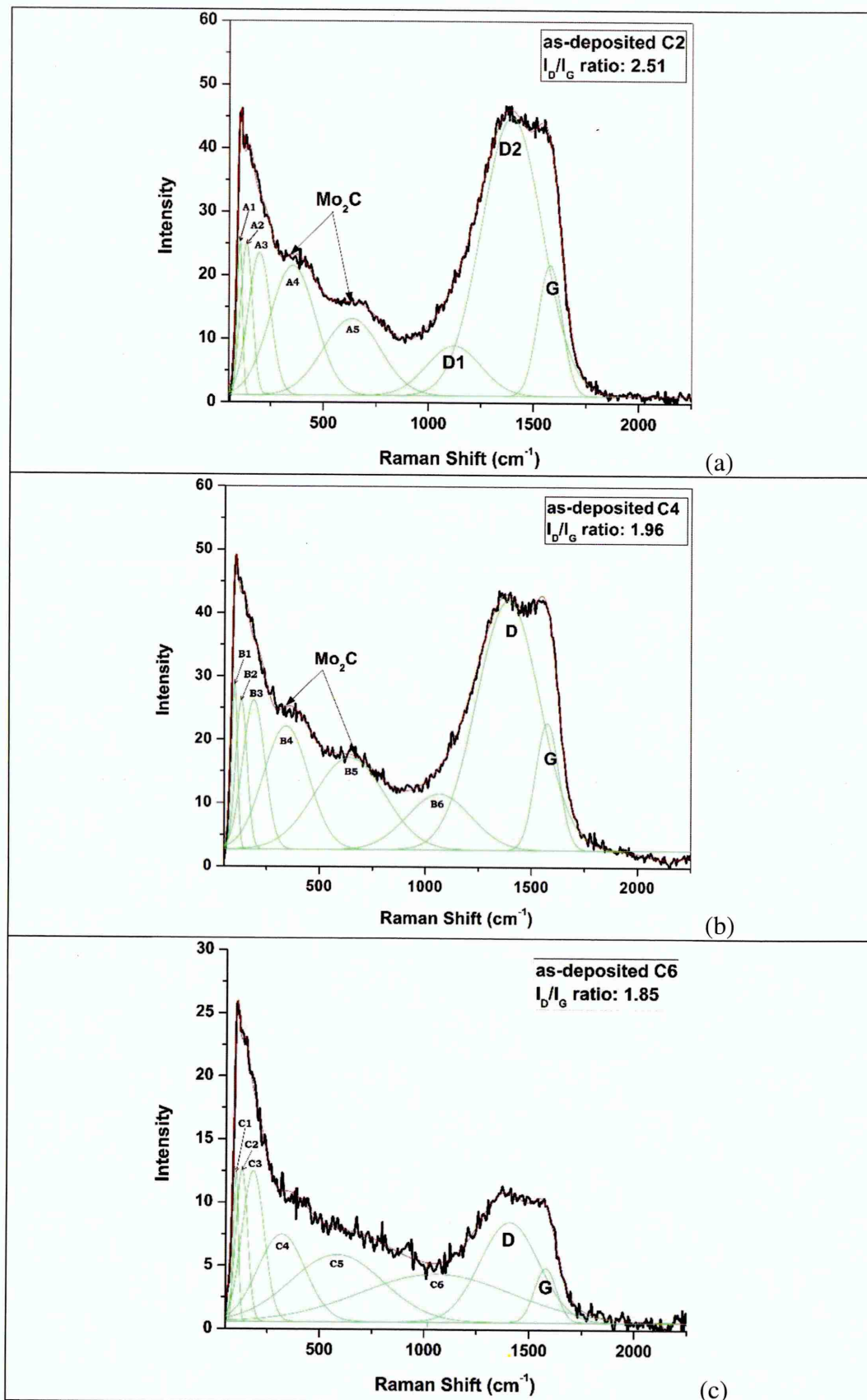


Figure 4.1-9: (a – c) Raman spectra collected from as-deposited Mo-W-C coatings

4.1.3. Nanohardness and elastic properties

Nanohardness and elastic modulus of as-deposited Mo–W–C coatings are estimated from the characteristic loading-unloading curves as shown in figure 4.1-10. Absence of discrete steps in the loading curves indicates no fracture of the coatings. At an applied load of 10 mN, the indentation depth at the end of loading period is observed as ~200 nm, ~180 nm and ~180 nm for coatings C2, C4 and C6 respectively and the displacement during unloading is found ~100 nm, ~100 nm and ~110 nm respectively. As the indentation depth is $<1/10^{\text{th}}$ of the total coating thickness, therefore this hysteresis loss is believed to be influenced by the dense coating microstructure.

Figure 4.1-11 shows the nanohardness and elastic modulus of as-deposited Mo–W–C coatings under 10 mN applied load. The nanohardness of C2, C4 and C6 is observed as ~1336 HV, ~1677.5 HV and ~1702 HV respectively and the elastic modulus is found as ~194.5 GPa, ~236.2 GPa and ~268.5 GPa respectively. The amorphous carbon matrix and the hard metal carbide phases of the as-deposited coatings simultaneously influence the coating hardness. Moreover, the higher hardness of C4 and C6 is attributed to the formation of hard metal carbide phases during coating growth as understood from the GAXRD patterns (see figure 4.1-7).

The hardness and elastic modulus values obtained in this study are found different when compared with the single metal-doped coatings such as Mo-DLC and W-DLC. It was found from the literatures that the incorporation of Mo into the DLC coating promoted formation of sp^2 sites leading to reduction of hardness and elastic modulus [105]. On the other hand, hardness and elastic modulus of W-DLC coatings depends on several factors including deposition process, concentration of W and bias voltage [102, 153]. This study shows that the addition of both Mo and W into the carbon-based coating results in almost linear increase in the hardness and elastic modulus values due to formation of hard metal carbide phases.

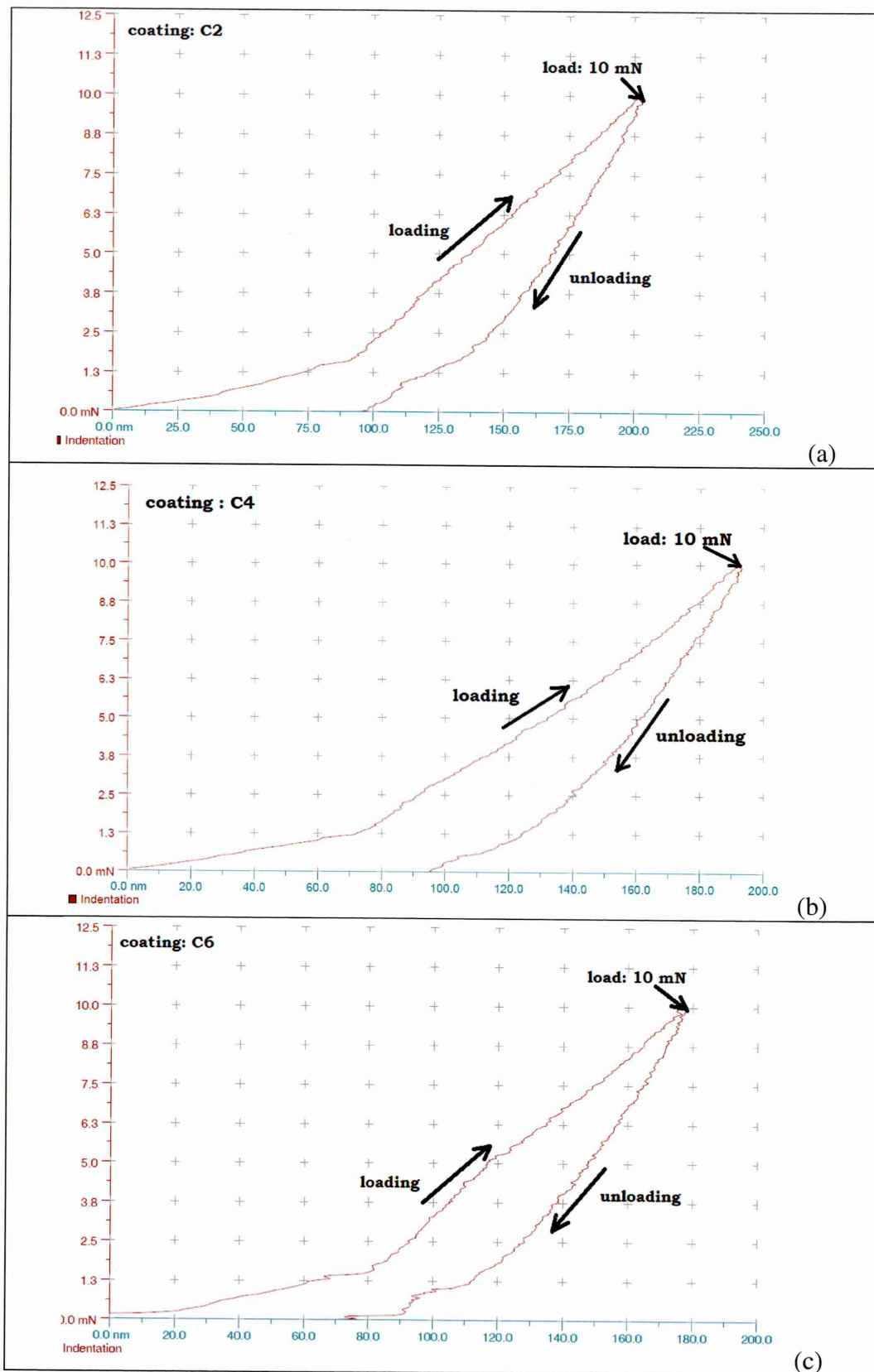


Figure 4.1-10: (a – c) Characteristic loading-unloading curves of as-deposited Mo-W-C coatings

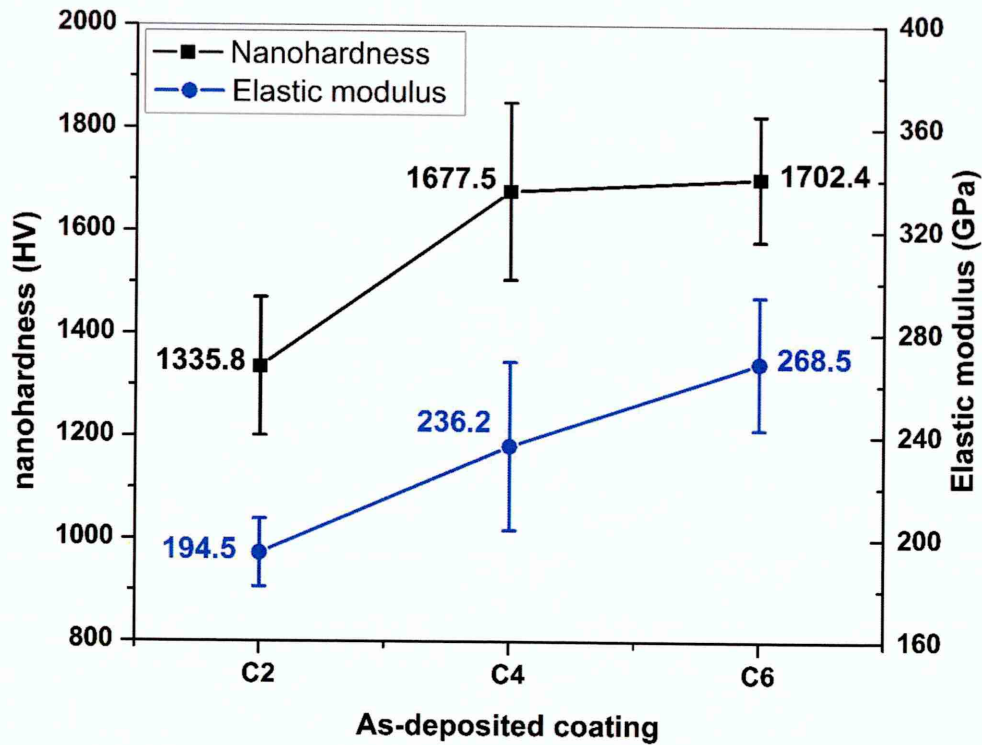


Figure 4.1-11: Nanohardness and elastic modulus of as-deposited Mo–W–C coatings

4.1.4. Adhesion strength

The adhesion of as-deposited Mo–W–C coatings is quantified by determining the critical load (L_c) at which adhesive failure is initiated due to the coating delamination. C2 withstands low critical load up to 34.6 N (figure 4.1-12a), whereas C4 and C6 survive high critical loads up to 80.8 N (figure 4.1-12b) and 85 N (figure 4.1-12c) respectively, after which the substrate is exposed due to adhesive failure. The coating thickness, structure as well as the hardness influences the adhesive failure. Figures 4.1-12d – 4.1-12f show the scratch track end of the as-deposited coatings at 100 N applied load. No flaking and interfacial spallation is observed inside and outside of the scratch track end demonstrating excellent adhesion strength. This strong adhesion is credited to the effective metal ion etching delivered by HIPIMS technology. The excellent adhesion strength of C4 and C6 to the base layer is due to the similar makeup of the base layer and coatings that allows intensive linking between identical elements across the interface. This provides conditions of lower free energy on the surface i.e. more nucleation sites, which enhance the bonding strength between two layers.

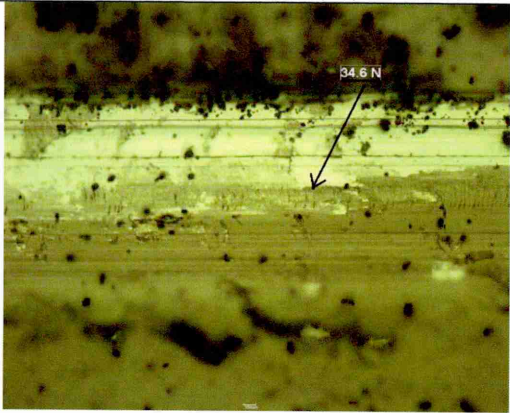
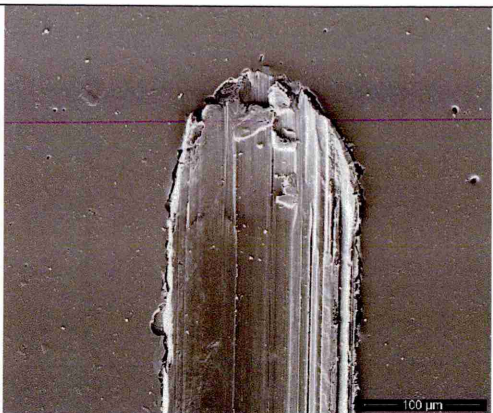
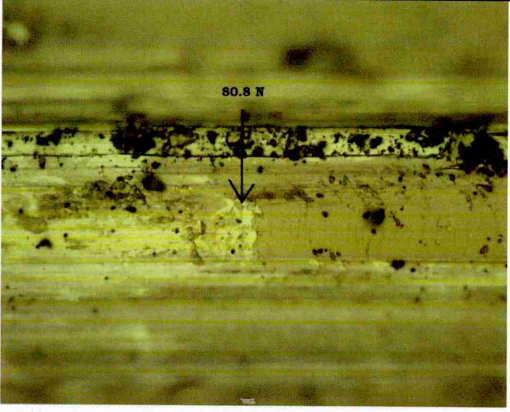
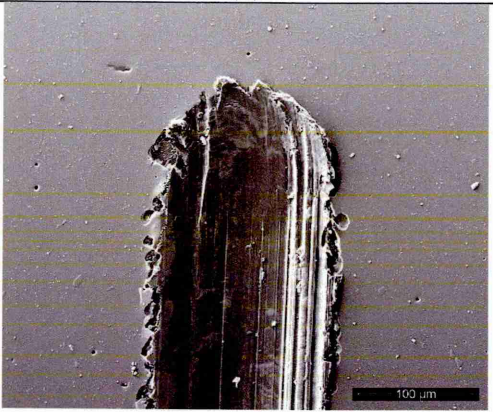
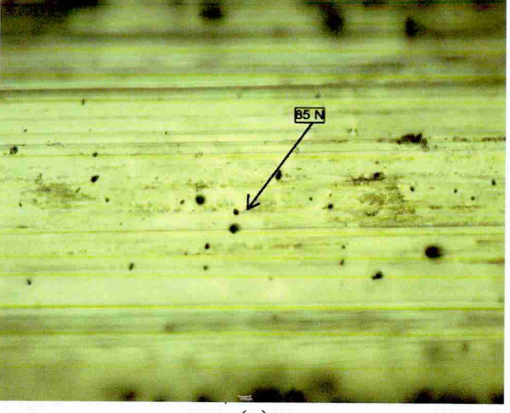
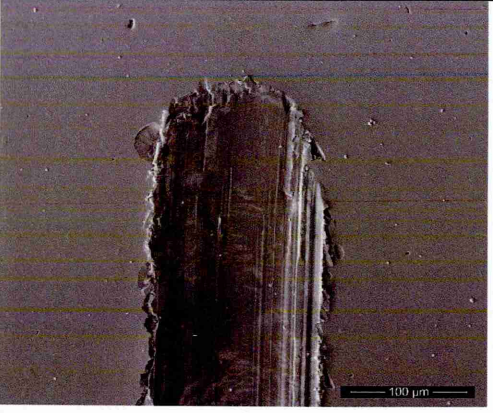
Coating	Critical load (L_c)	Scratch track end
C2	 (a)	 (d)
C4	 (b)	 (e)
C6	 (c)	 (f)

Figure 4.1-12: Adhesive strength of as-deposited Mo–W–C coatings showing (a – c) critical loads and (d – f) SEM images of the respective scratch track ends at 100 N applied load

The interfacial adhesion strength of as-deposited Mo–W–C coatings is evaluated by Rockwell hardness test under 1500 N applied load. The optical images of the indents shown in figure 4.1-13 indicate HF2, HF3 and HF4 type strong interfacial adhesion for

C2, C4 and C6 respectively. Little cracks and slight delamination of the coating are observed around the edge of the indent on C2. Indents on both C4 and C6 show larger cracks and more delamination of the coating around the edge of the indents. The indent and the coating delamination at the indent edge are further investigated using EDX analysis.

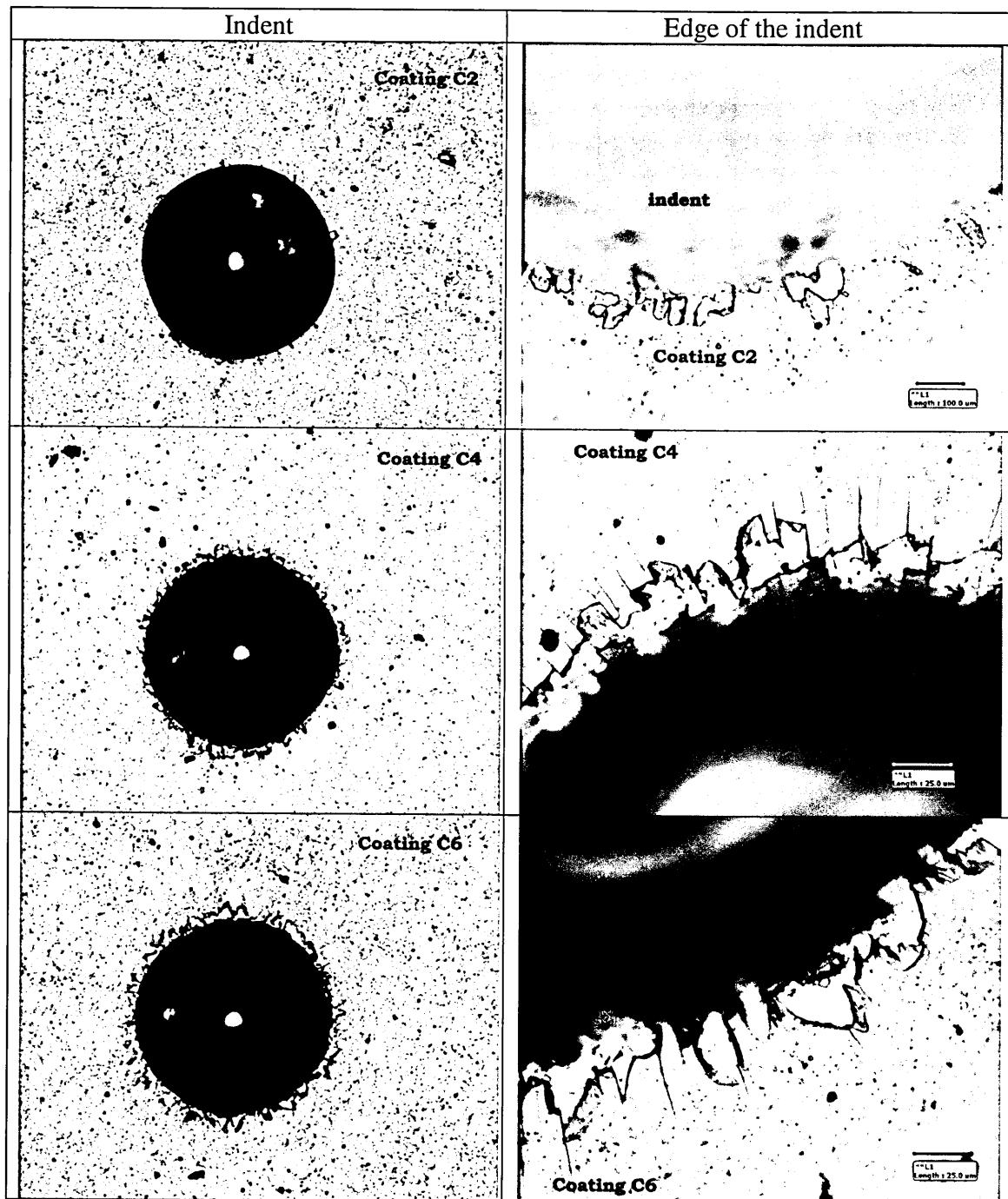


Figure 4.1-13 : Optical images of the indents indicating interfacial adhesion strength of as-deposited Mo-W-C coatings

Figures 4.1-14 – 4.1-16 show the EDX analysis of the indents on as-deposited Mo–W–C coatings. The EDX spectra collected from positions ‘a’ (undamaged coated surface) and ‘b’ (middle of the indent) show same patterns indicating absolutely no damage of Mo–W–C coatings within the indent. The SEM image in figure 4.1-14 shows that the delamination occurs in few locations at the edge of the indent for C2. Two layers are clearly observed within the zoomed view of one such scar. The upper layer (encircled in black in the SEM image and *position II* in EDX spectrum) shows same pattern of C2, whereas the bottom layer (encircled in red in the SEM image and *position I* in EDX spectrum) shows high intensity Fe peaks because of reduced coating thickness. Unlike C2, the delamination is observed at several locations around the indents on C4 (figure 4.1-15) and C6 (figure 4.1-16). The enlarged view of the scars indicates the coatings remain intact in the upper layer, however little amount of coating is retained at the bottom layer. Moreover, higher coating delamination is observed for C6 compared to C4.

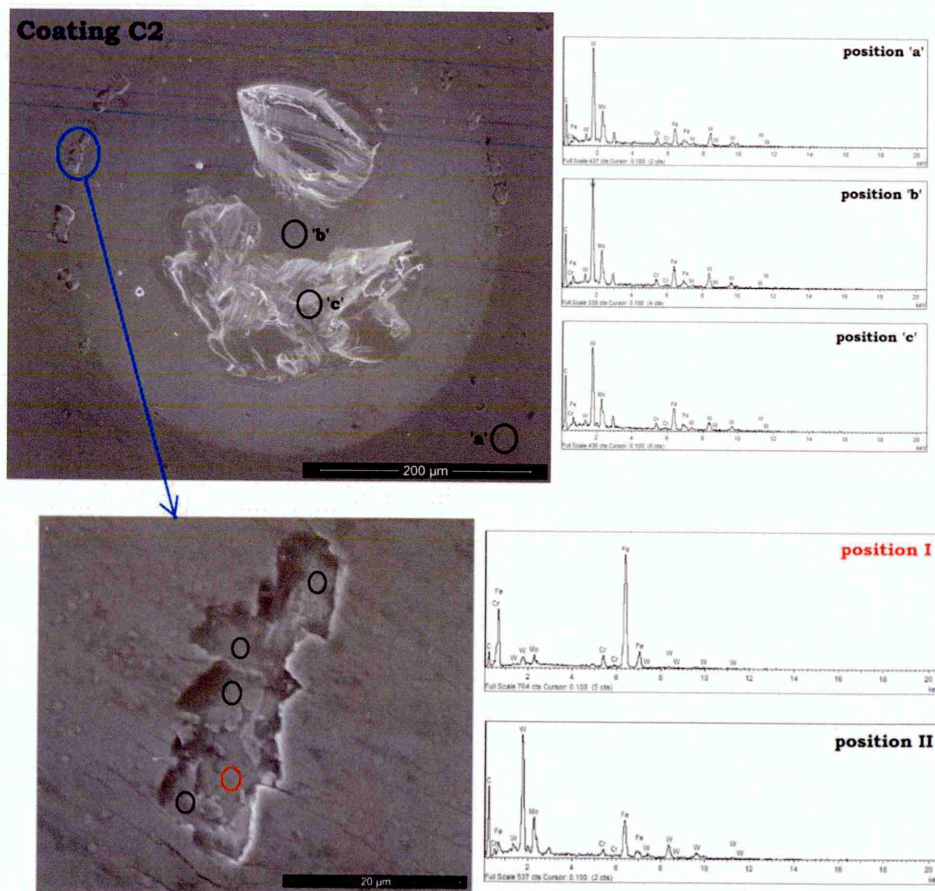


Figure 4.1-14: EDX analysis of the indent on as-deposited C2

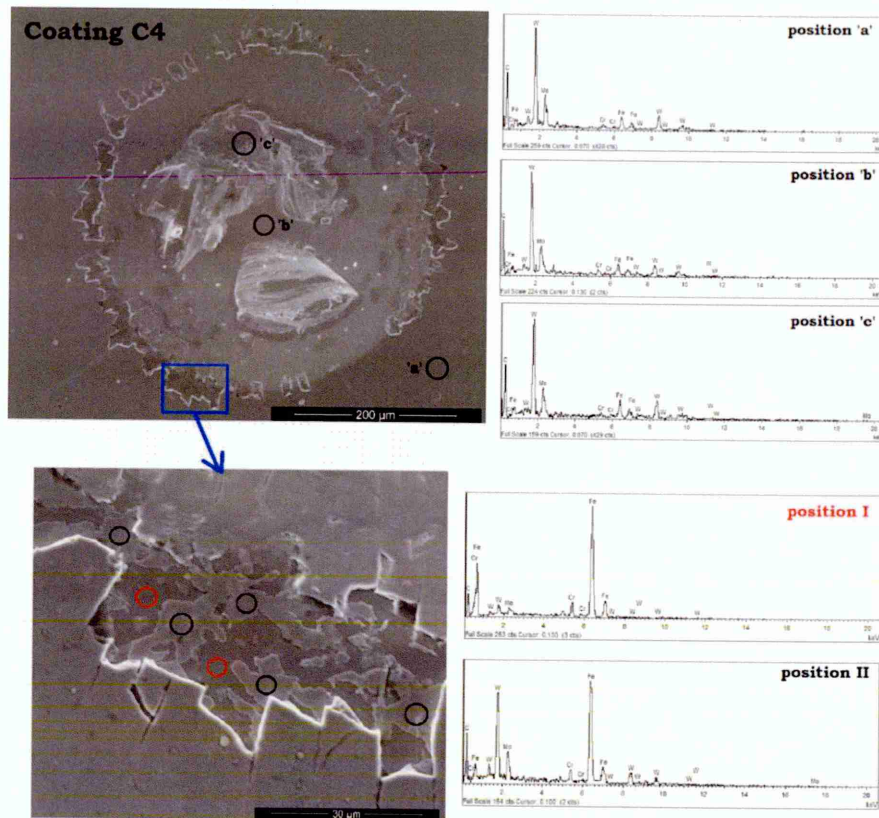


Figure 4.1-15: EDX analysis of the indent on as-deposited C4

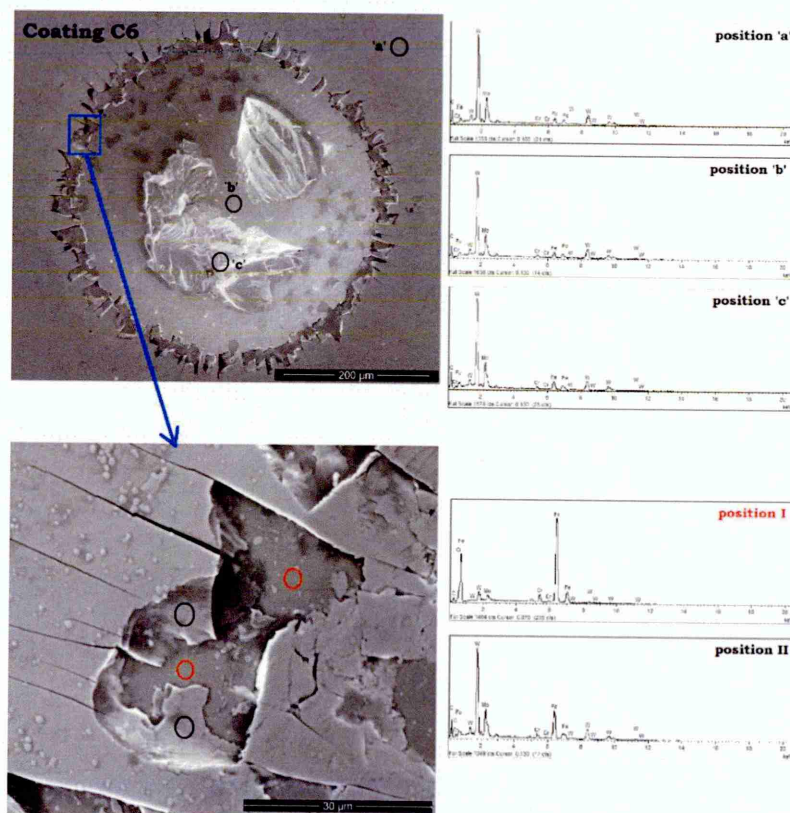


Figure 4.1-16: EDX analysis of the indent on as-deposited C6

4.1.5. Concluding remarks

Mo–W–C coatings were deposited on Si wafers, SS coupons and HSS and SS discs using combined HIPIMS and UBM techniques. Three coatings namely C2, C4 and C6 having different metal content were produced and their structural properties are summarized in table 4.1-1. These coatings contain nanocrystalline almost X-ray amorphous structure and provide good adhesion with substrate. The cross-sectional SEM images reveal dense columnar microstructure of C2 and C4 and completely granular microstructure of C6. The I_D/I_G ratio of as-deposited coatings is found in the range of 1.85 – 2.51 indicating their graphitic nature. The amorphous carbon matrix and hard metal carbide phases of as-deposited coatings results in higher hardness (~1330 – 1700 HV) and elastic modulus (~190 – 270 GPa).

Table 4.1-1: Structural properties of as-deposited Mo–W–C coatings

Properties	as-deposited Mo–W–C coatings		
	C2	C4	C6
cross-sectional microstructure	columnar	columnar	granular
phase composition	WC, W ₂ C, Mo ₂ C, WN		
I_D/I_G ratio	2.51	1.96	1.85
bilayer thickness (nm)	3.1	3.6	4.2
coating thickness (μm)	~1.9	~2.2	~2.8
average surface roughness (μm)	~0.053	~0.073	~0.074
nanohardness (HV)	~1336	~1677.5	~1702
elastic modulus (GPa)	~194.5	~236.2	~268.5
critical load (N)	34.6	80.8	85
interfacial adhesion type	HF2	HF3	HF4

4.2. Tribological behaviour of Mo–W–C coatings in dry and boundary lubricated conditions at ambient temperature

4.2.1. Introduction

The tribological behaviour of Mo–W–C coatings in dry (section 4.2.2) and boundary lubricated sliding (section 4.2.3) conditions at ambient temperature is discussed in this chapter. The pin-on-disc tribometer was used to perform the sliding tests against uncoated 100Cr6 steel and Al₂O₃ counterparts. Commercially available Mobil1 Extended life™ 10W-60 engine oil was used as lubricant during sliding tests. The tribological behaviour of both the coatings and the counterparts was investigated using various analytical techniques such as SEM, EDX, X-ray mapping, optical microscope, surface profilometer and Raman spectroscopy. The friction behaviour was well understood from the friction curves and the images of the wear scar on counterparts and the wear track on the coatings. The debris adhered to the counterparts and the wear tracks were investigated using EDX analysis, X-ray mapping and Raman spectroscopy. The wear coefficients of the coatings and the counterparts were measured with the help of surface profilometer and SEM. Based on the wear products generated during sliding, two different wear mechanisms are proposed for dry and lubricated sliding conditions. Section 4.2.4 describes the effect of metal dopants on the tribological behavior of carbon-based coatings at ambient temperature. Different state-of-the-art DLC coatings and chromium-doped carbon-based coating (Cr/C) were subjected to dry and lubricated sliding tests and their tribological behaviour was compared with Mo–W–C coatings. The main observations of this study are summarised in section 4.2.5.

4.2.2. Tribological behaviour of Mo–W–C coatings during dry sliding at ambient temperature

I. Experimental details

A CSM room temperature pin-on-disc tribometer was used to study the friction behaviour of Mo–W–C coatings against the uncoated 100Cr6 steel balls under 5 N static loads at ambient condition ($\sim 30^{\circ}\text{C}$ temperature and 30% relative humidity). Long sliding distance (7.5 km) was chosen to study the effect of metal dopants on friction behaviour with time. The tribological behaviour of both coatings and counterparts was investigated using SEM, EDX, X-ray mapping, optical microscopy, surface profilometer and Raman spectroscopy. The secondary electron detector and the optical microscope were used for topographical imaging and imaging of the transfer layer formed on the ball surfaces. The X-ray mapping was done on the wear scar of the counterparts in order to identify the elemental composition of the adhered debris. Raman spectra were collected from the wear scar on the ball surfaces (240 s exposure time, single acquisition to achieve a better signal-to-noise ratio) and the wear track on the coatings (60 s exposure time, averaged over 5 acquisitions). The friction behaviour of Mo–W–C coatings is discussed in section II. The wear behaviour of both coatings and counterparts are discussed in sections III and IV respectively and the relevant wear mechanism is proposed in section V.

II. Friction behaviour of Mo–W–C coatings during dry sliding

The friction curves of Mo–W–C coatings during dry sliding at ambient condition are shown in figure 4.2-1. During initial run-in period of 200 m, an average friction coefficient of ~ 0.324 , ~ 0.417 and ~ 0.369 is observed for C2, C4 and C6 respectively. In steady-state period, the friction coefficient decreases to ~ 0.219 , ~ 0.333 and ~ 0.333 respectively. Therefore overall mean friction coefficient of C2, C4 and C6 is measured as ~ 0.333 , ~ 0.335 and ~ 0.223 respectively. The friction curves of C2 and C4 are smooth during run-in period and initial steady-state period (up to ~ 1.5 km). With increase in sliding distance, a lot of oscillations are observed and the amplitude of oscillations is found significantly fluctuating for C2 rather than C4 towards the end of the tests (after ~ 5

km). Similarly, the friction curve of C6 shows a lot of oscillations throughout the steady-state period however the amplitude of oscillations remains almost constant leading to reduced friction value. The oscillations of the friction coefficient are attributed to the formation of wear debris and a physisorbed layer of the water molecules on the surface leading to stick-slip motion. It is already published in the literature that the water molecules reduce the friction coefficient of carbon-based coatings by passivating the dangling bonds of the carbon [3]. Further images, elemental composition and Raman analyses of the debris reveal strong influence of third-body abrasion on friction behaviour during sliding. Thus the effects of third-body abrasion and the moisture content on the friction behaviour of Mo–W–C coatings are explained in following sections.

a. Third-body abrasive wear

Figures 4.2-2a – 4.2-2c show the transfer layer formed on the steel counterparts after sliding against Mo–W–C coatings. The debris particles trapped inside the wear track during sliding, experience severe plastic deformation and promote third-body abrasive wear. Closer analyses of this phenomena reveal that there are two types of debris: (i) loose debris particles, which continuously abrade against each other and the wear surfaces during sliding (figures 4.2-2a – 4.2-2c) and (ii) debris particles, which cold-weld to the counterpart surface during sliding and form a strongly bonded transfer layer (figures 4.2-2d – 4.2-2f). The friction coefficient is determined by composition and thickness of the transfer layer and the loose debris particles rolling in the wear track. As found from X-ray mapping and Raman analyses, the transfer layer is mainly composed of powder-like fine graphitic carbon particles and various metal oxides (later discussed in section III).

b. Effect of moisture content

The humid test environment benefits the friction coefficient and determines the shape of the friction curves. As reported in literature, the water molecules are adsorbed on the coated surfaces during sliding and passivate the dangling bonds of the carbon at the sliding surface. The chemical inertness of the carbon atoms reduces the adhesive interactions between the sliding surfaces, which is manifested by the low values of the friction coefficients [3]. Further reduction in friction coefficients to ~0.333, ~0.335 and

~0.223 for C2, C4 and C6 respectively is assisted by the graphitic carbon particles present in the transfer layer due to the carbon against carbon sliding mechanism.

This leads to the assumption that wear debris act as a third body sliding media in the tribological contact and define the friction behaviour during sliding. The sliding contact between neighbouring particles in the transfer layer leads to higher friction coefficient ($\mu \sim 0.33$) for C2 and C4, whereas lower friction coefficient ($\mu \sim 0.22$) of C6 is attributed to the rolling contact between the coarse debris particles present in the transfer layer. C6 contains more hard metal carbide phases, which during sliding abrade less and form coarse debris particles. Therefore it can be speculated that physical properties and more precisely the "internal friction" of this media determine the actual value of friction coefficient. This concept is similar to the concept of the role of the viscosity in liquids.

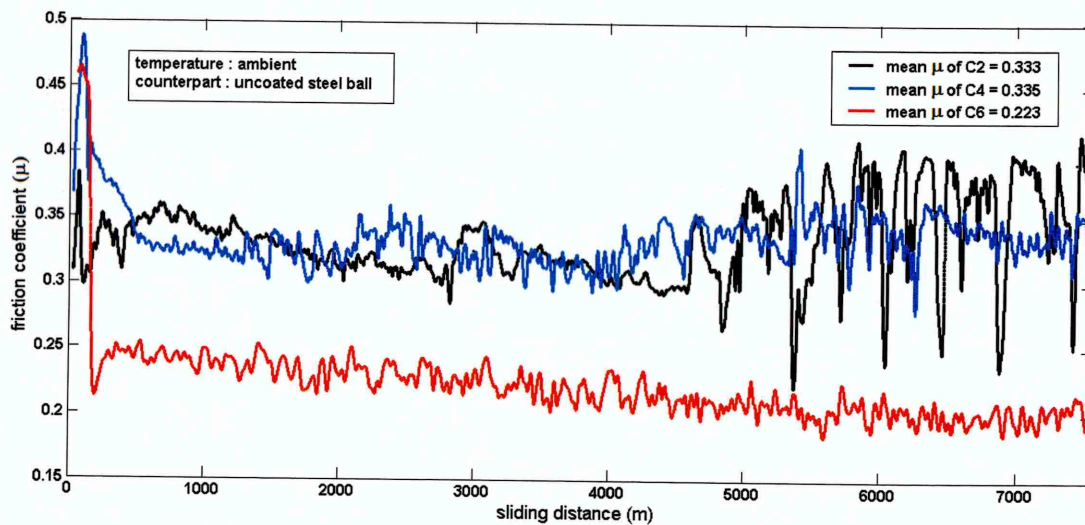


Figure 4.2-1: Friction behaviour of Mo-W-C coatings against steel counterparts

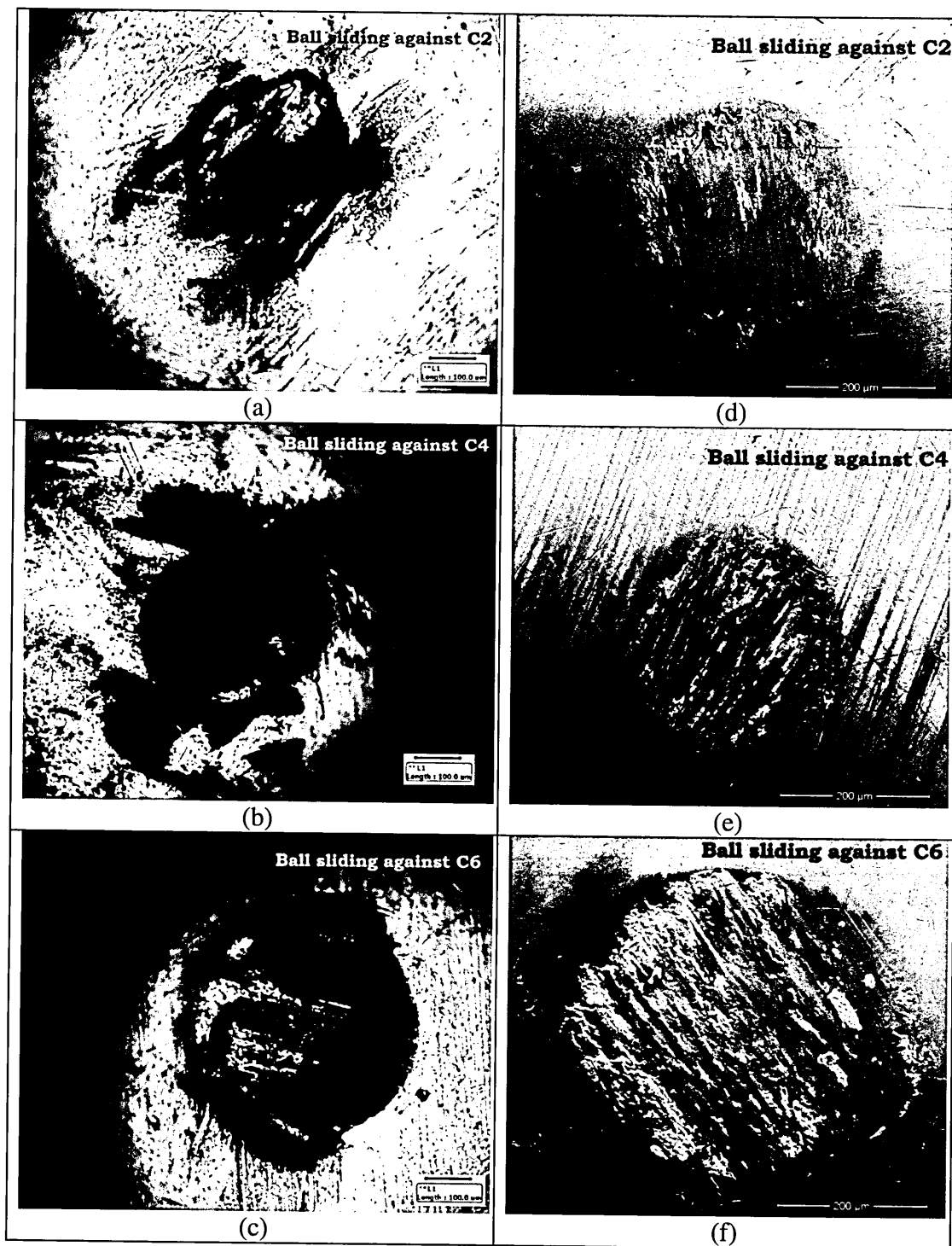


Figure 4.2-2: (a – c) Transfer layer formed on the steel counterparts and (d – f) debris strongly adhered to the counterpart surfaces after dry sliding

III. Wear behaviour of the steel counterparts during dry sliding

Figures 4.2-2d – 4.2-2f show the wear scar on the counterpart surfaces from which the wear coefficients of the counterparts are calculated using Archard's equation as $5.21 \times 10^{-18} \text{ m}^3 \text{N}^{-1} \text{m}^{-1}$, $3.78 \times 10^{-18} \text{ m}^3 \text{N}^{-1} \text{m}^{-1}$ and $12.8 \times 10^{-18} \text{ m}^3 \text{N}^{-1} \text{m}^{-1}$ after sliding against C2, C4 and C6 respectively. All the wear coefficient values are found exceptionally low (i.e. in the order of $\sim 10^{-18} \text{ m}^3 \text{N}^{-1} \text{m}^{-1}$) after 7.5 km of sliding. This high wear resistance is attributed to the formation of transfer layer during sliding which promotes minimum wear on the counterpart surfaces. This behaviour is explained in details in the following section.

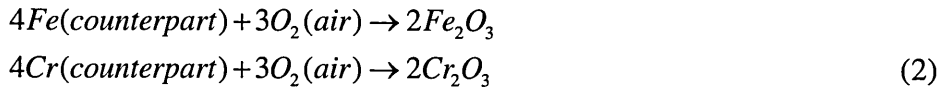
Figure 4.2-3 shows the X-ray mapping carried out on the wear scar of the counterparts after sliding against the Mo–W–C coatings. It is found that the adhered debris on the wear scars is composed of graphitic carbon particles, tungsten oxides and molybdenum oxides. The iron oxides generated from the counterpart during sliding, are accumulated mainly on the wear surfaces, which are free of adhered debris. The findings of X-ray mapping are further supported by Raman analyses as discussed below.

Figure 4.2-4a shows the Raman spectrum collected from the uncoated steel ball before sliding. The image of counterpart is provided in the inset and the encircled area shows the position of spectrum collection. The Raman spectrum is deconvoluted into five peaks labelled as P1 – P5 in the spectrum range of $\sim 50 - 1000 \text{ cm}^{-1}$. The details about deconvoluted peaks are listed in table A-2 (see appendix A). All these peaks are belonged to the uncoated steel ball, which is further confirmed by the EDX spectrum (with major elements Fe and Cr) as shown in the inset.

Figures 4.2-4b – 4.2-4d show the Raman spectra collected from the debris-free wear surface on the counterparts after sliding against C2, C4 and C6 respectively. The images of counterparts are provided in the inset of respective figures and the encircled areas show the position of spectrum collection. After deconvolution of the spectra, five peaks labelled as P1' – P5' are found in the spectrum range of $\sim 50 - 1000 \text{ cm}^{-1}$ for all three coatings. The details about deconvoluted peaks are listed in table A-2 (see appendix A). The spectra collected from the wear scars are found similar to the spectrum collected from the uncoated steel ball, however a shift in peak positions is observed after sliding. This is clearly understood from table A-2. The peaks P1 – P5 of the uncoated steel ball are shifted to peak positions P1' – P5' after sliding and this peak positions are further influenced

depending on the metal content of the coatings used as sliding counterparts. It is observed that peak positions P1' – P5' are shifted towards lower wavenumbers as the metal content increases in the coatings from C2 to C6.

The uncoated steel ball reacts with the oxygen during sliding due to flash temperatures up to 800°C [175] generated at the asperity contacts. As a result, little amount of Fe₂O₃ and Cr₂O₃ are formed and accumulated on the wear scar. Therefore no significant change is observed in the spectrum shape however, the peaks are shifted towards lower wavenumbers indicating the oxidation of the steel ball after sliding. For example when the sliding is carried out against C4 and C6, the overlapping of Fe₂O₃ and Cr₂O₃ peaks significantly increases the width of peak P4 (see figure 4.2-4a) to ~311 cm⁻¹ and ~301 cm⁻¹ respectively and shifts the peak centre to ~328 cm⁻¹ and ~323 cm⁻¹ respectively. Thus, this peak is expressed in the spectra as P4' [Fe₂O₃ + Cr₂O₃] (see figures 4.2-4c and 4.2-4d). The dominant Raman peaks of Fe₂O₃ and Cr₂O₃ are reported in the literature at ~293 – 298 cm⁻¹ [176] and ~300 cm⁻¹ and ~350 cm⁻¹ [177] respectively. Further the EDX spectra provided in the inset of figures 4.2-4c and 4.2-4d confirm the presence of Fe₂O₃ and Cr₂O₃ within the wear scar. It is believed that rest of the peaks are caused by the steel ball and they do not contain any metal oxides. Based on the Raman analyses and EDX spectra, the possible chemical reactions are listed in equation set (2). On the other hand, the peaks P1 – P5 of the uncoated steel ball are shifted to positions P1' – P5' when sliding against coating C2, but no metal oxide peaks are found.



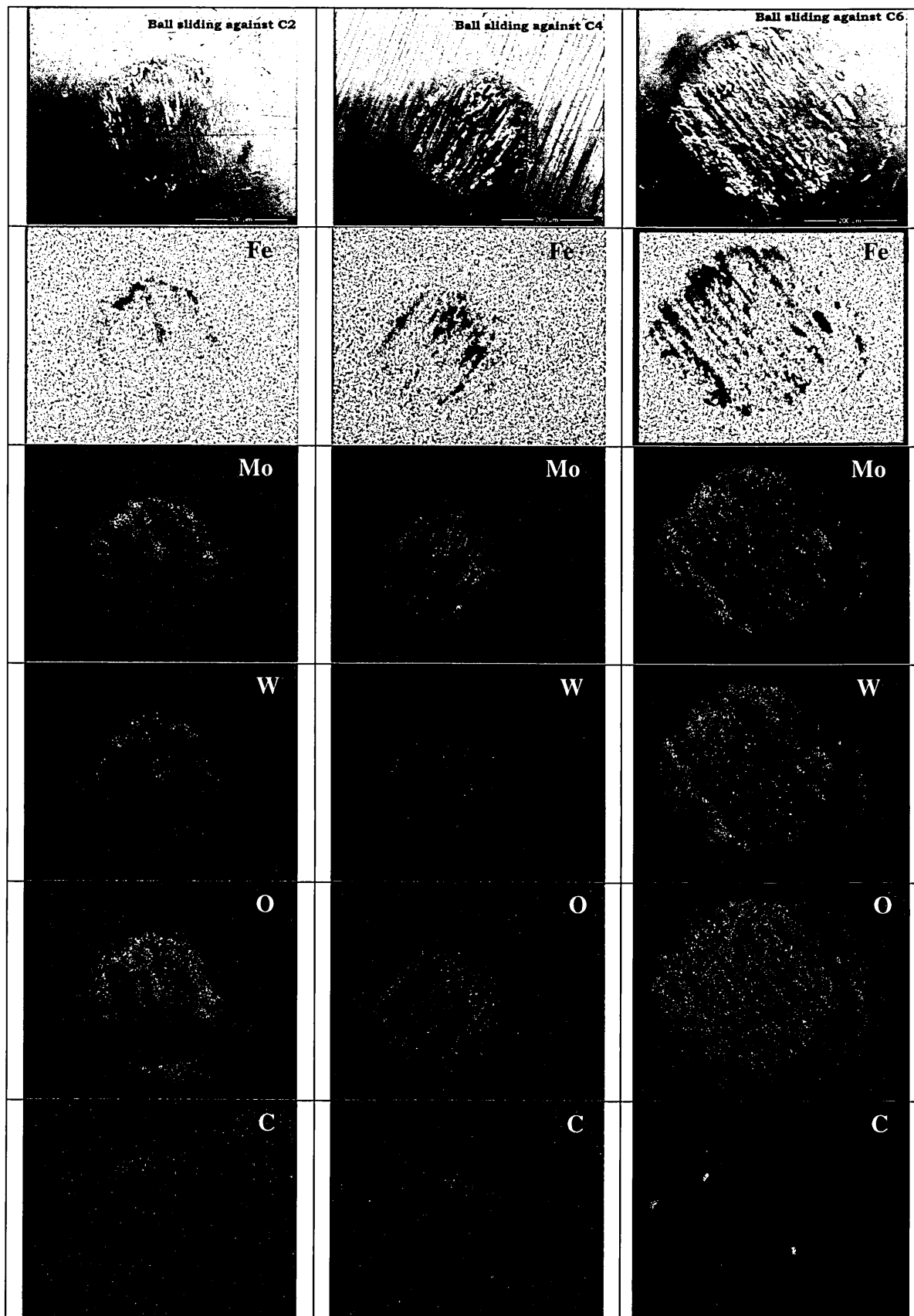
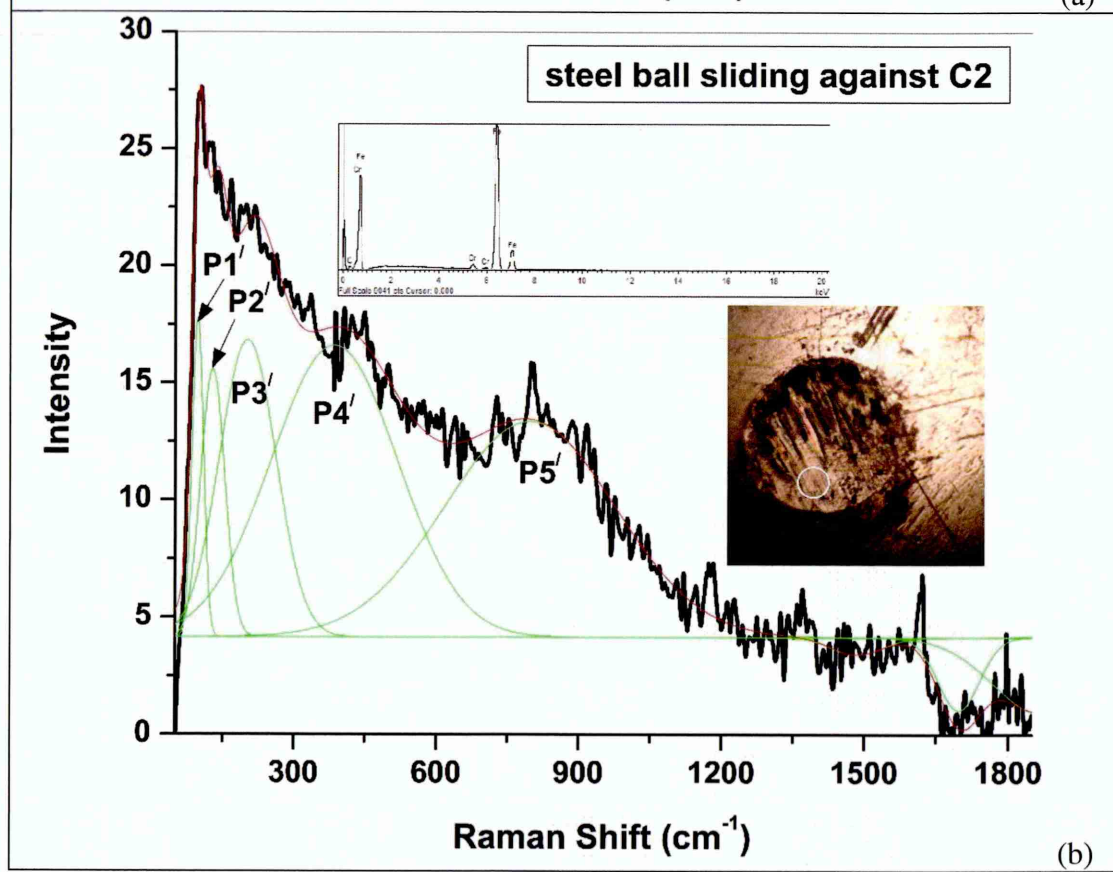
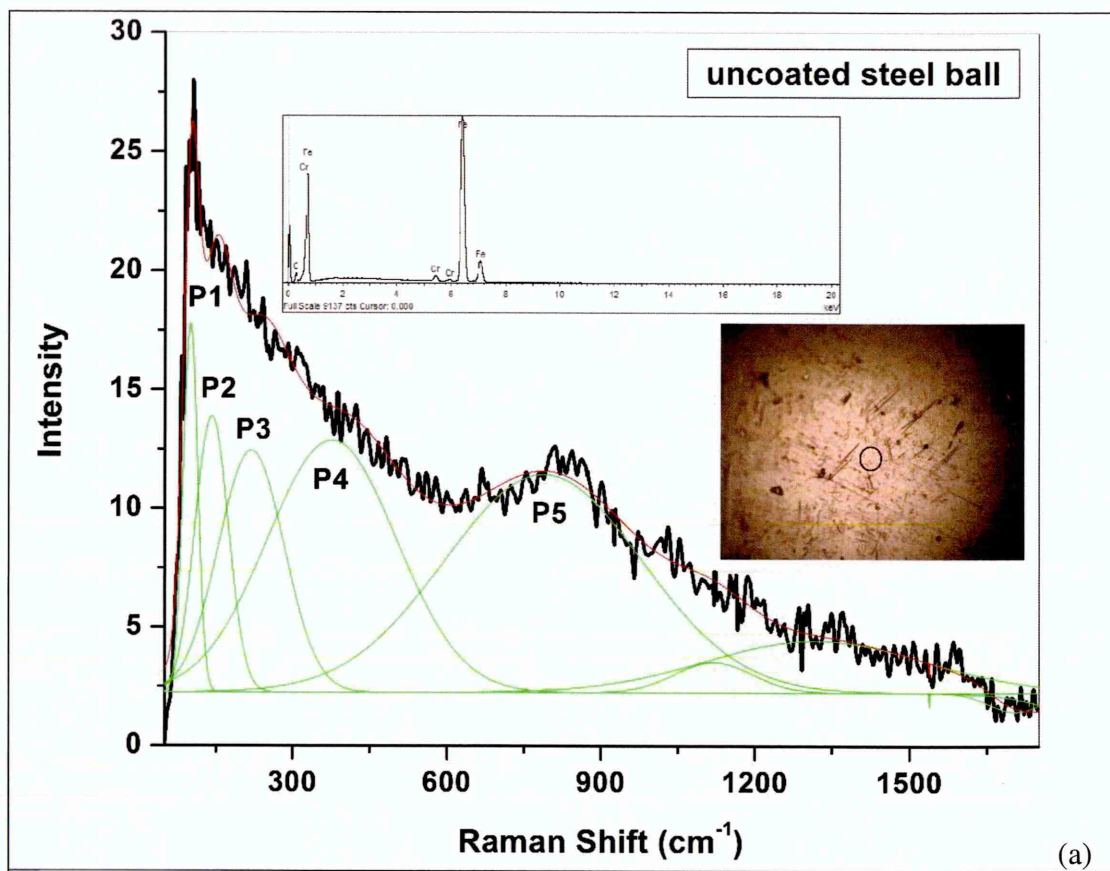


Figure 4.2-3: X-ray mapping of the debris adhered to the counterpart surfaces (steel ball) after dry sliding against Mo-W-C coatings



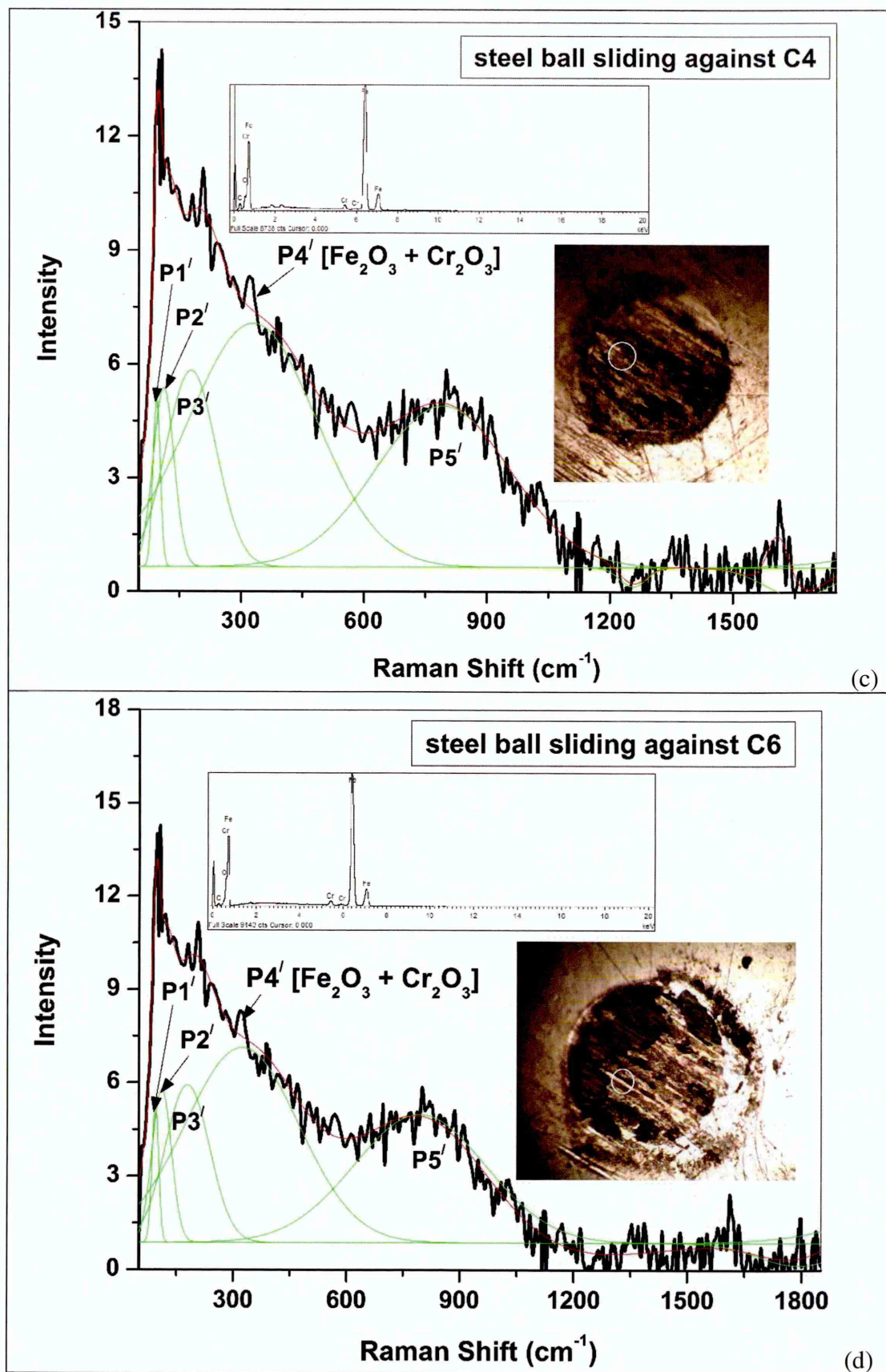


Figure 4.2-4: Raman spectra collected from the (a) uncoated steel ball and (b – d) wear scar on the steel balls after dry sliding against Mo–W–C coatings

Figure 4.2-5 shows the Raman spectra collected from the debris adhered to the counterparts after sliding against Mo–W–C coatings and after deconvolution of the spectra, corresponding Raman peaks are listed in table A-3 (see appendix A). The encircled area in the image of the wear surface shows the position of spectrum collection. The as-deposited coatings contain graphitic carbon and metal carbide phases (WC, W₂C and Mo₂C), which react with oxygen during sliding due to high flash temperature generated at the asperity contacts. As a result, different molybdenum and tungsten oxides are formed via diffusion mechanism based on gradual replacement of carbon atoms by the ones of oxygen. These metal oxides and the free graphitic carbon particles are transformed to the counterpart surface during sliding and form a transfer layer as understood from the Raman analysis. The EDX spectrum collected from the encircled area of the adhered debris further confirms the presence of metal oxides.

After deconvolution of the spectrum collected from the debris after sliding against C2 (figure 4.2-5a), the D and G peaks are observed at 1378.79 cm⁻¹ and 1586.05 cm⁻¹ respectively. The I_D/I_G ratio is calculated as 1.24 indicating graphitic nature of the carbon particles present in the adhered debris. Two peaks are appeared at two consecutive shoulders of the deconvoluted spectrum centred at ~303 cm⁻¹ and ~438 cm⁻¹ respectively, which are formed due to overlapping of WO₃, W₂₀O₅₈, MoO₃ and Mo₄O₁₁ peaks. The dominant Raman peaks of WO₃ and W₂₀O₅₈ are documented in the literature at ~417 cm⁻¹ and ~437 cm⁻¹ [178] and ~298 cm⁻¹ and ~319 cm⁻¹ [178] respectively, whereas the leading Raman peaks of MoO₃ and Mo₄O₁₁ are reported at ~292 cm⁻¹ [179] and ~306 cm⁻¹ and ~431 cm⁻¹ [180] respectively. The widest peak of the spectrum centred at ~720 cm⁻¹ belongs to WO₃ as it shows a sharp peak ~717 cm⁻¹ [178]. Another peak centred at ~920 cm⁻¹ possibly originates from the overlapping of several intermediate oxides of molybdenum such as Mo₄O₁₁, Mo₅O₁₄ and Mo₈O₂₃ formed during sliding. The dominant Raman peaks for Mo₄O₁₁, Mo₅O₁₄ and Mo₈O₂₃ are reported in the literature at ~907 cm⁻¹ [181], ~902 cm⁻¹ [182], ~902 cm⁻¹ and ~958 cm⁻¹ [183] respectively.

Figure 4.2-5b shows the Raman spectrum collected from the debris after sliding against C4. After deconvolution of the spectrum, two separate disordered peaks (D1 and D2) and the G peak are observed at 1172.91 cm⁻¹, 1392.64 cm⁻¹ and 1591.40 cm⁻¹ respectively. The I_D/I_G ratio is calculated as 1.03. The deconvoluted spectrum contains a sharp peak at

the shoulder centred at $\sim 335\text{ cm}^{-1}$, which is formed due to overlapping of MoO_2 , MoO_3 and WO_3 peaks; however some intermediate oxides of molybdenum and tungsten (Mo_4O_{11} and $\text{W}_{20}\text{O}_{58}$) can be present as well. The dominant Raman peaks of MoO_2 , MoO_3 and WO_3 are found in the literature at $\sim 357\text{ cm}^{-1}$ [174], $\sim 337\text{ cm}^{-1}$ [179], $\sim 331\text{ cm}^{-1}$ and $\sim 348\text{ cm}^{-1}$ [178] respectively. The leading Raman peaks of Mo_4O_{11} and $\text{W}_{20}\text{O}_{58}$ are observed at $\sim 340\text{ cm}^{-1}$ [180], $\sim 319\text{ cm}^{-1}$ and $\sim 341\text{ cm}^{-1}$ [178] respectively. Similar to C2, the deconvoluted spectrum of C4 contains a hump centred at $\sim 929\text{ cm}^{-1}$, which is possibly formed due to overlapping of different intermediate oxides of molybdenum such as Mo_4O_{11} , Mo_5O_{14} and Mo_8O_{23} . C4 contains more amount of metal compared to C2, thus more amount of metal oxides are formed during sliding as manifested by the hump in the spectrum.

Similar to C4, the Raman spectrum collected from the adhered debris after sliding against C6 (figure 4.2-5c) shows two separate disordered peaks (D1 and D2) and G peak at 1148.36 cm^{-1} , 1363.77 cm^{-1} and 1583.95 cm^{-1} respectively. The I_D/I_G ratio is calculated as 1. The deconvoluted spectrum contains a sharp peak at the shoulder centred at $\sim 280\text{ cm}^{-1}$, which is formed due to overlapping of Mo_2C , $\text{W}_{20}\text{O}_{58}$, MoO_3 and Mo_4O_{11} phases. Mo_2C shows the dominant Raman peak $\sim 280\text{ cm}^{-1}$ [174], whereas leading Raman peaks of $\text{W}_{20}\text{O}_{58}$, MoO_3 and Mo_4O_{11} are found at $\sim 281\text{ cm}^{-1}$, $\sim 298\text{ cm}^{-1}$ [178], $\sim 284\text{ cm}^{-1}$, $\sim 292\text{ cm}^{-1}$ [179] and $\sim 264\text{ cm}^{-1}$ [180] respectively. The Mo_2C peak indicates the presence of coating particles in the adhered debris. The spectrum contains two peaks at two consecutive shoulders of the spectrum centred at $\sim 433.5\text{ cm}^{-1}$ and $\sim 787\text{ cm}^{-1}$ respectively, which are formed due to overlapping of Mo_4O_{11} and WO_3 phases. The dominant Raman peaks of WO_3 are reported at $\sim 417\text{ cm}^{-1}$, $\sim 437\text{ cm}^{-1}$ and $\sim 807\text{ cm}^{-1}$ [178], whereas leading Raman peaks of Mo_4O_{11} are found $\sim 431\text{ cm}^{-1}$, $\sim 744\text{ cm}^{-1}$ and $\sim 790\text{ cm}^{-1}$ [180]. Based on the Raman analyses and the EDX spectrum, the possible chemical reactions are listed in equation set (3).

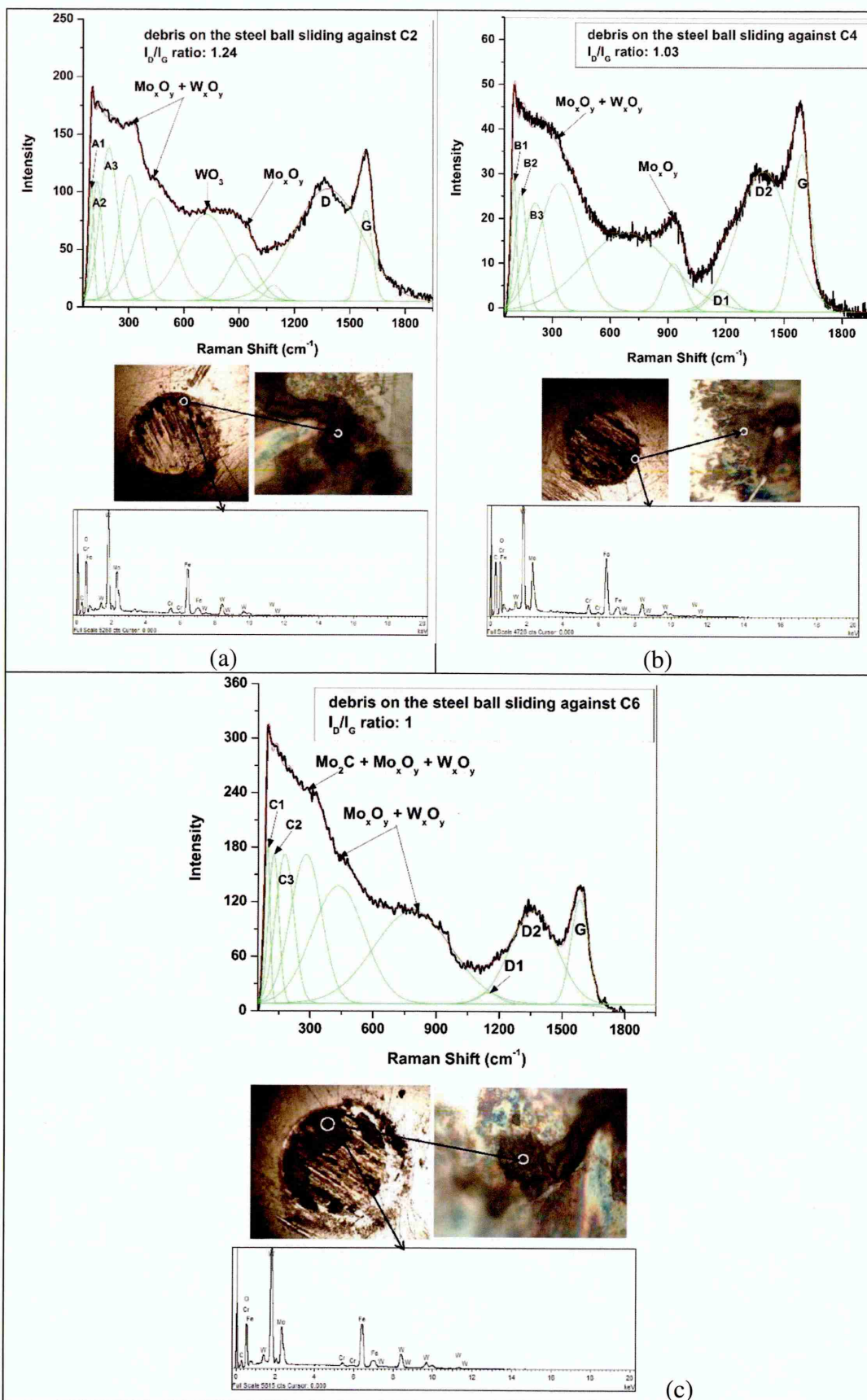
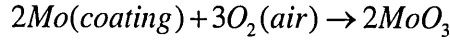
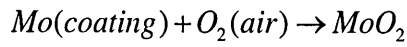
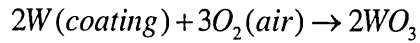
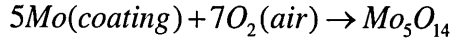
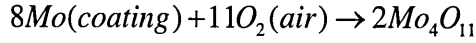
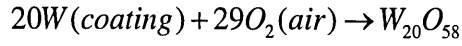


Figure 4.2-5: (a – c) Raman spectrum collected from the debris adhered to the steel counterparts after dry sliding against Mo–W–C coatings

Principal metal oxides:



Intermediate metal oxides:



IV. Wear behaviour of Mo–W–C coatings during dry sliding

Figures 4.2-6a and 4.2-6b show the SEM images of ~254 µm and ~264 µm wide wear tracks on the C2 and C4 respectively after sliding against steel balls. Both the wear tracks are smooth and no grooves are observed inside the tracks. The transfer layer promotes minimum wear during sliding thus the wear coefficients of C2 and C4 are found as $2.92 \times 10^{-16} \text{ m}^3\text{N}^{-1}\text{m}^{-1}$ and $3.87 \times 10^{-16} \text{ m}^3\text{N}^{-1}\text{m}^{-1}$ respectively. The coating remains intact within the wear tracks after the test as the EDX spectra collected within the wear tracks are found same as the spectrum of the as-deposited surfaces. The absence of oxygen in the EDX spectra indicates no adherence of metal oxides within the wear tracks. Furthermore, no accumulation of wear debris is observed outside the wear tracks. This can be attributed to the lower sticking probability due to cold welding phenomena of the debris to the surface of the coating material compared to the counterpart material.

Figure 4.2-6c shows the SEM image of ~405 µm wide wear track on C6. The track contains several grooves, which is attributed to the rolling friction between the hard and coarse particles present in the transfer layer. The presence of grooves increases the wear coefficient to $11.7 \times 10^{-16} \text{ m}^3\text{N}^{-1}\text{m}^{-1}$ after dry sliding, which is almost three times higher compared to other coatings. The accumulation of wear debris is observed outside the wear track. The EDX spectrum indicates that C6 remains intact within the wear track and no trace of metal oxides within the wear track is found.

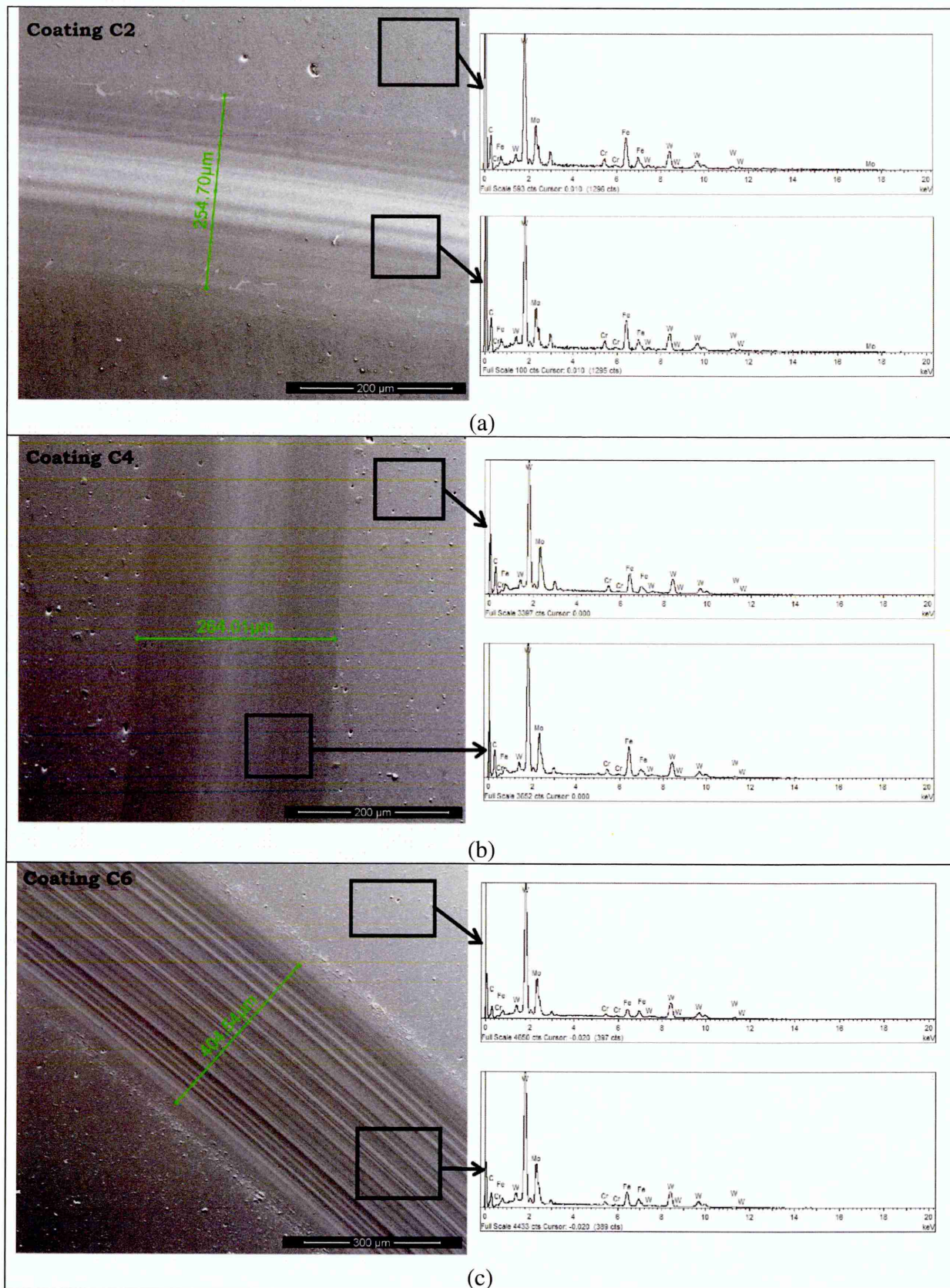


Figure 4.2-6: (a – c) SEM images of the wear track on the Mo–W–C coatings after dry sliding against steel ball

Figure 4.2-7 illustrates the wear track profiles of Mo–W–C coatings after sliding against steel ball. The depth of wear tracks was measured with the help of software associated with the surface profilometer. The average depths of wear tracks are found as $\sim 1.14\text{ }\mu\text{m}$, $\sim 1.19\text{ }\mu\text{m}$ and $\sim 1.55\text{ }\mu\text{m}$ for C2, C4 and C6 respectively, which are less than the thickness of respective coatings (see figure 4.1-1). This confirms that the coatings are retained intact within the wear track after large sliding distance (7.5 km) at ambient condition. The largest wear volume of C6 is attributed to the third-body abrasive wear between the coating, the steel ball and the hard and coarse wear debris particles generated from coating during sliding. On the other hand, sliding contact between debris particles results in smaller wear volume for C2 and C4 during sliding. The enhanced wear performance of Mo–W–C coatings is attributed to the dense microstructure, strong interfacial adhesion and high hardness.

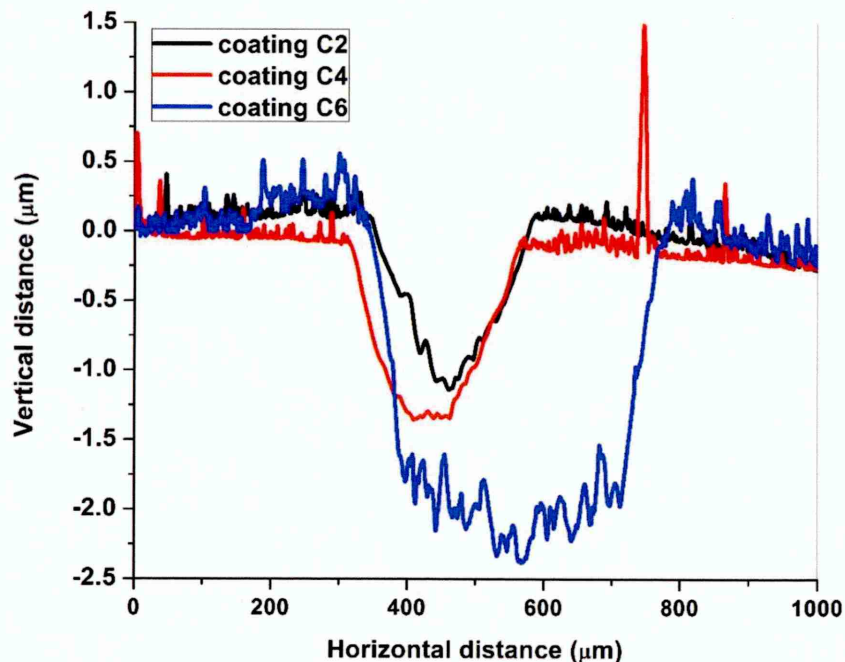


Figure 4.2-7: Wear track profile of Mo–W–C coatings after dry sliding against steel ball

EDX analysis in figure 4.2-6 indicates no adherence of metal oxides in the wear track after sliding, however the debris adhered to the counterpart surfaces contains tungsten and molybdenum oxides as observed by X-ray mapping and Raman analyses (see figures 4.2-3 and 4.2-5). Therefore few metal oxide particles, which are below the detection limit

for EDX analysis, can probably be present within the wear track and Raman spectroscopy is used to reveal that.

Figure 4.2-8 shows the Raman spectra collected within the wear track of Mo–W–C coatings after sliding and the deconvoluted peaks are listed in table A-4 (see appendix A). No significant change in shape of the spectra is observed after sliding when compared to the as-deposited surfaces (see figure 4.1-9). After deconvolution of the spectrum collected within the wear track of C2 (figure 4.2-8a), two separate disordered peaks (D1 and D2) and G peak are observed at 1218.5 cm^{-1} , 1416.97 cm^{-1} and 1575.97 cm^{-1} respectively. The I_D/I_G ratio is calculated as 2.47 after sliding, which is similar to the as-deposited surface. Moreover, the peaks A1 – A5 belong to the as-deposited surface indicating absence of metal oxides within the wear track of C2 after sliding.

The spectrum collected within the wear track of C4 (figure 4.2-8b) shows two separate disordered peaks (D1 and D2) and G peak at 1109.65 cm^{-1} , 1382.04 cm^{-1} and 1572.58 cm^{-1} respectively after deconvolution. The I_D/I_G ratio is increased to 2.64 after sliding. It is speculated that continuous rubbing of steel ball against wear debris causes severe plastic deformation of debris, which ultimately results in reduction of cluster size. The lower cluster size increases the breathing mode of six fold rings leading to the development of D peak and therefore an increase in D peak intensity is observed. However, it does not affect the stretching motion of sp^2 bonded carbon atoms leading to no change in the G peak intensity. As a result, the I_D/I_G ratio is increased after sliding indicating an increase in disorder of carbon-carbon bonds in the coating. It is believed that increase in disorder helps to reduce the friction coefficient due to irregularity of the bonds which in turn weakens the material. This is supported by the fact that the I_D/I_G ratio increases for nanocrystalline graphite, when the cluster size decreases [172].

The deconvoluted spectrum (figure 4.2-8b) further shows the presence of three peaks labelled as B3' – B5' and a small peak centred at $\sim 942\text{ cm}^{-1}$ in the spectrum range of $\sim 50 - 1000\text{ cm}^{-1}$ (see table A-4 of appendix A for details about deconvoluted peaks). Peaks B3 – B5 of the as-deposited C4 (see figure 4.1-9b) are shifted to lower wavenumbers after sliding and the respective peaks are labelled as B3' – B5'. The phases from as-deposited coating are still present within the wear track; however it is believed that the formation of new compounds after sliding results in shifting of peak position and increase in corresponding peak width. For example, Mo_2C phase from as-deposited C4 is retained in

the peaks centred at $\sim 320\text{ cm}^{-1}$ and $\sim 644\text{ cm}^{-1}$ but these peaks are further influenced by the formation of metal oxides. The leading Raman peaks of WO_3 are found at $\sim 326\text{ cm}^{-1}$ and $\sim 331\text{ cm}^{-1}$ [178] whereas $\text{W}_{20}\text{O}_{58}$ shows dominant Raman peaks at $\sim 319\text{ cm}^{-1}$ and $\sim 341\text{ cm}^{-1}$ [178] respectively. Thus peak B4' centred at $\sim 320\text{ cm}^{-1}$ is formed due to overlapping of Mo_2C , WO_3 and $\text{W}_{20}\text{O}_{58}$ phases and is named in the spectrum as $\text{Mo}_2\text{C}[\text{W}_x\text{O}_y]$, where W_xO_y indicates the WO_3 and $\text{W}_{20}\text{O}_{58}$ peaks together. Similarly, the leading Raman peaks of MoO_2 and MoO_3 are found at $\sim 640\text{ cm}^{-1}$, $\sim 666\text{ cm}^{-1}$ [174] and $\sim 667\text{ cm}^{-1}$ [179] respectively, whereas intermediate molybdenum oxide Mo_8O_{23} has a dominant Raman peak at $\sim 658\text{ cm}^{-1}$ [183]. Therefore peak B5' centred at $\sim 644\text{ cm}^{-1}$ is formed due to overlapping of Mo_2C , MoO_2 , MoO_3 and Mo_8O_{23} phases and is named in the spectrum as $\text{Mo}_2\text{C}[\text{Mo}_x\text{O}_y]$, where Mo_xO_y indicates the MoO_2 , MoO_3 and Mo_8O_{23} peaks altogether. Another small peak centred at $\sim 942\text{ cm}^{-1}$ and having a peak width of $\sim 150\text{ cm}^{-1}$ probably indicates the presence of WC phase as the leading Raman peak of WC is reported in the literature at $\sim 960\text{ cm}^{-1}$ [184].

After deconvolution of the spectrum collected within the wear track of C6 (figure 4.2-8c), five peaks labelled as C1 – C6' are observed (see table A-4 of appendix A for details about deconvoluted peaks) along with D and G peaks located at 1396.14 cm^{-1} and 1577.25 cm^{-1} respectively. The I_D/I_G ratio is increased to 2.23 after sliding indicating an increase in disorder of carbon-carbon bonds. Peak C1 belongs to as-deposited C6, whereas peaks C3 – C6 of the as-deposited coating (see figure 4.1-9c) are shifted to lower wavenumbers after sliding and the respective peaks are labelled as C3' – C6'. Among them, the shifting of peaks C3' and C4' is influenced by the formation of metal oxides during sliding. The leading Raman peaks of MoO_3 and $\text{W}_{20}\text{O}_{58}$ are found at $\sim 158\text{ cm}^{-1}$, $\sim 284\text{ cm}^{-1}$ and $\sim 292\text{ cm}^{-1}$ [179] and $\sim 298\text{ cm}^{-1}$ [178] respectively. Therefore peak C3' is appeared indicating presence of MoO_3 whereas peak C4' is formed due to overlapping of MoO_3 and $\text{W}_{20}\text{O}_{58}$.

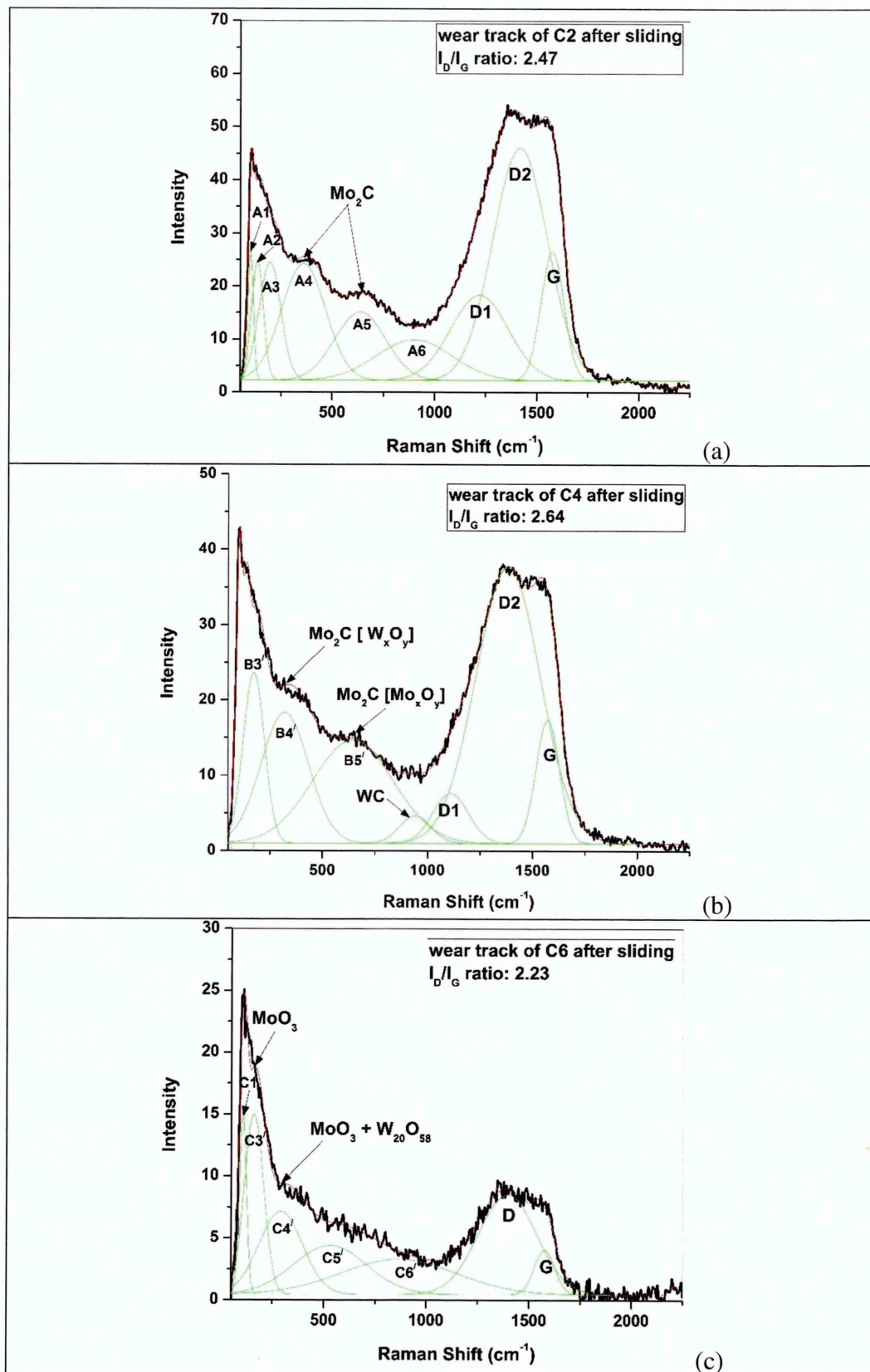


Figure 4.2-8: (a – c) Raman spectra collected within the wear tracks of Mo–W–C coatings after dry sliding against steel balls

It should be noted that the debris adhered to the counterparts shows lower degree of graphitisation ($I_D/I_G = 1.24, 1.03$ and 1 when sliding against C2, C4 and C6 respectively) compared to the as-deposited coating ($I_D/I_G = 2.51, 1.96$ and 1.85 for C2, C4 and C6 respectively) and the debris particles found in the wear track ($I_D/I_G = 2.47, 2.64$ and 2.23 for C2, C4 and C6 respectively). The debris particles originated from the coatings are severely damaged during sliding and smeared all over the wear track. Thus the spectra collected from the wear tracks show an increased degree of graphitisation i.e. higher I_D/I_G ratio compared to the as-deposited coatings. On the other hand, the spectra collected from the debris adhered to the counterparts (see figure 4.2-5) show typical D and G peaks, which are similar to that observed in the amorphous carbon coatings rather than the graphitic carbon coatings. This indicates more disorder of the carbon-carbon bonds of the debris particles adhered to the counterpart surface rather than wear tracks. Because of this disorder, the graphitic cluster size is significantly decreased and the distortion of clusters eventually opens up the aromatic rings resulting in a decrease in D peak intensity. This does not affect the relative motion between sp^2 carbon bonds, thus G peak intensity remains same. Therefore, a significant decrease in I_D/I_G ratio is observed for adhered debris compared to as-deposited coatings indicating a possible transformation of nanocrystalline graphitic particles to amorphous phase due to severe plastic deformation during sliding [172].

V. Wear mechanism during dry sliding at ambient temperature

The friction and wear behaviour during dry sliding is simultaneously influenced by the powder-like graphitic carbon particles and the metal oxide particles (different principal and intermediate oxides of W and Mo, iron oxides and chromium oxides) present in the transfer layer. Raman analysis of the counterparts and the coatings reveal the wear mechanism during dry sliding.

The wear debris generated during sliding contains tungsten carbide, molybdenum carbide and free graphitic carbon particles from the coating and particles from the uncoated steel ball. The flash temperature at the asperity contacts reaches up to 800°C [175] during sliding, which promotes chemical reactions between the wear debris and the oxygen from environment. As a result, different metal oxides are formed within the wear track and transformed to the counterpart surface during sliding. Raman analyses indicate the

presence of principal and intermediate oxides of W and Mo (WO_3 , $\text{W}_{20}\text{O}_{58}$, MoO_3 , MoO_2 , Mo_4O_{11} , Mo_5O_{14} and Mo_8O_{23}) and iron and chromium oxides (Fe_2O_3 and Cr_2O_3) in the transfer layer. These metal oxides have stronger chemical affinity towards steel rather than coating, thus they are strongly adhering to the ball surface (see figure 4.2-5). It is therefore concluded that the wear mechanism of Mo–W–C coatings during dry sliding is *oxidative*.

It is well known that WO_3 consists of a three-dimensional array of corner-linked WO_6 octahedra, MoO_2 has a distorted rutile structure consisting of edge-shared MoO_6 octahedra and both the Fe_2O_3 and Cr_2O_3 have their structure similar to that of corundum crystallites. None of these structures promotes sliding. On the other hand, MoO_3 is composed of distorted MoO_6 octahedra, which forms chains by sharing the edges. The chains are cross-linked by oxygen atoms and form an unusual layered structure. Therefore MoO_3 acts effectively as a solid lubricant unlike other oxides and promotes sliding at ambient condition. The oxidation of tungsten and molybdenum carbide debris particles during sliding form MeO_3 structures (where Me corresponds to = W, Mo) consisting of corner-shared MeO_6 octahedra. The heat generated at the asperity contacts promotes chemical reaction between these metal oxides and the powdered metal present in the transfer layer. The reduction of MeO_3 compounds results in different intermediate oxides unless MeO_2 structures (WO_2 and MoO_2) containing edge-shared MeO_6 octahedra are formed. In between the MeO_3 and MeO_2 structures, a series of intermediate oxides with a stoichiometry of $\text{Me}_n\text{O}_{3n-1}$ may form and they are known as Magnéli phase oxides. These oxides contain slabs of corner-shared octahedra and share edges with the octahedra of the identical adjacent slabs. These slabs promote the crystallographic shear [185].

The different metal oxides generated from Mo–W–C coatings due to *oxidative* wear mechanism play an important role in reduction of the friction coefficient at ambient condition. Among the various metal oxides formed during sliding, most beneficial are MoO_3 and Magnéli phase oxides, which act as solid lubricants due to their unique layered structure and therefore promote sliding. The sliding is further benefitted by the presence of graphitic carbon particles in the transfer layer, which eventually reduce the mean friction coefficient of Mo–W–C coatings in the range of $\sim 0.2 - 0.3$. Consequently, the wear is significantly minimised as indicated by the wear coefficient found in the order of $\sim 10^{-16} \text{ m}^3\text{N}^{-1}\text{m}^{-1}$ after 7.5 km of sliding distance.

4.2.3. Tribological behaviour of Mo–W–C coatings during boundary lubricated sliding condition at ambient temperature

I. Experimental details

A CSM room temperature pin-on-disc tribometer was used to study the friction behaviour of Mo–W–C coatings against uncoated 100Cr6 steel and Al₂O₃ counterparts under boundary lubricated condition at ambient temperature (~25°C – 30°C). The coated discs and the counterparts were completely immersed into the lubricant during sliding, thus no direct contact with air was possible. The static load was fixed to 5 N for all sliding tests. In the first stage of experiments, the sliding tests were repeated three times for each coating against steel balls for large sliding distance (7.5 km). C4 shows minimum friction coefficient compared to others, thus another sliding test was carried out in similar conditions for a larger sliding distance of 15 km. In second stage, C4 was subjected to another sliding test against Al₂O₃ ball for a relatively short sliding distance (600 m) at ambient condition (~25°C).

Optical microscopy, surface profilometer and Raman spectroscopy were used to reveal the wear behaviour of Mo–W–C coatings. The topographical imaging of the wear tracks was carried out using optical microscope and the wear coefficients were measured using surface profilometer. Raman spectra were collected from the wear tracks with 60 s exposure time. The tribological behaviour of Mo–W–C coatings against steel and Al₂O₃ balls are discussed in sections II and III respectively and the relevant wear mechanism is proposed in section IV.

Highly viscous Mobil1 Extended life™ 10W-60 synthetic engine oil was used as lubricant during sliding. The number '10W-60' indicates that the oil is multigrade, i.e. the oil has two viscosity grades '10W' and '60'. '10W' means it has same flowing characteristics as a SAE 10 single-grade oil (typical viscosity ~4.1 cst) when starts from cold (W indicates Winter). '60' indicates that the oil is less thin than a SAE 60 single-grade oil (typical viscosity ~24 cst) when temperature rises to 100°C. According to the manufacturer's website, this oil has a density of 0.86 g/ml at 15.6° C and the viscosity is 152.7 cst and 22.7 cst at 40°C and 100°C respectively. This oil contains different polymer additives (mostly AW additives such as ZDDP and EP additives) but no friction modifiers (such as

MoDTC). Sulphated ash (1.4 wt%) and phosphorus compounds (0.13 wt%) are the main ingredients of this oil. Sulphated ash is composed of sulphur-based and chlorine-based compounds and different metal additives including K, Ba, Ca, Mg, Na and sometimes Sn and Zn. The metal additives are more reactive to phosphorus compounds compared to sulphur-based and chlorine-based compounds. Therefore, if the oil contains phosphorus compounds, the metal additives react with them under suitable conditions and produce metal phosphates and metal oxides (applicable for Sn and Zn only). Thus the sulphur-based and chlorine-based compounds become free to react chemically with other metals if present in the system depending on appropriate temperature and other operating conditions [186]. Typical properties of this oil are listed in Table 4.2-1.

Table 4.2-1: Typical properties of Mobil1 Extended life™ 10W-60 engine oil [187]

Oil properties	Standard	Value
Viscosity at 40°C	ASTM D445	152.7 cst
Viscosity at 100°C		22.7 cst
Viscosity Index	–	178
Sulphated Ash (wt%)	ASTM D874	1.4
Phosphorous (wt%)	ASTM D4951	0.13
Density at 15.6°C (g/ml)	ASTM D4052	0.86
Flash Point (°C)	ASTM D92	234

II. Tribological behaviour of Mo–W–C coatings during lubricated sliding against steel counterparts

Figure 4.2-9 shows the friction behaviour of Mo–W–C coatings against uncoated 100Cr6 steel balls in lubricated sliding condition. Unlike dry sliding, the initial run-in period of Mo–W–C coatings is found very short (< 50 m) in lubricated condition. The friction curves of C2 are observed very smooth and no stick-slip motion is noticed. The mean friction coefficients of C2 for three tests are found as ~0.047, ~0.065 and ~0.08 respectively (figure 4.2-9a). Significant reduction in mean friction coefficient is observed for C4 with a mean value of ~0.033, ~0.037 and ~0.049 for three respective tests (figure 4.2-9b). C6 shows a slight increase in mean friction coefficients to ~0.052, ~0.056 and ~0.066 for three tests respectively (figure 4.2-9c). No stick-slip motion is observed for C4 and C6, however C4 shows smoother friction curves compared to C6. Overall the average friction coefficients of C2, C4 and C6 after three lubricated sliding tests are calculated as ~0.064, ~0.04 and ~0.058 respectively, whereas it is found as ~0.333,

~0.335 and ~0.223 respectively after dry sliding (see figure 4.2-1). Thus addition of lubricant decreases the mean friction coefficient of C2, C4 and C6 by ~80.8%, ~88.1% and ~74% respectively at ambient temperature.

The wear scar on the steel balls is found negligible after 7.5 km of sliding in lubricated condition and figures 4.2-10a – 4.2-10c show very shallow wear tracks on the coated discs. The width of wear track is found much smaller for C6 (~48 μm) compared to C2 and C4 (~101 μm and ~121 μm respectively). The profiles of the wear track and the coated surface beside it (as reference) are shown in figures 4.2-10d – 4.2-10f. Both profiles look almost similar indicating negligible wear of Mo–W–C coatings similar to their counterparts after lubricated sliding. This indicates excellent wear resistance of Mo–W–C coatings at ambient temperature.

C4 shows lowest mean friction coefficient (~0.033 – 0.049) during lubricated sliding compared to others. The friction coefficients become stable at the end of sliding distance, therefore another sliding test was carried out for a larger distance of 15 km under similar test conditions. Figure 4.2-11 shows the friction behaviour and the image of the wear track is provided in the inset. The friction curve looks very smooth. The initial value of friction coefficient is observed as high as ~0.08. However it gradually decreases to ~0.05 after 1.4 km of sliding distance, followed by friction coefficients varying in the range of ~0.04 – 0.05 for rest of the sliding distance. The overall mean friction coefficient is found as ~0.05 and a very shallow wear track with a width of ~166 μm is observed after 15 km sliding distance.

As reported in the literature, the friction coefficients of 2 μm thick W-DLC coatings coating deposited using reactive sputtering process are found in the range of ~0.05 – 0.08 when sliding against steel counterparts in the presence of lubricant, which consists of base oil PAO mixed with commercial sulphur-based EP additives [64]. On the other hand, the current research shows further reduction in the mean friction coefficient to ~0.033 – 0.05 for C4 when sliding against steel ball in the presence of commercially available engine oil, which contains similar ingredients. Thus combined doping of Mo and W results in lower friction coefficient compared to single W doping into the carbon-based coating.

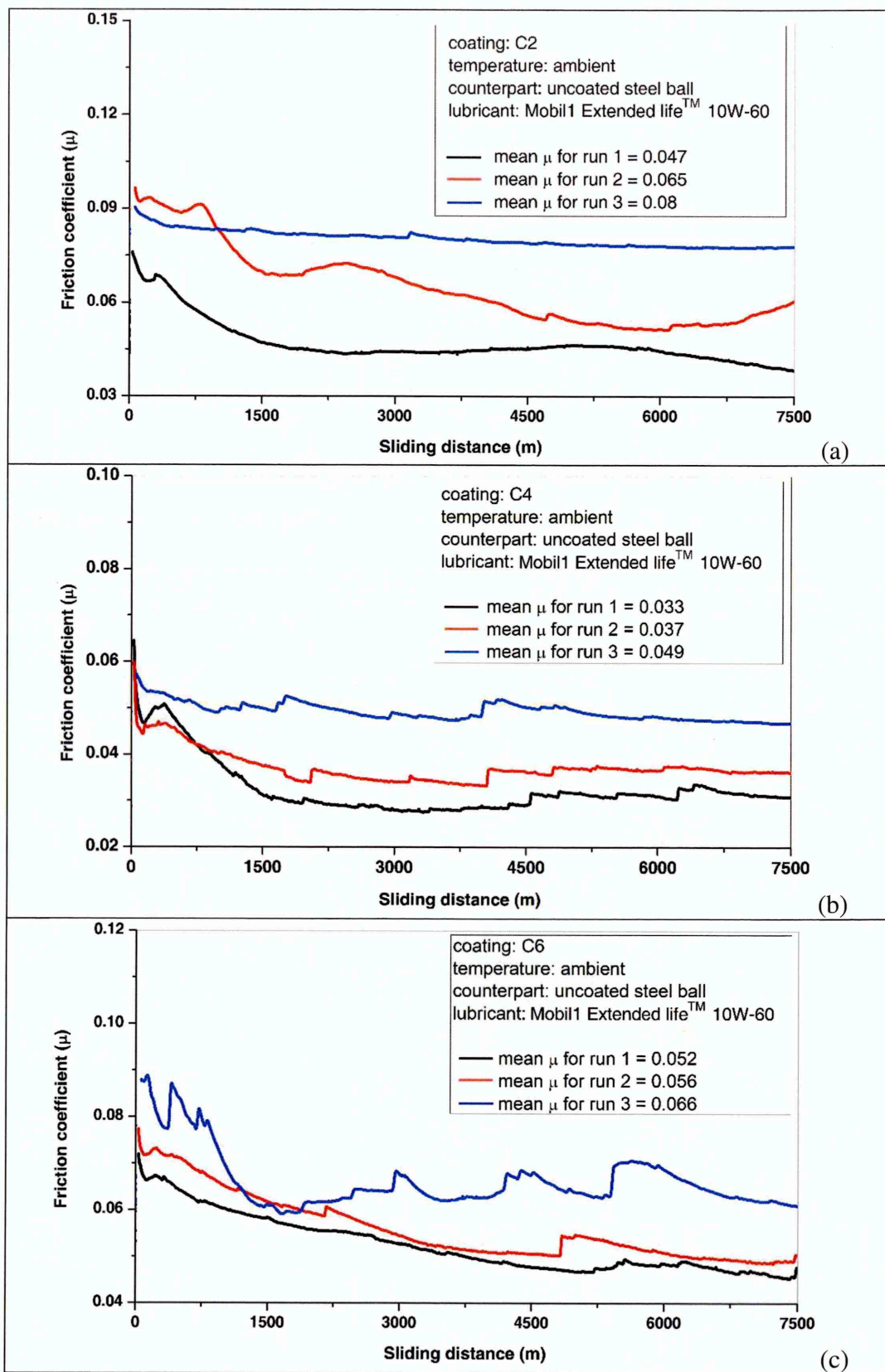


Figure 4.2-9: (a – c) Friction behaviour of Mo–W–C coatings in lubricated condition against steel counterparts

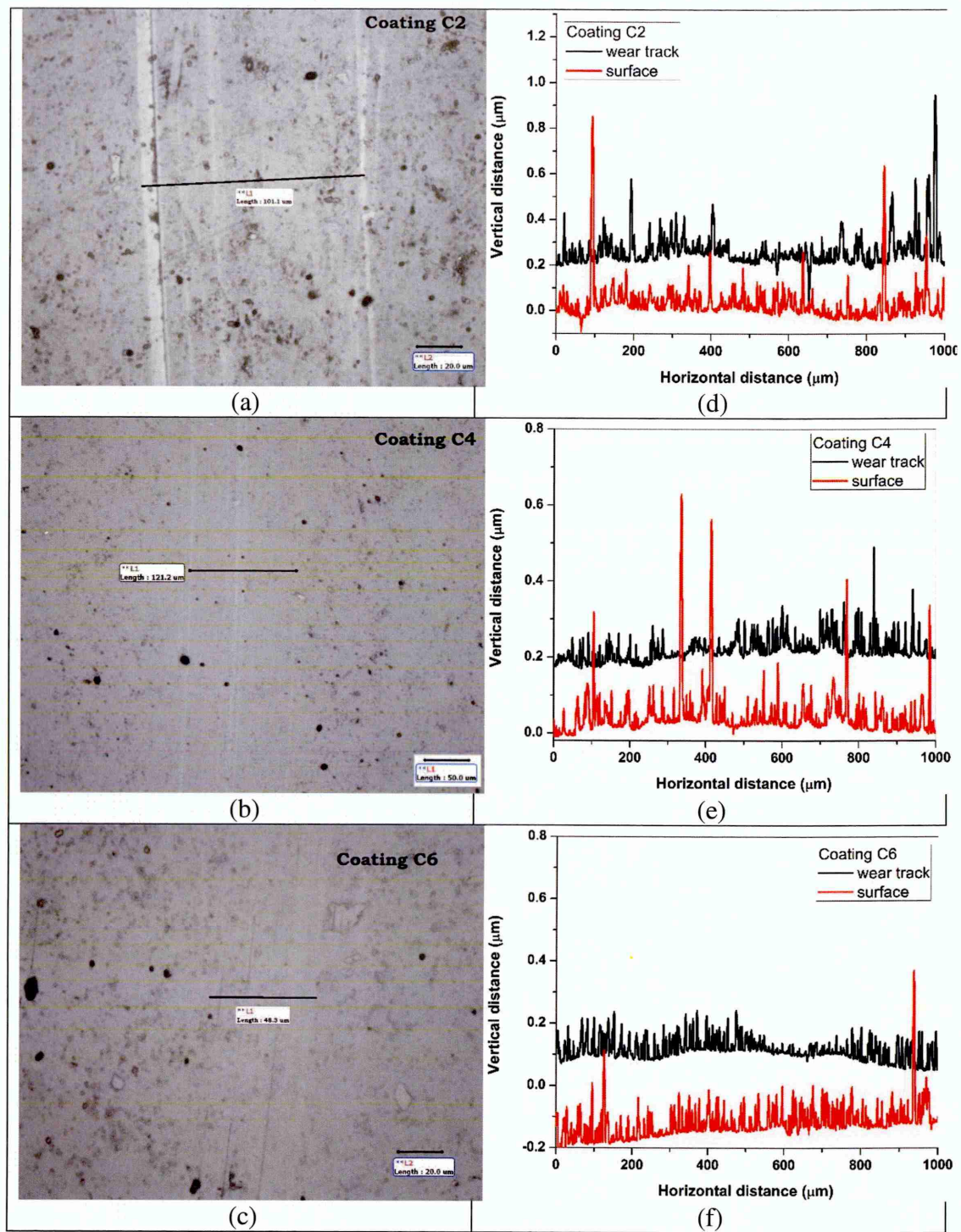


Figure 4.2-10: Wear track profiles of the Mo-W-C coatings after lubricated sliding against steel balls

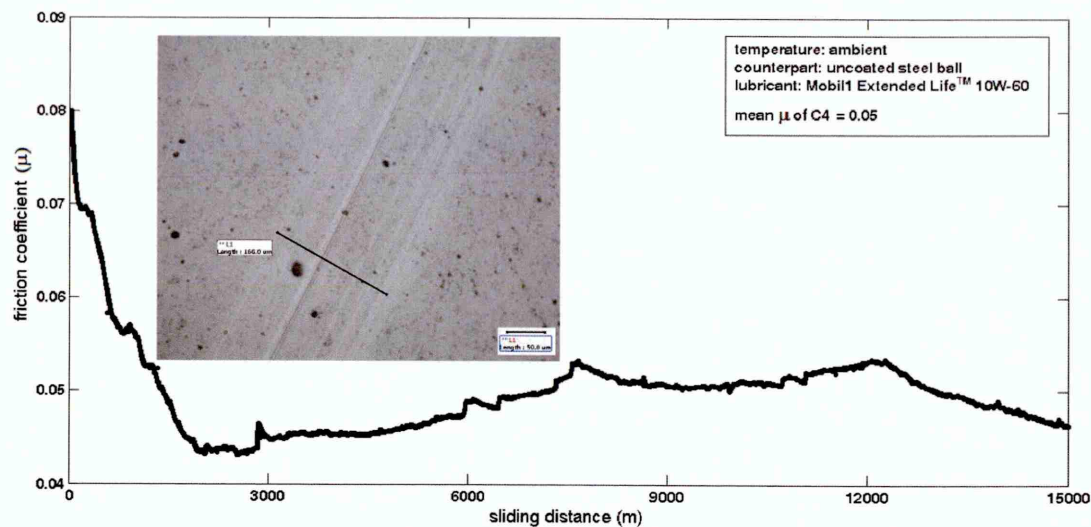


Figure 4.2-11: Friction behaviour of coating C4 in lubricated sliding condition against steel counterpart for a sliding distance of 15 km

The wear behaviour of Mo–W–C coatings during lubricated sliding is further investigated using Raman spectroscopy. The lubricant is carefully cleaned from the wear track after sliding, so that no trace of oil is left in the wear track but the wear products remain unaffected. After complete removal of the oil, the Raman spectrum is collected within the wear track.

Figure 4.2-12 shows the Raman spectrum collected from the thin lubricant film placed on a glass slide. The spectrum collected from the dry glass slide is provided as reference. The exact chemical compounds present in the lubricant are unknown, thus the peaks cannot be identified. The spectrum collected from the lubricant film (see figure 4.2-12) is observed completely different from the spectra collected from the wear tracks of Mo–W–C coatings after sliding against steel (see figure 4.2-13) and Al_2O_3 balls (see figure 4.2-16), which indicates that the wear tracks are completely free of oil during spectrum collection.

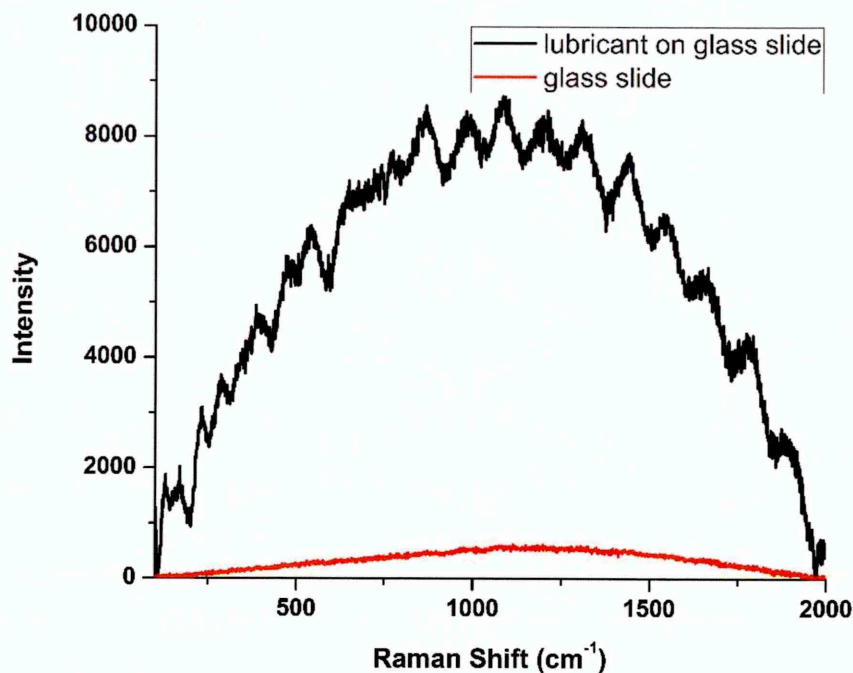


Figure 4.2-12: Raman spectrum collected from the thin lubricant film (Mobil1 Extended lifeTM 10W-60) placed on a glass slide

Figure 4.2-13 shows the Raman spectra collected within the wear track of Mo–W–C coatings after lubricated sliding and the details of the deconvoluted peaks are listed in table A-5 (see appendix A). After deconvolution of the spectrum collected from the wear track of C2 (figure 4.2-13a), the D and G peaks are found at 1385.84 cm^{-1} and 1572.06 cm^{-1} respectively. The I_D/I_G ratio is increased to 2.69 indicating an increase in disorder of carbon-carbon bonds after sliding. The shallow wear track contains Mo_2C peaks (centred at $\sim 368.5\text{ cm}^{-1}$ and at $\sim 626\text{ cm}^{-1}$) similar to the as-deposited surface but a shift in peak positions is observed due to sliding. Two other peaks centred at $\sim 235\text{ cm}^{-1}$ and $\sim 955\text{ cm}^{-1}$ are observed in the spectrum indicating the presence of Mo_2C and WC phases as the leading Raman peaks of Mo_2C and WC are reported in the literature at $\sim 234\text{ cm}^{-1}$ [174] and $\sim 960\text{ cm}^{-1}$ [184] respectively. Another sharp peak is appeared centred at $\sim 136.5\text{ cm}^{-1}$, which is assigned to WS_2 because the leading Raman peak of WS_2 powdered sample is found $\sim 128\text{ cm}^{-1}$ (see figure 4.2-14a).

Figure 4.2-13b shows the spectrum collected within the wear track of C4. The D and G peaks are found at 1390.85 cm^{-1} and 1572.61 cm^{-1} respectively after deconvolution of the spectrum. The I_D/I_G ratio is found as 2.72 indicating an increase in disorder of carbon-

carbon bonds after sliding. The Mo₂C peaks (centred at ~341 cm⁻¹ and at ~623 cm⁻¹) are observed within the shallow wear track similar to the as-deposited surface. The peak centred at ~993 cm⁻¹ indicates possible overlapping of Mo₂C and WC phases as the leading Raman peaks of Mo₂C and WC are reported in the literature at ~995 cm⁻¹ [174] and ~960 cm⁻¹ [184] respectively. The sharp peak centred at ~133 cm⁻¹ is assigned to WS₂ as the leading Raman peak of WS₂ powdered sample is observed ~128 cm⁻¹ (see figure 4.2-14a).

Figure 4.2-13c shows the spectrum collected within the shallow wear track of C6. After deconvolution of the spectrum, the D and G peaks are found at 1398.12 cm⁻¹ and 1582.44 cm⁻¹ respectively and the I_D/I_G ratio is increased to 2.46 indicating an increase in disorder of carbon-carbon bonds after sliding. The peaks labelled as C1 – C5' belong to the as-deposited surface however continuous sliding between the coating and the steel ball slightly shifts the peak positions towards lower wavenumbers. The peak centred at ~968 cm⁻¹ and having a width of ~304 cm⁻¹ indicates possible overlapping of Mo₂C and WC phases as the leading Raman peaks of Mo₂C and WC are reported in the literature at ~995 cm⁻¹ [174] and ~960 cm⁻¹ [184] respectively. A sharp peak centred at ~135 cm⁻¹ is appeared in the spectrum, which is assigned to WS₂ as the leading Raman peak of WS₂ powdered sample is observed ~128 cm⁻¹ (see figure 4.2-14a).

It is important to note that the Raman spectra collected from the wear tracks of Mo–W–C coatings after lubricated sliding contain a sharp WS₂ peak in the wavelength range of ~133 – 136 cm⁻¹. Neither the Mo–W–C coatings nor the lubricant contain WS₂, therefore it is definitely formed due to chemical reactions occurred between the coating and the lubricant during sliding. The tribological behaviour of Mo–W–C coatings during lubricated sliding is strongly influenced by these chemical reactions as explained in section IV.

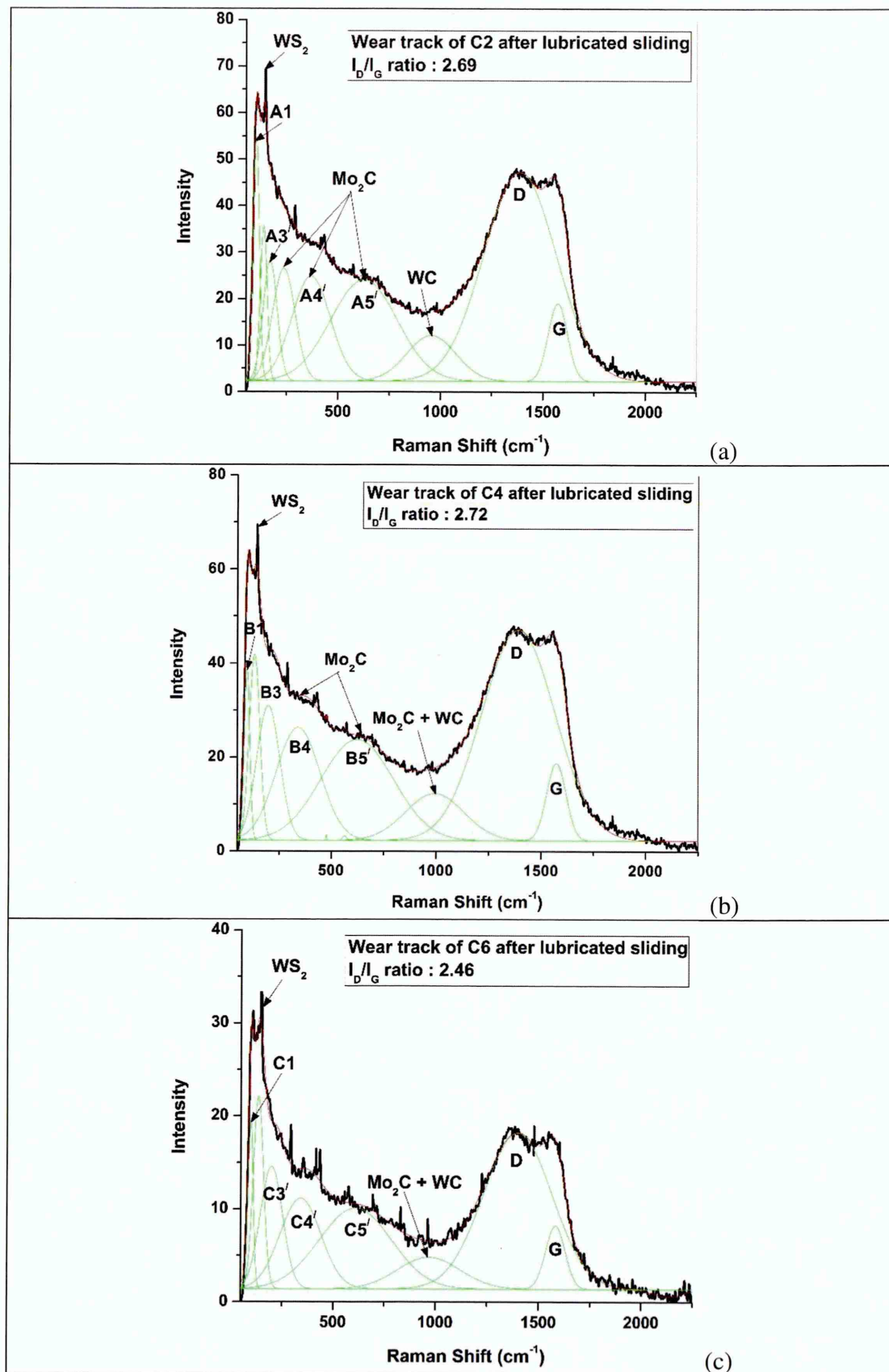


Figure 4.2-13: (a – c) Raman spectra collected within the wear tracks of Mo-W-C coatings after lubricated sliding against steel balls

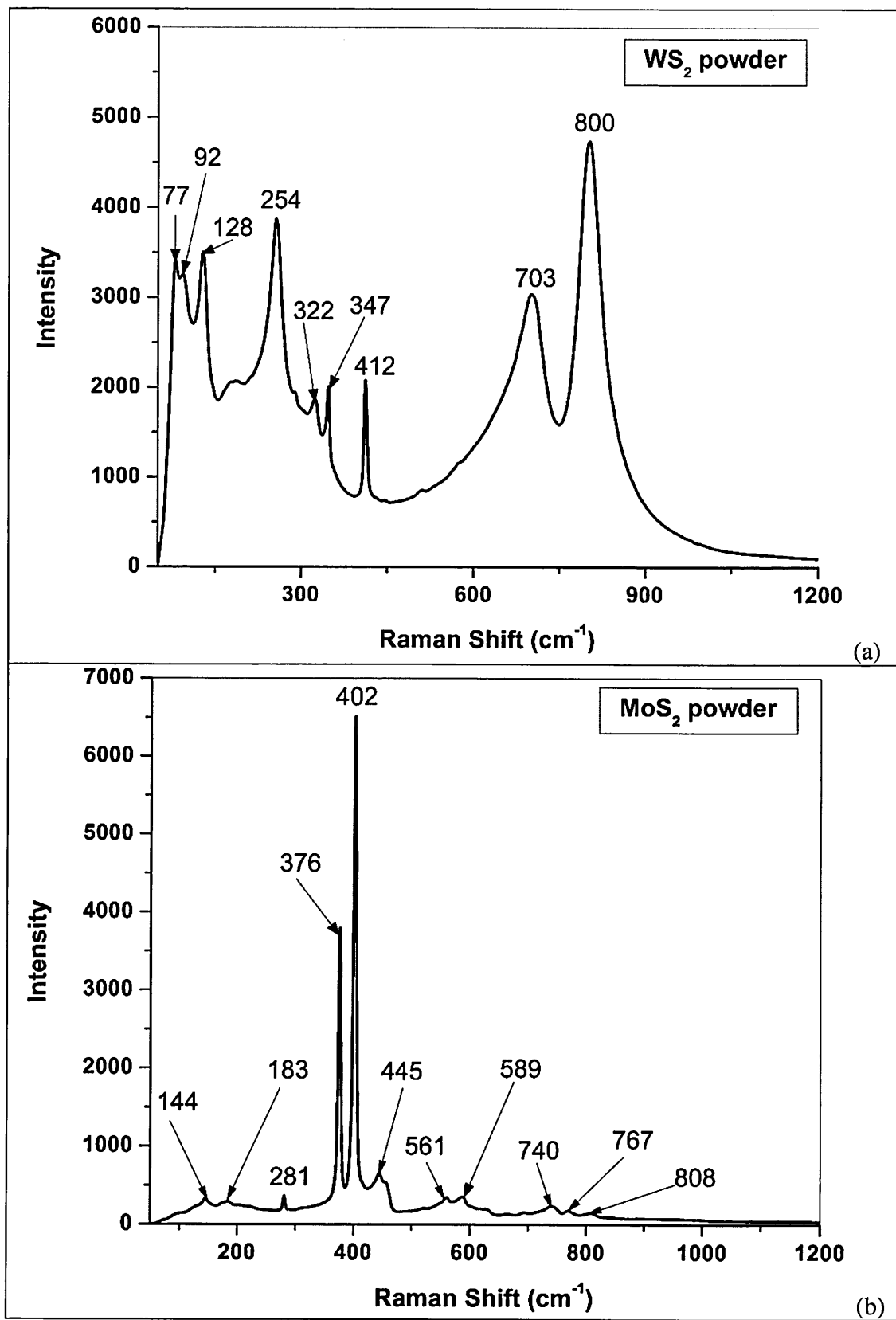


Figure 4.2-14: Raman spectra collected from (a) WS_2 and (b) MoS_2 powder

III. Tribological behaviour of C4 during lubricated sliding against Al₂O₃ ball

C4 shows lowest friction coefficient compared to others during lubricated sliding against steel ball, thus C4 is subjected to another sliding test against Al₂O₃ ball under similar test conditions. Figure 4.2-15 shows a very smooth friction curve of C4 with a mean friction coefficient of 0.072. The profiles of the wear track and the surface beside it are shown in the inset. The wear track is observed so shallow that its profile looks almost similar to the coated surface and simultaneously the wear of the Al₂O₃ ball is found negligible.

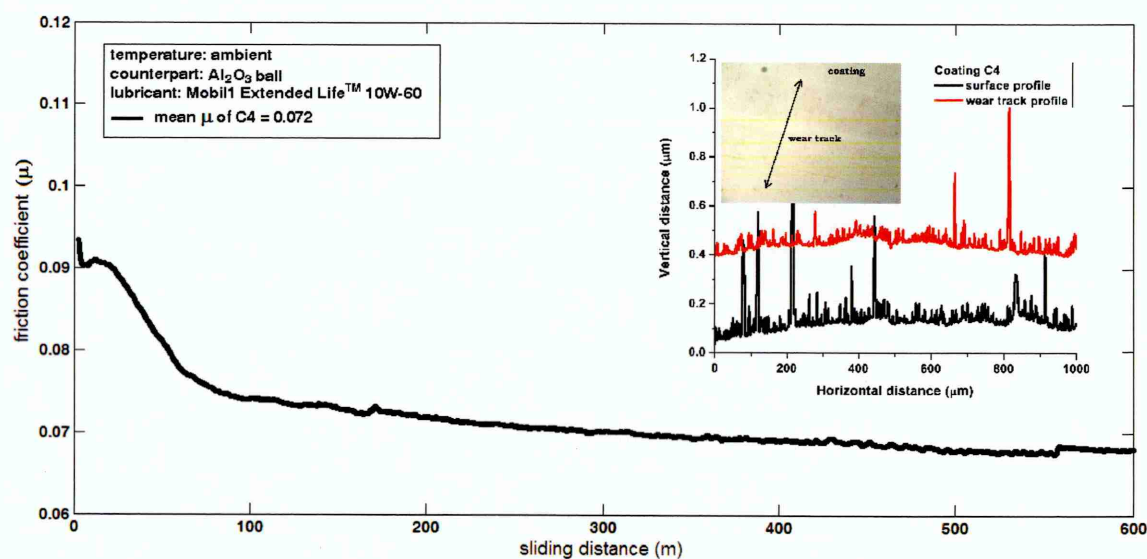


Figure 4.2-15: Friction behaviour of C4 during lubricated sliding against Al₂O₃ ball

Figure 4.2-16 shows the Raman spectrum collected from the wear track of C4 after sliding and the deconvoluted peaks are listed in table A-6 (see appendix A). After deconvolution of the spectrum, two separate disordered peaks (D1 and D2) and the G peak are found at 1122.34 cm⁻¹, 1379.65 cm⁻¹ and 1569.98 cm⁻¹ respectively. The I_D/I_G ratio is increased to 2.81 indicating an increase in disorder of carbon-carbon bonds after sliding. Mo₂C peaks (centred at ~360 cm⁻¹ and at ~637 cm⁻¹) are observed within the shallow wear track similar to the as-deposited surface. The peak centred at ~949 cm⁻¹ and having a width of ~244 cm⁻¹ indicates possible overlapping of Mo₂C and WC phases as the leading Raman peaks of Mo₂C and WC are reported in the literature at ~995 cm⁻¹ [174] and ~960 cm⁻¹ [184] respectively. The peak centred at ~253 cm⁻¹ is assigned to WS₂

because the leading Raman peak of WS₂ powdered sample is observed ~254 cm⁻¹ (see figure 4.2-14a). It should be noted that the presence of WS₂ peak is not so much prominent when sliding distance is as small as 600 m, however sharp WS₂ peak is observed when sliding distance is as large as 7.5 km (see figure 4.2-13b). The amount of WS₂ formed during sliding depends on the rubbing action taking place in between the sliding surfaces. Thus more amount of WS₂ is formed with increase in sliding distance. Overall, C4 shows improved tribological performance during boundary lubricated sliding at ambient condition irrespective of the counterpart material.

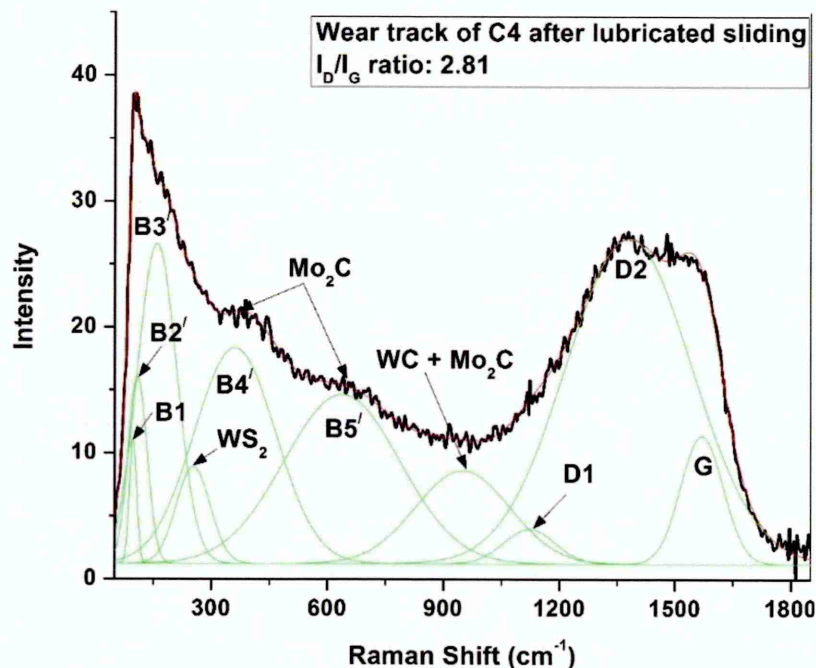


Figure 4.2-16: Raman spectra collected within the wear track of C4 after lubricated sliding against Al₂O₃ ball

IV. Tribo-chemically reactive wear mechanism during lubricated sliding at ambient temperature

Raman analyses of the Mo–W–C coatings (discussed in sections II and III) reveal the wear mechanism during boundary lubricated sliding at ambient condition. Raman spectra collected within the wear tracks indicate the presence of metal carbides (WC, Mo₂C etc.), metal sulphides (mostly WS₂) and graphitic carbon particles in the wear debris. The metal

carbides and graphitic carbon particles belong to Mo–W–C coatings, whereas WS₂ is the reaction product formed during lubricated sliding. The continuous rubbing action between the coating and the counterpart increases the flash temperature at the asperity contacts and the sulphur-containing compounds of the lubricant react with the sliding surfaces at that high temperature. As a result, WS₂ is formed where W comes from the coating and S comes from the EP additives present in the engine oil. The formation of WS₂ depends on the rubbing action taking place between sliding surfaces. Thus with increase in sliding distance, more amount of WS₂ is formed. When sliding distance is very large (i.e. 7.5 km), the Raman spectra contain sharp WS₂ peaks (within the wavelength range of ~133 – 136 cm⁻¹) indicating significant amount of WS₂ present in the wear track (see figure 4.2-13). Alternatively, the Raman spectrum indicates formation of very little amount of WS₂ in the wear track when sliding distance is as small as 600 m (see figure 4.2-16). Hence it is concluded that the wear mechanism of Mo–W–C coatings during boundary lubricated sliding is *tribochemically reactive* at ambient condition. Similar to WS₂, MoS₂ is likely to be formed during lubricated sliding. However it cannot be detected using Raman analyses probably due to its small amount. It is further observed that these debris particles have stronger affinity towards the coating rather than the counterpart, thus they adhere to the wear track by forming a thin tribo-layer.

WS₂ is a well-known solid lubricant. The structure consists of layers in which tungsten atoms are linked with six sulphides and form a trigonal prism rather than the usual octahedron structure. The layered structure promotes easy slipping between the layers and provides graphite-like lubricating properties [185]. Thus the low friction coefficient of Mo–W–C coatings (~0.04 – 0.07) is attributed to the formation of WS₂ as a reaction product and presence of graphitic carbon particles during lubricated sliding. Compared to dry sliding case, the reduction in friction coefficient is observed by 74 – 88% in lubricated condition. This significant reduction in friction simultaneously improves the wear resistance of Mo–W–C coatings. Even after a large sliding distance, negligible wear of Mo–W–C coatings is observed indicating its excellent tribological properties.

4.2.4. Influence of metal dopants on tribological behaviour of carbon-based coatings at ambient temperature

I. Introduction

The metal-doped carbon-based coatings provide a wide range of friction and wear coefficients, hardness and oxidation resistance depending on the nature of the metal dopants and deposition procedure as already discussed in chapter 2. Cr-doped carbon-based coatings were extensively studied by several researchers for this purpose. So, tribological performance of Cr-doped carbon-based coating (Cr/C) is evaluated at ambient temperature and then compared with Mo–W–C coatings (sections II and III respectively). On the other hand, commercially available state-of-the-art DLC coatings are potential candidates providing better tribological performance and higher thermal stability compared to metal-free DLC coatings. Thus tribological performance of Mo–W–C coatings are further compared with the state-of-the-art DLC coatings (section IV). The sliding tests were performed in dry and lubricated (engine oil) condition and corresponding friction and wear coefficients were measured. Based on the composition of the wear debris, the influence of metal dopants on the tribological behaviour of carbon-based coatings is explained.

II. Tribological performance of Cr-doped carbon-based coating (Cr/C) at ambient temperature

The nanostructured multilayer Cr-doped carbon-based coating (Cr/C) was deposited on hardened (62 HRC) high speed steel substrate by combined steered cathodic arc and unbalanced magnetron process known as Arc-Bond-Sputtering (ABS) [188, 189]. A CrN base layer was deposited by sputtering of Cr in a mixed nitrogen-argon atmosphere to enhance coating – substrate adhesion, followed by deposition of Cr/C coating using simultaneous sputtering of Cr and C in nonreactive argon atmosphere. More details of the experimental procedure was discussed elsewhere [132]. Cr/C coating was subjected to sliding tests in dry and lubricated condition against uncoated 100Cr6 steel balls at ambient temperature (~25°C and 15% relative humidity) under 5 N applied load. Raman

spectroscopy was used to study the wear debris present in the wear track and to understand the wear mechanism during dry and lubricated sliding.

Figure 4.2-17 shows the friction behaviour of C/Cr coating against steel ball in dry and lubricated sliding conditions and the respective wear track profiles are shown in the inset. The mean friction coefficient after dry sliding is found as 0.222, which reduces to 0.12 during lubricated sliding. During dry sliding, the coefficient of friction is strongly influenced by the humidity present in the test environment and the third-body abrasion between wear debris and sliding surfaces resulting in stick-slip motion. On the other hand, friction curve in lubricated sliding is very smooth and the initial run-in period is very short unlike that of dry sliding. The wear track after dry sliding (see inset of figure 4.2-17) is found as $\sim 1.2 \mu\text{m}$ deep and $\sim 500 \mu\text{m}$ wide, whereas it becomes very shallow ($\sim 0.75 \mu\text{m}$ deep and $\sim 50 \mu\text{m}$ wide) under lubricated condition. The wear coefficients after dry and lubricated sliding are found as $1.27 \times 10^{-15} \text{ m}^3\text{N}^{-1}\text{m}^{-1}$ and $9.62 \times 10^{-17} \text{ m}^3\text{N}^{-1}\text{m}^{-1}$ respectively. Further, no substrate exposure is observed during sliding as the depth of the wear tracks is found smaller than the coating thickness ($\sim 1.82 \mu\text{m}$) [190].

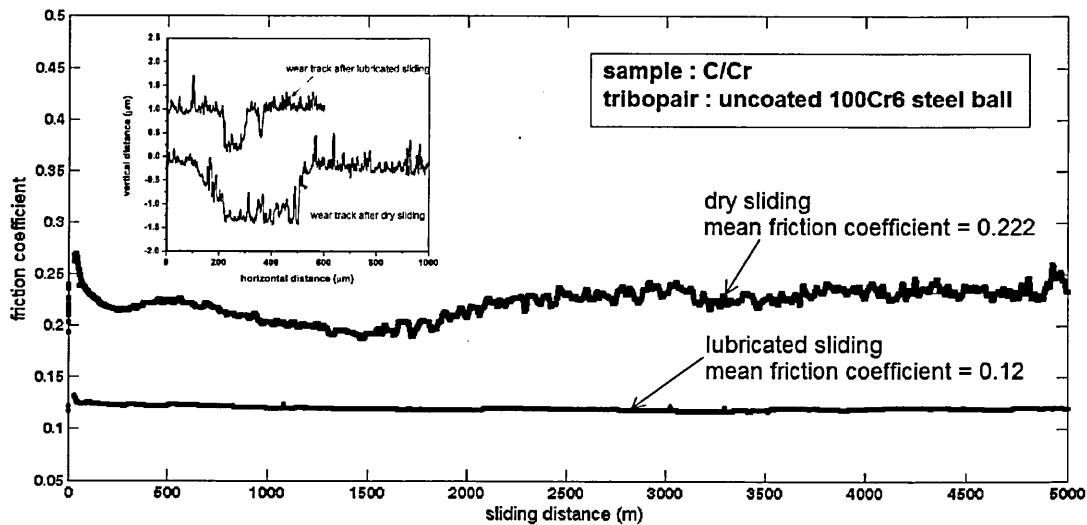


Figure 4.2-17: Friction behaviour and wear track profiles of C/Cr coating against steel ball in dry and lubricated sliding conditions

Figure 4.2-18a shows the Raman spectrum collected from as-deposited Cr/C coating. After deconvolution of the spectrum, six peaks labelled as P1 – P6 are observed along with dominant D and G peaks (see details of the deconvoluted peaks in table A-7 of

appendix A). The D and G peaks are located at $\sim 1382.6 \text{ cm}^{-1}$ and $\sim 1575.4 \text{ cm}^{-1}$ respectively and the I_D/I_G ratio is calculated as 2.175.

Figure 4.2-18b shows the Raman spectrum collected from the wear track after dry sliding. After deconvolution of the spectrum (see details of the deconvoluted peaks in table A-7 of appendix A), the D and G peak positions are found at $\sim 1388.25 \text{ cm}^{-1}$ and $\sim 1574.11 \text{ cm}^{-1}$ respectively. The I_D/I_G ratio is calculated as 2.254 indicating an increase in disorder of carbon-carbon bonds after sliding. Two peaks centred at $\sim 384 \text{ cm}^{-1}$ and $\sim 536 \text{ cm}^{-1}$ are assigned to Cr_2N and Cr_2O_3 respectively as the Raman peaks of Cr_2N and Cr_2O_3 are reported in the literature at $\sim 385 \text{ cm}^{-1}$ [191] and $\sim 527 - 530 \text{ cm}^{-1}$ [177]. A wide peak centred at $\sim 673 \text{ cm}^{-1}$ and having a width of $\sim 280 \text{ cm}^{-1}$ is found in the hump observed in the spectrum. It is believed that the peak is formed due to overlapping of three different peaks such as Cr_2O_3 , Fe_2O_3 and Fe_3O_4 . The Raman peaks of Cr_2O_3 is found at $\sim 552 \text{ cm}^{-1}$ and $\sim 613 \text{ cm}^{-1}$ [177], whereas Fe_2O_3 and Fe_3O_4 have their corresponding Raman peaks at $\sim 611 - 613 \text{ cm}^{-1}$ [192, 193] and $\sim 661 - 663 \text{ cm}^{-1}$ [192, 193] respectively as reported in the literature.

It is believed that Cr_2N originates from CrN base layer due to occurrence of two simultaneous events such as, through slow nitrogen out diffusion and due to the reaction between the base layer of the coating and the nitrogen from atmosphere during sliding in air. The depth of wear track is found $\sim 1.2 \text{ }\mu\text{m}$ (see figure 4.2-17), which indicates that CrN interlayer may be exposed during sliding against steel ball in air; however the substrate remains protected. Due to high flash temperature created at the asperity contacts during sliding, CrN interlayer reacts with nitrogen from environment and forms Cr_2N . As the wear process continues, nitrogen from Cr_2N phase is depleted by introduction of oxygen from ambient atmosphere and metastable CrON phase is formed. The nitrogen from CrON is further replaced by oxygen and form very stable Cr_2O_3 [194]. The presence of Cr_2O_3 peaks indicate that the oxidation mechanism is based on the gradual replacement of nitrogen with oxygen during sliding. Chromium from the coating provides additional source for formation of Cr_2O_3 through direct reaction with oxygen, which is promoted by the high flash temperatures generated at the asperity contacts during sliding.

The wear track depth is found smaller than the coating thickness, it is therefore expected that the iron oxides (Fe_2O_3 and Fe_3O_4) cannot originate from the HSS substrate, but from the uncoated steel ball used as a counterpart. The presence of metal oxides in the wear

track indicate *oxidative* wear mechanism during dry sliding. Based on the Raman analyses, the equation set 4 lists the possible chemical reactions during dry sliding of Cr/C coating.



Figure 4.2-18c shows the Raman spectrum collected from wear track after lubricated sliding. After deconvolution of the spectrum (see details of the deconvoluted peaks in table A-7 of appendix A), the D and G peak positions are found at 1382.63 cm^{-1} and 1573.26 cm^{-1} respectively. The I_D/I_G ratio is calculated as 2.269 indicating an increase in disorder of carbon-carbon bonds after sliding. The peak centred at $\sim 205\text{ cm}^{-1}$ is assigned to CrCl_3 , as the Raman peak of CrCl_3 is reported in the literature at $\sim 207.5 \pm 2\text{ cm}^{-1}$ [195]. Two wide peaks are appeared at two subsequent shoulders of the Raman spectrum centred at $\sim 349\text{ cm}^{-1}$ and $\sim 653\text{ cm}^{-1}$ respectively. It is believed that the peak centred at $\sim 349\text{ cm}^{-1}$ is formed is due to overlapping of Cr_2C , CrCl_3 , Cr_2S_3 , and FeS_2 peaks. Raman peaks of Cr_2C , CrCl_3 , and FeS_2 are reported in literature at $\sim 344\text{ cm}^{-1}$ [196] and $\sim 342 \pm 2\text{ cm}^{-1}$ [195] and $\sim 341\text{ cm}^{-1}$ [197] respectively. On the other hand, the peak centred at $\sim 653\text{ cm}^{-1}$ is formed due to overlapping of Cr_2C , Cr_2N , CrN and Cr_2S_3 peaks. From the literature, Raman peaks of Cr_2C are found at $\sim 544\text{ cm}^{-1}$, $\sim 601\text{ cm}^{-1}$ and $\sim 695\text{ cm}^{-1}$ [196], whereas Cr_2N and CrN have their respective Raman peaks at $\sim 586\text{ cm}^{-1}$, $\sim 667\text{ cm}^{-1}$ and $\sim 760\text{ cm}^{-1}$ [191] and $\sim 660\text{ cm}^{-1}$ [191]. Due to unavailability of data of the Raman peaks of Cr_2S_3 , spectrum was collected from pure Cr_2S_3 powder as shown in figure 4.2-19. The Cr_2S_3 peaks are observed at $\sim 301\text{ cm}^{-1}$, $\sim 341\text{ cm}^{-1}$, $\sim 536\text{ cm}^{-1}$ (most intense and sharp), $\sim 602\text{ cm}^{-1}$ and $\sim 1353\text{ cm}^{-1}$ respectively.

Similar to dry sliding case, CrN base layer is converted to Cr_2N due to slow nitrogen out-diffusion, but could not be able to form stable Cr_2O_3 due to absence of oxygen during lubricated sliding. On the other hand, presence of CrCl_3 , Cr_2S_3 and FeS_2 peaks in the spectrum indicates *tribo-chemically reactive* wear mechanism. Due to high flash temperature at the asperity contacts, the sulphide and chloride compounds of the engine oil chemically react with C and Cr of the coating and the uncoated steel ball during sliding and form compounds such as CrCl_3 , Cr_2S_3 and FeS_2 in the wear track. These compounds

adhere to the wear track forming a thin tribo-layer. Based on the Raman analyses, the equation set 5 lists the possible chemical reactions during the lubricated sliding of Cr/C coating.

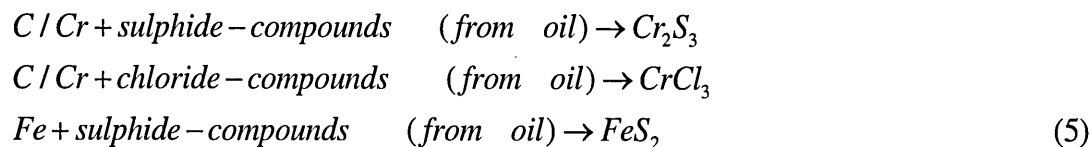


Figure 4.2-20a shows the atomic structure of $CrCl_3$, in which Cr^{+3} cations occupy two-third of the octahedral structure and Cl^- anions form a cubic closed packed structure around it resulting in a layered arrangement. The octahedral structures having Cr^{+3} cation at the centre and Cl^- anions placed at the edges (see inset of figure 4.2-20a) are bonded with each other by sharing the edges and form stacking of $CrCl_3$ layers. The absence of cohesive effect of Cr^{+3} cations makes these bonds (formed due to sharing of Cl^- anions) weak. This weak bonding between adjacent atomic layers helps the $CrCl_3$ atomic planes to easily slide over another indicating its lubricant nature [185]. Figure 4.2-20b shows the stacking of layers in the $CrCl_3$ crystal structure that promotes slipping during sliding. It is believed that this lubricious compound $CrCl_3$ is responsible for further reducing the friction coefficient during lubricated sliding and increased coating-life due to higher wear resistance. In addition, the hexagonal crystal structure of Cr_2S_3 does not promote any slipping between atomic planes like $CrCl_3$, thus Cr_2S_3 does not help in reducing friction. Hence, it could be concluded that the friction coefficient of Cr/C coating is reduced in boundary lubrication condition due to the formation of solid lubricant such as $CrCl_3$ via tribo-chemical reaction mechanism.

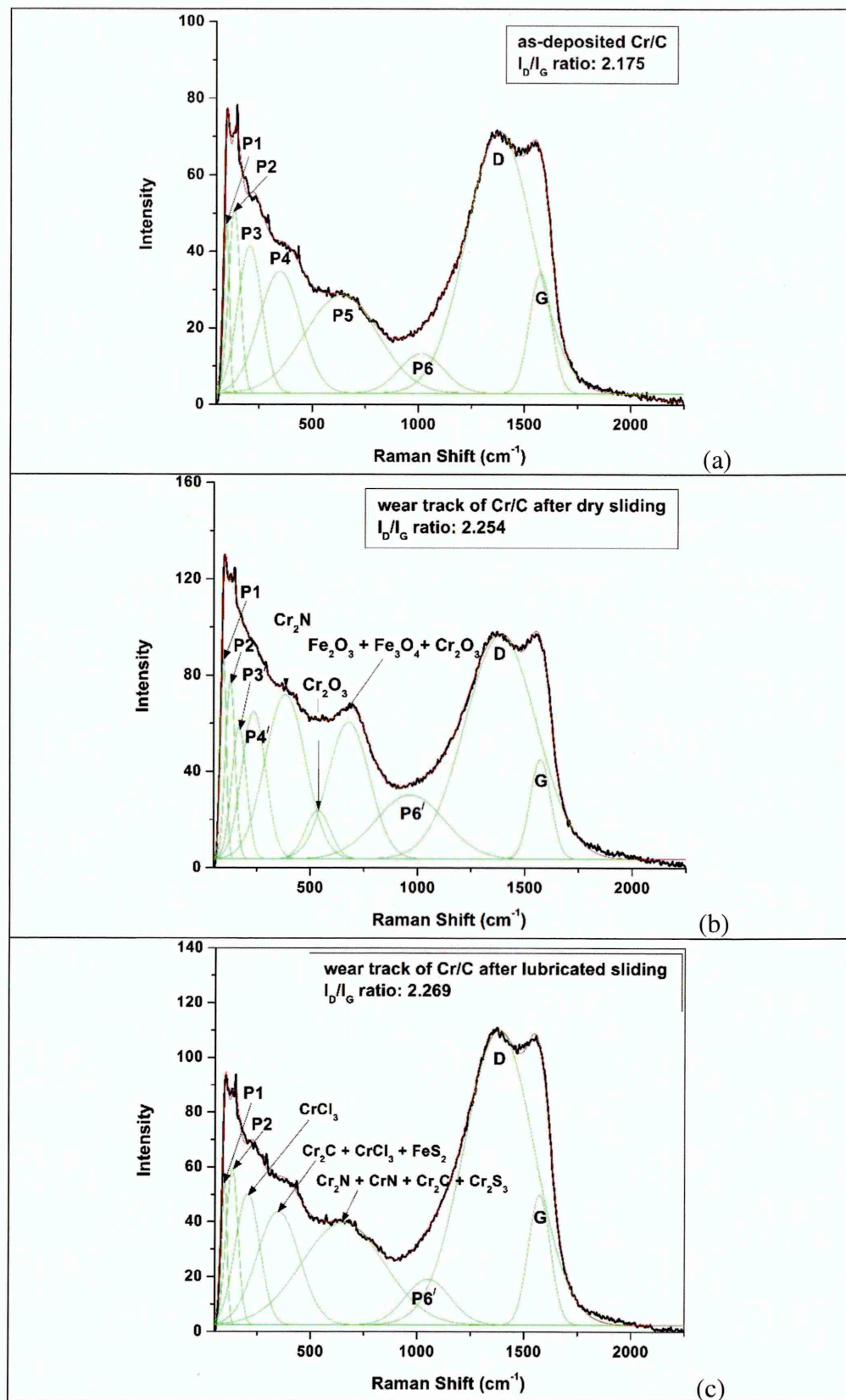


Figure 4.2-18: Raman spectra collected from the (a) as-deposited Cr/C coating and the wear track after (b) dry and (c) lubricated sliding against steel balls

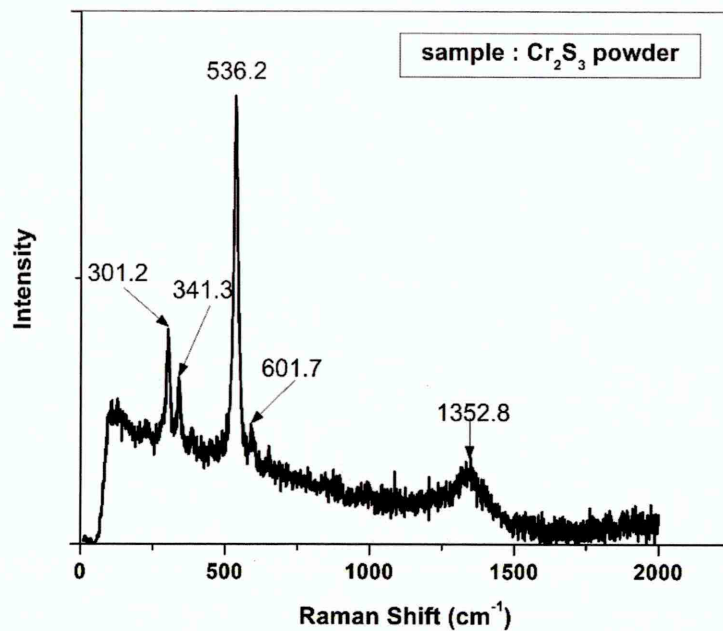


Figure 4.2-19: Raman spectrum collected from Cr_2S_3 powder sample

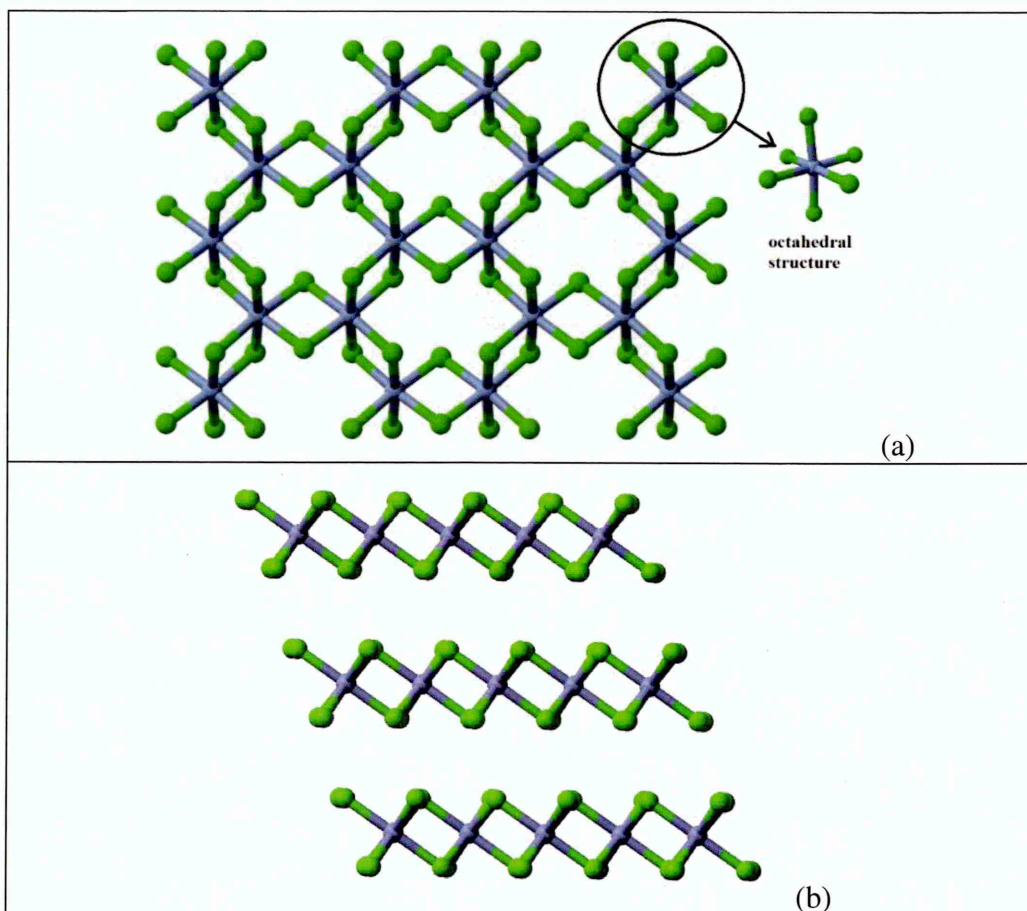


Figure 4.2-20: (a) Atomic structure of CrCl_3 [198] and (b) stacking of layers in CrCl_3 crystal structure [199]

III. Comparison of tribological performance of Cr/C and Mo–W–C coatings

Figure 4.2-21 shows the friction behaviour of Cr/C and Mo–W–C coatings during dry sliding at ambient temperature. The mean friction coefficients of C6 and Cr/C are found almost same (0.223 and 0.222 respectively), which are lower compared to the friction coefficients provided by C2 and C4 (0.335 and 0.333 respectively). Figure 4.2-22 shows the wear track profiles and the wear coefficients (inset) of Cr/C and Mo–W–C coatings after dry sliding. The wear coefficient of Cr/C coating is observed as $12.7 \times 10^{-16} \text{ m}^3 \text{ N}^{-1} \text{ m}^{-1}$ after 5 km of sliding, whereas Mo–W–C coatings provide wear coefficient in the range of $2.92 - 11.7 \times 10^{-16} \text{ m}^3 \text{ N}^{-1} \text{ m}^{-1}$ after 7.5 km of sliding. It should be noted that the sliding distance is less for Cr/C coating compared to Mo–W–C coatings, but it shows higher wear coefficient. Thus Mo–W–C coatings provide similar friction coefficient but better wear resistance than Cr/C coating.

Figure 4.2-23 shows the friction behaviour of Cr/C and Mo–W–C coatings in lubricated condition. The mean friction coefficient of Cr/C coating is found as 0.12, which is more than two times higher compared to that of Mo–W–C coatings ($\mu \sim 0.047, 0.033$ and 0.052 for C2, C4 and C6 respectively) in lubricated condition. This significant reduction in friction coefficients of Mo–W–C coatings is attributed to the formation of lubricious WS_2 due to tribo-chemical reactions occurred between Mo–W–C coatings and engine oil. On the other hand, mainly non-lubricious Cr_2S_3 and little amount lubricious CrCl_3 are formed during lubricated sliding of Cr/C coating. Thus friction coefficient of Cr/C coating is observed higher compared to Mo–W–C coatings. Further, the wear track profiles after lubricated sliding are shown in figure 4.2-24. Cr/C coating shows a large wear track with a wear coefficient of $9.62 \times 10^{-17} \text{ m}^3 \text{ N}^{-1} \text{ m}^{-1}$ after a sliding distance of 5 km, whereas almost negligible wear is observed for Mo–W–C coatings after a sliding distance of 7.5 km. Thus it is concluded that the combined doping of Mo and W into the carbon-based coating provides better tribological performance in boundary lubricated sliding condition compared to single Cr-doping.

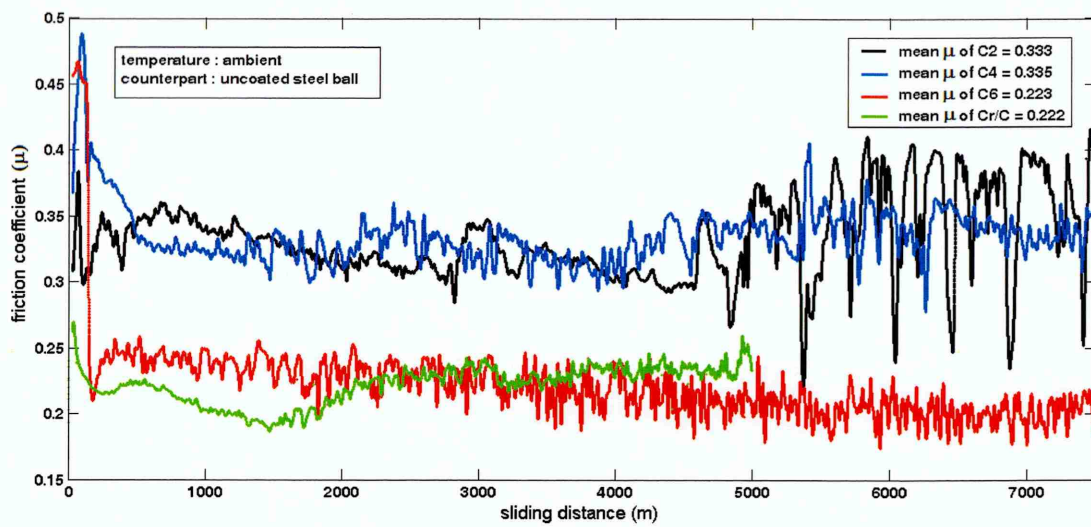


Figure 4.2-21: Friction behaviour of Cr/C and Mo-W-C coatings against steel balls

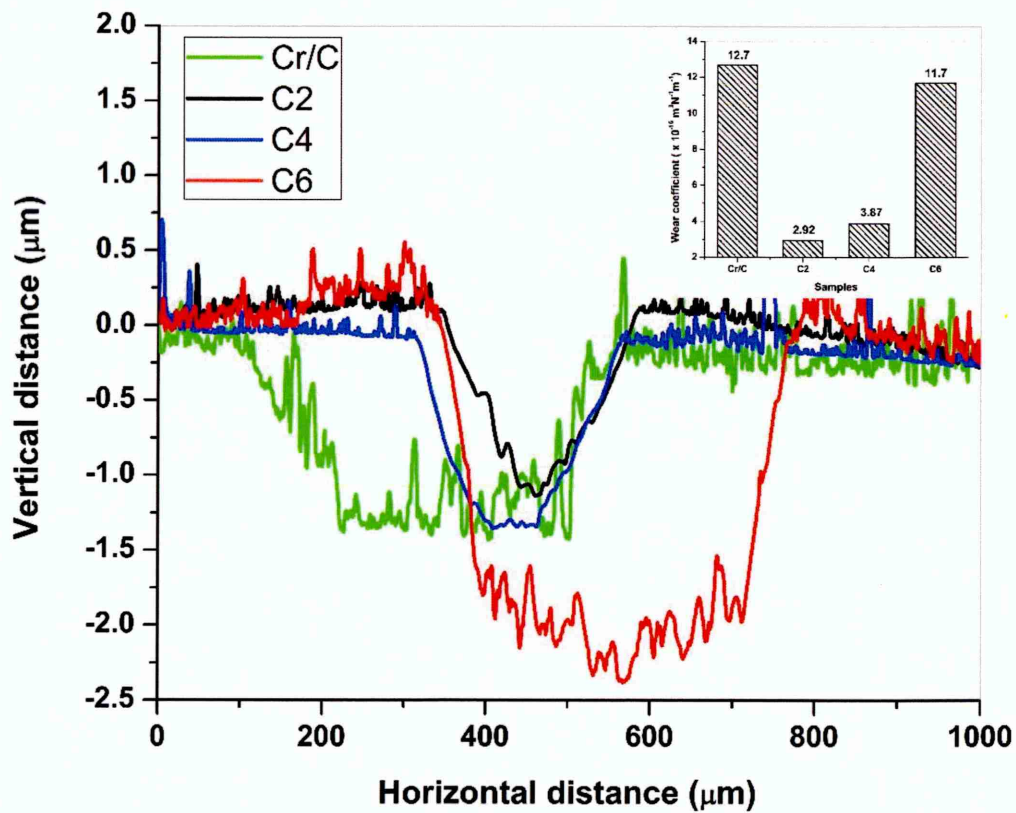


Figure 4.2-22: Wear track profiles and wear coefficients of Cr/C and Mo-W-C coatings after dry sliding against steel balls

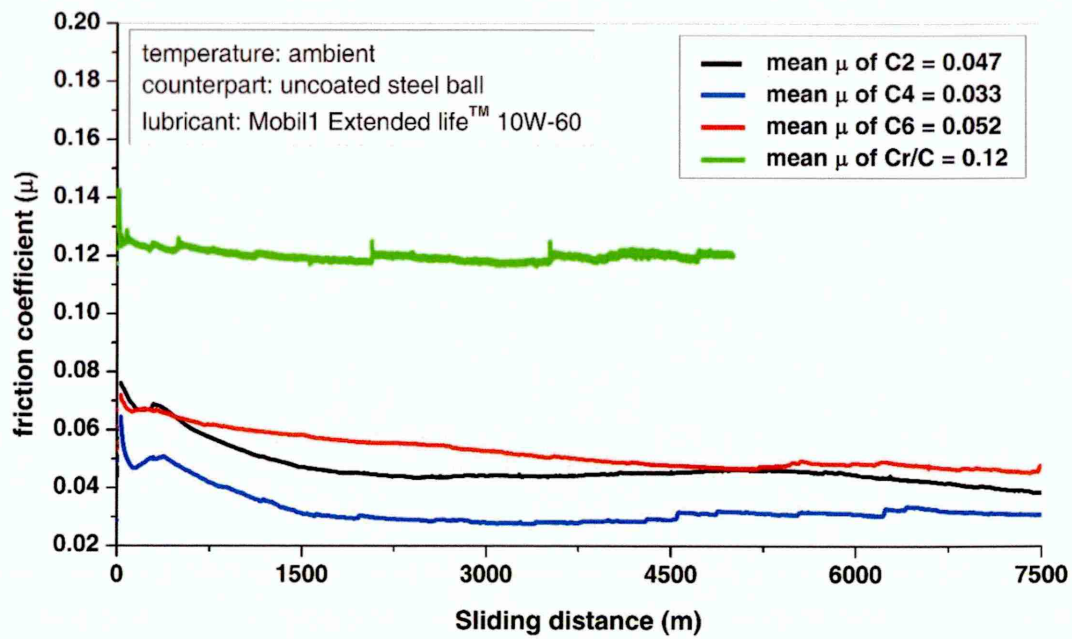


Figure 4.2-23: Friction behaviour of Cr/C and Mo-W-C coatings in lubricated condition against steel counterparts

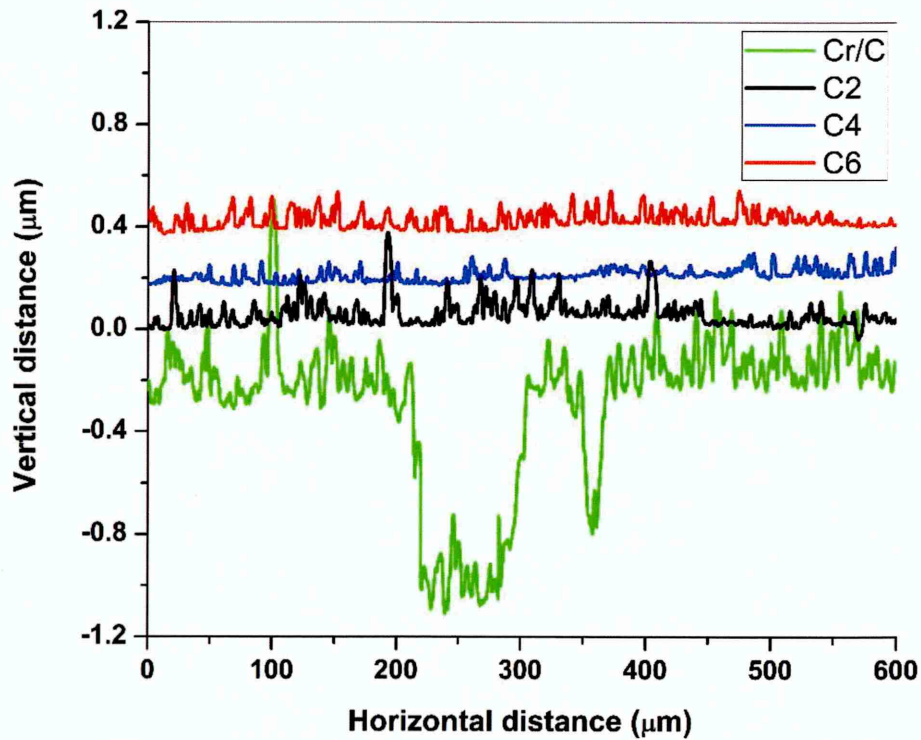


Figure 4.2-24: Wear track profiles of Cr/C and Mo-W-C coatings after lubricated sliding against steel balls

IV. Comparison of tribological performance of state-of-the-art DLC coatings and C4 at ambient temperature

A. Dry and lubricated sliding against 100Cr6 steel balls

Tribological performance of commercially available state-of-the-art DLC coatings is investigated during dry and lubricated sliding against steel balls under 5 N normal load. Figure 4.2-25 shows the friction behaviour of C4 and state-of-the-art DLC coatings against steel balls during dry sliding at ambient condition ($\sim 20^\circ\text{C}$ and $\sim 25\%$ relative humidity). The mean friction coefficients of C4 and state-of-the-art DLC coatings named *DLC-A*, *DLC-B*, *DLC-C* and *DLC-D* are found as ~ 0.335 , ~ 0.297 , ~ 0.23 , ~ 0.169 and ~ 0.224 respectively. Significant stick-slip motion is observed for C4 and *DLC-A* leading to higher friction coefficient compared to other coatings. Figure 4.2-26 shows the wear track profiles of DLC coatings and the images of respective tracks are provided in the inset. *DLC-A* shows $\sim 255.5\ \mu\text{m}$ wide wear track with lots of grooves in it. Comparatively smooth wear tracks are observed for other coatings, however the track width is found as $\sim 515.6\ \mu\text{m}$, $\sim 150.4\ \mu\text{m}$ and $\sim 430.3\ \mu\text{m}$ for coatings *DLC-B*, *DLC-C* and *DLC-D* respectively. The wear coefficients of all four DLC coatings are found in the order of $\sim 10^{-17}\ \text{m}^3\text{N}^{-1}\text{m}^{-1}$ after 7.5 km of dry sliding, which is extremely low. Alternatively, coating C4 shows a $\sim 264\ \mu\text{m}$ wide wear track and wear coefficient in the order of $\sim 10^{-16}\ \text{m}^3\text{N}^{-1}\text{m}^{-1}$ after same sliding distance. Thus state-of-the-art DLC coatings provide better tribological performance compared to C4 during dry sliding at ambient condition.

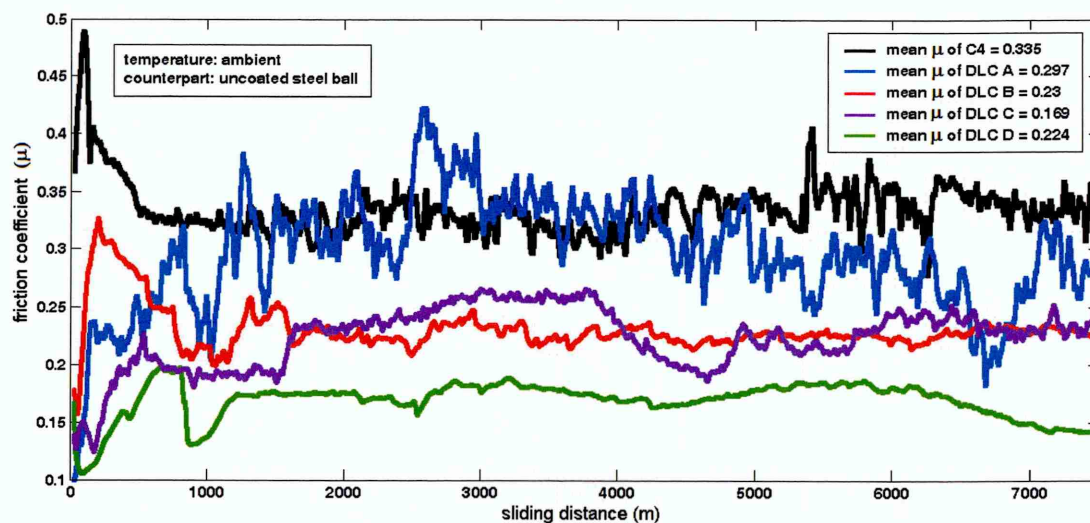


Figure 4.2-25: Friction behaviour of C4 and state-of-the-art DLC coatings

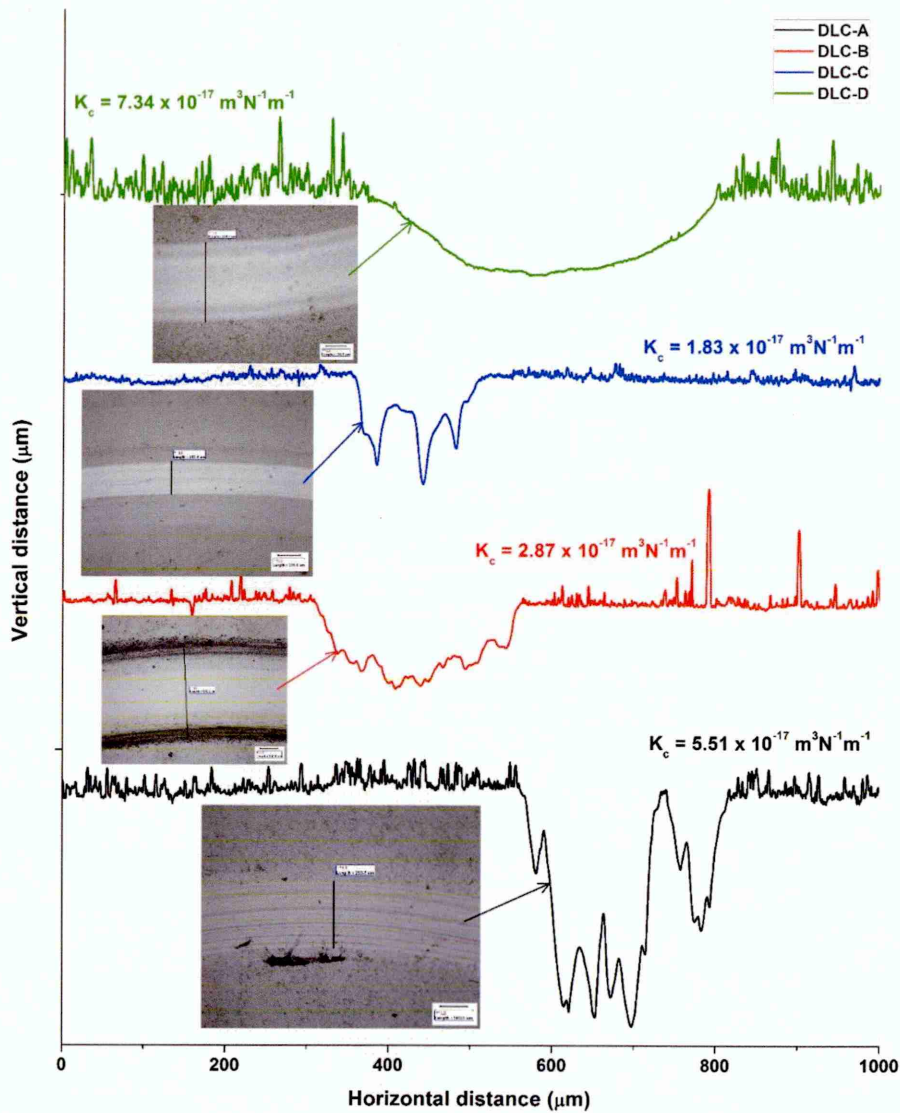


Figure 4.2-26: Wear track profile of state-of-the-art DLC coatings after dry sliding against steel balls

Figure 4.2-27 shows the friction behaviour of C4 and DLC coatings against steel ball during lubricated sliding ($\sim 25 - 30^{\circ}\text{C}$ and Mobil1 Extended lifeTM 10W-60 engine oil as lubricant). All the friction curves are observed very smooth throughout the sliding distance and the mean friction coefficients of C4, *DLC-A*, *DLC-B*, *DLC-C* and *DLC-D* are found as 0.033, 0.043, 0.07, 0.092 and 0.05 respectively. The lowest friction coefficient is provided by *DLC-A* compared to other DLC coatings, thus tribological performance of C4 is compared with *DLC-A*. The architecture of $\sim 3\ \mu\text{m}$ thick *DLC-A* coating consists of a thin Cr base layer, followed by a sputtered Cr-WC adhesion layer, a W:C-H intermediate layer and a PACVD deposited a:C-H layer on the top. Henceforth, *DLC-A* is expressed as *DLC*(Cr/Cr-WC/W:C-H/a:C-H). The hardness of this

coating (4389 HV) is found more than three times higher compared to C4 (1677.5 HV). Figure 4.2-28 shows the wear track profile of both coatings after lubricated sliding and the wear track images are provided in the inset. Negligible wear is observed for C4, whereas shallow wear track and a wear coefficient of $7.96 \times 10^{-19} \text{ m}^3 \text{N}^{-1} \text{m}^{-1}$ are observed for $\text{DLC}(\text{Cr}/\text{Cr}-\text{WC}/\text{W}: \text{C}-\text{H} / \text{a}: \text{C}-\text{H})$. Thus C4 provides better tribological performance compared to the state-of-the-art DLC coatings during lubricated sliding at ambient condition.

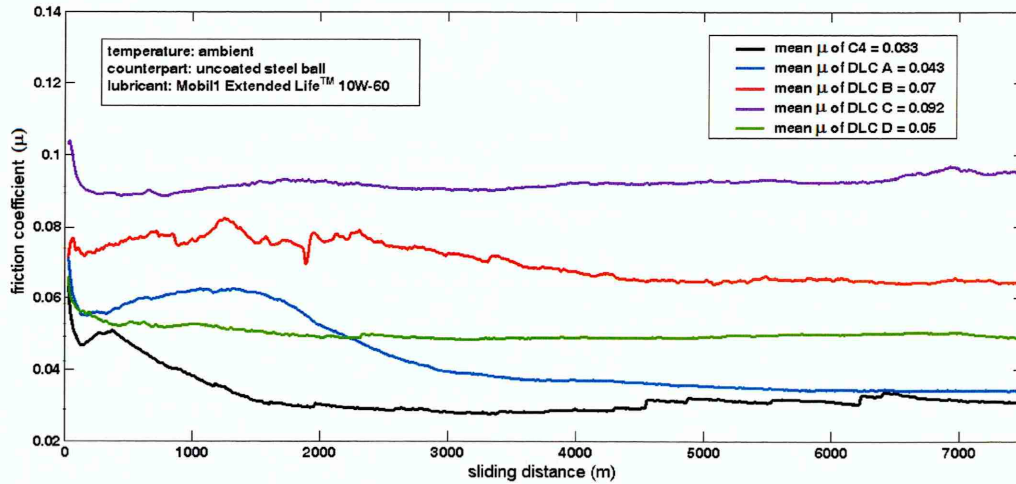


Figure 4.2-27: Friction behaviour of state-of-the-art DLC coatings and coating C4 against steel balls during lubricated sliding

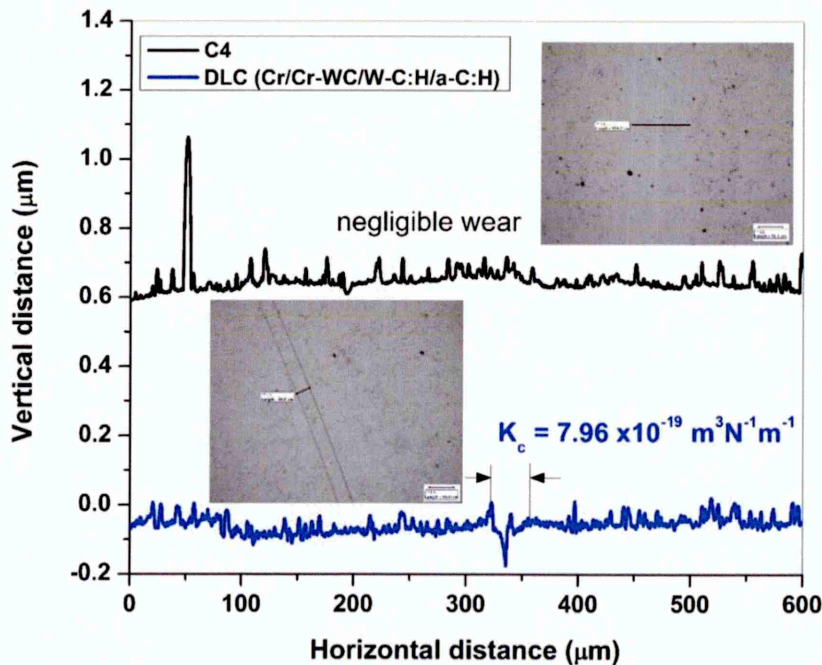


Figure 4.2-28: Wear track profiles of $\text{DLC}(\text{Cr}/\text{Cr}-\text{WC}/\text{W}: \text{C}-\text{H} / \text{a}: \text{C}-\text{H})$ and C4 against steel ball after lubricated sliding

The wear behaviour of $DLC(Cr/Cr-WC/W:C-H/a:C-H)$ coating after dry and lubricated sliding is investigated using Raman spectroscopy. Figure 4.2-29a shows the Raman spectrum collected from as-deposited DLC coating. The spectrum is dominated by G peak located at 1545.89 cm^{-1} because of its diamond-like structure and two separate disordered peaks (D1 and D2) are found at 1268.12 cm^{-1} and 1402.26 cm^{-1} . The I_D/I_G ratio is found as 0.59. After dry sliding, the spectrum is still dominated by G peak located at 1554.07 cm^{-1} , however the disordered peaks (D1 and D2) are shifted to the higher wavenumber at 1299.9 cm^{-1} and 1472.62 cm^{-1} respectively (figure 4.2-29b). The I_D/I_G ratio increases to 1.06. Further shift in the disordered (D1 and D2) and G peak positions are observed when Raman spectrum is collected from the wear track after lubricated sliding. The D1, D2 and G peaks are found at 1301.5 cm^{-1} , 1481.4 cm^{-1} and 1558.93 cm^{-1} respectively (figure 4.2-29c) and the I_D/I_G ratio further increases to 1.14. The increase in I_D/I_G ratio and the dispersion of G peak position towards higher wavenumbers indicate the transformation of coating's diamond-like structure into graphite-like structure due to continuous rubbing action in between sliding surfaces.

Figure 4.2-30 shows the Raman spectrum collected from the debris formed during dry sliding of $DLC(Cr/Cr-WC/W:C-H/a:C-H)$ coating. The spectrum contains dominant tungsten oxide (W_xO_y) peaks and hard amorphous carbon particles as indicated by the I_D/I_G ratio of 0.76. Therefore low friction and high wear resistance of DLC coating during dry sliding are mostly attributed to its very high hardness (4389 HV). In lubricated condition, the high hardness of DLC coating leads to further decrease in friction and wear coefficients.

On the other hand, oxidative wear mechanism of C4 forms lubricious MoO_3 during dry sliding (see figures 4.2-5b and 4.2-8b). The transfer layer containing MoO_3 and soft graphitic carbon particles reduces friction but cannot provide high wear resistance similar to DLC coating. The scenario completely changes during lubricated sliding when solid lubricant such as WS_2 is formed due to tribochemically reactive wear mechanism of C4. The transfer layer containing WS_2 leads to significant reduction in friction and improved wear resistance compared to DLC coating. Thus DLC coating provide better tribological performance during dry sliding, however C4 outperforms DLC during lubricated sliding at ambient temperature.

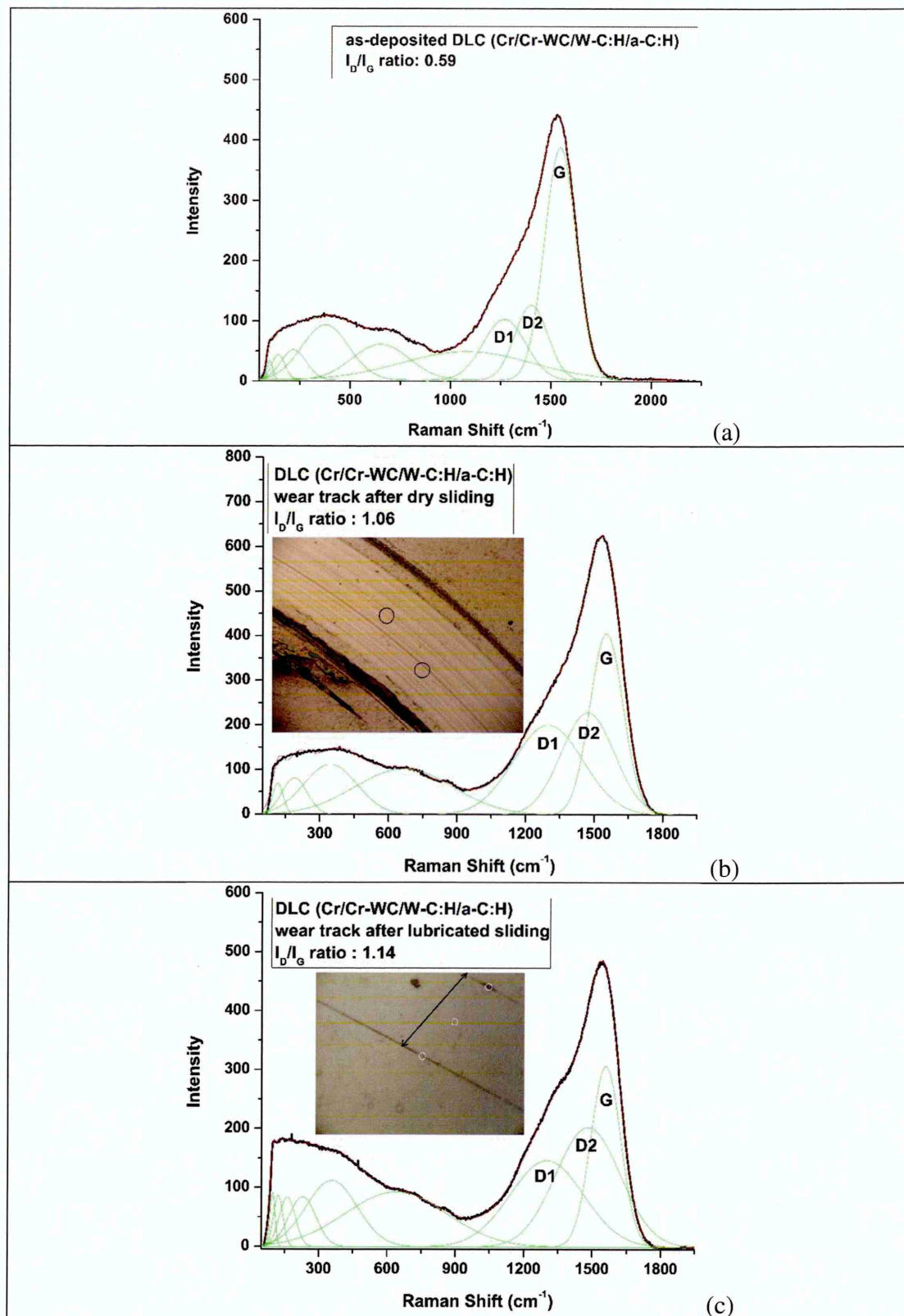


Figure 4.2-29: Raman spectra collected from the (a) as-deposited $\text{DLC}(\text{Cr}/\text{Cr}-\text{WC}/\text{W}-\text{C}-\text{H}/\text{a}-\text{C}-\text{H})$ coating and the wear track after (b) dry and (c) lubricated sliding against steel balls

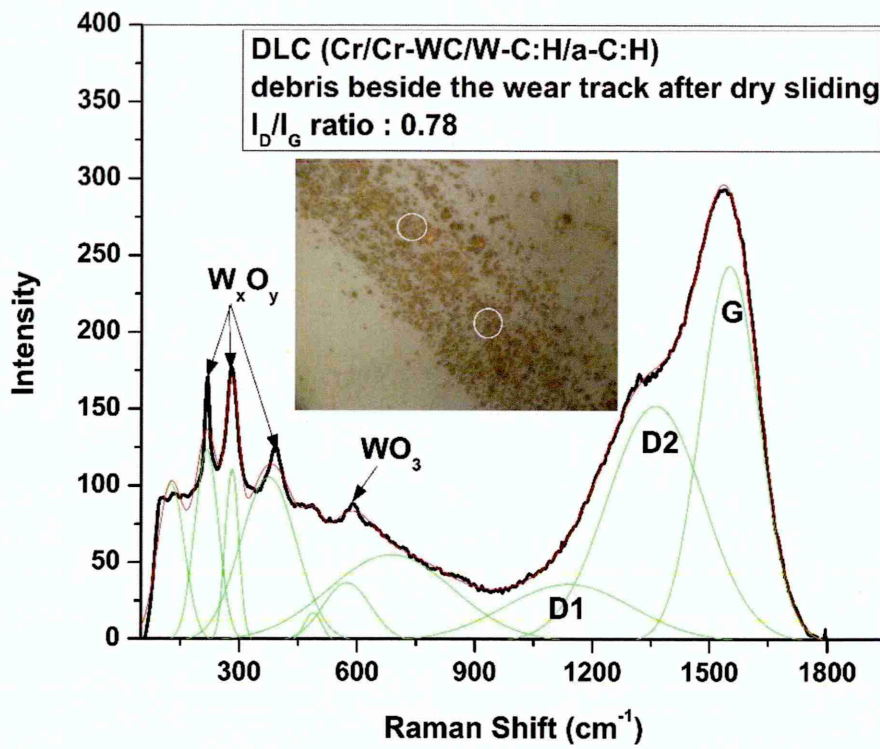


Figure 4.2-30: Raman spectrum collected from the debris beside the wear track of $DLC(Cr/Cr-WC/W-C-H/a-C-H)$ coating after dry sliding

B. Dry and lubricated sliding against Al_2O_3 balls

Tribological performance of C4 and $DLC(Cr/Cr-WC/W-C-H/a-C-H)$ coatings are further investigated against Al_2O_3 counterparts under 5 N normal load. Figure 4.2-31 shows the friction behaviour of both coatings during dry sliding ($\sim 25^\circ C$ and 30% relative humidity). The friction curve of DLC shows a short run-in period followed by a smooth steady-state period, whereas dominant stick-slip motion is observed in the friction curve of C4. Thus DLC shows lower friction coefficient (~ 0.146) compared to C4 (~ 0.235). The wear track profiles (see inset) indicate shallow wear track ($\sim 40 \mu m$ wide) of DLC after dry sliding, whereas $\sim 300 \mu m$ wide wear track with accumulated debris on its both sides is observed for C4. The wear coefficients are calculated as $5.91 \times 10^{-16} m^3 N^{-1} m^{-1}$ and $5.25 \times 10^{-17} m^3 N^{-1} m^{-1}$ for C4 and DLC respectively. Thus DLC coating provides better tribological performance during dry sliding compared to C4.

Figure 4.2-32 shows the friction curves of both coatings during lubricated sliding ($\sim 25^\circ\text{C}$ and engine oil used as lubricant). The friction curves are observed very smooth and mean friction coefficients are found as ~ 0.072 and ~ 0.079 for C4 and DLC respectively. Both coatings show negligible wear due to formation of shallow wear tracks (see inset for wear track profiles). It should be noted that the mean friction coefficient of C4 and DLC reduces to 69.4% and 45.9% respectively after addition of lubricant.

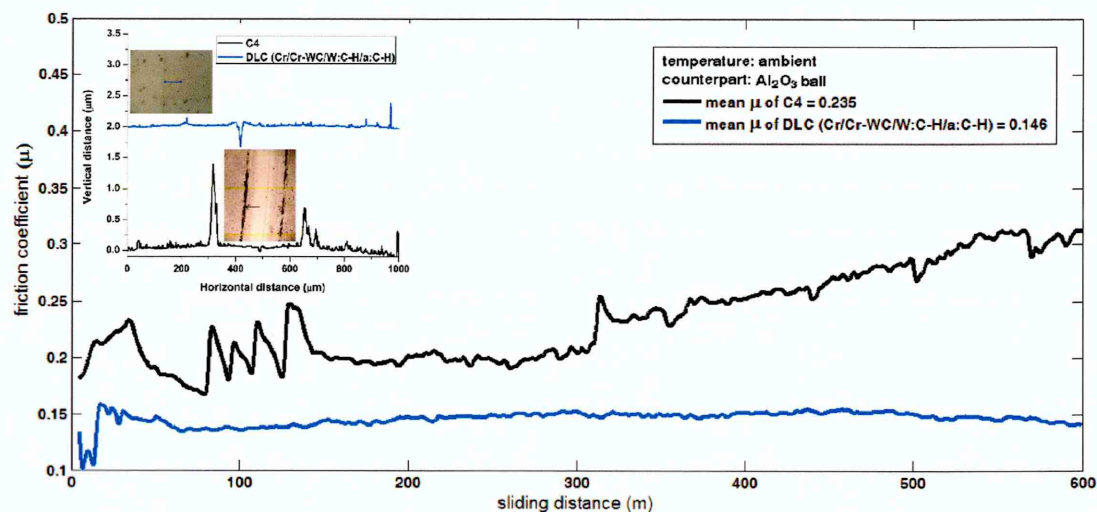


Figure 4.2-31: Friction behaviour and wear track profiles of C4 and $\text{DLC}(\text{Cr}/\text{Cr}-\text{WC}/\text{W}:\text{C}-\text{H}/\text{a}:\text{C}-\text{H})$ after dry sliding against Al_2O_3 balls

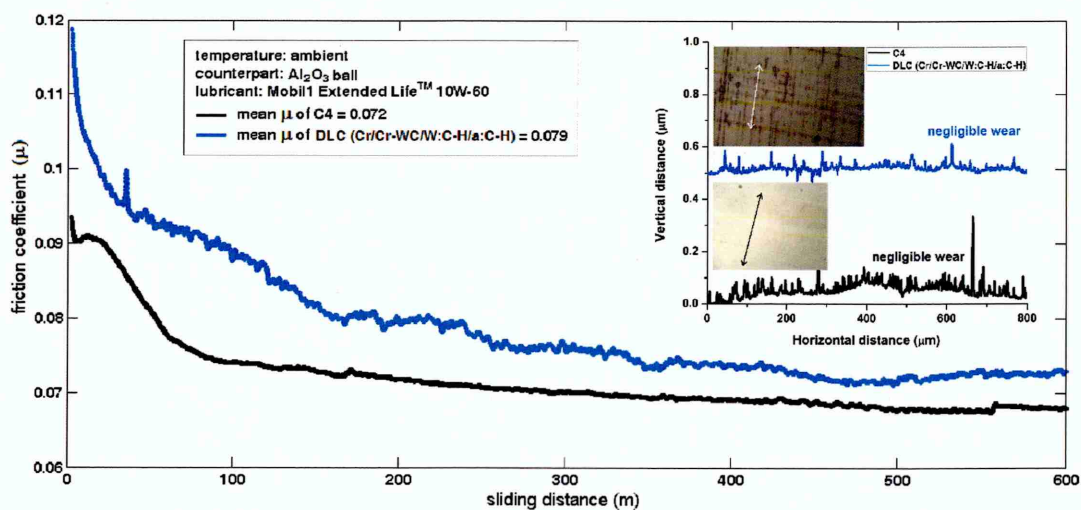


Figure 4.2-32: Friction behaviour and wear track profiles of C4 and $\text{DLC}(\text{Cr}/\text{Cr}-\text{WC}/\text{W}:\text{C}-\text{H}/\text{a}:\text{C}-\text{H})$ after lubricated sliding against Al_2O_3 balls

The wear behaviour of $DLC(Cr/Cr-WC/W:C-H/a:C-H)$ coating after dry and lubricated sliding is investigated using Raman spectroscopy. Figure 4.2-33a shows Raman spectrum collected from the wear track after dry sliding. Similar to as-deposited coating, two separate disordered peaks (D1 and D2) are found at 1306.19 cm^{-1} and 1453.45 cm^{-1} respectively, however G peak located at 1551.99 cm^{-1} dominates the spectrum because of its diamond-like structure. The I_D/I_G ratio slightly increases to 0.74. After lubricated sliding, the spectrum collected from the wear track is still dominated by G peak located at 1552.94 cm^{-1} , however the disordered peaks are slightly shifted to the higher wavenumber at 1315.49 cm^{-1} and 1471.5 cm^{-1} respectively (figure 4.2-33b). The I_D/I_G ratio increases to 0.84. Therefore almost no transformation of coating's diamond-like structure is observed after sliding due to short sliding distance (600 m). Thus it is concluded that low friction and wear coefficients of DLC coating are attributed to its diamond-like structure. On the other hand, C4 shows higher friction coefficient during dry sliding because of oxidative wear mechanism, whereas formation of WS_2 (see figure 4.2-16) during lubricated sliding provides lower friction coefficient compared to DLC. Thus C4 provides better tribological performance compared to DLC in lubricated condition.

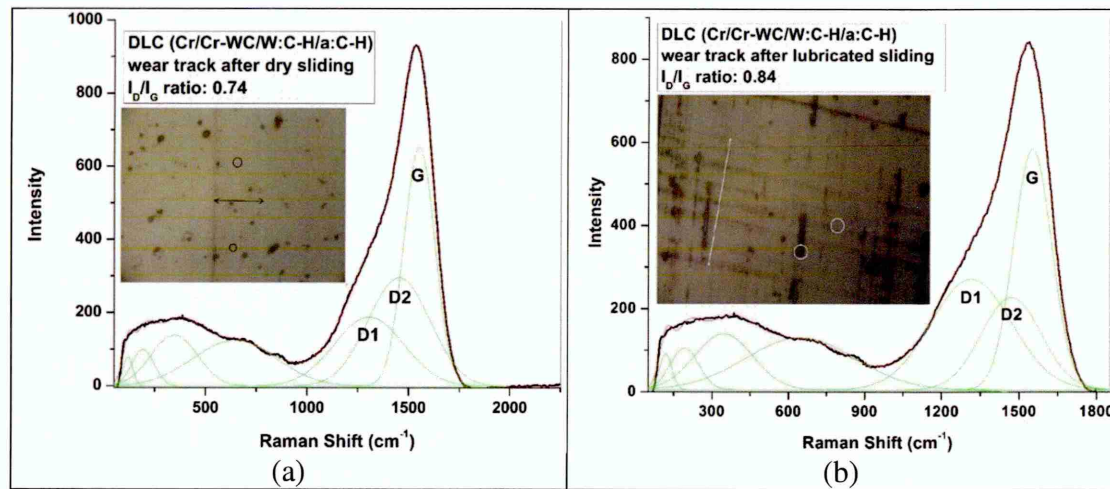


Figure 4.2-33: Raman spectra collected from the wear track of $DLC(Cr/Cr-WC/W:C-H/a:C-H)$ after (a) dry and (b) lubricated sliding against Al_2O_3 balls

4.2.5. Concluding remarks

The tribological properties of Mo–W–C coatings at ambient temperature are discussed in this chapter. Mo–W–C coatings show *oxidative* and *tribochemically reactive* wear mechanisms during dry and lubricated sliding conditions. They provide overall better tribological performance compared to Cr/C coating. Further in lubricated condition, Mo–W–C coatings are able to outperform commercially available state-of-the-art DLC coatings.

The friction behaviour of Mo–W–C coatings during dry sliding is strongly influenced by the third-body abrasive wear and the humid test environment. A transfer layer, composed of fine graphitic carbon particles and different metal oxides including principal metal oxides (WO_3 , MoO_2 , MoO_3 , Fe_2O_3 and Cr_2O_3) and Magnéli phase oxides (Mo_4O_{11} , Mo_5O_{14} , Mo_8O_{23} , $\text{W}_{18}\text{O}_{49}$ and $\text{W}_{20}\text{O}_{58}$) is formed during sliding. Among them, MoO_3 and Magnéli phase oxides act as solid lubricants due to their layered structure. These metal oxides and the graphitic carbon particles reduce the friction and wear coefficients in the range of 0.22 – 0.33 and $\sim 10^{-16} \text{ m}^3\text{N}^{-1}\text{m}^{-1}$ respectively indicating excellent wear resistance. However, extremely high hardness of state-of-the-art DLC coating leads to better tribological performance ($\mu \sim 0.17 - 0.3$ and $K_c \sim 10^{-17} \text{ m}^3\text{N}^{-1}\text{m}^{-1}$) during dry sliding.

In lubricated sliding, Mo–W–C coatings show extremely low friction ($\mu \sim 0.03 - 0.05$) and negligible wear due to *tribochemically reactive* wear mechanism. This significant decrease in friction coefficient and improved wear resistance are attributed to the formation of solid lubricants (such as WS_2) during sliding. WS_2 is the reaction product formed at the asperity contacts, where W comes from Mo–W–C coatings and S comes from EP additives present in the engine oil. Further it is observed that with increase in sliding distance, more amounts of solid lubricants are formed. Thus unlike dry sliding, Mo–W–C coatings provide better tribological performance compared to state-of-the-art DLC coating ($\mu \sim 0.04 - 0.09$ and $K_c \sim 10^{-19} \text{ m}^3\text{N}^{-1}\text{m}^{-1}$) during lubricated sliding.

4.3. Oxidation behaviour of Mo–W–C coatings

4.3.1. Introduction

The oxidation behaviour of Mo–W–C coatings during isothermal and dynamic heat-treatments are discussed in this chapter. Section 4.3.2 describes the experimental details including oxidation tests and characterisation techniques used for evaluation of oxidation behaviour. The change in coating microstructure and phase composition during isothermal and dynamic oxidation are describes in section 4.3.3 and 4.3.4 respectively. The performance of Mo–W–C coatings is further compared with $DLC(Cr/Cr-WC/W:C-H/a:C-H)$ coating as discussed in section 4.3.5. The oxidation behaviour of both the coatings was investigated using SEM, X-ray mapping, XRD, Raman spectroscopy and nanoindentation. The metal oxide growth during oxidation was clearly observed from SEM images and X-ray mapping analyses carried out on the top surfaces and cross-sections of the heat-treated samples. XRD and Raman spectroscopy were used to reveal the changes in phase composition during heat-treatment. Nanohardness was measured in order to understand the influence of oxide growth and phase changes on coating hardness during oxidation. Section 4.3.6 summarises the main observations of this study.

4.3.2. Experimental details

The Mo–W–C coated samples were heated in the furnace from room temperature to the pre-set temperatures ranging from 400°C – 800°C with a step of 100°C during isothermal oxidation tests. The samples were kept at pre-set temperature for 2 hours in order to achieve proper oxidation and then cooled slowly in air. The same heat-treatment was carried out for $DLC(Cr/Cr-WC/W:C-H/a:C-H)$ coated samples up to 500°C and no tests were continued at higher temperatures due to local delamination of the coating at 500°C. The thermo-gravimetric tests were carried out from 20°C to 1000°C at a heating rate of 1°C per minute to understand the dynamic oxidation behaviour of both the coatings. The total duration of the test was 18 hours including the cooling phase after reaching the maximum test temperature of to 1000°C.

The secondary electron detector was used for topographical imaging of oxidised surfaces and the X-ray mapping was carried out on the fractured cross-section of the heat-treated samples in order to identify the distribution of elements along the coating thickness. The changes in phase composition of oxidised samples were studied by XRD analyses using Bragg-Brentano and glancing angle geometry and Raman analyses. The spectra were collected from the oxidised surfaces with 120 s exposure time. The indentations on the oxidised samples were repeated for 20 – 30 times under 10 mN load and the nanohardness was calculated from the resultant load-displacement curves.

4.3.3. Isothermal oxidation behaviour of Mo–W–C coatings

I. Surface morphology and coating microstructure

Figure 4.3-1 shows the surface morphology of heat-treated Mo–W–C coatings. A significant change in surface morphology is observed due to development of metal carbide phases at 400°C (confirmed by XRD and Raman analyses discussed in sections II and III). A thin and dense metal oxide layer is formed at 500°C, which uniformly covers the coated surface. At 600°C, the oxide layer becomes thicker and significant metal oxide growth is observed at 700°C resulting in an irregular surface features. At 800°C, large islands of metal oxides are observed on the surfaces of C4 and C6 whereas separate metal oxide columns are formed on the surface of C2. The metal oxide growth and the surface finish of the oxidised samples vary depending on the metal content of Mo–W–C coatings.

Figure 4.3-2 shows the surface roughness of Mo–W–C coatings during isothermal heat-treatment. No significant change in average surface roughness (R_a) of the as-deposited coatings is found up to 600°C (see inset). Within thin temperature range, the R_a value is observed within the range of $\sim 0.03 - 0.12 \mu\text{m}$, however a sudden rise to $\sim 0.18 - 0.29 \mu\text{m}$ is observed at 700°C due to significant metal oxide growth, which is clearly observed in the SEM images (see figure 4.3-1). At 800°C, rapid oxidation occurs leading to further increase in R_a value due to the volume expansion of oxide phases. The R_a value is found lower for C2 and C4 ($\sim 0.53 \mu\text{m}$ and $\sim 0.36 \mu\text{m}$ respectively), however a drastic rise in R_a value to $\sim 1.33 \mu\text{m}$ is observed for C6 due to its highest metal content.

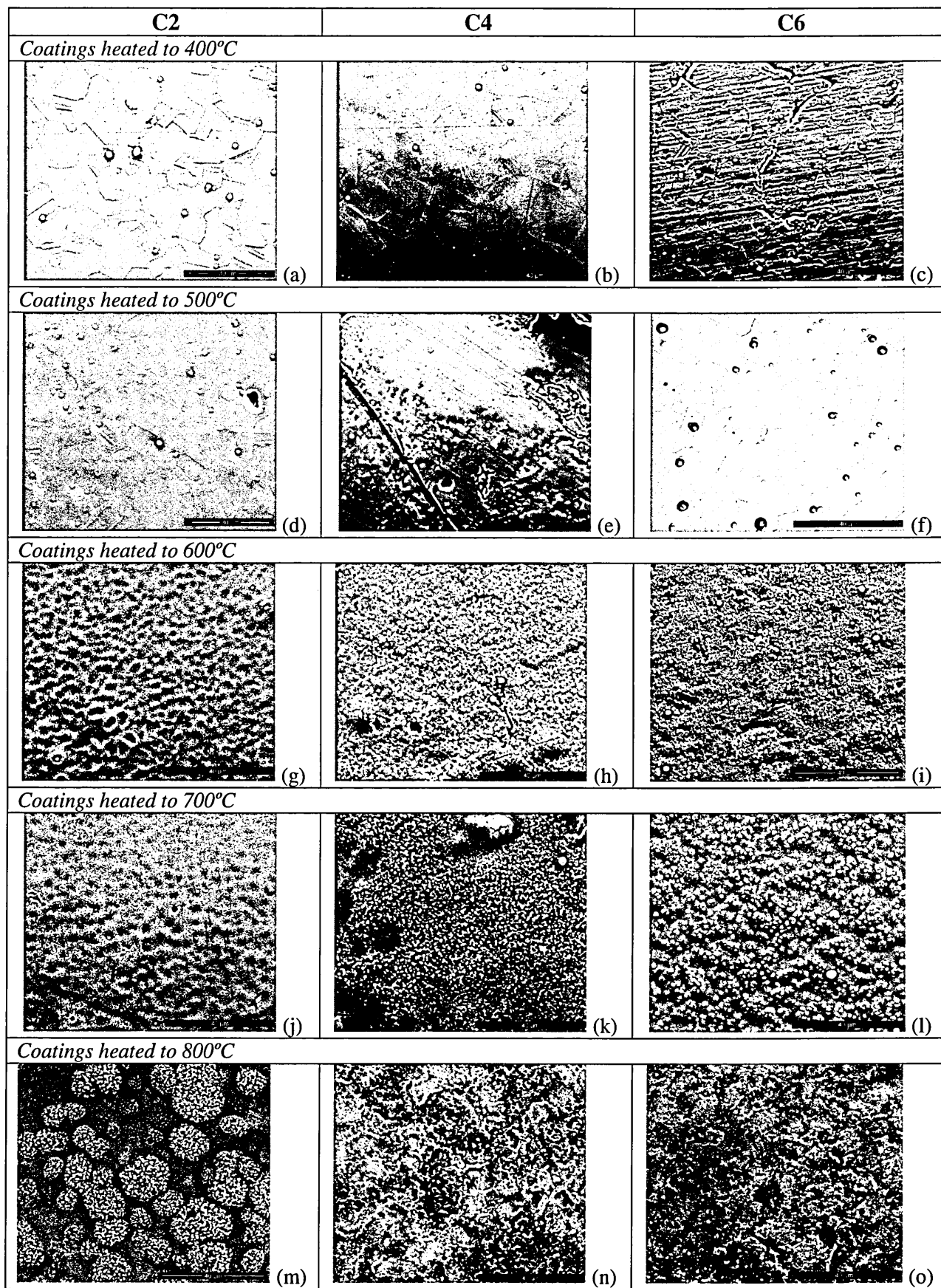


Figure 4.3-1: Surface morphology of heat-treated Mo-W-C coatings (400°C – 800°C)

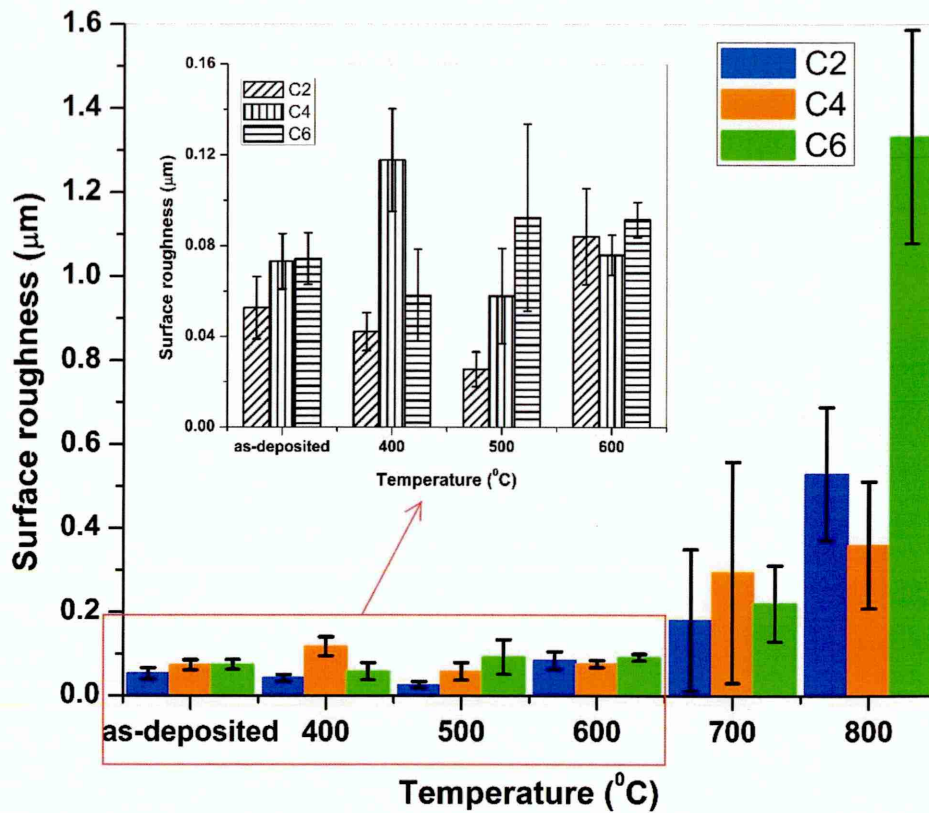


Figure 4.3-2: Average surface roughness of isothermally oxidised Mo-W-C coatings

For better understanding of the isothermal oxidation behaviour, the X-ray mapping was carried out on the cross-section of the heat-treated Mo-W-C coated samples. The X-ray maps clearly indicate the elemental distribution across the coating thickness. For example, figure 4.3-3 shows the X-ray mapping results carried out on the cross-section of heat-treated C4. The yellow outline on the SEM images indicates the cross-sectional area on which X-ray mapping is done.

Figure 4.3-3a shows the X-ray maps of C4 after heat-treated to 400°C. The as-deposited C4 is nanocrystalline and has dense columnar microstructure with a thickness of ~2.2 μm (see figure 4.1-1). The columnar microstructure becomes smooth after heat-treatment and no change in coating thickness (~2.2 μm) is observed. The as-deposited coating retains its elemental composition (Mo, W and C) at 400°C and no trace of oxygen is found in the coating. No outward diffusion of substrate elements (such as Cr and Fe) into the coating is observed indicating no effect of temperature on C4 at 400°C.

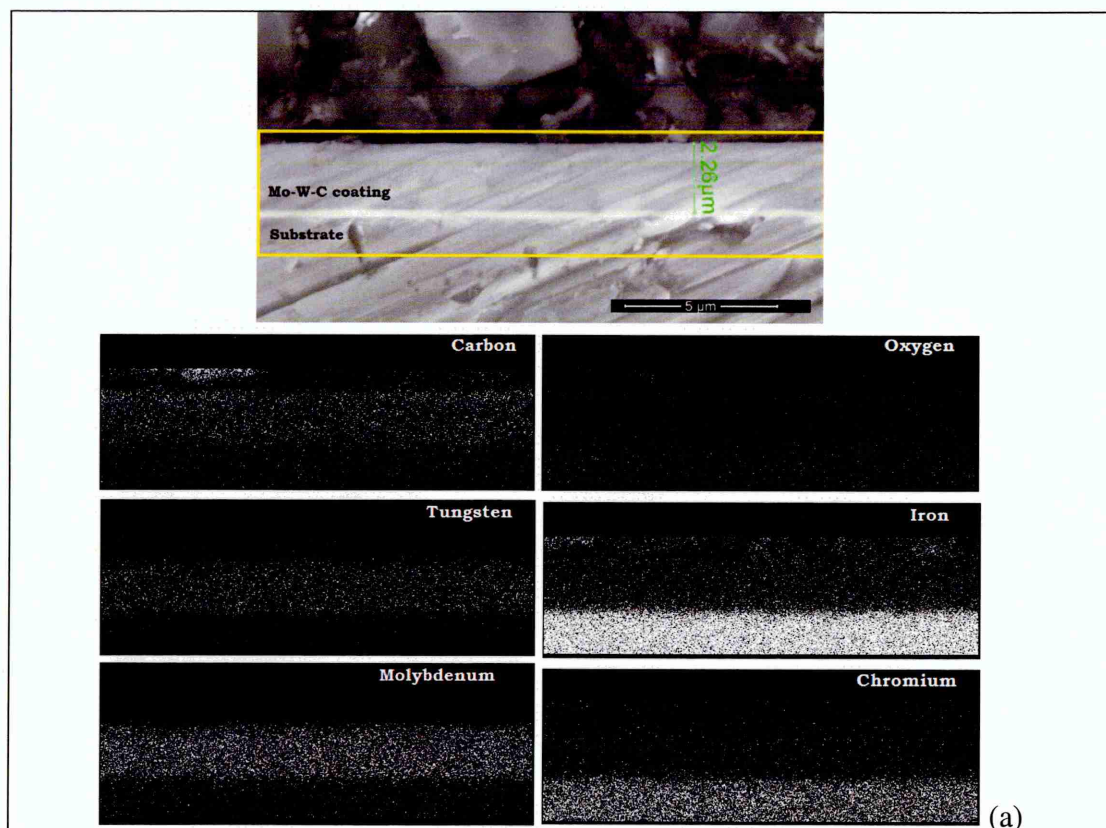
The SEM image in figure 4.3-1e indicates the formation of a thin and dense metal oxide layer on the surface of C4 at 500°C, which is supported by X-ray mapping (see figure 4.3-3b). The strong presence of Mo, W and C is observed along with a little amount of oxygen uniformly distributed within the coating material. An outward diffusion of Cr and Fe is also present at 500°C indicating this temperature can be considered as an onset of the coating oxidation. The coating thickness (~2 μm) is found almost unchanged, which indicates that the oxidation processes are still in their initial stages.

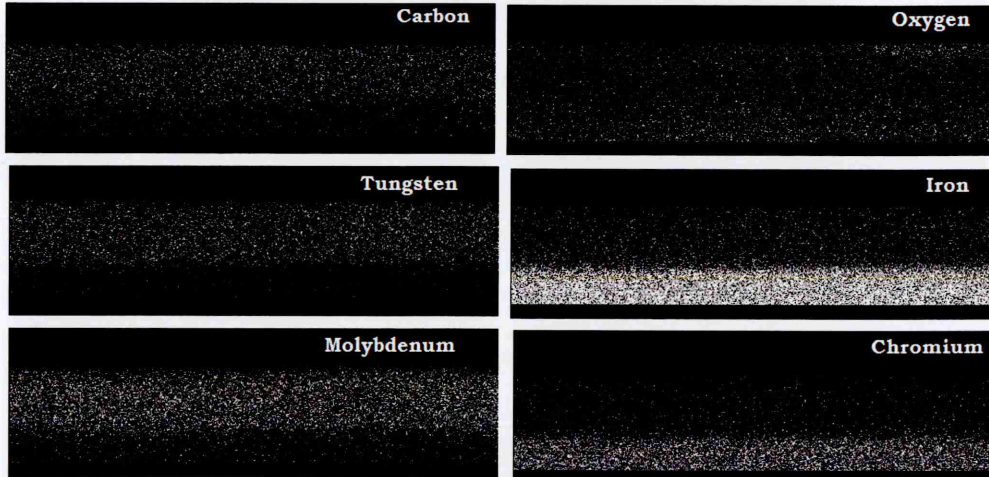
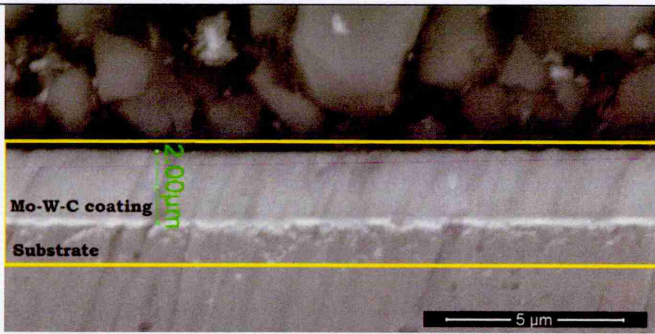
As indicated in the SEM image of figure 4.3-1h, the oxide layer becomes thicker at 600°C. The cross-section image in figure 4.3-3c reveals that the total oxide scale thickness is ~3.6 μm due to the volume expansion of the oxide material. The coating can be still observed as a thin (~500 nm) layer underneath of the metal oxide layer which indicates that the coating material has been almost fully consumed and converted to a mixed oxide scale. The X-ray maps further support these observations by showing significant presence of oxygen in the scale along with Mo and W. However, few metal carbide phases (tungsten and molybdenum carbides) are still retained inside the oxide scale as indicated by the carbon map. The outward diffusion of substrate elements like Cr and Fe into the oxide scale is clearly visible.

The metal oxide growth becomes significant at 700°C resulting in an irregular surface finish (see figure 4.3-1k). The X-ray mapping results in figure 4.3-3d show strong presence of W and oxygen in the metal oxide scale indicating formation of tungsten oxides. As reported in the literature, the molybdenum oxide (MoO_3) starts to evaporate after 600°C [200], thus the concentration of Mo is found significantly low at 700°C. A very thin carbon rich top layer is observed in the X-ray map which is attributed to the presence of a thin metal carbide layer on the top surface. Diffusion of substrate elements such as Cr and Fe into the coating is also observed, which leads to formation of iron and chromium oxides and possibly chromium carbide. The metal oxides are formed in two separate layers as indicated in the SEM image (see figure 4.3-3d) and therefore the total oxide scale thickness is increased to ~4.2 μm .

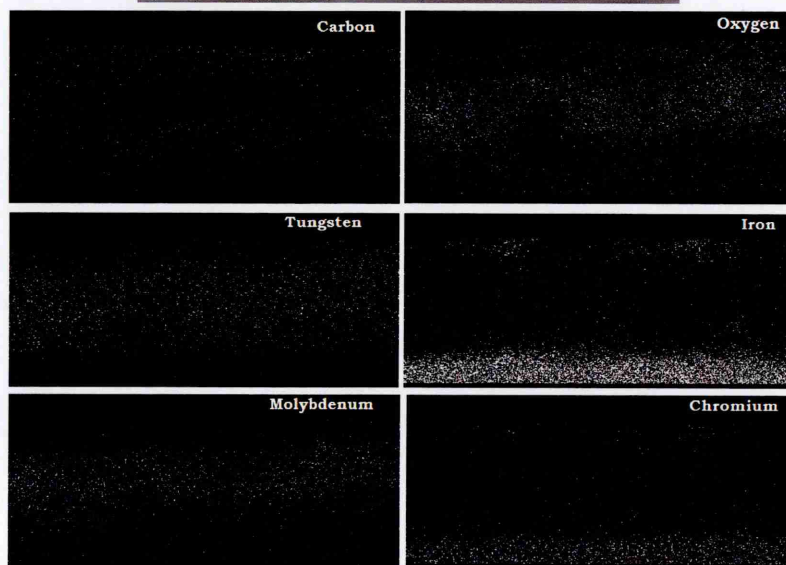
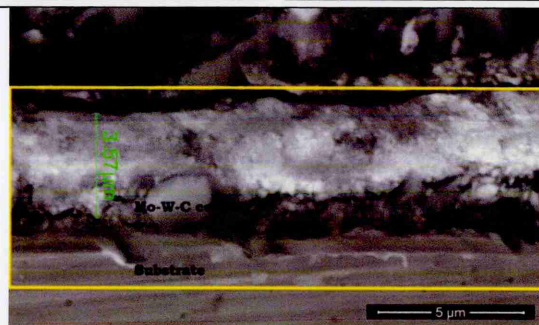
When heated to 800°C, large islands of metal oxides are observed on the surface as shown in figure 4.3-1n. This is further supported by the strong presence of oxygen in the X-ray map shown in figure 4.3-3e. At this temperature, Mo is almost depleted from the coating due to rapid evaporation of molybdenum oxides [200]. Moreover the onset of sublimation

of tungsten oxide is at 750°C [201], thus the top surface of the oxide scale becomes depleted of tungsten. Apart from compositional changes, the sublimation of both Mo and W based oxides at this high temperature (800°C) leads to a reduction of thickness of the oxide scale to ~3.3 μm . Despite the sublimation process however, the X-ray map clearly shows that the remaining oxide scale at predominantly consists of tungsten oxides. Similar to the 700°C case, Carbon has been mapped in a thin top layer where it exists in a form of carbide phases. Both W and Mo are known as a strong carbide forming elements which together with the Cr which is out-diffused from the substrate. While the tungsten and molybdenum oxides are volatile at 800°C, the top surface becomes richer to metal carbides. At this temperature the carbides itself will oxidise via gradual replacement of carbon atoms by oxygen atoms where the extent of oxidation will depend on the exposure time. In parallel, the outward diffusion of substrate elements continues to produce a mixture of iron and chromium oxides along with the tungsten and molybdenum oxides.





(b)



(c)

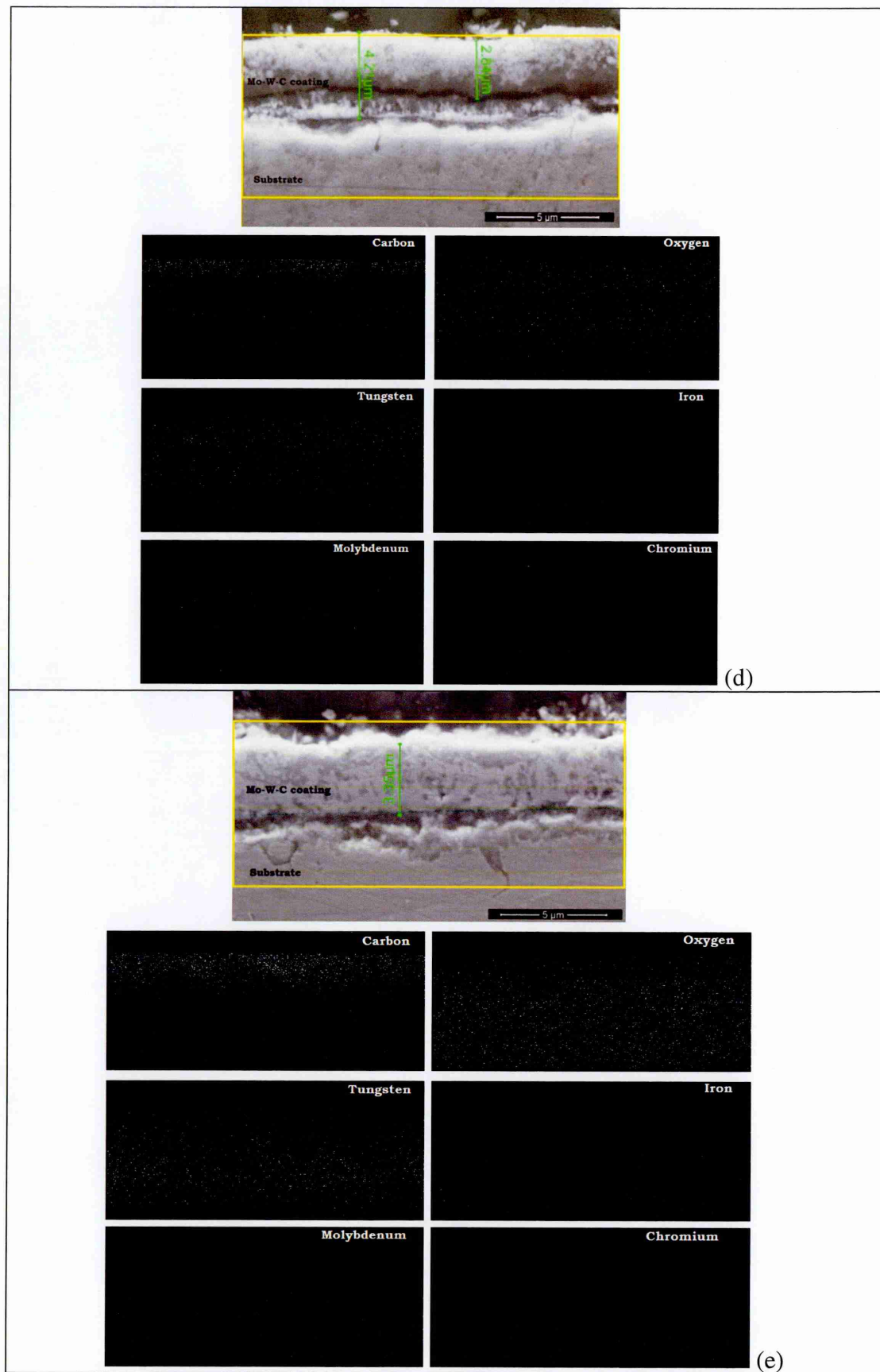


Figure 4.3-3: X-ray mapping on the cross-sections of C4 after heat-treated at (a) 400°C, (b) 500°C, (c) 600°C, (d) 700°C and (e) 800°C

II. Phase composition using X-ray diffraction

Figure 4.3-4 shows the XRD patterns collected using Bragg-Brentano geometry indicating change in phase composition of as-deposited Mo–W–C coatings after isothermal oxidation. The XRD patterns show that the as-deposited Mo–W–C coatings are consisted of a mixture of amorphous carbon and metal carbides (such as WC, W_2C , and Mo_2C). When heat-treated at 400°C, more metal carbide phases (W_2C and Mo_2C) are developed. No metal oxide phases are appeared in the XRD patterns indicating absolutely no oxidation occurs at 400°C. The metal carbide phases are retained up to 500°C; however small amount of metal oxides (such as WO_3 , W_5O_{14} and MoO_3) is also observed indicating that the 500°C temperature can be defined as onset of oxidation of Mo–W–C coating. Although diffusion of substrate elements such as Fe and Cr have been observed by X-ray mapping (see figure 4.3-3b) at 500°C, but no crystallographic phases based on these elements are detected by XRD analyses most probably due to their small amount.

A complete change in the shape of the XRD patterns is observed when Mo–W–C coatings are heat-treated in the temperature range of 600°C – 800°C. At 600°C, most of the metal carbide phases are transformed to different tungsten oxides (such as principal oxide WO_3 and intermediate oxides W_5O_{14} and $W_{18}O_{49}$) and molybdenum oxides (such as principal oxide MoO_3 and intermediate oxides Mo_9O_{26} and $Mo_{17}O_{47}$), which are indicated in the XRD patterns as W_xO_y and Mo_xO_y , respectively. Few tungsten carbide phases (WC and W_2C) are also observed in the XRD patterns forming a mixture with the oxide scale. Similarly to the 500°C case, no crystallographic phases based on substrate elements are detected by XRD analyses at 600°C.

The XRD patterns of Mo–W–C coatings exposed to 700°C show a decrease in Mo_xO_y peak intensities due to the sublimation of Mo_xO_y . No significant change in the intensities of W_xO_y peaks is observed indicating their stability at this temperature. Further significant out-diffusion and oxidation of substrate elements are observed at 700°C. The tungsten carbide phases (WC and W_2C) are still retained inside the oxide scale however, the intensity is reduced.

Upon exposure to 800°C, no W_xO_y and Mo_xO_y peaks in the 2θ range of $\sim 38^\circ$ and $44^\circ - 49^\circ$ are detected for C4 and C6 due to increased sublimation rate of the metal oxides. A

Figure 10 shows the XRD patterns of Coating C2 at various temperatures. The patterns are stacked vertically, showing the evolution of the crystalline structure. The x-axis represents the diffraction angle 2θ in degrees, ranging from 20 to 70. The y-axis represents Intensity. The legend indicates the following conditions:

- as-deposited (black line)
- 400°C (green line)
- 500°C (blue line)
- 600°C (red line)
- 700°C (orange line)
- 800°C (yellow line)

Key peaks are labeled with their corresponding phases and Miller indices:

- as-deposited:** WC, W_2C , Mo_2C , $SS [1\ 1\ 1]$, $SS [2\ 0\ 0]$, Mo_xO_y , W_xO_y , Cr_2O_3 .
- 400°C:** MoO_3 , WO_3 , Mo_xO_y , W_xO_y , WC , W_2C , Mo_2C , $SS [1\ 1\ 1]$, $SS [2\ 0\ 0]$, Mo_xO_y , W_xO_y , Cr_2O_3 .
- 500°C:** Mo_xO_y , W_xO_y , WC , W_2C , Mo_2C , $SS [1\ 1\ 1]$, $SS [2\ 0\ 0]$, Mo_xO_y , W_xO_y , Cr_2O_3 .
- 600°C:** Mo_xO_y , W_xO_y , WC , W_2C , Mo_2C , $SS [1\ 1\ 1]$, $SS [2\ 0\ 0]$, Mo_xO_y , W_xO_y , Cr_2O_3 .
- 700°C:** Mo_xO_y , W_xO_y , WC , W_2C , Mo_2C , $SS [1\ 1\ 1]$, $SS [2\ 0\ 0]$, Mo_xO_y , W_xO_y , Cr_2O_3 .
- 800°C:** Mo_xO_y , W_xO_y , WC , W_2C , Mo_2C , $SS [1\ 1\ 1]$, $SS [2\ 0\ 0]$, Mo_xO_y , W_xO_y , Cr_2O_3 .

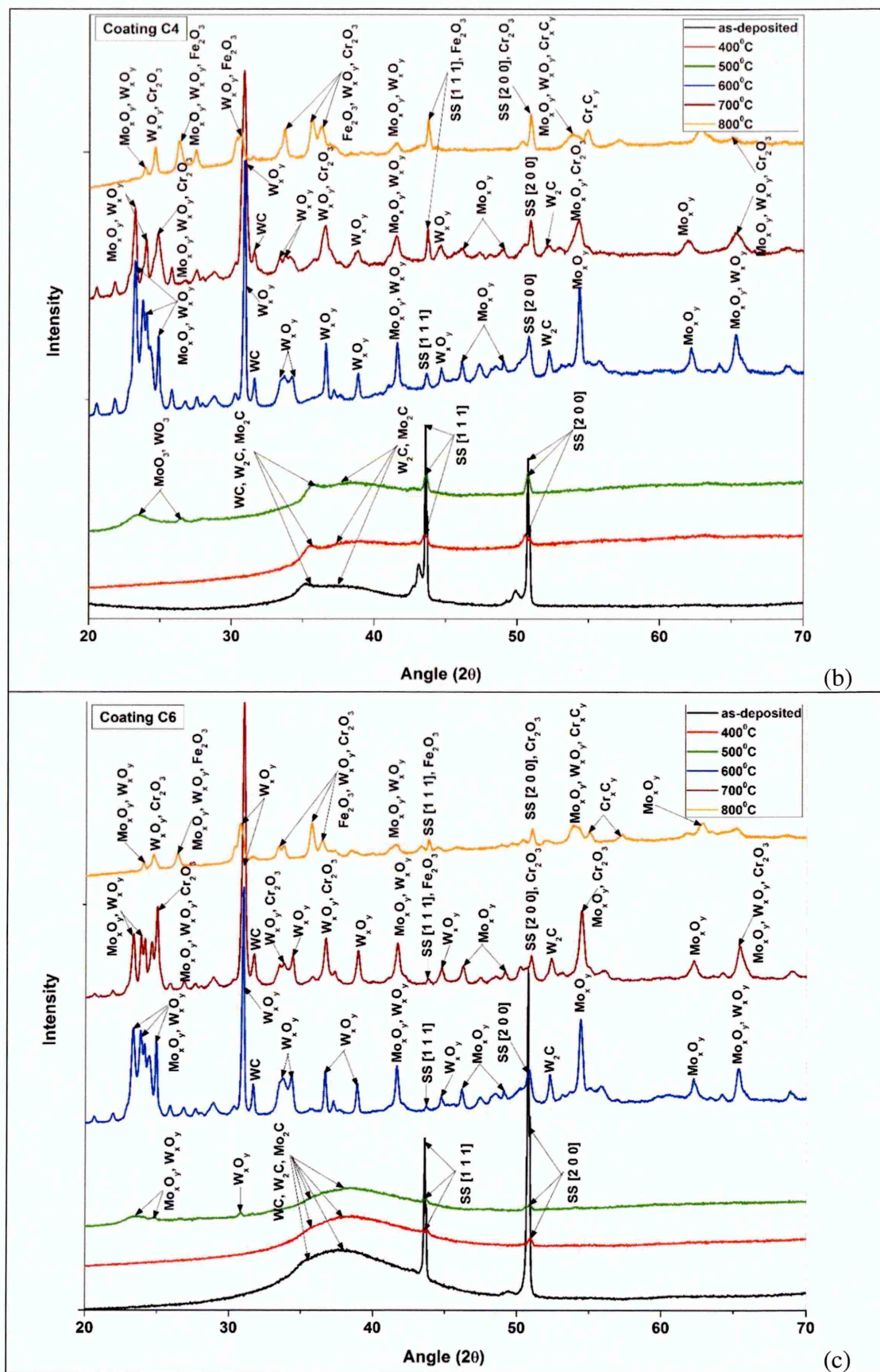


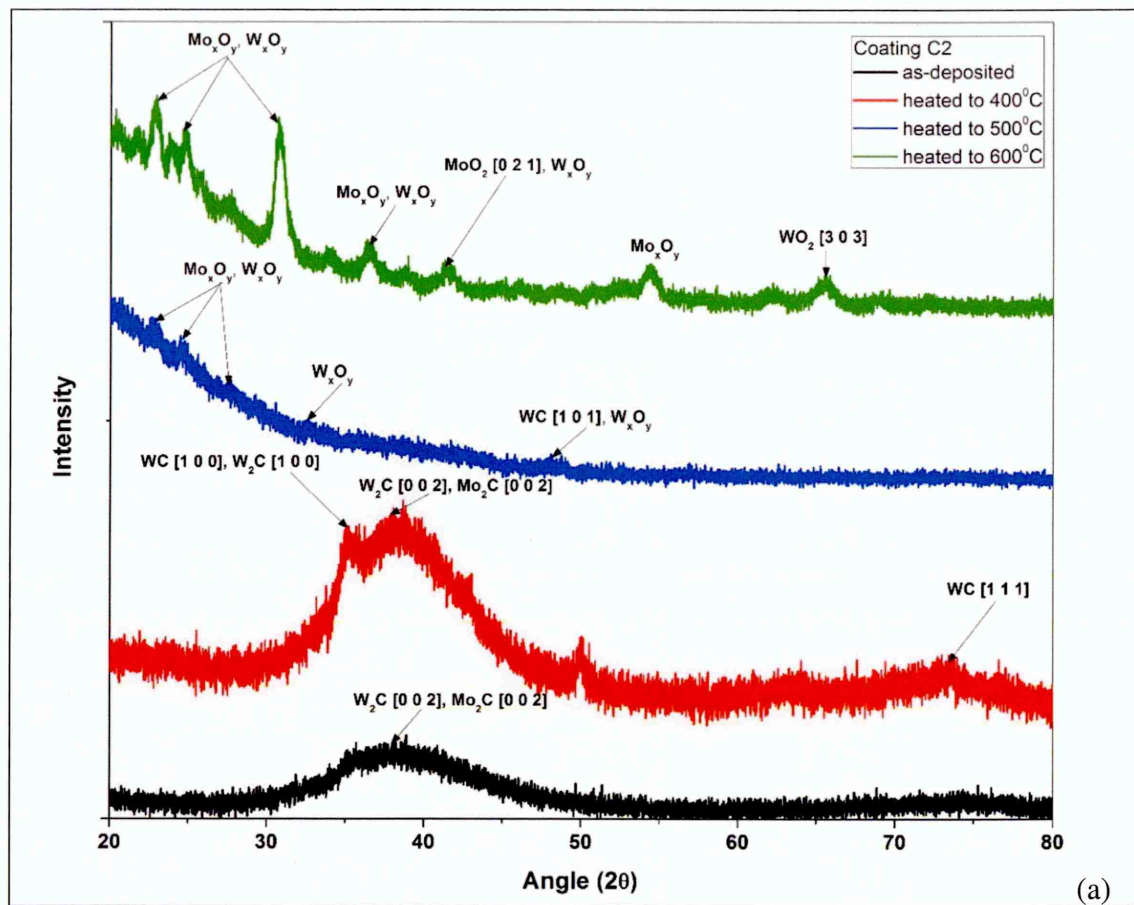
Figure 4.3-4: (a – c) XRD patterns of as-deposited and isothermally oxidised Mo–W–C coatings collected using Bragg-Brentano geometry

The XRD analyses using Bragg-Brentano geometry shows no oxidation of Mo–W–C coatings at 400°C, initiation of oxidation at 500°C but no exposure of substrate up to 600°C. For better understanding of the oxidation behaviour up to 600°C, the glancing angle XRD (GAXRD) was carried out to investigate the respective changes in coating composition during heat-treatment. Figure 4.3-5a shows the GAXRD patterns of C2 in as-deposited condition and after heat-treated at 400°C – 600°C. A broad peak within the range $\sim 35^\circ - 38^\circ$ is observed in the GAXRD pattern of as-deposited C2 indicating its nanocrystalline almost X-ray amorphous structure and the presence of hexagonal W_2C [002] and Mo_2C [002] phases. These phases are retained at 400°C and the peak intensity is significantly increased due to the formation of hexagonal WC [100], WC [111] and W_2C [100] phases. As a result, the nanocrystalline structure of as-deposited coating is transformed into crystalline structure at 400°C and a significant change in surface morphology is observed (see figure 4.3-1a). No metal oxide phases are found in the GAXRD pattern at 400°C indicating absolutely no oxidation of C2. A complete change in the shape of the GAXRD pattern at 500°C shows formation of metal oxides. A hexagonal WC [101] peak still exists but rest of the metal carbides react with oxygen at 500°C and form an oxide layer containing W_xO_y and Mo_xO_y . At 600°C, the peak intensities of mixed oxide scale (W_xO_y and Mo_xO_y) are significantly increased due to further oxidation, however no iron and chromium oxides are found indicating the substrate remains unexposed at 600°C. These findings support the results obtained from XRD patterns collected using Bragg-Brentano geometry (see figure 4.3-4a).

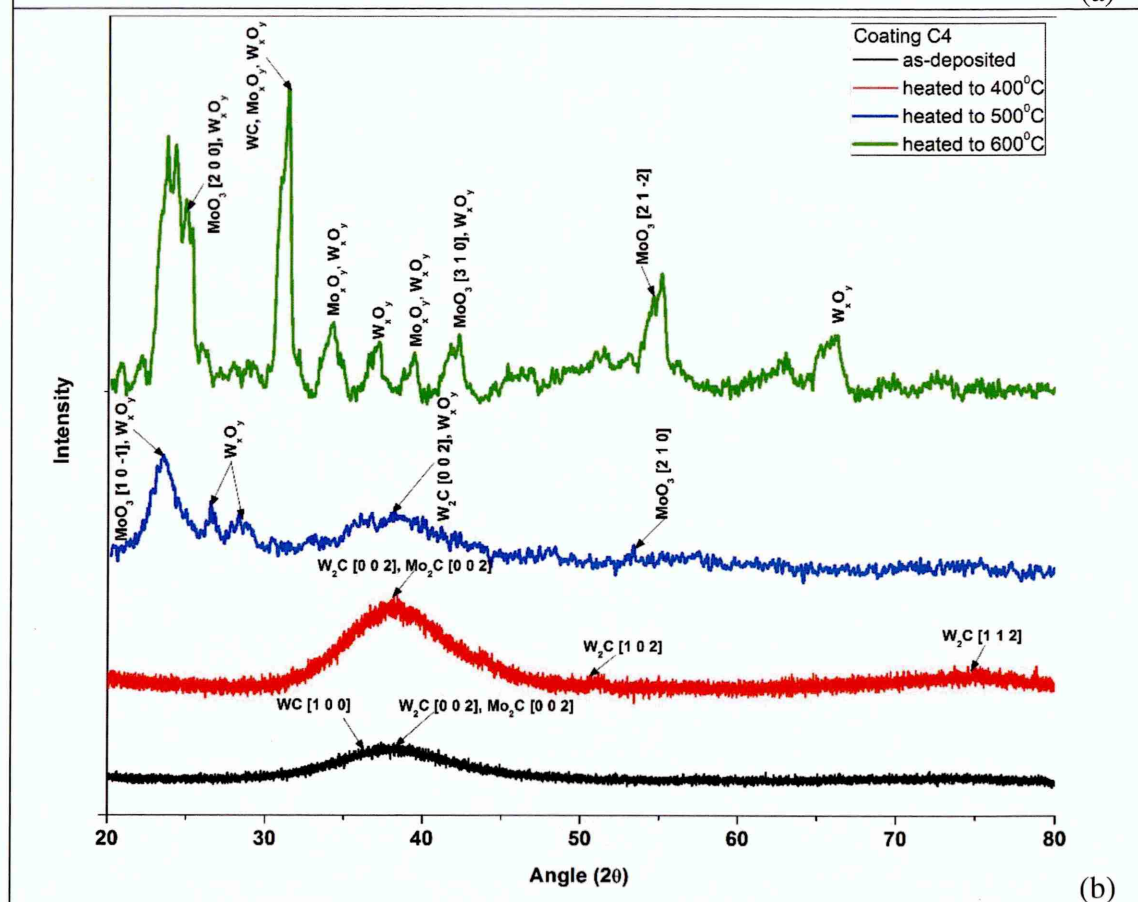
Figure 4.3-5b shows the GAXRD patterns of as-deposited C4 and after heat-treatment. Similar to C2, a single broad peak is observed in the GAXRD pattern of as-deposited C4 indicating its nanocrystalline almost X-ray amorphous structure and the presence of hexagonal WC [100], W_2C [002] and Mo_2C [002] phases. When heated to 400°C, the W_2C [002] and Mo_2C [002] phases are retained and the peak intensity is significantly increased due to the formation of more metal carbide phases. Two new peaks are appeared indicating the presence of hexagonal W_2C [102] and W_2C [112] phases. The nanocrystalline structure of as-deposited C4 is transformed into crystalline structure at 400°C, which significantly changes the surface morphology of the heat-treated coating (see figure 4.3-1b). Absolutely no oxidation occurs for C4 at 400°C as indicated by the absence of metal oxide phases in the GAXRD pattern. When heated to 500°C, the hexagonal W_2C [002] phase is retained however the peak intensity is rapidly decreased.

The rest of the metal carbides react with oxygen at 500°C and form an oxide layer containing MoO_3 and W_xO_y . A complete change in the GAXRD pattern shape is observed at 600°C as the coating is converted to a mixed oxide scale (W_xO_y and Mo_xO_y). However the WC [001] phase is still retained inside the mixed oxide scale (W_xO_y and Mo_xO_y) as appeared in the pattern at $\sim 31.5^\circ$. No iron and chromium oxides are found in the GAXRD pattern confirming that the substrate is not exposed at 600°C. These findings support the results obtained from X-ray mapping (see figure 4.3-3) and XRD patterns collected using Bragg-Brentano geometry (see figure 4.3-4b).

Figure 4.3-5c shows the GAXRD patterns of as-deposited C6 and after heat-treatment (400°C – 600°C). The broad peak, as observed in as-deposited C2 and C4, is found wider ($\sim 34.5^\circ - 38^\circ$) for C6 and consists of a mixture of hexagonal W_2C [100], W_2C [002] and Mo_2C [002] phases. These phases are retained up to 400°C, and the peak intensity is significantly increased due to the formation of more metal carbide phases. A hexagonal WC [111] peak is appeared in the GAXRD pattern but no metal oxide phases are observed indicating absolutely no oxidation occurs for C6 at 400°C. The presence of these metal carbide phases transforms the nanocrystalline structure of as-deposited C6 into crystalline structure at 400°C (see figure 4.3-1c). At 500°C, the hexagonal W_2C [002], Mo_2C [002] and WC [101] phases are retained, however the peak intensity is rapidly decreased due to formation of the oxide layer containing W_xO_y and Mo_xO_y . A complete change in the GAXRD pattern shape is observed at 600°C due to the formation of a mixed oxide scale (W_xO_y and Mo_xO_y), however the substrate remains unexposed. Though WC phase is observed at 600°C in the XRD pattern collected using Bragg-Brentano geometry (see figure 4.3-4c) but its absence in GAXRD pattern indicates that the WC phase is probably retained inside the mixed oxide scale.



(a)



(b)

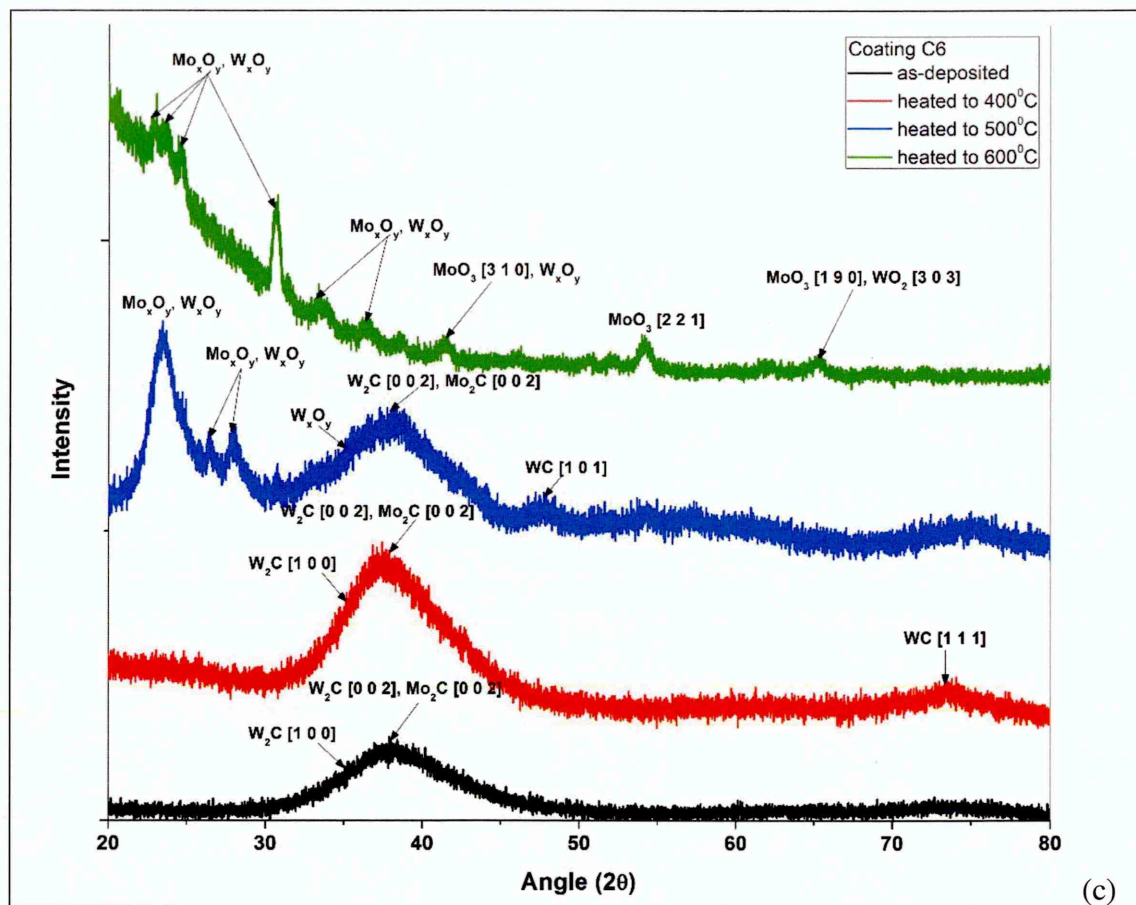


Figure 4.3-5: (a – c) Glancing angle XRD patterns of as-deposited and isothermally oxidised (400°C – 600°C) Mo–W–C coatings

III. Phase composition using Raman spectroscopy

Figures 4.3-6 – 4.3-8 show the Raman spectra collected from the as-deposited and isothermally oxidised Mo–W–C coatings. The as-deposited coatings contain disordered and sp^2 bonded graphitic carbon peaks (D and G peak respectively) and presence of Mo_2C peaks is observed for C2 and C4 only. More details on the Raman analyses of as-deposited Mo–W–C coatings has been described in chapter 4.1. The I_D/I_G ratio of as-deposited C2, C4 and C6 is found as 2.51, 1.96 and 1.85 respectively. When heated to 400°C, all the peaks of as-deposited coatings are retained and a strong WC peak is developed at $\sim 960\text{ cm}^{-1}$ (see figures 4.3-6a, 4.3-7a and 4.3-8a). This completely agrees with the findings of XRD patterns that the metal carbide phases are developed at 400°C (see figures 4.3-4 and 4.3-5). The development of metal carbide phases decreases the amount of free carbon

present in the as-deposited coatings. Thus the I_D/I_G ratio slightly decreases to 2.05, 1.64 and 1.81 for C2, C4 and C6 respectively at 400°C indicating the decrease in disordering of carbon-carbon bonds in the coating.

As the temperature increases to 500°C, the graphitic carbon peaks are retained along with few metal carbide phases and rest of the phases are oxidised indicating initial oxidation of Mo–W–C coatings (see figures 4.3-6a, 4.3-7a and 4.3-8a). After deconvolution of the spectra, the WC and Mo₂C peaks are found along with W_xO_y and Mo_xO_y peaks. W_xO_y indicates the presence of WO₃, W₁₈O₄₉ and W₂₀O₅₈ phases, whereas Mo_xO_y indicates the presence of MoO₃, Mo₄O₁₁, Mo₅O₁₄ and Mo₈O₂₃ phases. The formation of the metal oxide layer on the surface prevents depletion of free carbon from the coatings. As a result, the I_D/I_G ratio rises to 2.4 and 2.56 for C4 and C6 respectively establishing coating's graphitic nature at 500°C. This increase in I_D/I_G ratio from 400°C to 500°C indicates increase in the disordering of carbon-carbon bonds in the coating due to heat-treatment. This is further supported by the upshifting of G peak position of as-deposited C4 and C6 (1574.32 cm⁻¹ and 1579.37 cm⁻¹ respectively) after heat-treated to 400°C (1589.38 cm⁻¹ and 1591.52 cm⁻¹ respectively) and 500°C (1586.63 cm⁻¹ and 1590.18 cm⁻¹ respectively). On the other hand, C2 contains more amount of carbon compared to other coatings, thus the depletion of carbon is higher when heated to 500°C. The formation of metal oxide layer on the surface of C2 prevents further depletion of carbon and thus the I_D/I_G ratio slightly decreases to 1.91. Similar to C4 and C6, the graphitic nature of C2 is retained up to 500°C.

At 600°C, a complete change in the shape of the spectra is observed due to further oxidation of Mo–W–C coatings. The D and G peaks are completely disappeared for C4 and C6 indicating loss of their graphitic nature (figures 4.3-7b and 4.3-8b). On the other hand, graphitic nature of C2 is still retained as indicated by the further decrease in I_D/I_G ratio to 1.22 due to depletion of carbon (see figure 4.3-6b). The WC peak is retained and various tungsten oxides (W_xO_y) and molybdenum oxides (Mo_xO_y) peaks are appeared in the spectrum. The absence of metal oxide peaks from the substrate confirms no substrate exposure at 600°C.

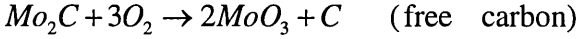
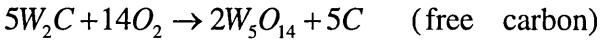
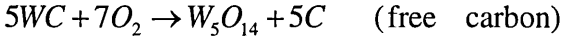
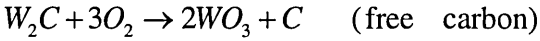
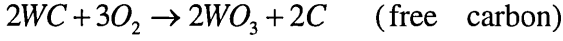
Figures 4.3-6b, 4.3-7b and 4.3-8b show that the evaporation of Mo_xO_y decreases the respective peak intensities at 700°C and the presence of Fe₂O₃ and CrO₂ peaks confirms the substrate exposure. This further supports the findings of X-ray mapping and XRD analyses. Only C2 retains its graphitic nature at 700°C (I_D/I_G ratio is found as 1.2) but at

the same time, presence of Cr_2C peak is observed. At 800°C , both W_xO_y and Mo_xO_y are vaporised leading to a significant decrease in the respective peak intensities; thus the spectra are magnified by 10 – 15 times during plotting for better visualisation. The presence of Fe_2O_3 , Cr_2O_3 , CrO_2 and Cr_2C peaks in the spectrum indicates severe oxidation of substrate at 800°C . The WC peak is only observed in the spectrum of C4 up to 800°C , however its intensity is significantly decreased with rise in temperature.

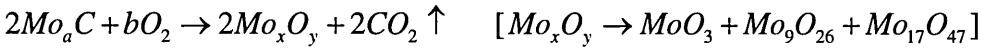
The Mo–W–C coatings show similar Raman peaks when isothermally oxidised to a particular temperature. Hence, the deconvoluted peaks of the Raman spectra collected from heat-treated C4 (400°C – 800°C) are listed tables A-8 – A-12 (see appendix A) for example. Further, based on the results obtained from the XRD and Raman analyses, the possible reactions occurred during isothermal oxidation of Mo–W–C coatings are listed in the equation set (6).

- 400°C: Development of metal carbide phases and NO oxidation of Mo – W – C coatings

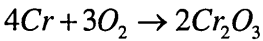
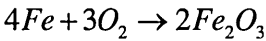
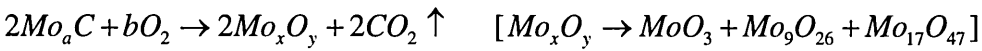
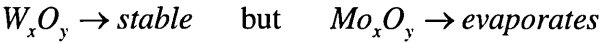
- 500°C: Onset of oxidation



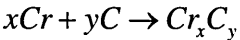
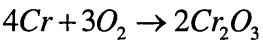
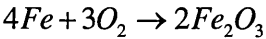
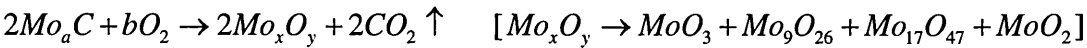
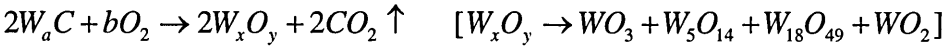
- 600°C: Oxidation continues



- 700°C : Oxidation continues and exposure of substrate



- 800°C : Severe oxidation of both the coating and the substrate



(6)

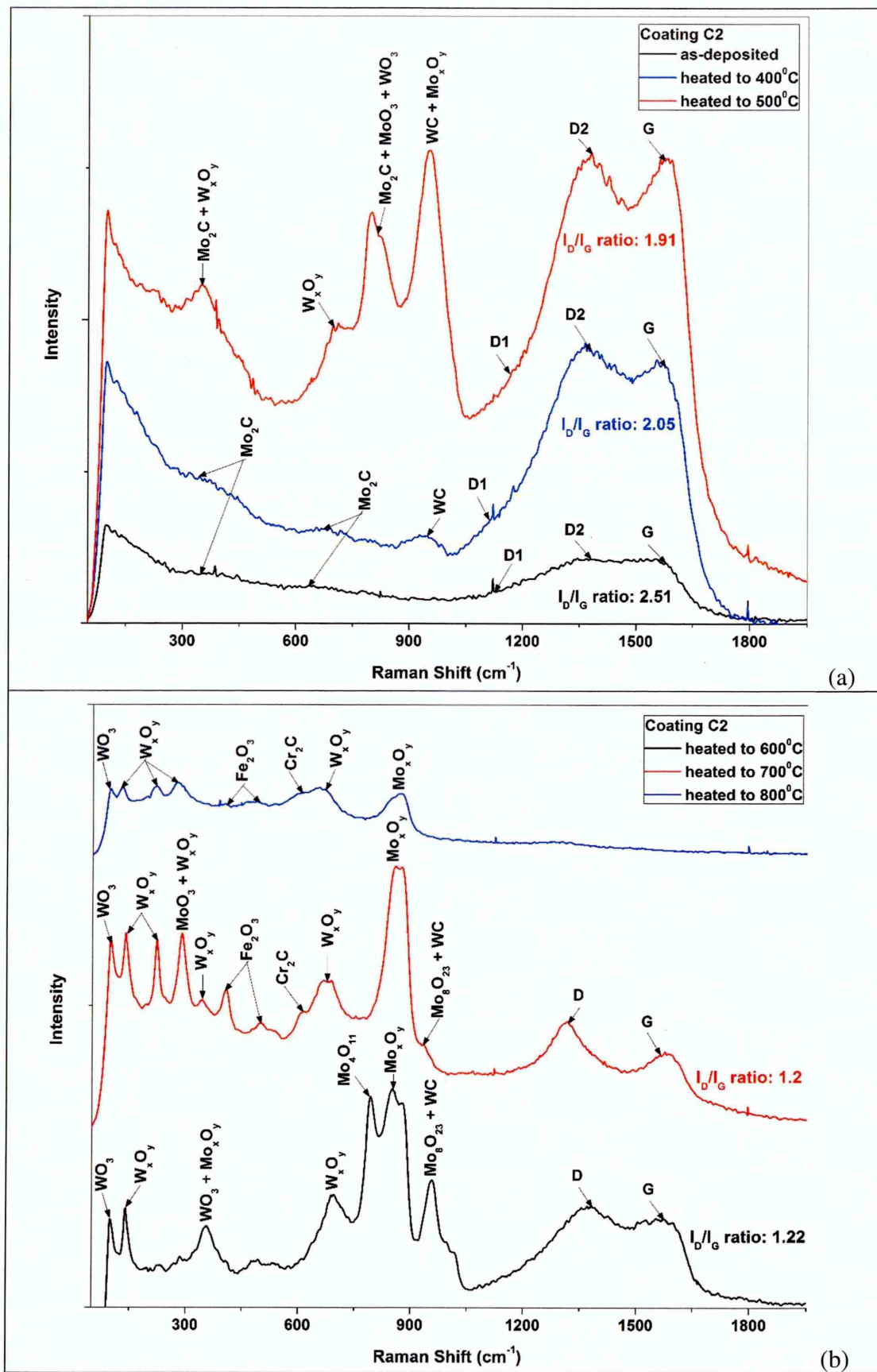


Figure 4.3-6: Raman spectra of C2 (a) as-deposited – heat-treated at 500°C and (b) heat-treated at 600°C – 800°C

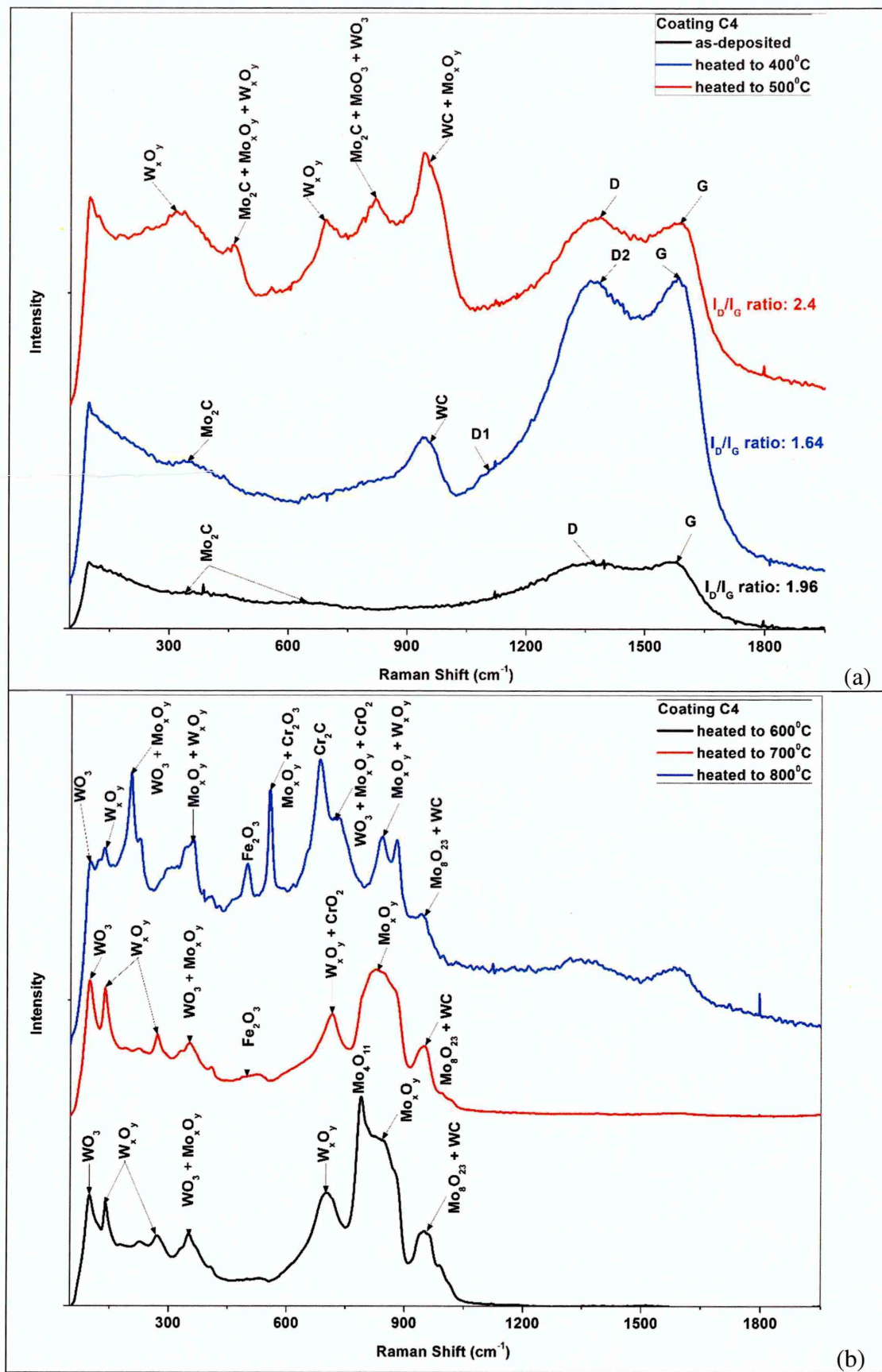


Figure 4.3-7: Raman spectra of C4 (a) as-deposited – heat-treated at 500°C and (b) heat-treated at 600°C – 800°C

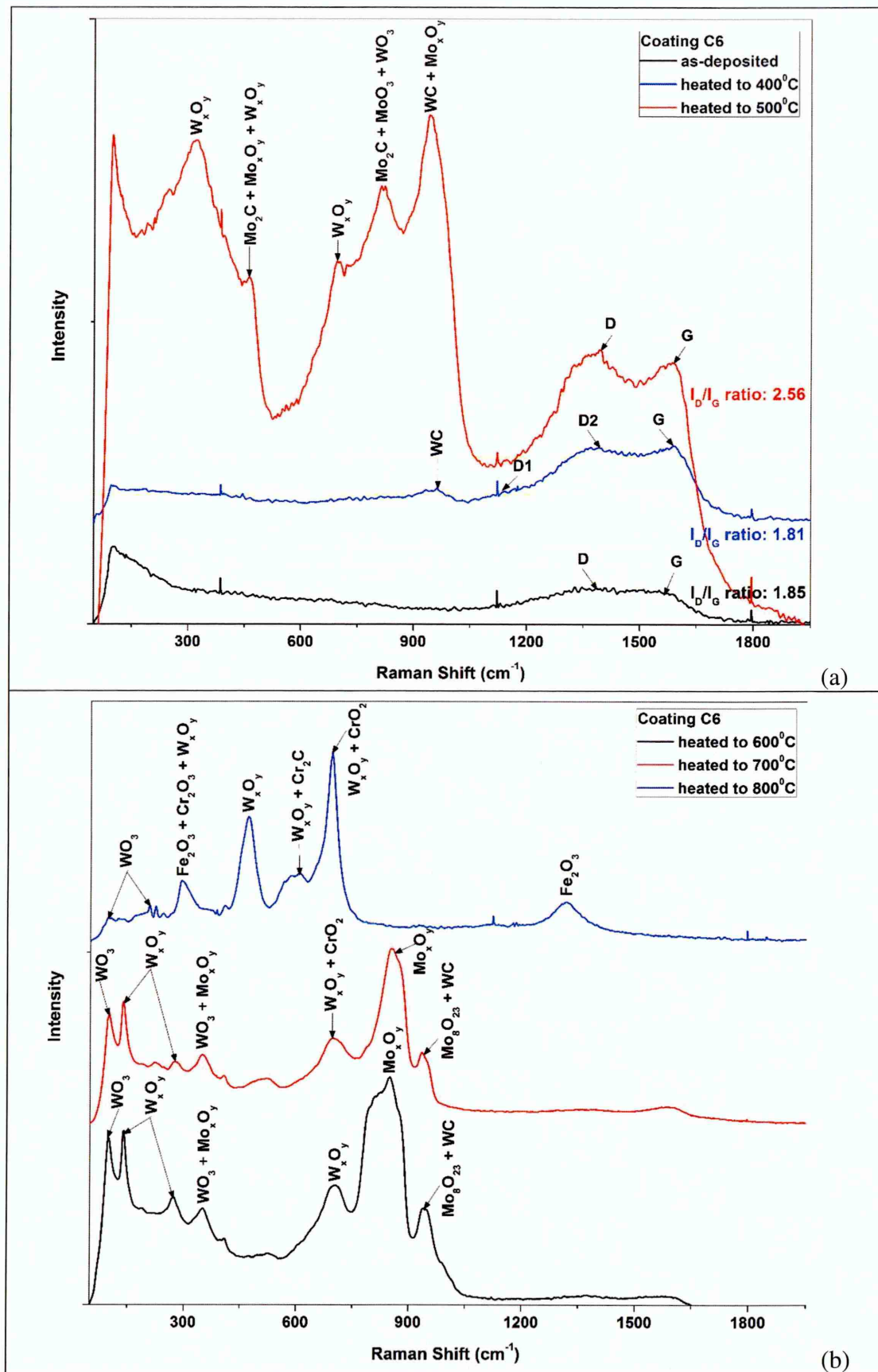


Figure 4.3-8: Raman spectra of C6 (a) as-deposited – heat-treated at 500°C and (b) heat-treated at 600°C – 800°C

IV. Nanohardness

Figure 4.3-9 shows the nanohardness of as-deposited and heat-treated Mo–W–C coatings. The nanohardness of as-deposited C2, C4 and C6 is measured as 1335.8 HV, 1677.5 HV and 1702.4 HV respectively, which is expected for metal-doped graphitic-like carbon-based coatings with hard metal carbide phases. When heated to 400°C, formation of more metal carbide phases (as confirmed by XRD and Raman analyses in earlier sections) significantly increases the coating hardness to 2030 HV, 2747 HV and 2450.8 HV respectively. With further increase in temperature up to 500°C, some of the metal carbide phases are retained, whereas rest are oxidised. The hardness of tungsten and molybdenum oxides was observed in the range of ~500 – 900 HV in room temperature (almost two times lower compared to their carbide forms) and further decrease in hardness to ~500 – 750 HV was reported when heated to 500°C [202]. Thus the decrease in hardness of Mo–W–C coatings at 500°C can be attributed to the initiation of oxidation. The hardness of C2, C4 and C6 are found as 1253.5 HV, 1646 HV and 1423.8 HV respectively at 500°C. At 600°C, the metal oxide scale becomes softer leading to further reduction in coating hardness to 547.7 HV, 817.6 HV and 669.3 HV respectively.

The oxidation of both the coating and the substrate at 700°C forms a thicker but softer mixed metal oxide scale, which lowers the coating hardness to 498.7 HV and 575.5 HV for C4 and C6 respectively. However formation of chromium carbides due to oxidation of the substrate increases the hardness of C2 to 573 HV at 700°C. At 800°C, C2 is severely oxidised leading to a rapid decrease in coating hardness to 206.5 HV. A minor increase in the coating hardness to 540.4 HV is observed for C4 due to the formation of chromium carbides whereas hardness of C6 slightly decreases to 541.7 HV.

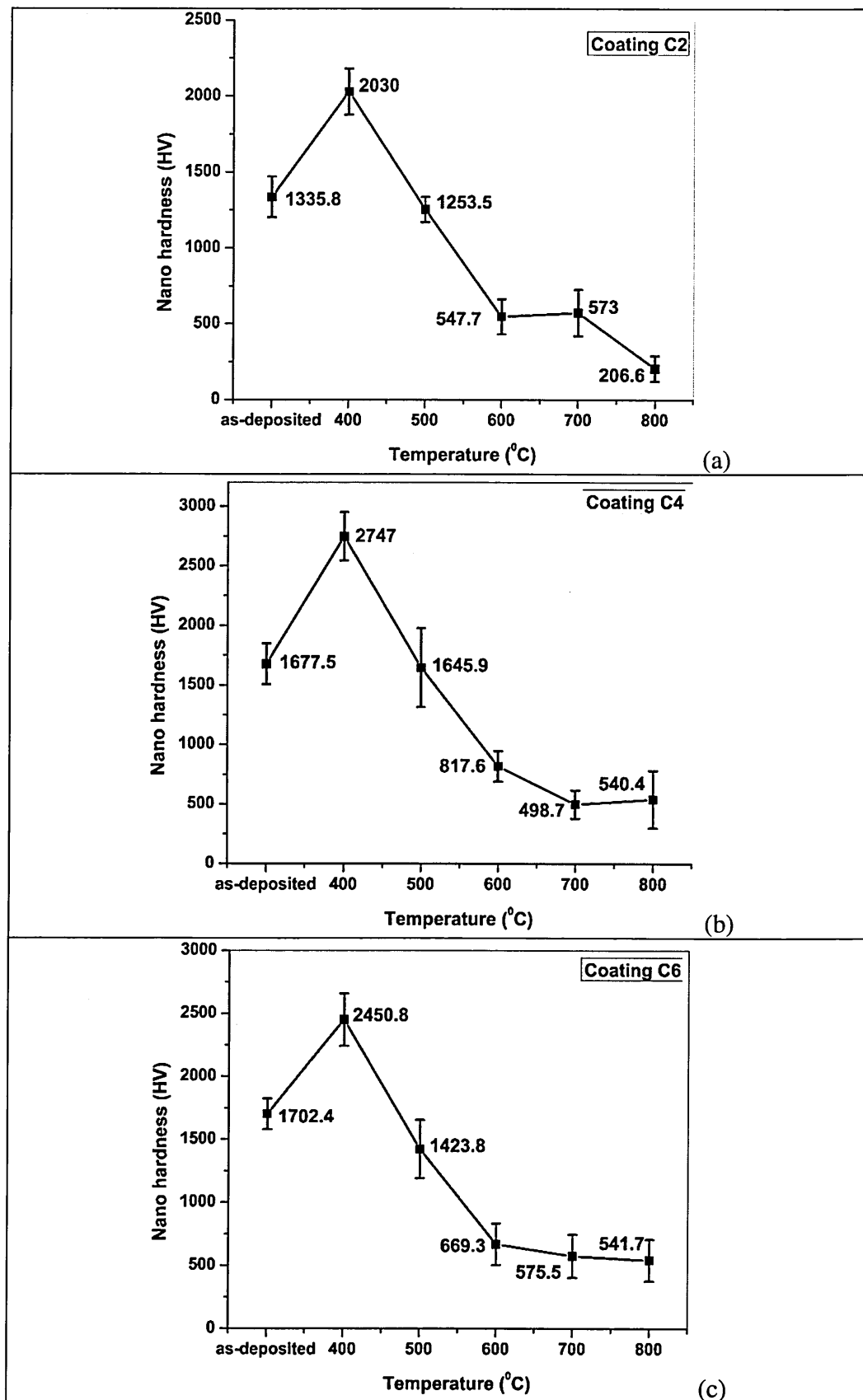


Figure 4.3-9: (a – c) Nanohardness of Mo-W-C coatings in as-deposited condition and after isothermal oxidation

4.3.4. Dynamic oxidation behaviour of Mo–W–C coatings

I. Thermo-gravimetric analysis (TGA)

Figure 4.3-10 shows the dynamic oxidation behaviour of Mo–W–C coatings obtained from thermo-gravimetric tests. C2 shows no mass gain up to $\sim 800^{\circ}\text{C}$ and further rise in the temperature up to $\sim 1000^{\circ}\text{C}$ results in rapid and large mass gain (~ 17 mg) due to formation of metal oxides. C4 and C6 shows no change in mass up to $\sim 600^{\circ}\text{C}$ and then slight mass gain is observed (~ 3 mg and ~ 5 mg respectively) up to $\sim 800^{\circ}\text{C}$. As the temperature increases to $\sim 1000^{\circ}\text{C}$, larger mass gain is observed for both the coatings (~ 27 mg and ~ 37 mg for C4 and C6 respectively). Thus the onset of rapid oxidation is considered $\sim 800^{\circ}\text{C}$. Figure 4.3-11 shows the surface morphology of the coated samples after thermo-gravimetric tests. Separate columns of metal oxides are formed on the surface of C2, which leads to drastic increase in average surface roughness to $\sim 1.2\text{ }\mu\text{m}$ (see figure 4.3-11a). Irregular growth of metal oxides is observed on the surfaces of C4 and C6, which leads to relatively low average surface roughness of $\sim 0.27\text{ }\mu\text{m}$ and $\sim 0.28\text{ }\mu\text{m}$ respectively (see figures 4.3-11b and 4.3-11c). The images of Mo–W–C coated coupons confirm absolutely no coating delamination after thermo-gravimetric tests.

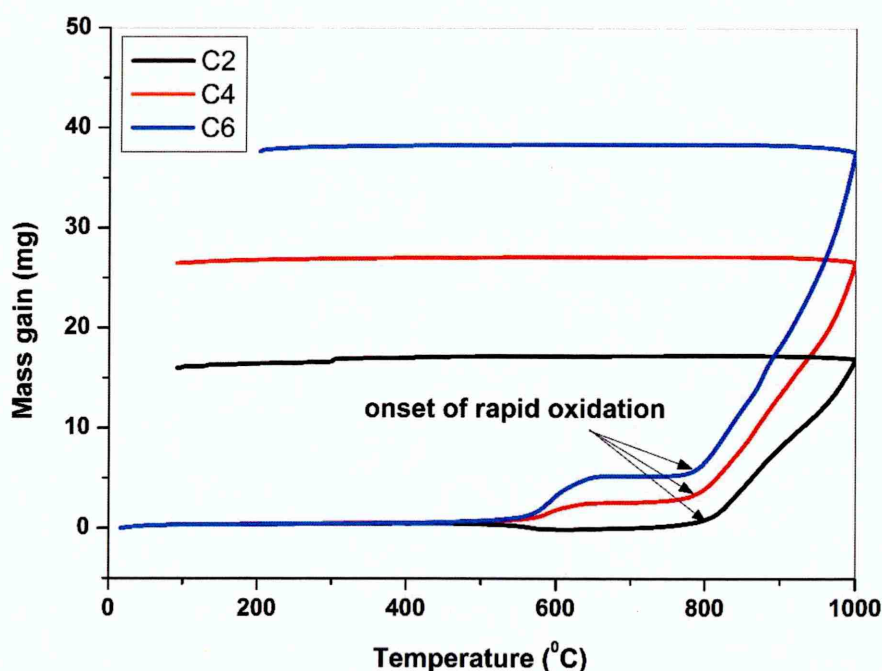


Figure 4.3-10: Thermo-gravimetric results obtained for Mo–W–C coatings

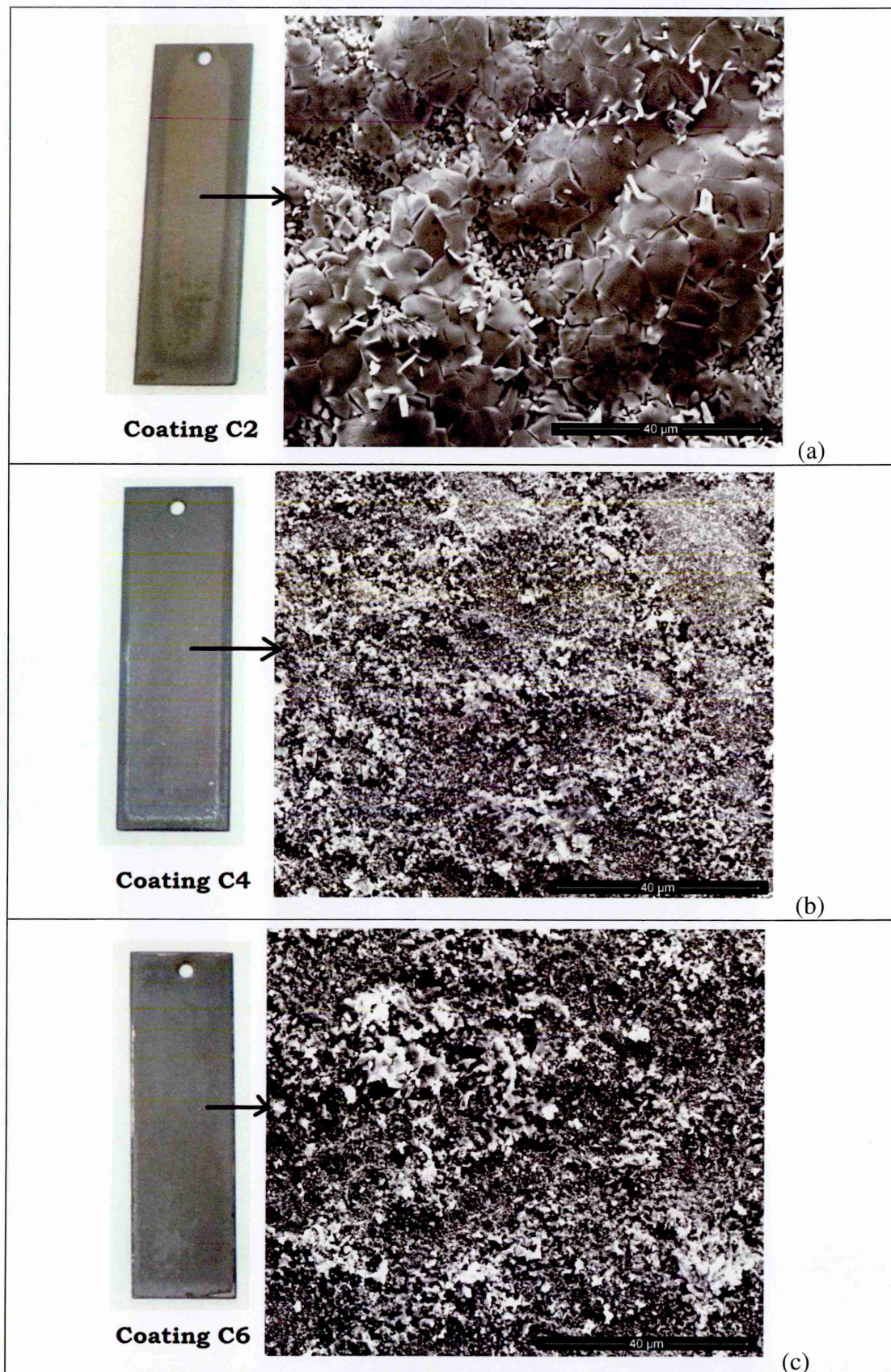


Figure 4.3-11: (a – c) SEM images showing the surface morphology of Mo–W–C coated samples after thermo-gravimetric tests

II. Phase composition using XRD and Raman spectroscopy

The phase composition of Mo–W–C coatings after thermo-gravimetric tests is revealed by XRD and Raman analyses. Figure 4.3-12 shows the XRD patterns collected from Mo–W–C coatings using Bragg-Brentano (see figure 4.3-12a) and glancing angle geometry (see figure 4.3-12b). The presence of W_xO_y , Fe_xO_y , Cr_xO_y and Cr_xC_y peaks indicates severe oxidation of both the coatings and the substrates. The oxidation of coatings forms W_xO_y , whereas Fe_xO_y , Cr_xO_y and Cr_xC_y are formed due to substrate exposure at 1000°C. The diffusion of substrate elements into the coating leads to formation of a mixed scale of metal oxides and metal carbides as indicated by the GAXRD patterns (see figure 4.3-12b). No molybdenum oxides are detected in the XRD patterns as they are evaporated before the temperature reaches to 1000°C. The findings of XRD analyses are further supported by the Raman spectra collected from the oxidised Mo–W–C surfaces as shown in figure 4.3-13. The deconvoluted peaks of the Raman spectra are listed in table A-13 (see appendix A).

Figure 4.3-14 shows the nanohardness of as-deposited Mo–W–C coatings and after dynamic oxidation. The hardness is found as ~989 HV, ~610 HV and ~645 HV for C2, C4 and C6 respectively after thermo-gravimetric tests. The higher hardness of C2 is attributed to the formation of hard chromium carbide phases, whereas hardness of C4 and C6 is reduced due to formation of softer mixed metal oxide scale.

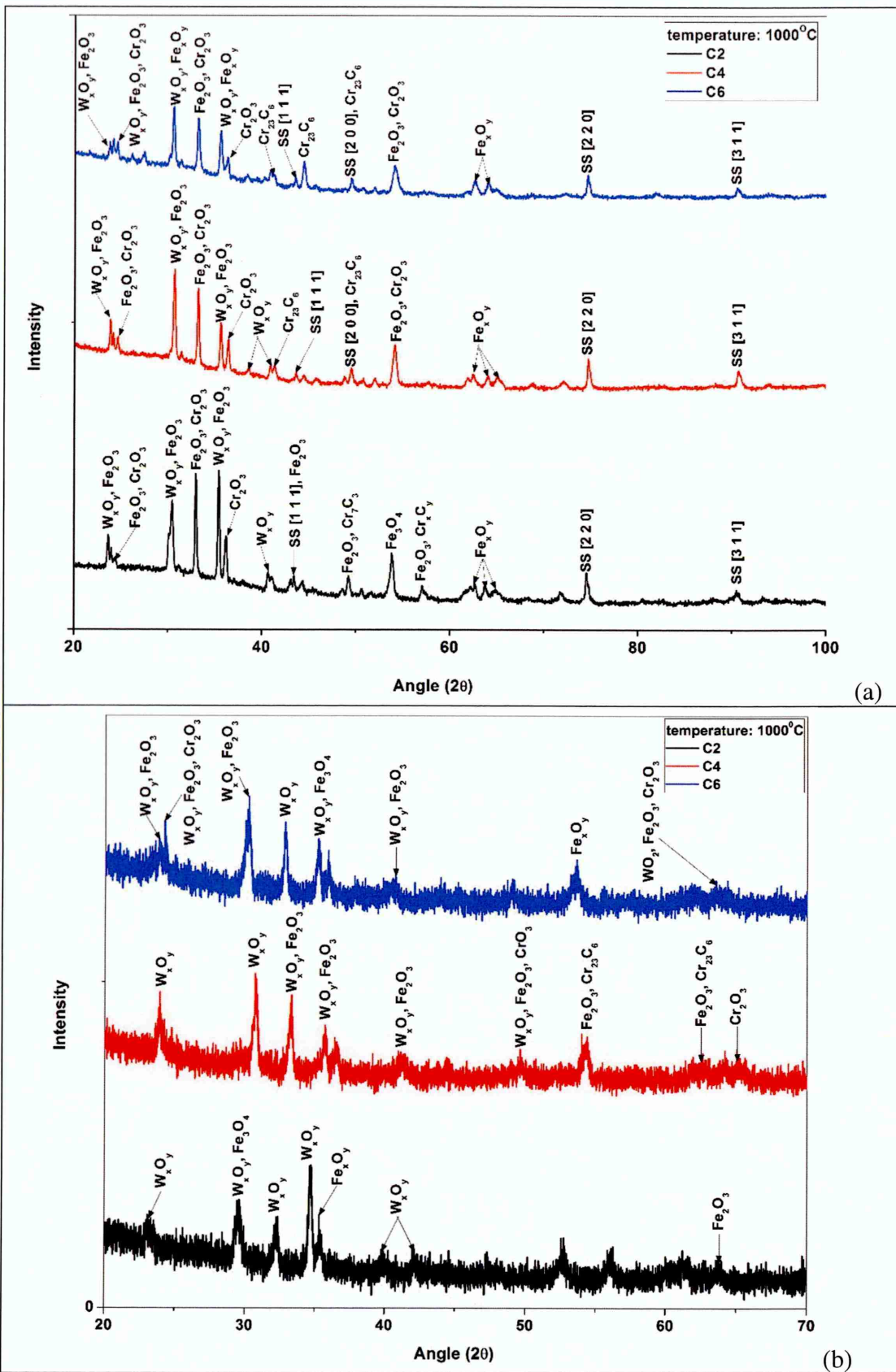


Figure 4.3-12: XRD patterns collected from Mo-W-C coatings after thermo-gravimetric tests using (a) Bragg-Brentano and (b) glancing angle geometry

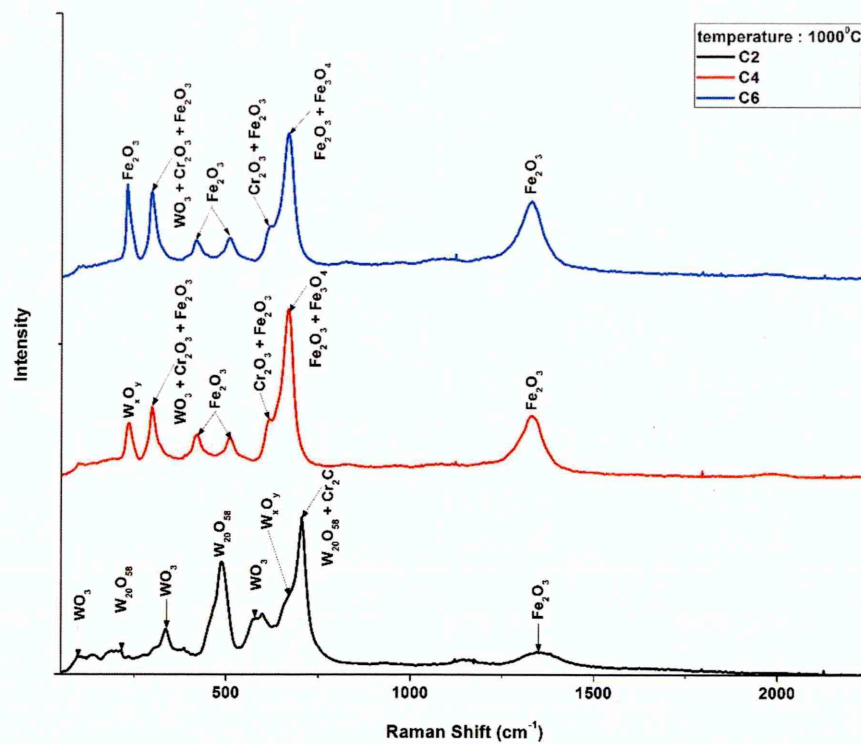


Figure 4.3-13: Raman spectra collected from Mo-W-C coatings after thermo-gravimetric tests

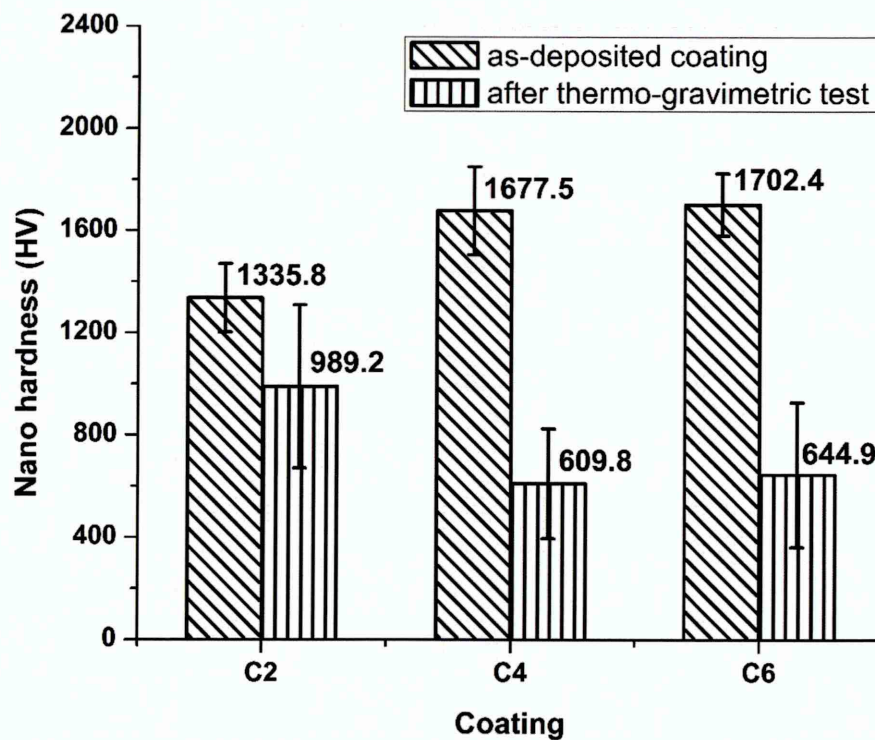


Figure 4.3-14: Nanohardness of Mo-W-C coatings in as-deposited condition and after thermo-gravimetric tests

4.3.5. Comparison of oxidation resistance of C4 and state-of-the-art DLC (Cr/Cr-WC/W:C-H/a:C-H) coatings

The as-deposited DLC (Cr/Cr-WC/W:C-H/a:C-H) coating contains Cr-WC adhesion layer, a W:C:H intermediate layer and an a-C:H layer on the top. The smooth surface finish ($R_a = 0.08 \mu\text{m}$) and the surface morphology of the as-deposited coating remains almost same after oxidised to 400°C as shown in figure 4.3-15a. Figure 4.3-15b shows the X-ray mapping done on the cross-section of the sample heat-treated to 400°C . The maps reveal strong presence of carbon at the top of the coating and a mixture of carbon and tungsten in the intermediate layer. The diffusion of substrate elements (Fe and Cr) into the coating is also observed. Oxygen is present throughout the coating thickness and into the substrate indicating that the coating does not provide secure protection against oxidation at 400°C . The thickness of the as-deposited coating ($\sim 3 \mu\text{m}$) remains almost same at 400°C .

Figure 4.3-16a shows the surface morphology of DLC coating at 500°C . The substrate surface is locally exposed at this temperature, whereas the remaining area is covered by porous oxide layer as understood from the X-ray maps. Figure 4.3-16b shows complete absence of carbon but presence of tungsten, iron and oxygen in the X-ray maps. This indicates that the substrate itself is fully oxidised on the surface and partially covered by the tungsten-based oxide layer. The local surface exposure can be due to two processes developing in parallel. On one hand, the exposure temperature is high enough to trigger the formation of gaseous hydrogen, CH_x and CO_2 compounds. In parallel, the oxidation of W:C-H layer and outward diffusion of Fe produces different oxides, which lead to delamination of the top carbon layer and subsequent substrate exposure due to their volume expansion. It is important to note that initial oxidation of C4 is observed at 500°C , however no coating delamination takes place due to excellent adhesion of C4 with substrate.

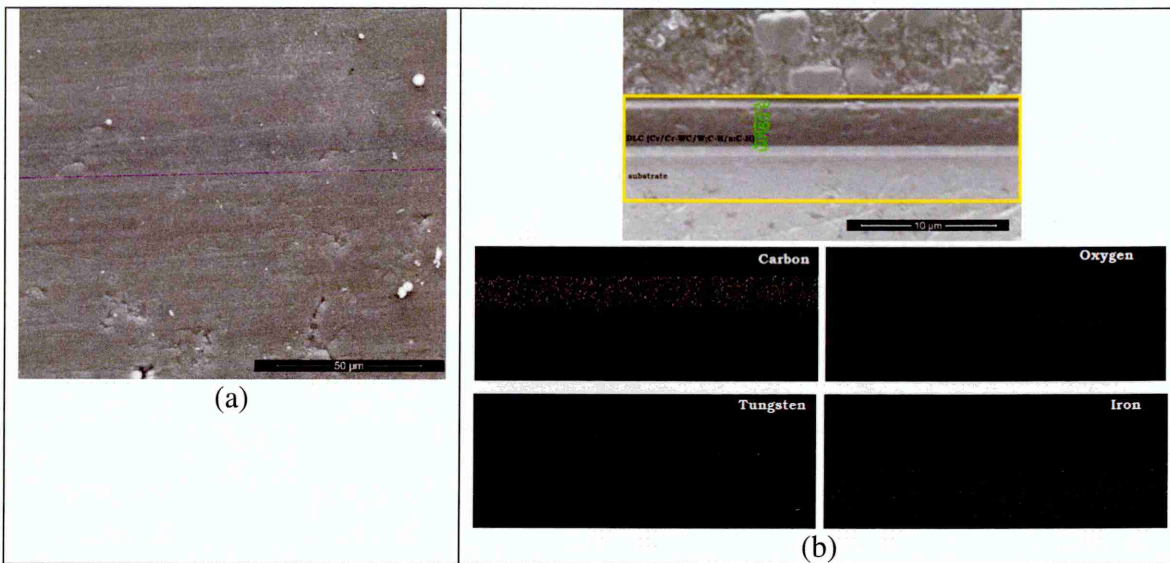


Figure 4.3-15: (a) Surface morphology and (b) X-ray mapping on the cross-section of $DLC(Cr/Cr-WC/W:C-H/a:C-H)$ coated sample isothermally heated to 400°C

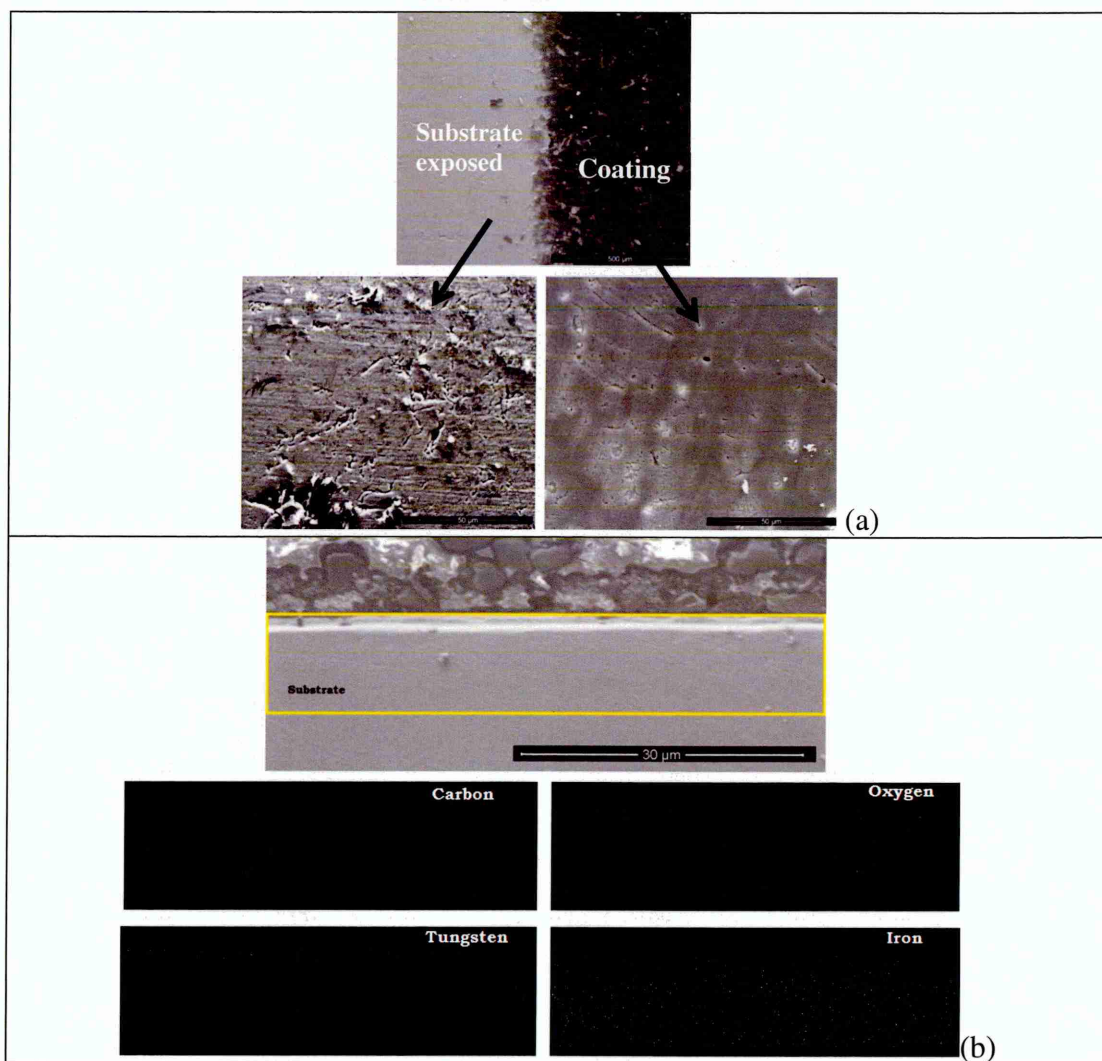


Figure 4.3-16: (a) Surface morphology and (b) X-ray mapping on the cross-section of $DLC(Cr/Cr-WC/W:C-H/a:C-H)$ coated sample isothermally heated to 500°C

Figure 4.3-17 shows the XRD patterns collected using Bragg-Brentano geometry, which indicates change in phase composition of $DLC(Cr/Cr-WC/W:C-H/a:C-H)$ coating during isothermal oxidation (up to 500°C). The as-deposited coating contains two dominant peaks at $\sim 44.5^{\circ}$ and $\sim 66.4^{\circ}$ (labelled as 'a' and 'b' respectively in the XRD pattern) due to the hydrogenated amorphous top layer (a:C-H), whereas WC [1 0 0] and W_2C [1 0 1] peaks are observed due to the W:C-H intermediate layer. When exposed to 400°C , the a:C-H top layer releases hydrogen and gaseous CH_x species, which results in exposure of intermediate W:C-H layer. Therefore the peaks 'a' and 'b' are completely disappeared and different tungsten oxide peaks [$W_xO_y \rightarrow WO_3 + WO_2 + W_5O_{14} + W_{18}O_{49}$] are formed. The Fe_2O_3 and Cr_2O_3 peaks are observed in the XRD pattern indicating oxidation of substrate and Cr-containing base layer. The a:C-H top layer is completely depleted at 500°C and further oxidation of W:C-H layer exposes the substrate. As a result, dominant W_xO_y , Fe_2O_3 and Cr_2O_3 peaks are appeared in the XRD pattern. These observations further support the findings of X-ray mapping (see figures 4.3-15 and 4.3-16).

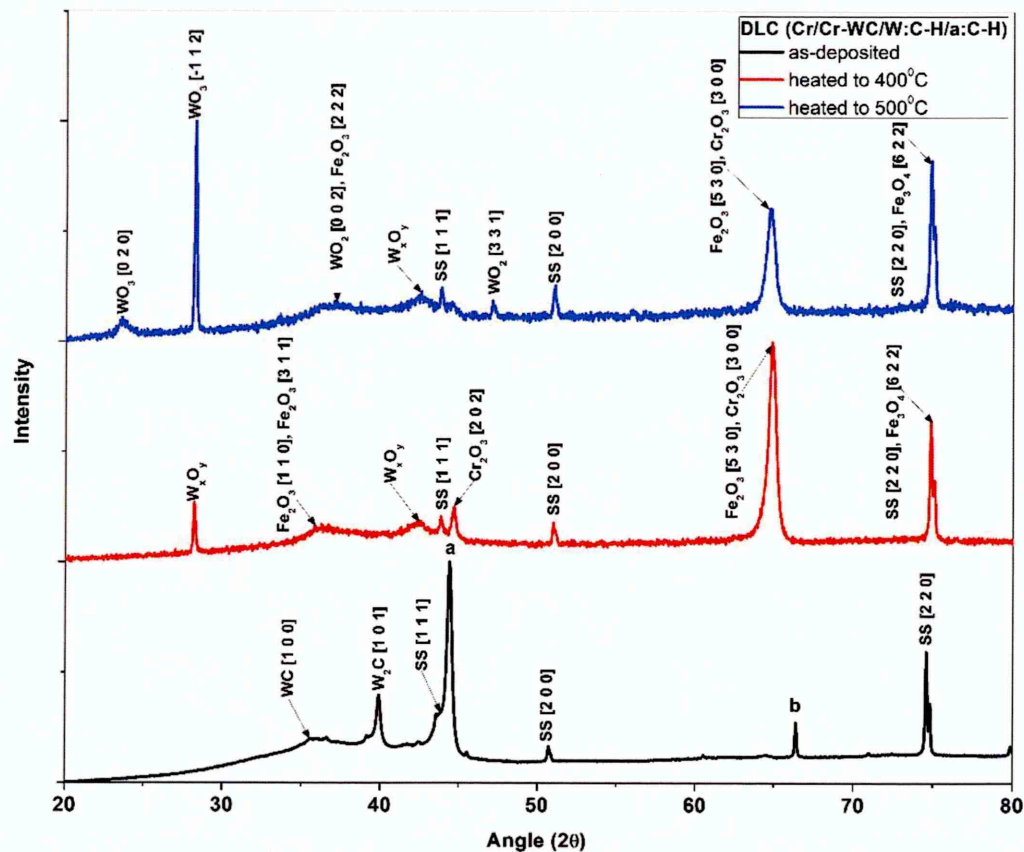


Figure 4.3-17: XRD patterns (using Bragg-Brentano geometry) of as-deposited and isothermally heat-treated $DLC(Cr/Cr-WC/W:C-H/a:C-H)$ coating

Figure 4.3-18 shows the Raman spectra collected from the as-deposited and heat-treated $\text{DLC}(\text{Cr}/\text{Cr}-\text{WC}/\text{W}:\text{C}-\text{H}/\text{a}:\text{C}-\text{H})$ coating. The as-deposited coating contains significant amount of sp^3 bonded carbon, thus the spectrum is dominated by G peak indicating its amorphous, diamond-like structure. The I_D/I_G ratio is found as 0.59 (see figure 'a' in the inset). When heated to 400°C , the sp^3 bonded carbons are converted into sp^2 bonded carbons (i.e. the graphitisation starts) leading to significant increase in D peak intensity. As a result, I_D/I_G ratio rapidly increases to 1.01 (see figure 'b' in the inset). Upon further heating up to 500°C , a distinct disordered peak is appeared in the spectrum indicating complete transformation of diamond-like structure into the graphite-like structure. Thus the I_D/I_G ratio further increases to 1.04 (see figure 'c' in the inset). This gradual increase in I_D/I_G ratio indicates the rise in ordering of DLC coating with increase in temperature. This is further supported by the upshifting of G peak position of the as-deposited coating (1545.89 cm^{-1}) after heat-treatment (1574.32 cm^{-1} and 1583.28 cm^{-1} when heated to 400°C and 500°C respectively). The initiation of graphitisation at 400°C confirms poor thermal stability of DLC coating compared to C4.

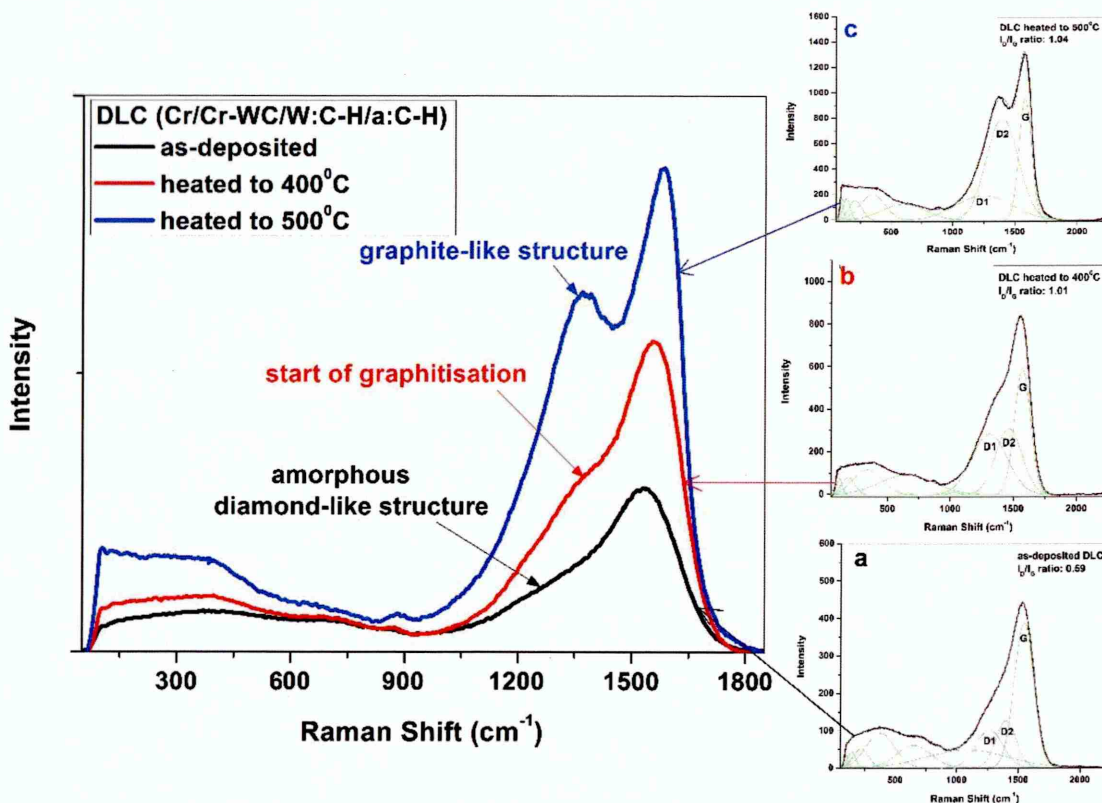
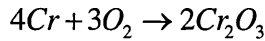
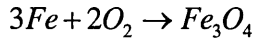
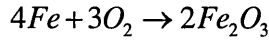
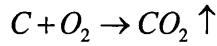
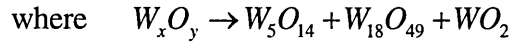
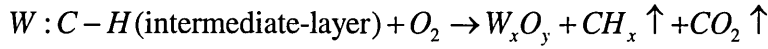
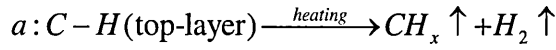


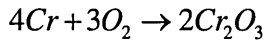
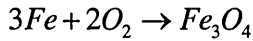
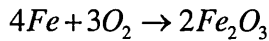
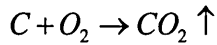
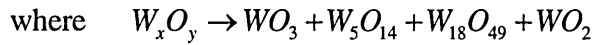
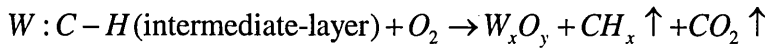
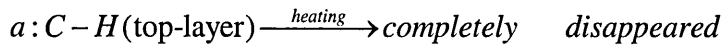
Figure 4.3-18: Raman spectra of as-deposited and isothermally heat-treated $\text{DLC}(\text{Cr}/\text{Cr}-\text{WC}/\text{W}:\text{C}-\text{H}/\text{a}:\text{C}-\text{H})$ coating

As understood from the results obtained from XRD and Raman analyses, the possible chemical reactions occurred during isothermal oxidation of $DLC(Cr/Cr-WC/W:C-H/a:C-H)$ coating are listed in the equation set (7).

- 400°C: oxidation initiates and substrate marginally exposed



- 500°C: severe oxidation and substrate completely exposed



(7)

Figure 4.3-19 shows that the hardness of $DLC(Cr/Cr-WC/W:C-H/a:C-H)$ coating as a function of the temperature significantly differs from C4. The high amount of sp^3 bonded carbon present in as-deposited DLC coating results in nanohardness of 4389 HV, which is ~2.6 times higher than the nanohardness of coating C4 (1677.5 HV). After exposed to 400°C, the nanohardness of DLC coating reduces to 4376 HV due to the start of graphitisation as revealed by the Raman spectroscopy (see figure 4.3-18). At 500°C, the diamond-like structure is completely converted into the graphite-like structure which leads to a drastic decrease in the coating hardness to 811 HV. It should be noted that the DLC coating retains its superior hardness (>4300 HV) up to 400°C, whereas formation of metal carbide phases increases the hardness of C4 to 2747 HV at 400°C. At 500°C, the complete structural change of DLC coating results in drastic decrease in coating hardness to 811 HV, whereas initial oxidation of C4 at that temperature still

retains its hardness value to 1646 HV. This significant change in coating hardness indicates poor thermal stability of DLC coating compared to C4.

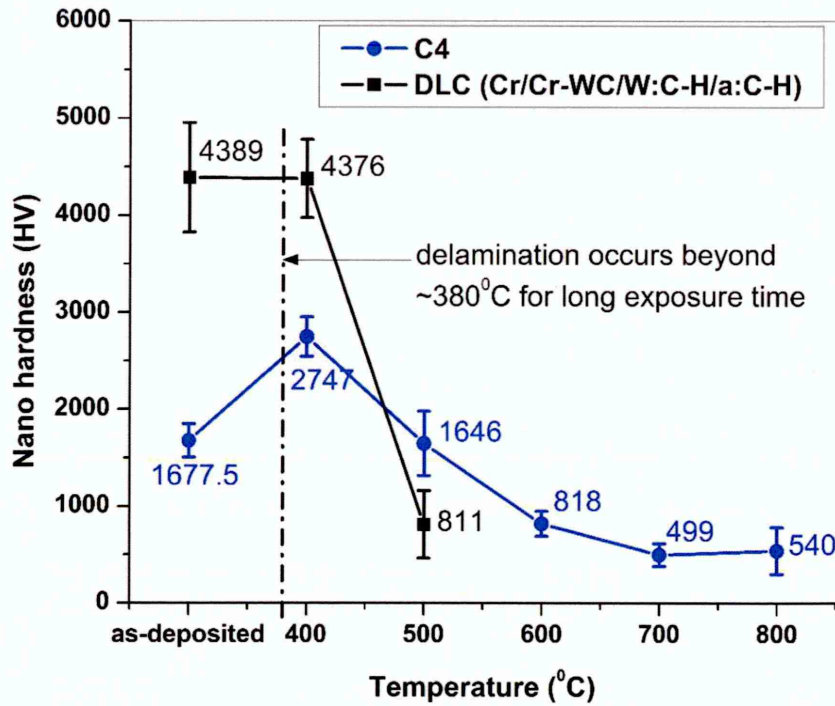


Figure 4.3-19: Nanohardness of C4 and $DLC(Cr/Cr-WC/W:C-H/a:C-H)$ coatings in as-deposited condition and after isothermal oxidation

Figure 4.3-20 shows the dynamic oxidation behaviour of C4 and DLC coatings as obtained from thermo-gravimetric analysis. C4 shows no change in mass up to $\sim 600^{\circ}\text{C}$, followed by a slight increase in mass gain to ~ 3 mg when heated up to $\sim 800^{\circ}\text{C}$. Further rise in the temperature up to $\sim 1000^{\circ}\text{C}$ results in rapid and large mass gain (~ 23 mg) due to the formation of heavy metal oxides. The image of coated sample and the magnified image of oxidised surface (provided in the inset) indicates no coating delamination during the test. On the other hand, mass of the DLC coated sample remains constant up to $\sim 380^{\circ}\text{C}$, however further heating up to $\sim 650^{\circ}\text{C}$ results in gradual decrease of the mass at a rate of $\sim 5 \text{ mg}^{\circ}\text{C}^{-1}$. This mass loss is due to the evaporation and local delamination of the DLC coating as described earlier. Unlike C4, delamination is observed (see inset) for DLC coating due to the volume expansion of the oxide layer. As a result, the surface roughness of DLC coated sample is observed much higher ($R_a = 0.4 \mu\text{m}$) compared to C4 ($R_a = 0.27 \mu\text{m}$) after the test. Overall, the thermo-gravimetric analysis indicates that C4 and DLC coatings resist oxidation up to $\sim 800^{\circ}\text{C}$ and $\sim 380^{\circ}\text{C}$ respectively and further heat-treatment significantly degrades the coating properties.

It should be noted that the delamination occurs for DLC coating at $\sim 380^\circ\text{C}$ during thermo-gravimetric test, however no delamination occurs for the same coating when isothermally heated to 400°C . The coating was heat-treated for 2 hours during isothermal test whereas a slow heating rate like 1°C per minute takes more than 6 hours to reach 380°C during thermo-gravimetric test. Therefore, long exposure time of 6 hours leads to local delamination of the coating at $\sim 380^\circ\text{C}$.

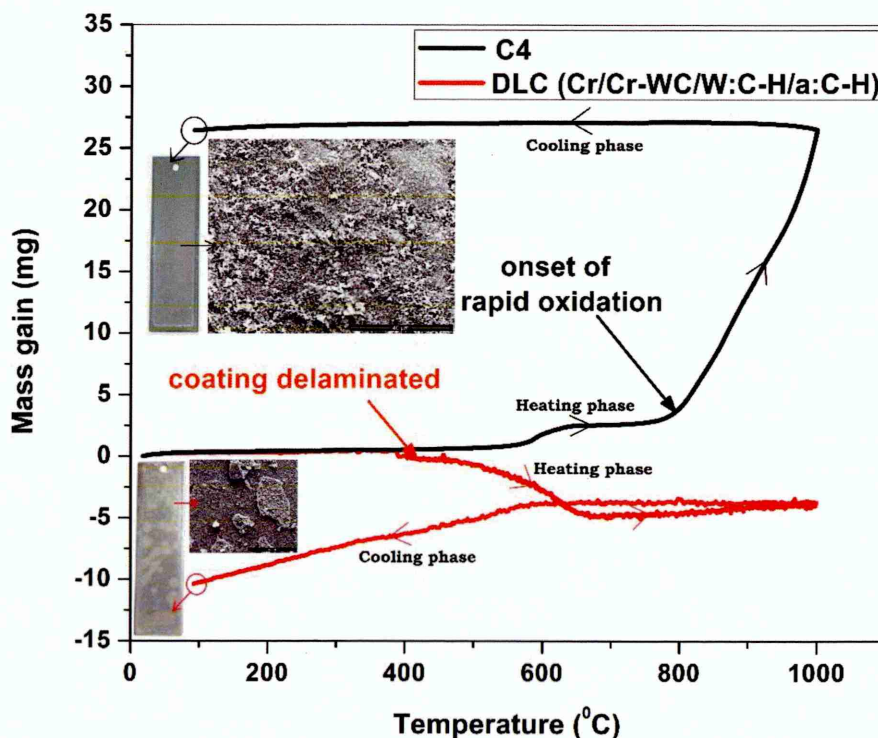


Figure 4.3-20: Dynamic oxidation behaviour of C4 and $\text{DLC}(\text{Cr}/\text{Cr}-\text{WC}/\text{W}:\text{C}-\text{H}/\text{a}:\text{C}-\text{H})$

4.3.6. Concluding remarks

A number of surface analyses techniques reveal the isothermal and dynamic oxidation behaviour of Mo-W-C coatings and compares the performance with a state-of-the-art $\text{DLC}(\text{Cr}/\text{Cr}-\text{WC}/\text{W}:\text{C}-\text{H}/\text{a}:\text{C}-\text{H})$ coating. The isothermal tests were carried out in the temperature range of $400^\circ\text{C} - 800^\circ\text{C}$ in furnace, whereas temperature was increased to 1000°C at a heating rate of 1°C per minute for the dynamic oxidation test (TGA).

- The as-deposited Mo–W–C coatings have nanocrystalline structure and average nanohardness of ~1300 – 1700 HV. When exposed to 400°C, the development of metal carbide phases transforms the nanocrystalline structure into crystalline structure. This increases the coating hardness in the range of ~2000 – 2750 HV and the analytical techniques confirm that absolutely no oxidation occurs at 400°C. The graphitic nature of as-deposited coatings is preserved up to 500°C, however coating hardness is reduced to ~1250 – 1650 HV due to initial oxidation. Further progress of oxidation process at 600°C and 700°C forms a thicker but softer mixed oxide scale leading to drastic decrease in coating hardness (~500 – 820 HV). The severe oxidation of both the coatings and the substrates are clearly observed at 800°C.
- Graphitisation of the amorphous $DLC(Cr/Cr-WC/W:C-H/a:C-H)$ coating starts at 400°C and the diamond-like structure is completely converted into the graphite-like structure at 500°C. Thus DLC coating obtains its high hardness up to 400°C (>4300 HV), but drastically reduces to 811 HV at 500°C. The exposure of tungsten-containing intermediate layer and the substrate indicates initial oxidation at 400°C. When exposed to 500°C, the top hydrogenated carbon layer is completely disappeared due to formation of gaseous CH_x and CO_2 compounds and simultaneously the coating is locally delaminated due to volume expansion of oxides from intermediate layers and substrate.
- During isothermal tests, the oxidation is initiated for Mo–W–C coatings at 500°C but the as-deposited graphitic nature is still preserved. At the same temperature, the state-of-the-art DLC coating is locally delaminated due to volume expansion of metal oxides produced from both the coating and the substrate. Simultaneously the diamond-like structure is completely converted into the soft graphite-like structure indicating its poor oxidation resistance when compared to the Mo–W–C coatings.
- The thermo-gravimetric test results show that Mo–W–C coatings resist oxidation up to ~800°C and no coating delamination is observed during the test because of its high adhesion strength with the substrate. On the other hand, the evaporation and local delamination of DLC coating is observed beyond ~380°C. This confirms excellent thermal stability of Mo–W–C coatings compared to standard DLC coating in dynamic condition.

4.4. Tribological behaviour of Mo–W–C coatings in dry and boundary lubricated conditions at elevated temperature

4.4.1. Introduction

It has been established till now that the Mo–W–C coatings are able to minimise friction and wear during sliding at ambient temperature (see chapter 4.2) and to resist oxidation up to $\sim 600^{\circ}\text{C}$ (see chapter 4.3). This chapter investigates the tribological performance of Mo–W–C coatings at elevated temperature and importance of combined Mo and W doping in friction and wear behaviour. Section 4.4.2 describes the tribological behaviour of Mo–W–C coatings during dry sliding in the temperature range of $200^{\circ}\text{C} - 500^{\circ}\text{C}$ and the performance at ambient temperature is provided as a reference. Section 4.4.3 explains the same during boundary lubricated sliding (Mobil1 Extended lifeTM 10W-60 engine oil used as lubricant) at 200°C . This temperature is higher than the temperature experienced by components used in valve-train assembly (150°C), but lower than the maximum temperature of piston-cylinder assembly (300°C) [43]. The flash temperature of the lubricant is only 234°C [187], thus lubricated sliding tests cannot be carried out at higher temperature. Section 4.4.4 compares the tribological performance of C4 with $\text{DLC}(\text{Cr} / \text{Cr} - \text{WC} / \text{W} : \text{C} - \text{H} / \text{a} : \text{C} - \text{H})$ at high temperature.

The sliding tests were performed in a CSM high temperature pin-on-disc tribometer against uncoated 100Cr6 steel and Al_2O_3 balls. The Al_2O_3 balls have low thermal coefficient of linear expansion ($5.4 \times 10^{-6} \text{ m m}^{-1}\text{C}^{-1}$) compared to the steel balls ($12 \times 10^{-6} \text{ m m}^{-1}\text{C}^{-1}$) [203], thus the dry and lubricated sliding tests were carried out against Al_2O_3 and steel balls respectively. SEM, EDX, X-ray mapping, optical microscope, surface profilometer and Raman spectroscopy were used to reveal the tribological behaviour of both the coatings and the counterparts. Based on the wear products found within the wear tracks and on the ball surfaces, different wear mechanisms are proposed for dry and lubricated sliding of Mo–W–C coatings at elevated temperature.

4.4.2. Tribological behaviour of Mo–W–C coatings during dry sliding at elevated temperature

I. Experimental details

A CSM high temperature pin-on-disc tribometer was used to study the friction behaviour of Mo–W–C coatings against Al_2O_3 balls under 5 N static load at ambient (30°C and ~25% – 30% relative humidity) and elevated temperature (200°C, 400°C and 500°C) conditions. The friction and wear behaviour of both the coatings and the counterparts are discussed in sections II and III respectively. The topographical imaging of the wear tracks and the transfer layer formed on the ball surfaces were carried out using secondary electron detector and optical microscope. The wear coefficients were calculated with the help of surface profilometer and optical microscope. Raman spectra were collected from the counterpart surfaces and the wear tracks with 60 s exposure time. The relevant wear mechanism is discussed in section IV.

II. Friction behaviour at elevated temperature

Figure 4.4-1 shows the friction behaviour of Mo–W–C coatings against Al_2O_3 balls is investigated at ambient (30°C) and elevated temperature (200°C – 500°C), which is simultaneously influenced by stick-slip motion and third-body abrasive wear during sliding. Significant stick-slip motion is observed for C2 at ambient temperature whereas friction curves of C4 and C6 are found almost smooth during steady-state period (figure 4.4-1a). The mean friction coefficients are found as ~0.267, ~0.116 and ~0.252 for C2, C4 and C6 respectively. At 200°C, the mean friction coefficients are rapidly increased to ~0.6, ~0.686 and ~0.625 respectively and dominant stick-slip motion is observed for C2 and C4 compared to C6 (figure 4.4-1b). The amplitude of oscillations is further increased at 400°C. Both C2 and C4 shows low friction coefficient ($\mu < 0.4$) up to 400 m and 250 m respectively, followed by a rapid increase in friction value due to dominant stick-slip motion. Thus the mean friction coefficient of C2 and C4 (~0.622 and ~0.685 respectively) retains almost similar to that observed at 200°C. On the other hand, C6 shows almost steady stick-slip motion throughout the sliding distance but a drop in mean friction coefficient to ~0.568 is observed (figure 4.4-1c). When heated to 500°C, the amplitude of stick-slip motion is significantly decreased. Mo–W–C coatings show low friction

coefficient ($\mu < 0.2$ up to 200 m, 100 m and 50 m for C2, C4 and C6 respectively), followed by a sudden rise in friction ($\mu \sim 0.4 - 0.7$) for rest of the sliding distance. Thus mean friction coefficients are observed as ~ 0.439 , ~ 0.422 and ~ 0.41 for C2, C4 and C6 respectively at 500°C (figure 4.4-1d). Overall, Mo–W–C coatings show a significant increase in friction up to 400°C, however a reduction in mean friction coefficient is observed at 500°C.

The debris particles generated from the coatings and the counterparts are severely deformed during dry sliding and promote third-body abrasion. Therefore the transfer layer formed between sliding surfaces contains two types of debris: (i) loose particles accumulated on the worn area of the counterpart surfaces (see figure 4.4-2) and (ii) debris strongly adhered to the wear tracks (see figures 4.4-5 – 4.4-7). It is important to note that most of the debris is adhered to the wear track of Mo–W–C coatings when Al_2O_3 is used as sliding counterpart rather than steel. No adhered debris is observed on the Al_2O_3 ball surfaces at ambient temperature (see figure 4.4-2a), whereas little amount of debris is found adhered to the ball surfaces at elevated temperature (see figures 4.4-2b – 4.4-2d). The transfer layer is composed of graphitic carbon particles and various metal oxides, which influence the friction behaviour at elevated temperature as revealed by Raman analyses.

Figure 4.4-3 shows the Raman spectra collected from the debris adhered to the Al_2O_3 balls after sliding against C2 at elevated temperature and details of the deconvoluted peaks are listed in table A-14 (see appendix A). The debris formed at 200°C and 400°C contains different tungsten oxides (W_xO_y), Al_2O_3 and graphitic carbon particles having I_D/I_G ratio of 1.51 and 1.18 respectively. None of these oxides promotes sliding and further the decrease in degree of graphitisation with increase in temperature leads to high friction coefficient. At 500°C, lubricious MoO_3 is found in the adhered debris along with W_xO_y , Al_2O_3 and graphitic carbon particles. The I_D/I_G ratio further decreases to 1.15, therefore the reduction in friction coefficient at 500°C is mostly attributed to the formation of MoO_3 phases rather than the presence of graphitic carbon particles. Similar results are found for counterparts sliding against C4 and C6.

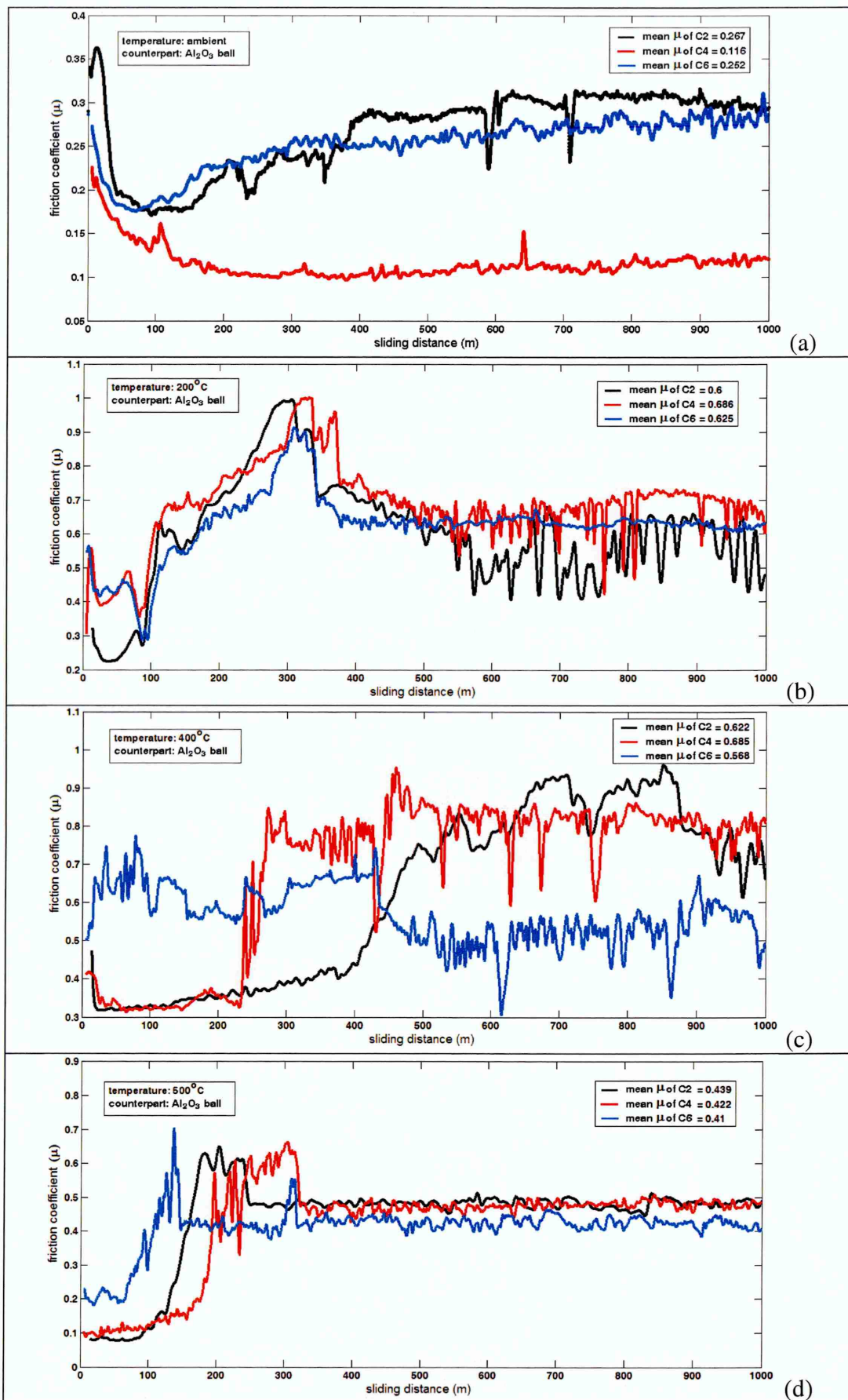


Figure 4.4-1: Friction behaviour of Mo-W-C coatings after dry sliding against Al_2O_3 balls at (a) ambient temperature, (b) 200°C, (c) 400°C and (d) 500°C

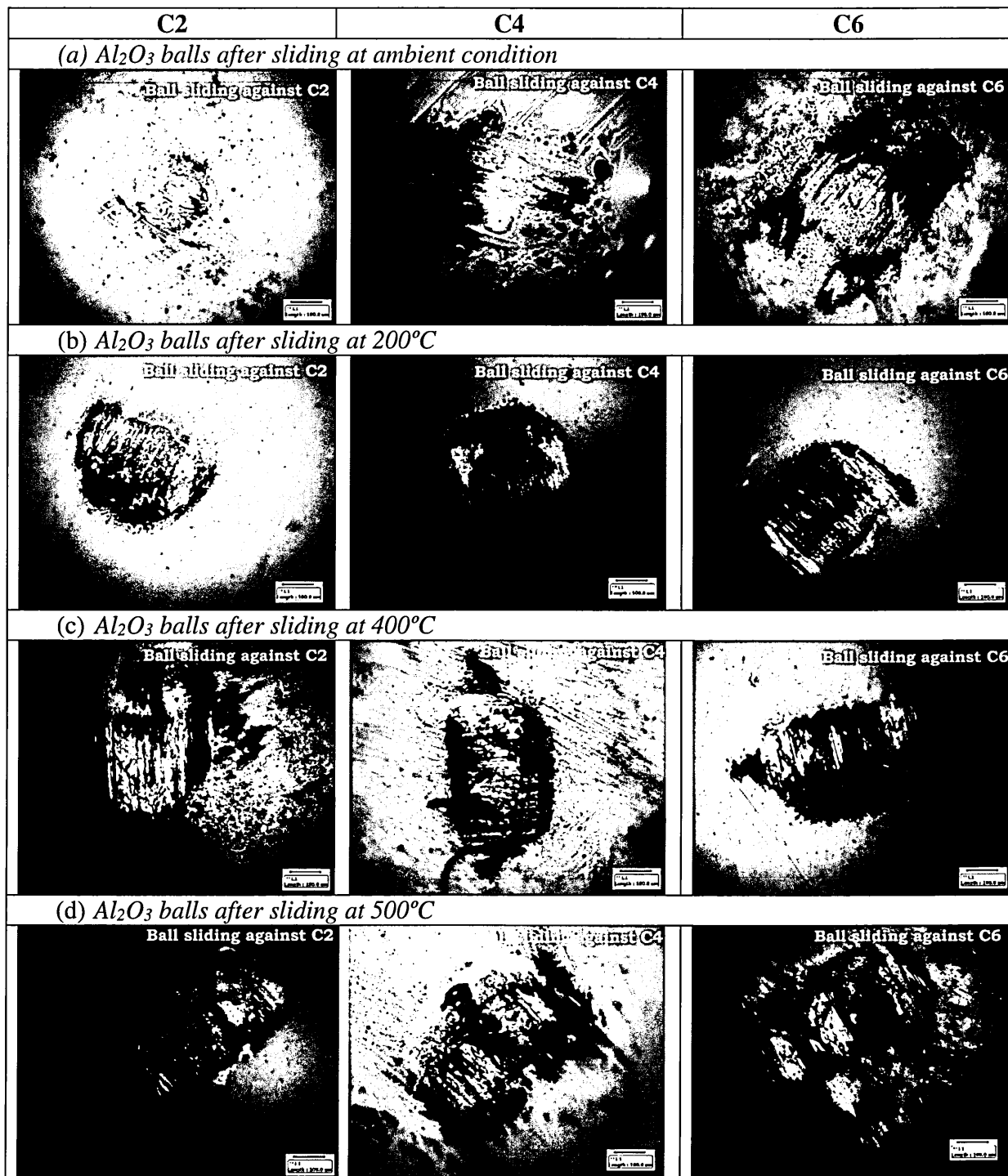


Figure 4.4-2: Transfer layer formed on the Al₂O₃ counterparts after dry sliding against Mo–W–C coatings at (a) ambient temperature, (b) 200°C, (c) 400°C and (d) 500°C

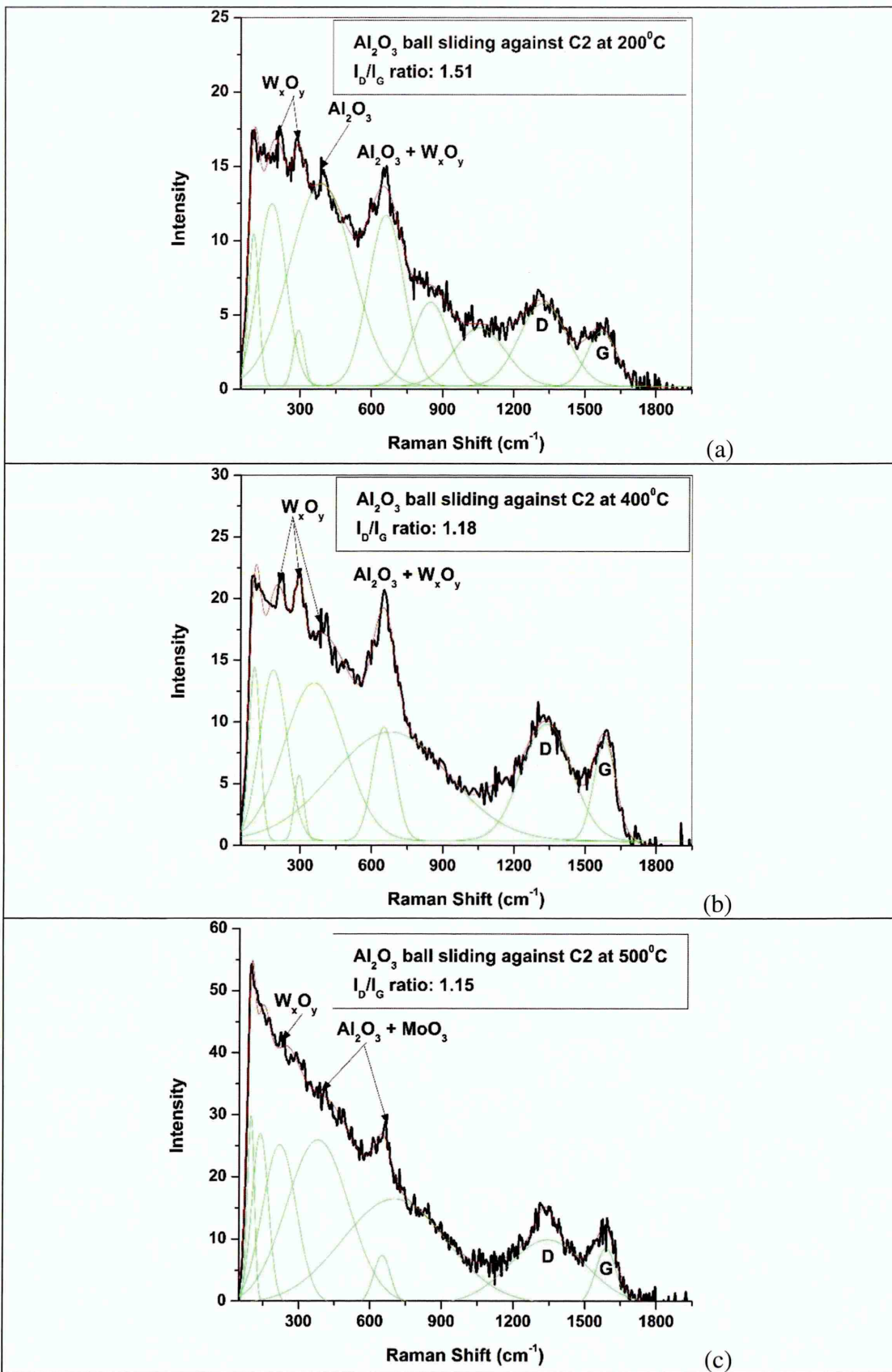


Figure 4.4-3: Raman spectra collected from the debris adhered to the Al_2O_3 balls after sliding against C2 at (a) 200°C , (b) 400°C and (c) 500°C

III. Wear behaviour at elevated temperature

The wear coefficients of Al_2O_3 balls are found in the order of $\sim 10^{-12} \text{ m}^3 \text{ N}^{-1} \text{ m}^{-1}$ after sliding against Mo–W–C coatings as shown in figure 4.4-4. At ambient temperature, the wear coefficients are observed in the range of 0.2 – 0.5, which increases to 1.0 – 1.7 as the temperature reaches to 400°C and further increase to 2 – 2.4 is observed at 500°C . This increase in wear coefficient depends on third-body abrasive wear during sliding. With increase in test temperature, more metal oxides are formed but their hardness is reduced. As a result, the third-body abrasion severely damages both the coatings and the counterparts leading to formation of wide and deep wear tracks and large wear scars.

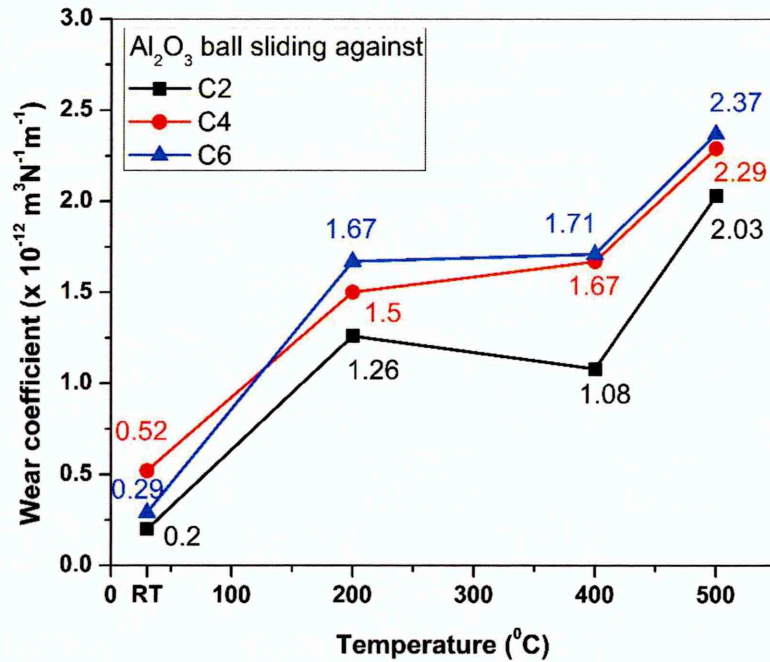


Figure 4.4-4: Wear coefficient of Al_2O_3 balls after dry sliding against Mo–W–C coatings at ambient and elevated temperature

Figures 4.4-5 – 4.4-7 show the wear tracks of Mo–W–C coatings after sliding against Al_2O_3 balls at ambient and elevated temperature. The SEM images and the EDX spectra indicate that Mo–W–C coatings are retained intact within the wear tracks ($\sim 57 - 67 \mu\text{m}$ wide) at ambient temperature (see figures 4.4-5a, 4.4-6a and 4.4-7a). Further the EDX spectrum indicates the presence of metal oxides in the wear debris accumulated beside the wear track of C4 (see figure 4.4-6a), whereas no debris is observed for C2 and C6. At elevated temperature, the metal oxides are found within the wear track of C2, C4 and C6 as indicated by the EDX spectra. A significant increase in the width and depth of the wear tracks are observed due to severe third-body abrasion during sliding. The SEM images

show that the width of wear tracks increases in the range of $\sim 334 - 402 \mu\text{m}$ (see figures 4.4-5b, 4.4-6b, 4.4-7b), $\sim 383 - 448 \mu\text{m}$ (see figures 4.4-5c, 4.4-6c, 4.4-7c) and $\sim 519 - 608 \mu\text{m}$ (see figures 4.4-5d, 4.4-6d, 4.4-7d) at 200°C , 400°C and 500°C respectively. Moreover, the high intensity Fe peaks present in the EDX spectra indicate possible exposure of substrate after dry sliding at elevated temperature. This is further confirmed by measuring the wear track profiles as explained in next section.

Figure 4.4-8 shows the wear track profiles of Mo-W-C coatings after dry sliding. At ambient condition, the average depth of wear tracks is found in the range of $\sim 0.12 - 0.21 \mu\text{m}$ (figure 4.4-8a), which is less than the thickness of respective coatings ($\sim 1.9 - 2.8 \mu\text{m}$ as shown in figure 4.1-1). Thus Mo-W-C coatings are retained intact within the wear track at ambient temperature. At 200°C , the average depth of wear tracks is measured in the range of $\sim 5.8 - 8.5 \mu\text{m}$ (figure 4.4-8b), which confirms complete delamination of the coatings within the wear tracks and thus the substrate is exposed. As the temperature rises to 400°C and 500°C , the average depth of wear tracks further increases in the range of $\sim 5 - 11 \mu\text{m}$ (figures 4.4-8c and 4.4-8d). These results completely support the findings of EDX spectra as observed in figures 4.4-5 – 4.4-7.

Figure 4.4-9 shows the wear coefficients of Mo-W-C coatings after sliding. At ambient condition, the wear coefficients of Mo-W-C coatings are found in the range of $\sim 0.5 - 2 \times 10^{-16} \text{m}^3\text{N}^{-1}\text{m}^{-1}$. The severe third-body abrasion and the substrate exposure at elevated temperature drastically increases the wear coefficients in the range of $\sim 1.69 - 2.83 \times 10^{-14} \text{m}^3\text{N}^{-1}\text{m}^{-1}$, $\sim 1.06 - 3.93 \times 10^{-14} \text{m}^3\text{N}^{-1}\text{m}^{-1}$ and $\sim 3.47 - 4.67 \times 10^{-14} \text{m}^3\text{N}^{-1}\text{m}^{-1}$ when sliding tests are done at 200°C , 400°C and 500°C respectively.

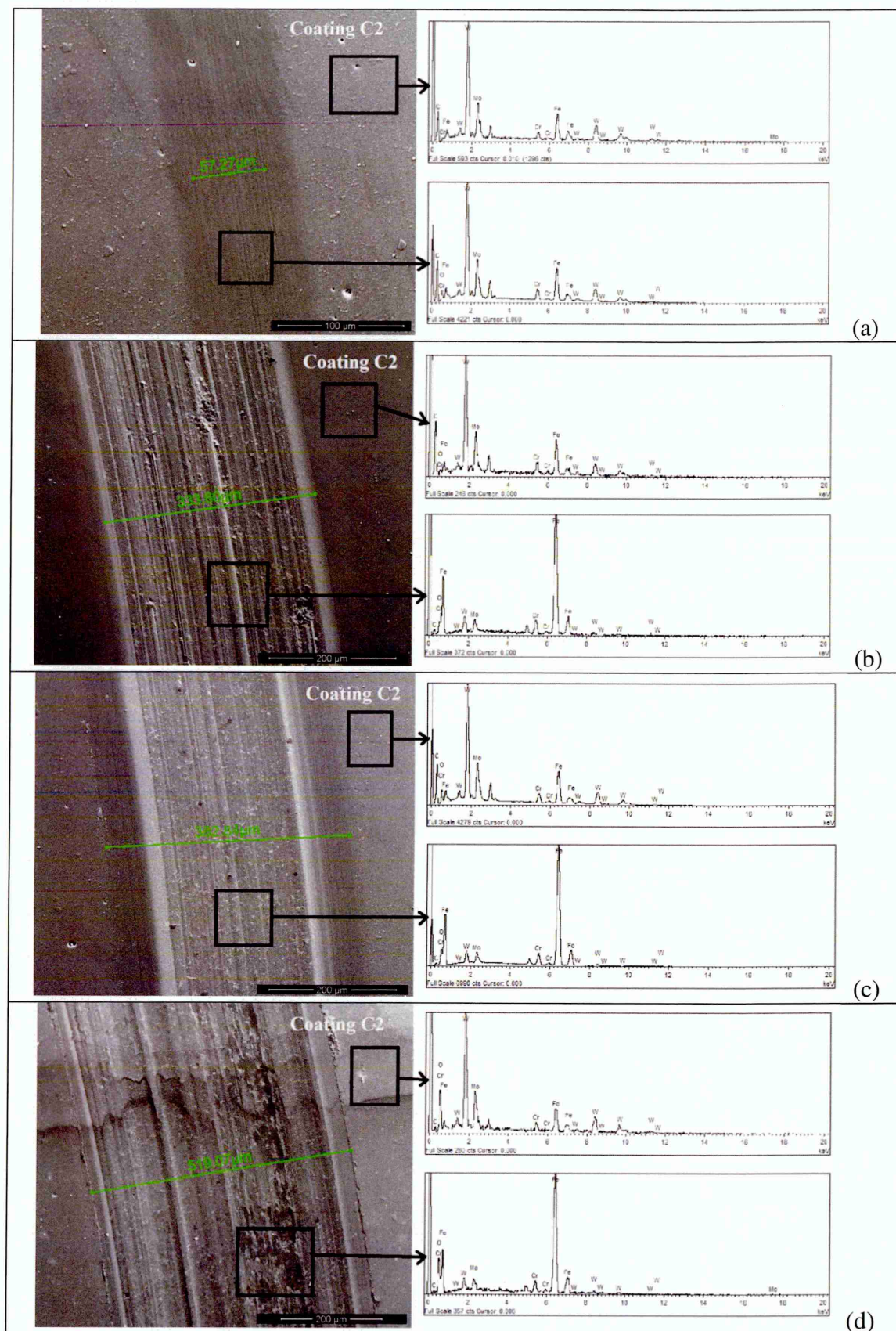


Figure 4.4-5: SEM images of the wear tracks of C2 after dry sliding against Al_2O_3 balls at (a) ambient temperature, (b) 200°C, (c) 400°C and (d) 500°C

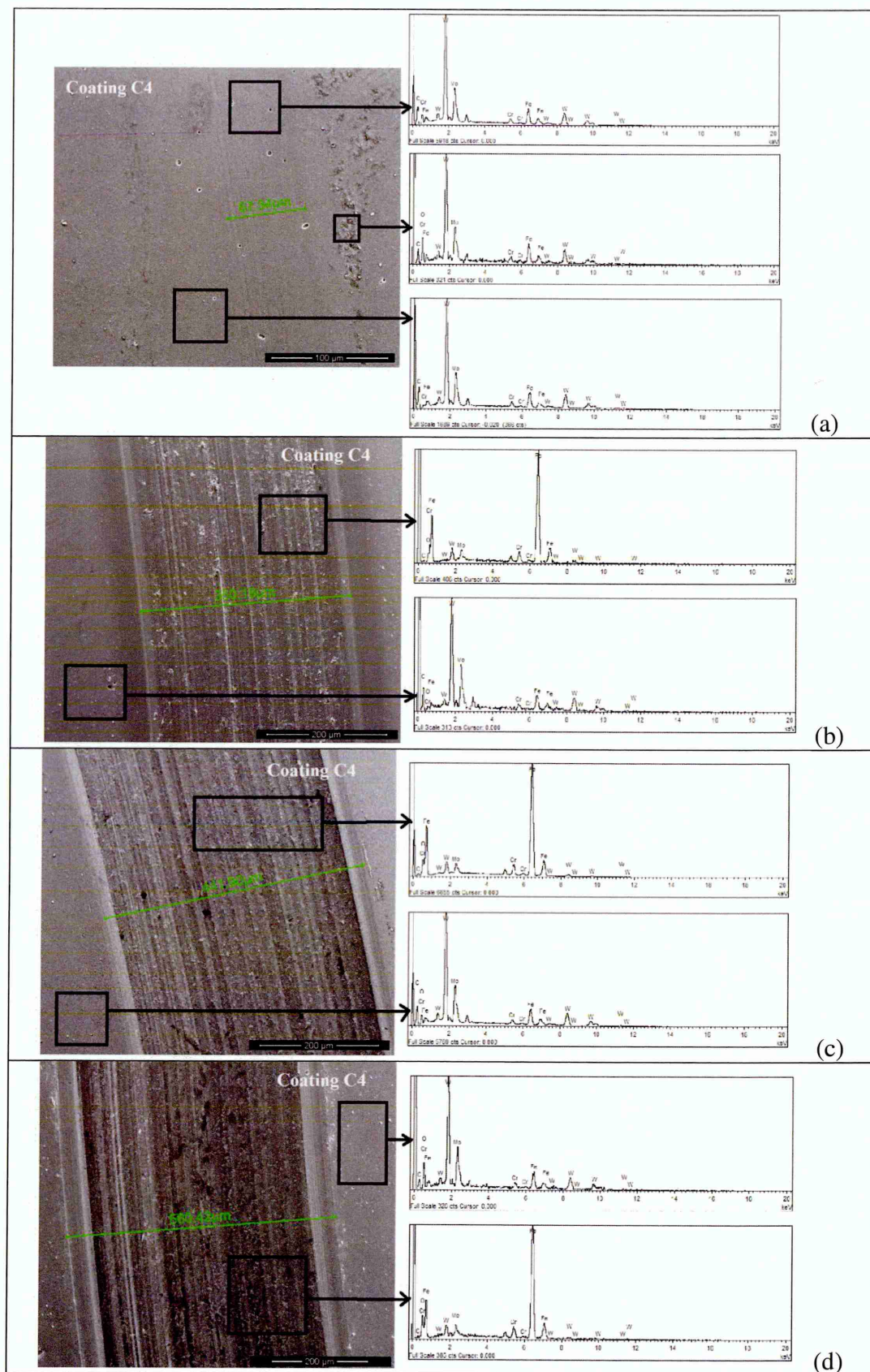


Figure 4.4-6: SEM images of the wear tracks of C4 after dry sliding against Al_2O_3 balls at (a) ambient temperature, (b) 200°C, (c) 400°C and (d) 500°C

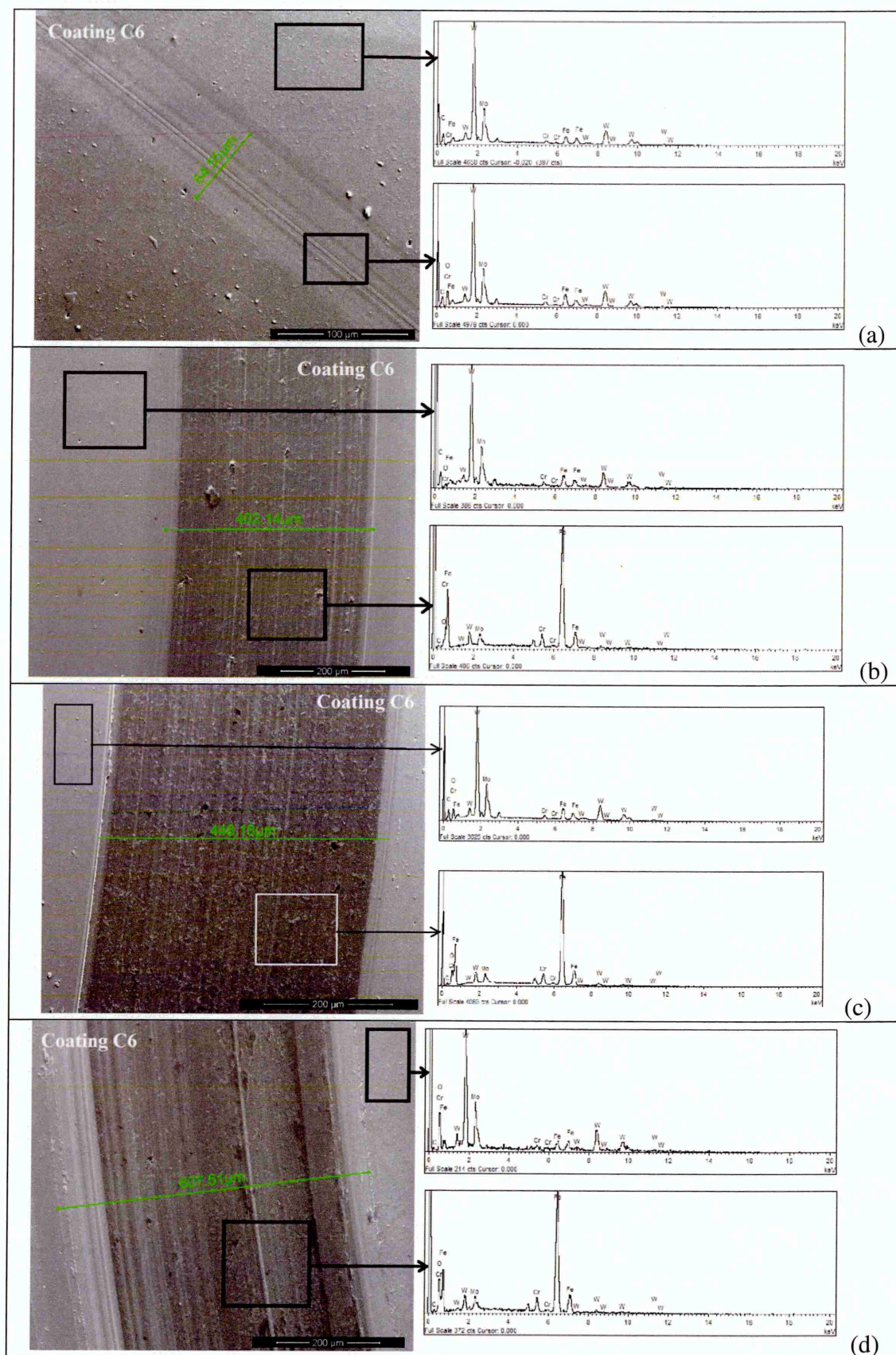


Figure 4.4-7: SEM images of the wear tracks of C6 after dry sliding against Al_2O_3 balls at (a) ambient temperature, (b) 200°C, (c) 400°C and (d) 500°C

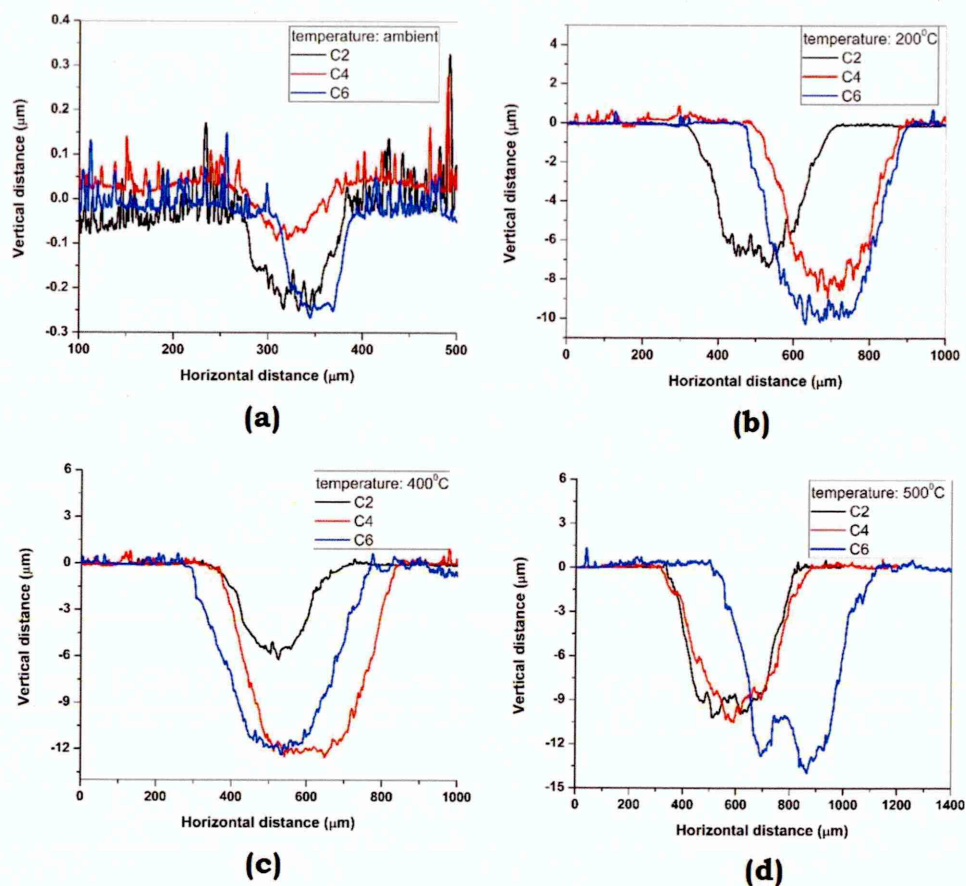


Figure 4.4-8: Wear track profiles of Mo-W-C coatings after dry sliding against Al_2O_3 balls at (a) ambient temperature, (b) 200°C, (c) 400°C and (d) 500°C

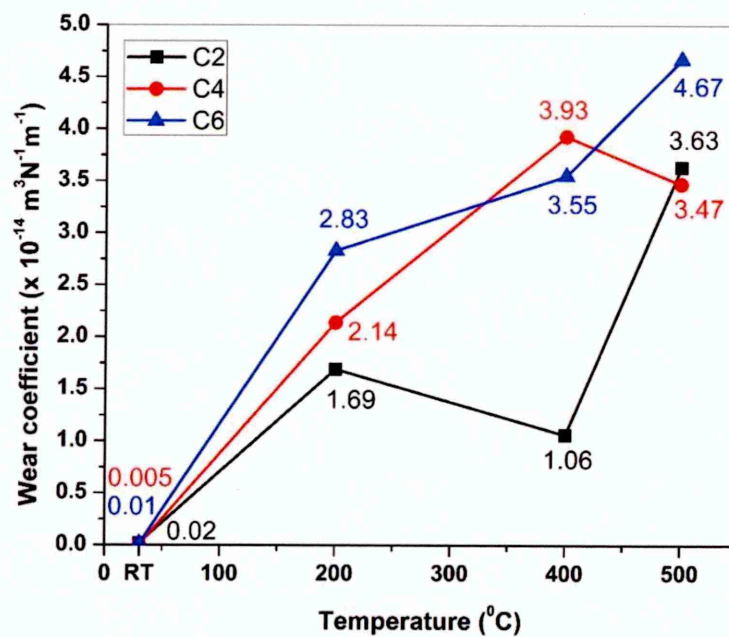


Figure 4.4-9: Wear coefficient of Mo-W-C coatings after dry sliding against Al_2O_3 balls at ambient and elevated temperature

The wear behaviour of Mo–W–C coatings are further investigated using Raman spectroscopy. Figure 4.4-10 shows the Raman spectra collected from the wear tracks and the adhered debris after sliding at ambient condition and details of the deconvoluted peaks are listed in table A-15 (see appendix A). The spectra collected from the wear tracks are found similar to the as-deposited coatings and no adherence of ball material is observed within the track. The I_D/I_G ratio is found as 2.02, 2.12 and 2.43 for C2, C4 and C6 respectively indicating presence of graphitic carbon particles within the track. Mostly tungsten oxides (W_xO_y) are observed in the debris adhered to the track along with a little amount of MoO_3 . W_xO_y are formed when heated to 400°C [204], whereas MoO_3 forms ~550°C [205]. Thus it is clear that the flash temperature generated at the asperity contacts is >550°C. Formation of lubricious MoO_3 during sliding maintains the mean friction coefficient of Mo–W–C coatings in the range of ~0.116 – 0.267.

Figure 4.4-11 shows the Raman spectra collected from the wear tracks of Mo–W–C coatings after sliding at 200°C and table A-16 (see appendix A) lists the deconvoluted peaks. The adhered debris is observed in the middle of the wear track rather than the edges, thus the spectra are collected from the encircled area in the middle (position 1) and near the edge (position 2) of the wear track (see inset). The wear debris of position 1 contains graphitic carbon particles and different metal oxides including W_xO_y , MoO_3 and Fe_2O_3 . The presence of Fe_2O_3 indicates exposure of substrate within the wear track and all these oxides together increase the mean friction coefficient in the range of ~0.6 – 0.686. In addition, Mo–W–C coatings are still retained near the edges and presence of few W_xO_y peaks indicate oxidation of the coatings. As a result, the I_D/I_G ratio is decreased in the range of 1.45 – 2.38 after sliding.

Figure 4.4-12 shows the Raman spectra collected from the wear tracks of the Mo–W–C coatings after sliding at 400°C and the deconvoluted peaks are listed in table A-17 (see appendix A). The wear debris found in the middle of the wear track (position 1) contains no graphitic carbon particles but different metal oxides including W_xO_y , MoO_3 and Fe_2O_3 are observed. The strong presence of Fe_2O_3 indicates exposure of substrate within the wear track. The mean friction coefficient of C2 and C4 retains almost same at 400°C, however a decrease is observed for C6 due to formation of MoO_3 during sliding. The spectra collected from the wear track edges (position 2) indicate oxidation of Mo–W–C coatings but no exposure of substrate. The I_D/I_G ratio is decreased to 1.73 – 1.8 because of severe third-body abrasion during sliding.

Figure 4.4-13 shows the Raman spectra collected from the wear tracks of Mo–W–C coatings after sliding at 500°C and the deconvoluted peaks are listed in table A-18 (see appendix A). The wear debris contains W_xO_y , MoO_3 and dominant Fe_2O_3 peaks indicating complete substrate exposure within the wear track. Distinct MoO_3 peaks are observed in the spectra at $\sim 820\text{ cm}^{-1}$ indicating formation of significant amount of lubricious MoO_3 , which reduces mean friction coefficient of Mo–W–C coatings in the range of $\sim 0.41 - 0.439$. Moreover, no graphitic carbon particles are observed within the wear track at this high temperature.

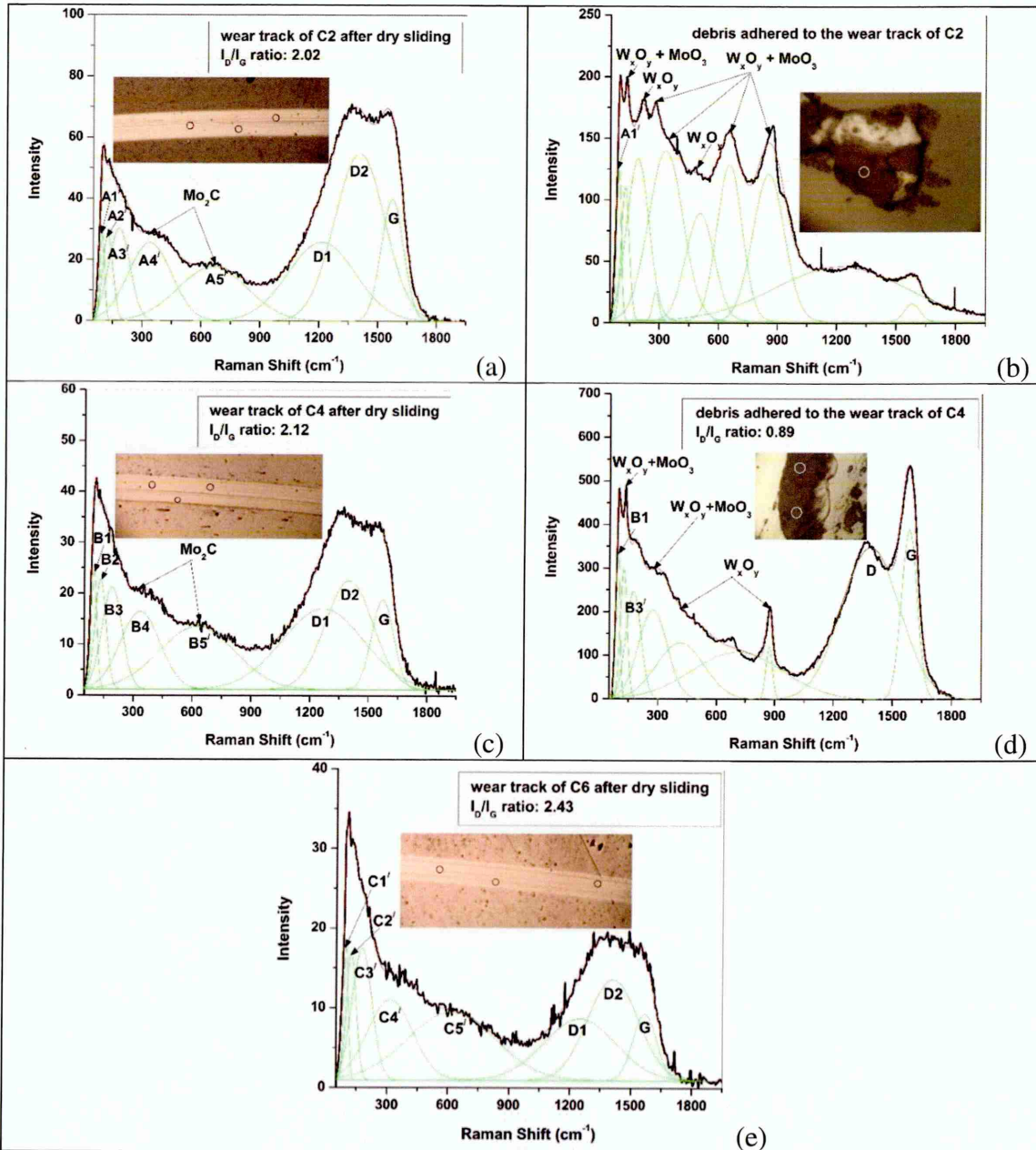


Figure 4.4-10: (a – e) Raman spectra collected from the wear tracks of Mo–W–C coatings after sliding against Al_2O_3 balls at ambient temperature

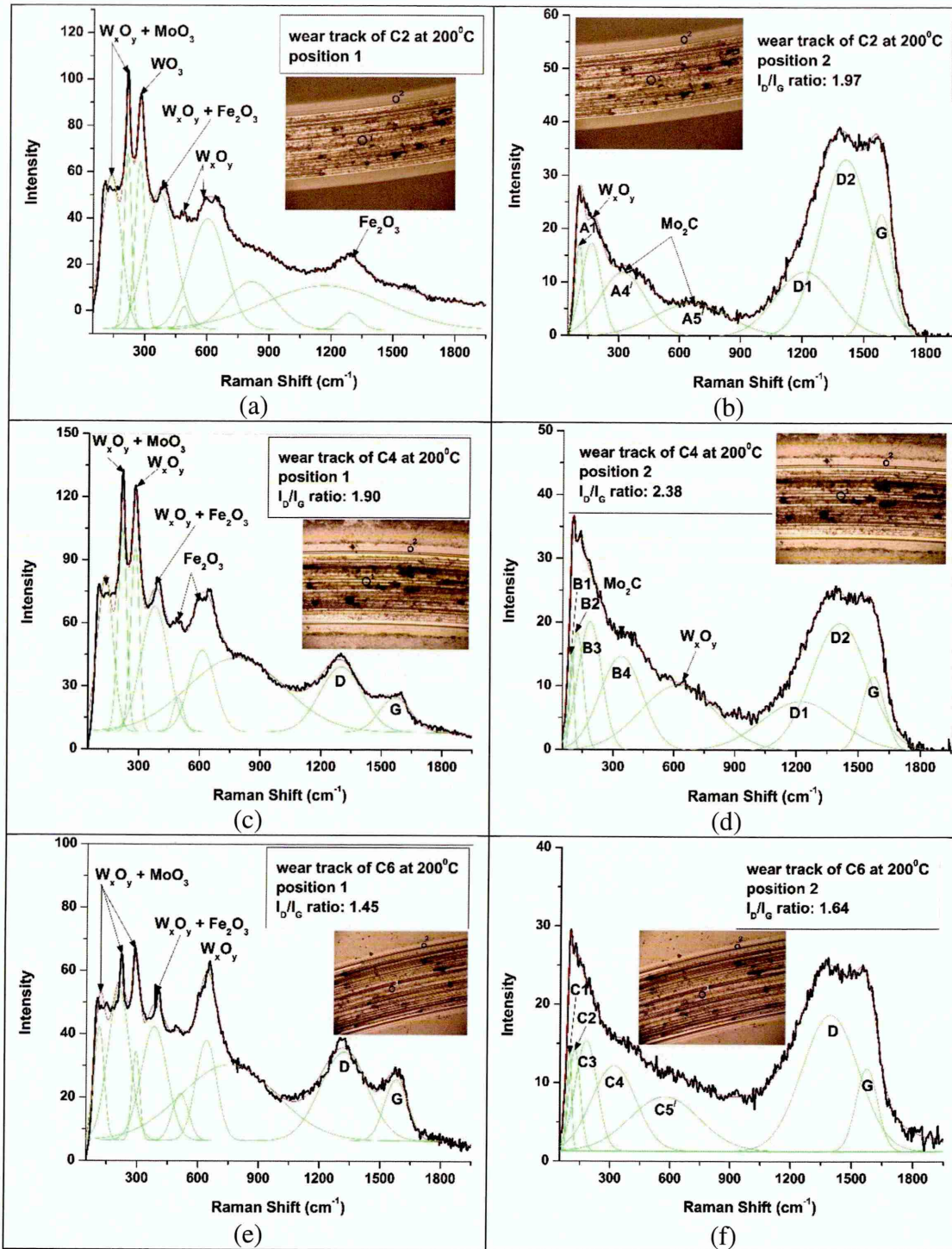


Figure 4.4-11: (a – f) Raman spectra collected from the wear tracks of Mo–W–C coatings after sliding against Al_2O_3 balls at 200°C

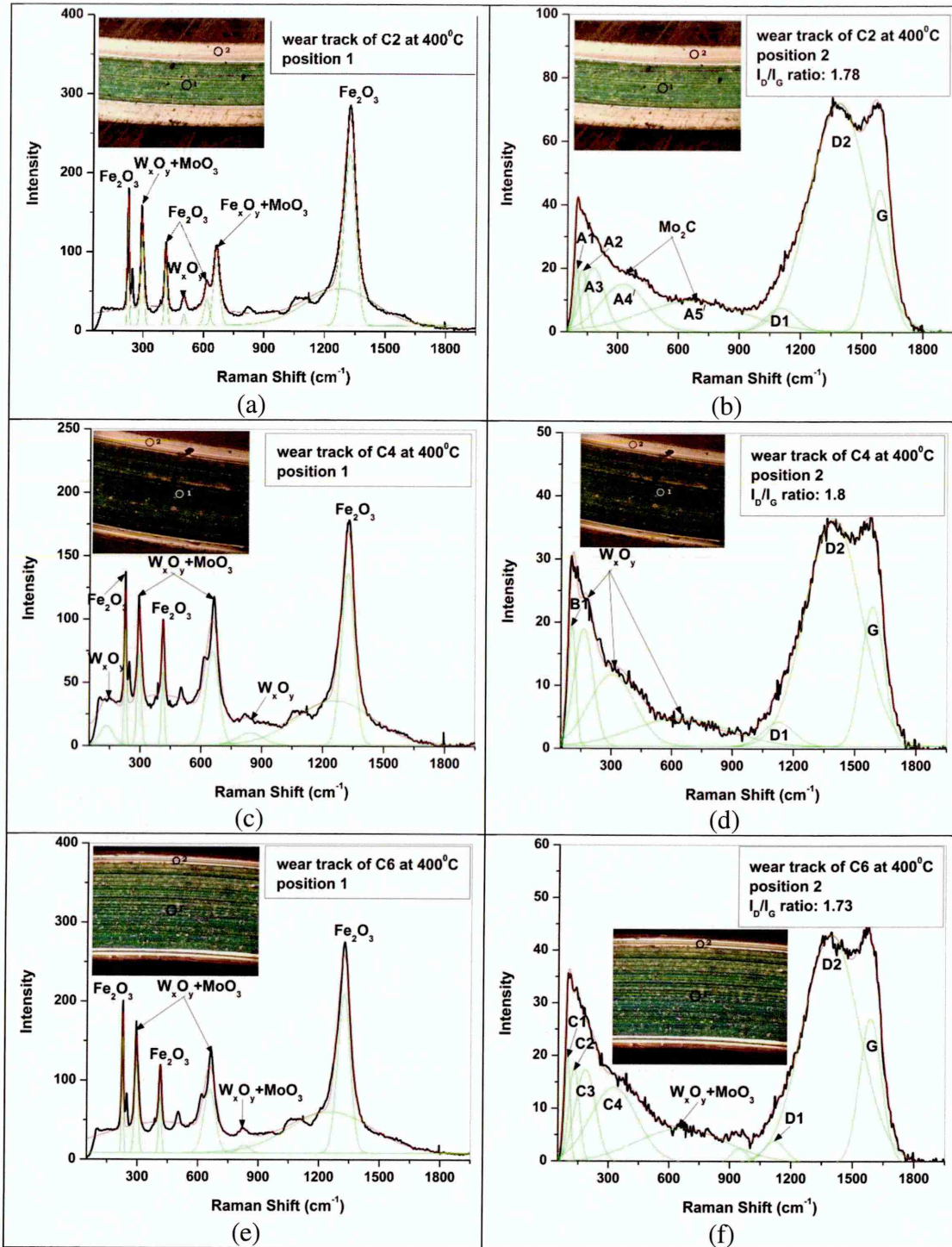


Figure 4.4-12: (a – f) Raman spectra collected from the wear tracks of Mo–W–C coatings after sliding against Al_2O_3 balls at 400°C

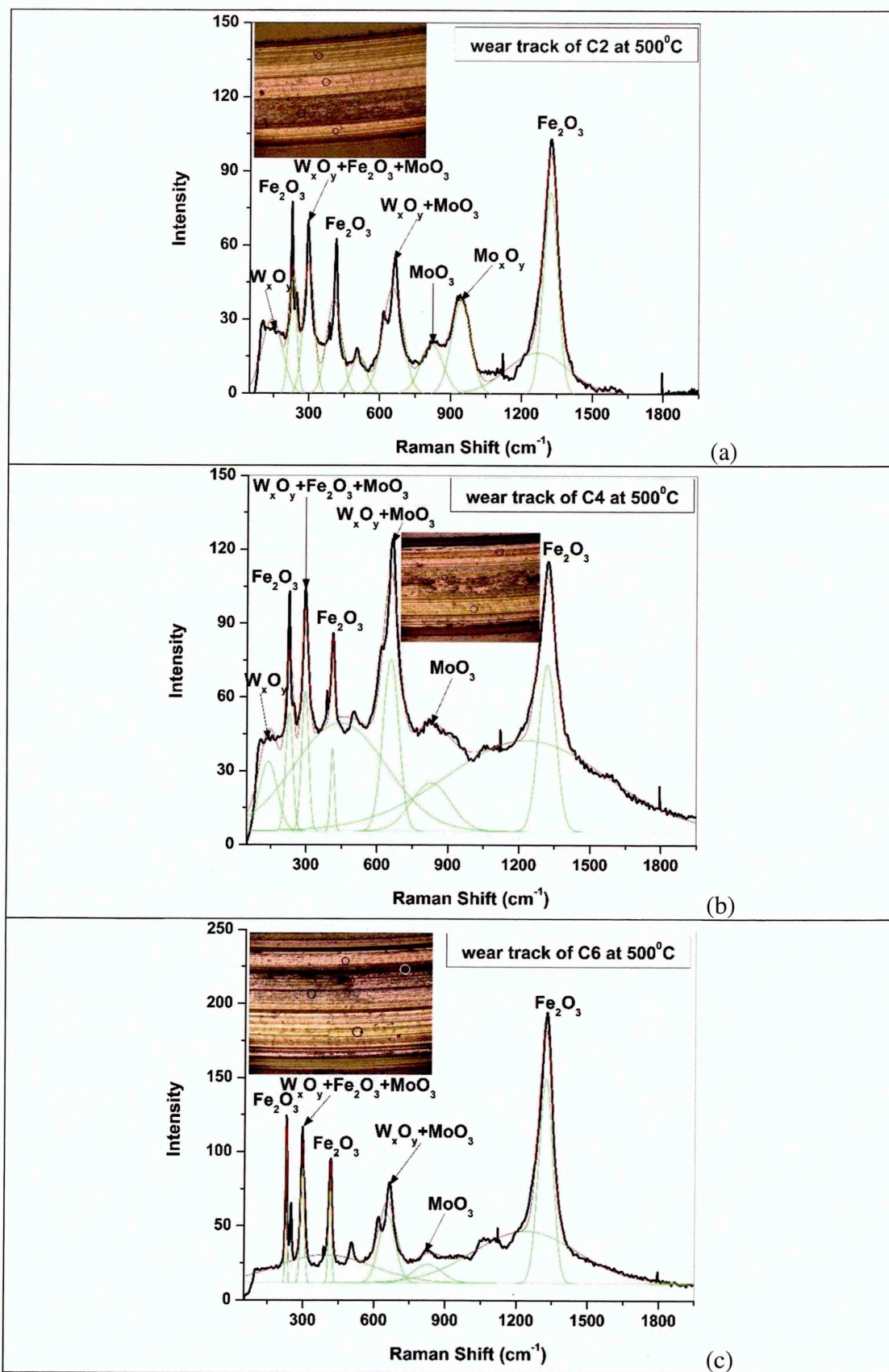


Figure 4.4-13: (a – c) Raman spectra collected from the wear tracks of Mo–W–C coatings after sliding against Al_2O_3 balls at 500°C

IV. Wear mechanism during dry sliding at elevated temperature

The friction and wear behaviour of Mo–W–C coatings during dry sliding at elevated temperature is influenced by formation of different metal oxide particles in the transfer layer. Raman analyses of the coatings and the counterparts reveal the wear mechanism. At ambient temperature, W_xO_y and MoO_3 are formed at the asperity contacts due to *oxidative* wear mechanism. The increase in test temperature favours formation of more metal oxides during sliding, however their hardness decreases almost linearly with rise in temperature [202]. As a result, the coatings are severely damaged due to third-body abrasion during sliding leading to wider wear track and exposure of the substrate within the wear track. Therefore high intensity Fe_2O_3 peaks are observed along with W_xO_y and MoO_3 peaks at elevated temperature. These metal oxides have stronger chemical affinity towards the coatings rather than counterparts, thus they are strongly adhered within the wear track. The wear mechanism at elevated temperature is found *oxidative* similar to ambient condition.

The friction coefficient at ambient temperature is influenced by presence of graphitic carbon particles and MoO_3 in the transfer layer. It is already discussed that MoO_3 acts effectively as solid lubricant unlike other metal oxides. The sliding is further promoted by the graphitic carbon particles, which maintains the mean friction coefficient of Mo–W–C coatings in the range of $\sim 0.116 - 0.267$ and the wear coefficient is observed in the order of $\sim 10^{-16} \text{ m}^3\text{N}^{-1}\text{m}^{-1}$. With rise in temperature up to 400°C , the graphitic nature of the carbon particles is decreased and more amount of metal oxides are formed leading to a rapid increase in friction and wear coefficients ($\mu > 0.6$ and $K_c \sim 10^{-14} \text{ m}^3\text{N}^{-1}\text{m}^{-1}$ respectively). At 500°C , no graphitic carbon particles are found within the wear track however formation of significant amount of lubricious MoO_3 reduces the mean friction coefficient in the range of $\sim 0.41 - 0.439$. The reduction in hardness of the metal oxides results in severe third-body abrasion during sliding, thus the wear coefficients are retained the in the range of $\sim 10^{-14} \text{ m}^3\text{N}^{-1}\text{m}^{-1}$.

4.4.3. Tribological behaviour of Mo–W–C coatings during boundary lubricated sliding at elevated temperature (200°C)

I. Experimental details

A CSM high temperature pin-on-disc tribometer was used to study the friction behaviour of Mo–W–C coatings against 100Cr6 steel balls under 5 N normal load in boundary lubricated condition (Mobil1 Extended lifeTM 10W-60 engine oil used as lubricant) at 200°C. The friction behaviour is discussed in section II and the wear behaviour of both the coatings and the counterparts are described in sections III and IV respectively. The secondary electron detector and the optical microscope were used for topographical imaging of the transfer layer formed on the ball surfaces and within the wear tracks. The X-ray mapping was done on the wear scar of the counterpart surfaces in order to identify the elemental composition of the adhered debris. The wear coefficient of the coatings and the counterparts was calculated with the help of surface profilometer and optical microscope. Raman spectra were collected from the counterpart surfaces and the wear tracks with 60 s exposure time. The relevant wear mechanism is discussed in section V.

II. Friction behaviour of Mo–W–C coatings during lubricated sliding

Figure 4.4-14 shows the friction behaviour of Mo–W–C coatings against uncoated 100Cr6 steel balls in lubricated condition at 200°C. C2 shows an initial run-in period of ~270 m with a mean friction coefficient of ~0.074 followed by a drastic decrease in friction coefficient to ~0.036 for rest of the sliding distance (i.e. ~1.5 km). C4 shows a friction coefficient of ~0.095 up to a sliding distance of ~440 m and then a slow but steady decrease in friction coefficient is observed for rest of the sliding distance leading to a mean friction value of ~0.065. A similar trend is observed for C6, which shows an average friction coefficient of ~0.087 for initial ~630 m distance and then it decreases to ~0.061 for rest of the sliding distance. Overall, the mean friction coefficients of C2, C4 and C6 are found as ~0.042, ~0.072 and ~0.07 respectively. It should be noted that the friction coefficients of C4 and C6 continuously decrease with increase in sliding distance, whereas almost stable friction coefficient is observed for C2. This indicates a possibility for C4 and C6 providing further reduction in friction compared to C2 if the sliding tests

are carried out for larger distances. In that case, C4 will provide best tribological performance in lubricated condition compared to other coatings irrespective of test temperature.

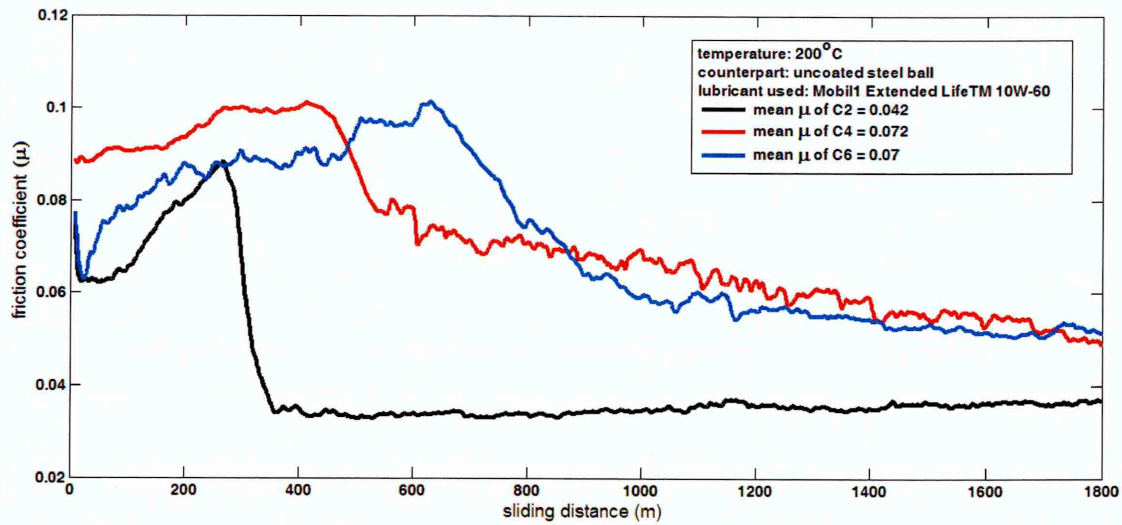


Figure 4.4-14: Friction behaviour of Mo-W-C coatings at 200°C in lubricated condition against steel counterparts

III. Wear behaviour of steel counterparts during lubricated sliding

Figures 4.4-15a – 4.4-15c show the transfer layer formed on the steel counterparts and figures 4.4-15d – 4.4-15f show the debris strongly adhered to the counterparts after lubricated sliding against Mo-W-C coatings at 200°C. Based on these wear scars, the wear coefficients of the counterparts are calculated as $10.8 \times 10^{-13} \text{ m}^3\text{N}^{-1}\text{m}^{-1}$, $3.44 \times 10^{-13} \text{ m}^3\text{N}^{-1}\text{m}^{-1}$ and $6.17 \times 10^{-13} \text{ m}^3\text{N}^{-1}\text{m}^{-1}$ after sliding against C2, C4 and C6 respectively.

The elemental composition of the debris adhered to the counterpart surfaces after lubricated sliding is further investigated using X-ray mapping as shown in figure 4.4-16. The tungsten, molybdenum and sulphur maps show their presence only on the adhered debris. Carbon and iron are present all over the wear scar, however the intensity of iron is observed lower within the adhered debris. These maps indicate that the adhered debris is composed of graphitic carbon particles and sulphides of tungsten and molybdenum. The lower intensity of iron within the debris shows the possible absence of iron sulphides.

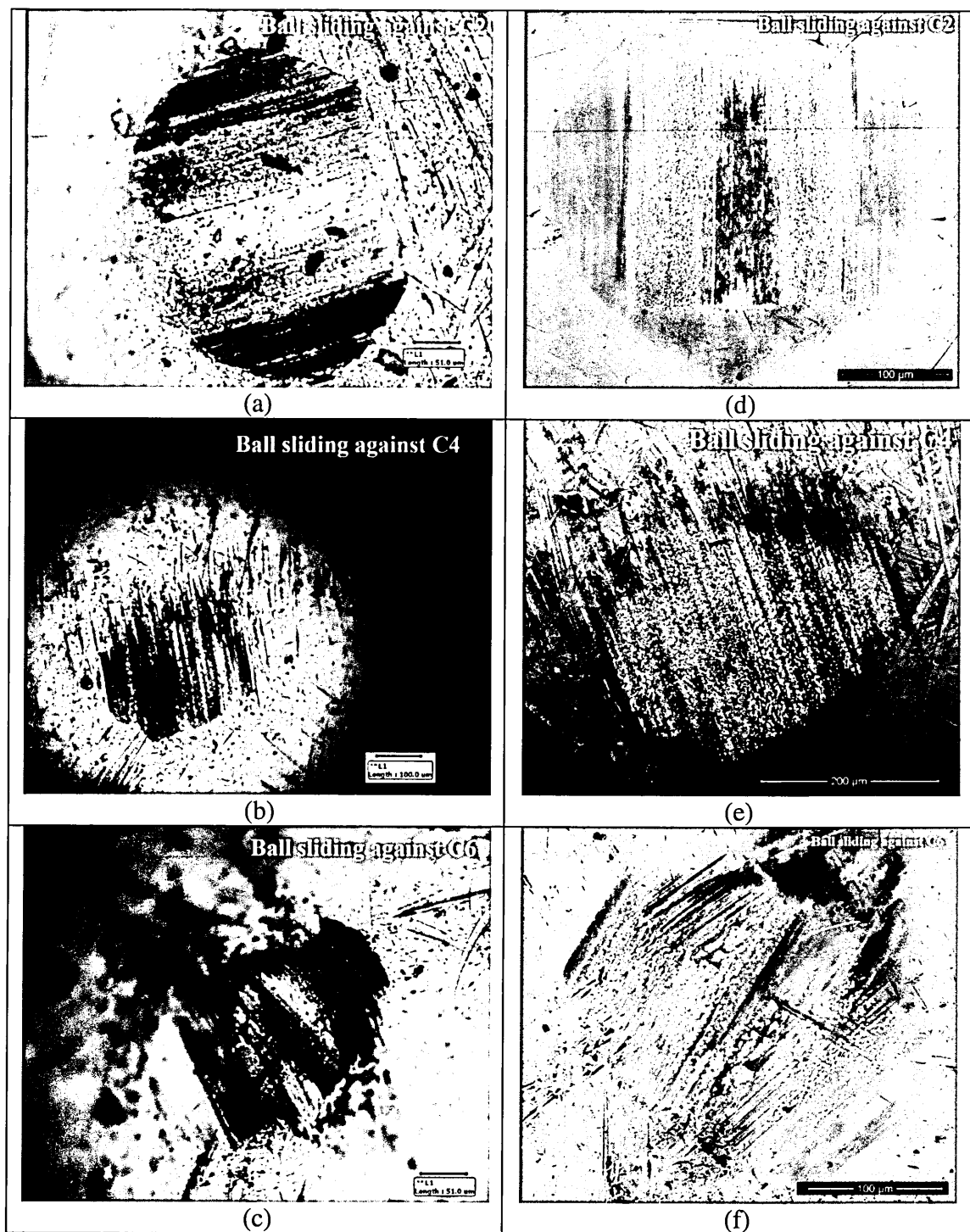


Figure 4.4-15: (a – c) Transfer layer formed on the steel counterparts and (d – f) debris strongly adhered to the steel counterparts after lubricated sliding at 200°C

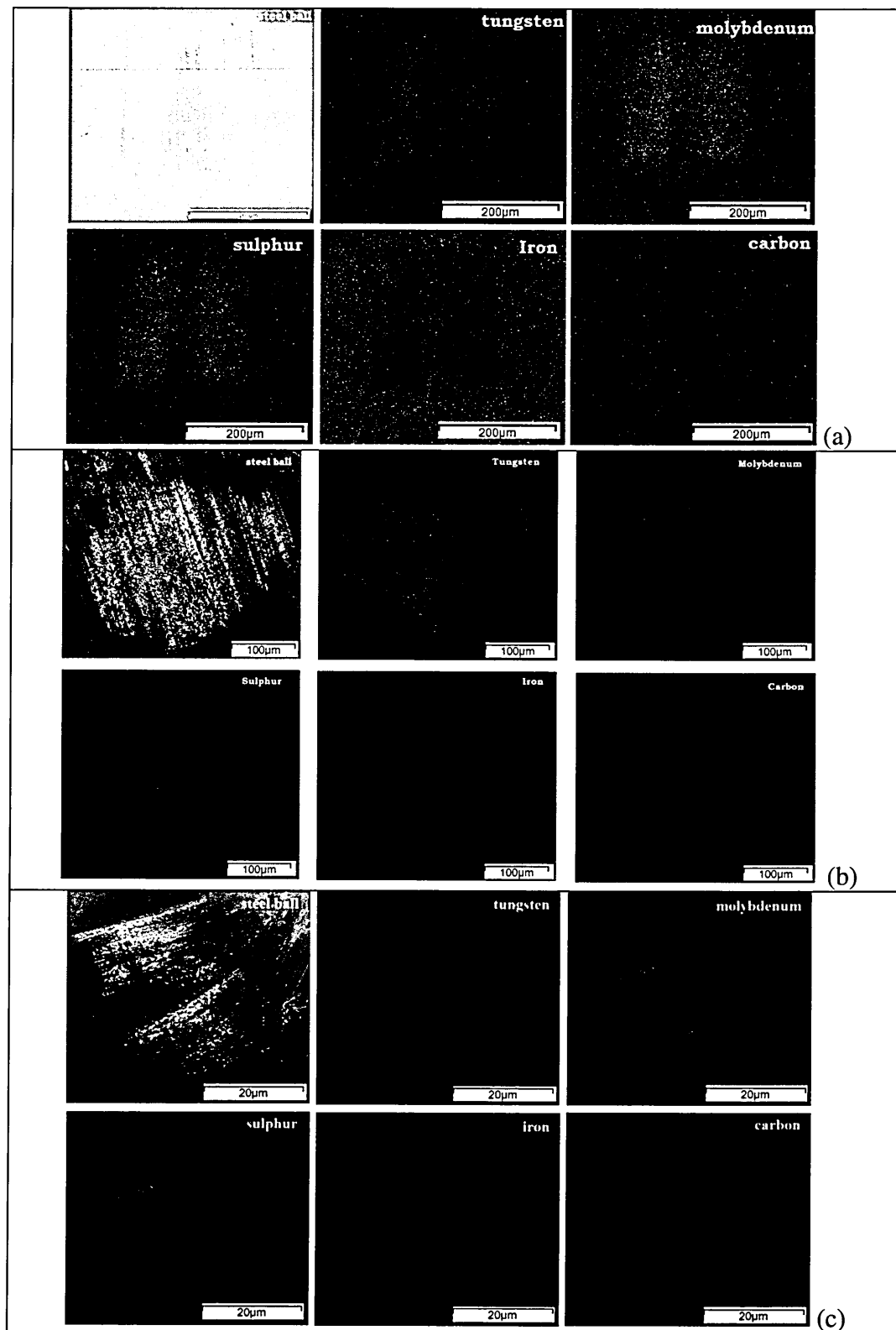
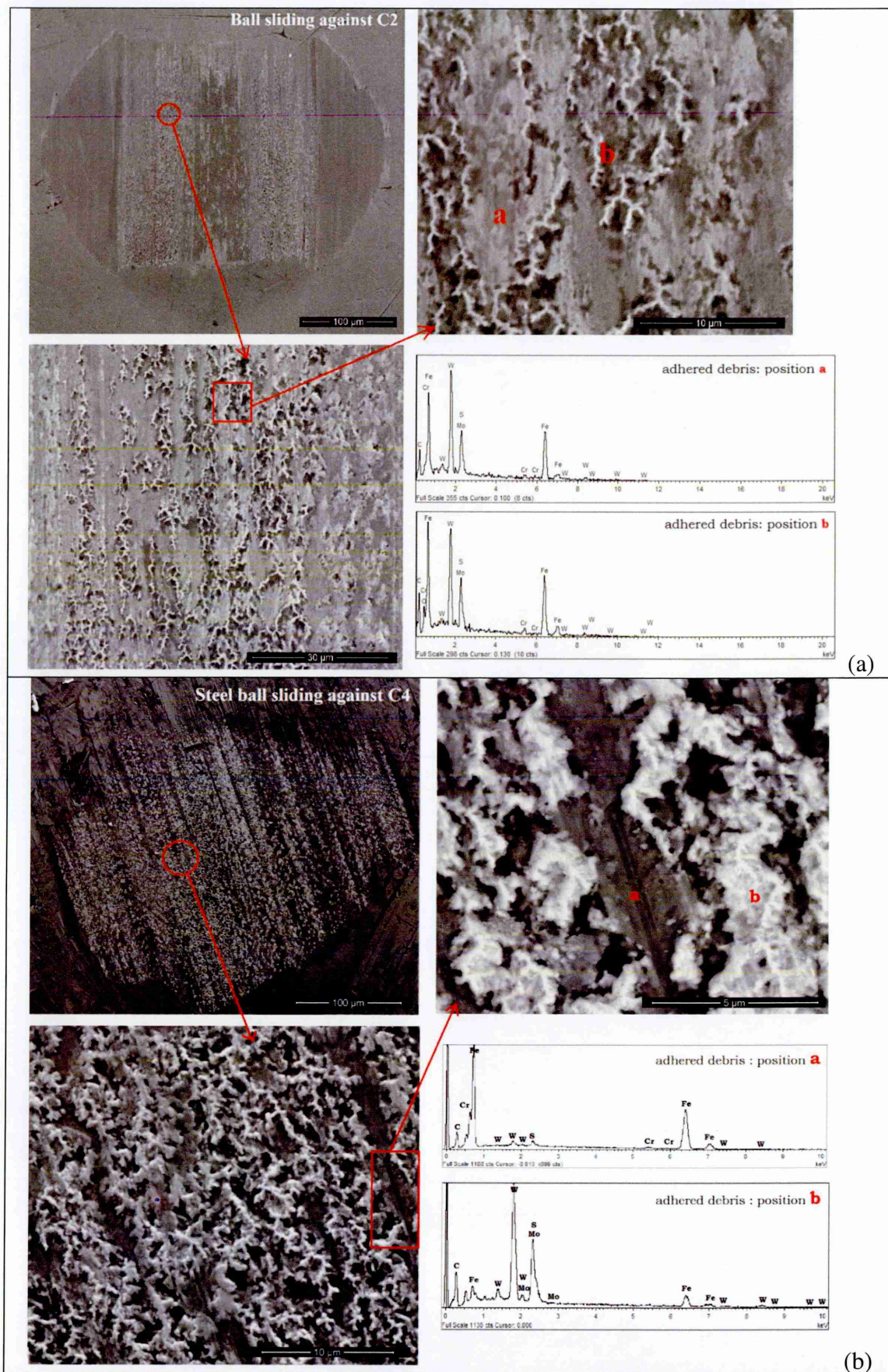


Figure 4.4-16: (a – c) X-ray mapping of the debris adhered to the steel counterpart after lubricated sliding against Mo-W-C coatings at 200°C

Figure 4.4-17 shows the SEM images and the EDX analyses of the debris adhered to the counterparts after lubricated sliding against Mo–W–C coatings at 200°C. The first image shows the complete view of the debris adhered to the ball surface and then two images of the debris are shown at two different magnifications. The images taken at largest magnification clearly point out *position a*, where the debris is smeared on the ball surface and *position b*, where the debris is accumulated and thickened on the ball surface. The EDX analysis is carried out on these two positions in order to understand the elemental composition of the adhered debris. The counterpart sliding against C2 shows same EDX spectra having strong peaks of Fe, Cr, C, W, Mo and S when collected from *position a* and *position b* (see figure 4.4-17a). Peaks of Fe, Cr and C indicate steel ball surface, whereas peaks of W, Mo and S indicate formation of a layer containing both WS₂ and MoS₂ on the ball surface.

Unlike C2, different EDX spectra are observed when collected from *position a* and *position b* of the debris formed after sliding against C4 and C6 (see figures 4.4-17b and 4.4-17c). The EDX spectrum collected from *position a* shows strong peaks of Fe, Cr and C and weak peaks of W, Mo and S. Thus *position a* basically indicates the ball surface, which is possibly covered by graphitic carbon, MoS₂ and WS₂ particles formed during sliding. The EDX spectrum collected from *position b* shows strong presence of W, Mo and S, which indicates that the accumulated debris on *position b* is a thick layer consisted of a mixture of WS₂ and MoS₂. It is believed that both WS₂ and MoS₂ are formed due to the chemical reactions taking place at the asperity contacts during lubricated sliding and adhered to the ball surface. The test temperature of 200°C favours the formation of these metal sulphides at the asperity contacts rather than ambient temperature as indicated by the EDX spectrum (see section 4.2.3 of chapter 4.2). Both WS₂ and MoS₂ are well known solid lubricants, which significantly reduce the friction coefficient during lubricated sliding at elevated temperature.



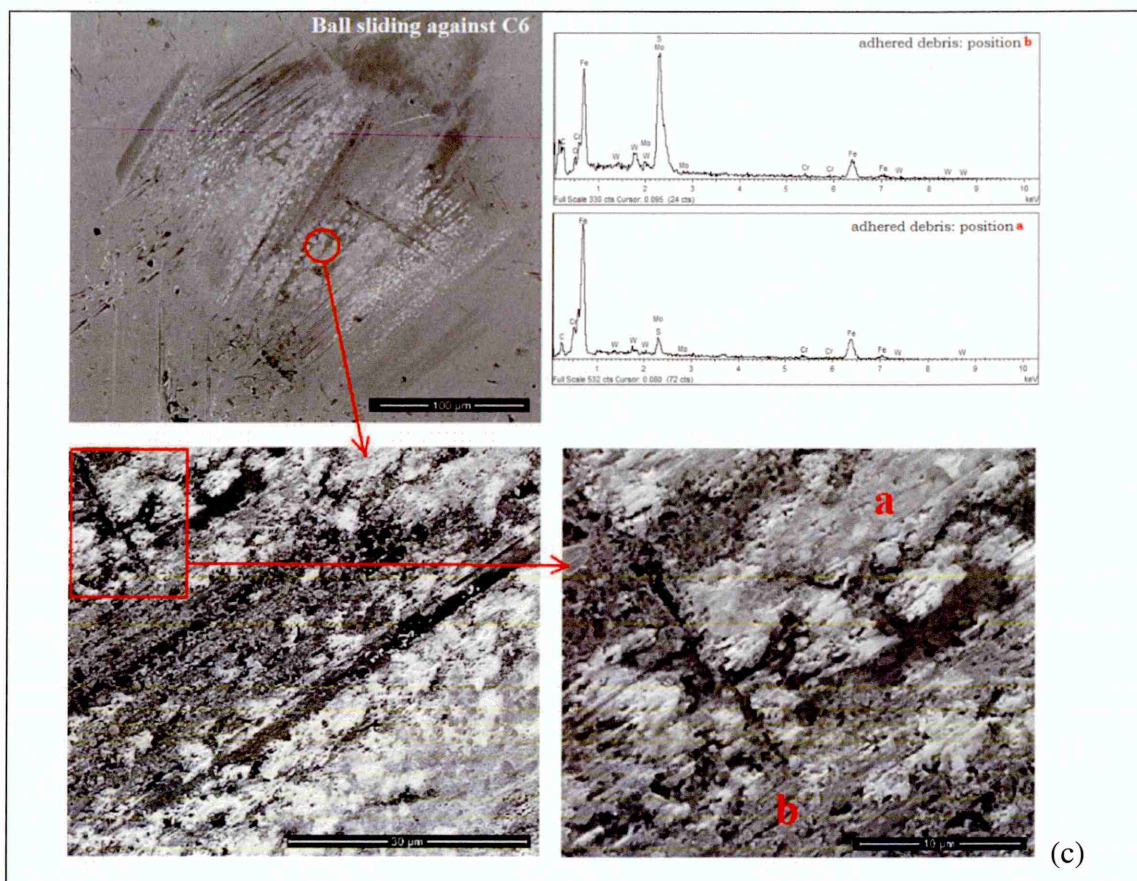


Figure 4.4-17: (a – c) SEM images and EDX analysis of the debris adhered to the steel counterpart after lubricated sliding against Mo–W–C coatings at 200°C

Figure 4.4-18 shows the Raman spectrum collected from the debris adhered to the steel ball after lubricated sliding against C2 at 200°C. The image of the debris is provided in the inset and the encircled areas show the positions of spectrum collection i.e. *position a* and *position b*. After deconvolution of the spectrum collected from *position a*, six peaks are observed within the spectrum range of $\sim 50 - 600 \text{ cm}^{-1}$ as listed in table A-19 (see appendix A). Peaks P1 – P4' belong to the steel ball whereas two sharp and dominant peaks centred at $\sim 382.5 \text{ cm}^{-1}$ and $\sim 408 \text{ cm}^{-1}$ indicate strong presence of MoS_2 and WS_2 phases. On the other hand, the spectrum collected from *position b* shows distinct and dominant D and G peaks at $\sim 1361.33 \text{ cm}^{-1}$ and $\sim 1591.06 \text{ cm}^{-1}$ respectively. The I_D/I_G ratio is calculated as 2.14 indicating graphitic nature of the carbon particles present in the debris. Two sharp peaks centred at $\sim 364.5 \text{ cm}^{-1}$ and $\sim 412 \text{ cm}^{-1}$ respectively are observed in the spectrum (table A-19 in appendix A lists all the deconvoluted peaks) indicating the presence of MoS_2 and WS_2 phases.

The Raman spectra collected from *position a* of the debris adhered to the steel ball after lubricated sliding against C4 and C6 at 200°C are shown in figures 4.4-19a and 4.4-20a respectively. The deconvoluted spectra contain distinct and dominant D and G peaks along with four other peaks within the spectrum range of ~50 – 600 cm⁻¹ as listed in table A-19. Peaks P1 – P3' belong to the steel ball, whereas peaks centred at ~323 cm⁻¹ (see figure 4.4-19a) and ~319 cm⁻¹ (see figure 4.4-20a) indicate strong presence of WS₂ phase. The debris formed after sliding against C4 shows two separate disordered peaks (D1 and D2) and G peak located at ~1349.53 cm⁻¹, ~1479.81 cm⁻¹ and ~1580.27 cm⁻¹ respectively and an I_D/I_G ratio of 1.41 (see figure 4.4-19a). Similarly, the debris adhered to the steel ball after sliding against C6 contains distinct D and G peaks located at ~1368.27 cm⁻¹ and ~1582.03 cm⁻¹ respectively and an I_D/I_G ratio of 1.3 (see figure 4.4-20a). These results support the findings of EDX analysis that *position a* on the ball surface is covered by amorphous carbon and WS₂ particles. It should be noted that EDX spectrum indicates possible formation of MoS₂ on *position a* of debris formed after sliding against C6 (see figure 4.4-17c), however it is not detected in the Raman analyses probably because of its little amount.

After deconvolution of the Raman spectra collected from the *position b* of the debris adhered to the steel ball after sliding against C4 and C6 respectively (see figures 4.4-19b and 4.4-20b), six peaks are found within the spectrum range of ~50 – 600 cm⁻¹ as listed in table A-19. Peaks P1' – P4' belong to the steel ball. The highest peak in the spectra belongs to WS₂ and MoS₂ phases (centred at ~406.5 cm⁻¹ and ~408 cm⁻¹ as shown in figures 4.4-19b and 4.4-20b respectively), whereas the second highest peak belongs to MoS₂ (centred at ~379 cm⁻¹ and ~381 cm⁻¹ as shown in figures 4.4-19b and 4.4-20b respectively). The MoS₂ and WS₂ phases are formed at the asperity contacts due to tribochemical reaction occurred between the coating and the sulphide-based EP additives of the engine oil during sliding. The rate of chemical reactions are promoted at 200°C, thus more amount of metal sulphides are formed as indicated by these high intensity peaks. Thus the Raman analyses completely agree with the X-ray mapping and EDX analyses confirming presence of graphitic carbon particles and solid lubricants like WS₂ and MoS₂ within the adhered debris. Based on these analytical results, the relevant chemical reaction is listed in equation set (8).



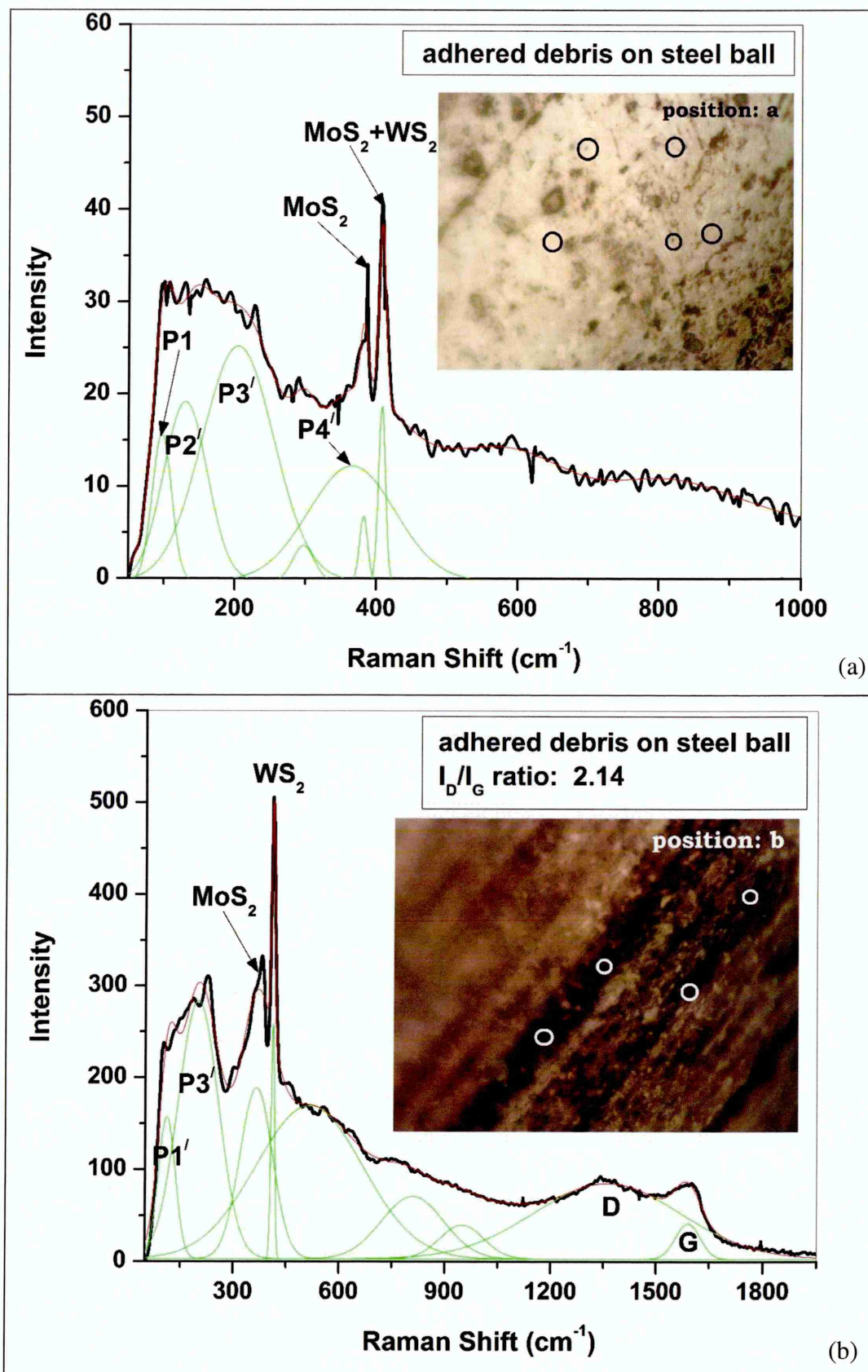


Figure 4.4-18: Raman spectra collected from the debris adhered to the steel counterpart after lubricated sliding against C2 at 200°C

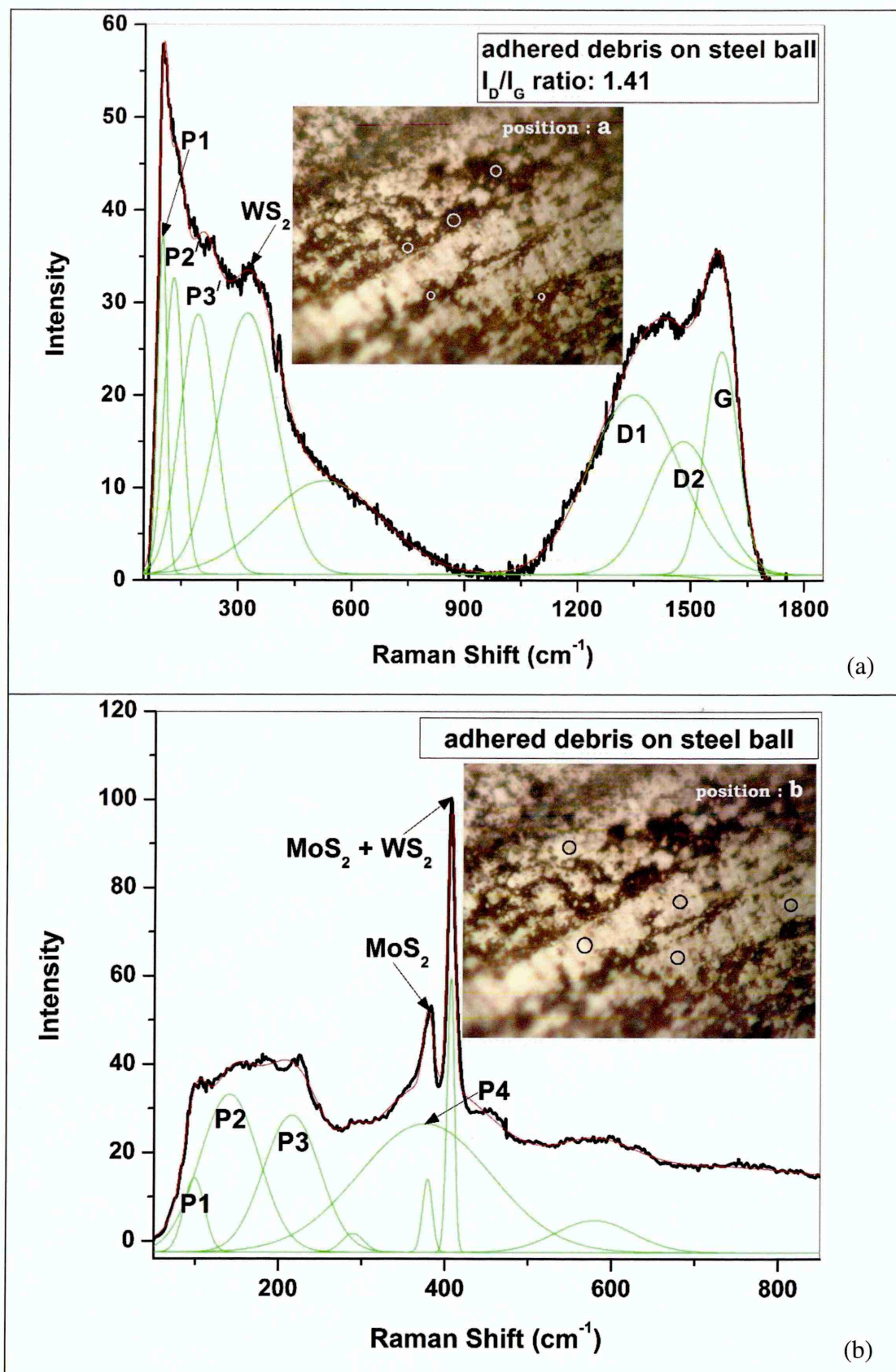


Figure 4.4-19: Raman spectra collected from the debris adhered to the steel counterpart after lubricated sliding against C4 at 200°C

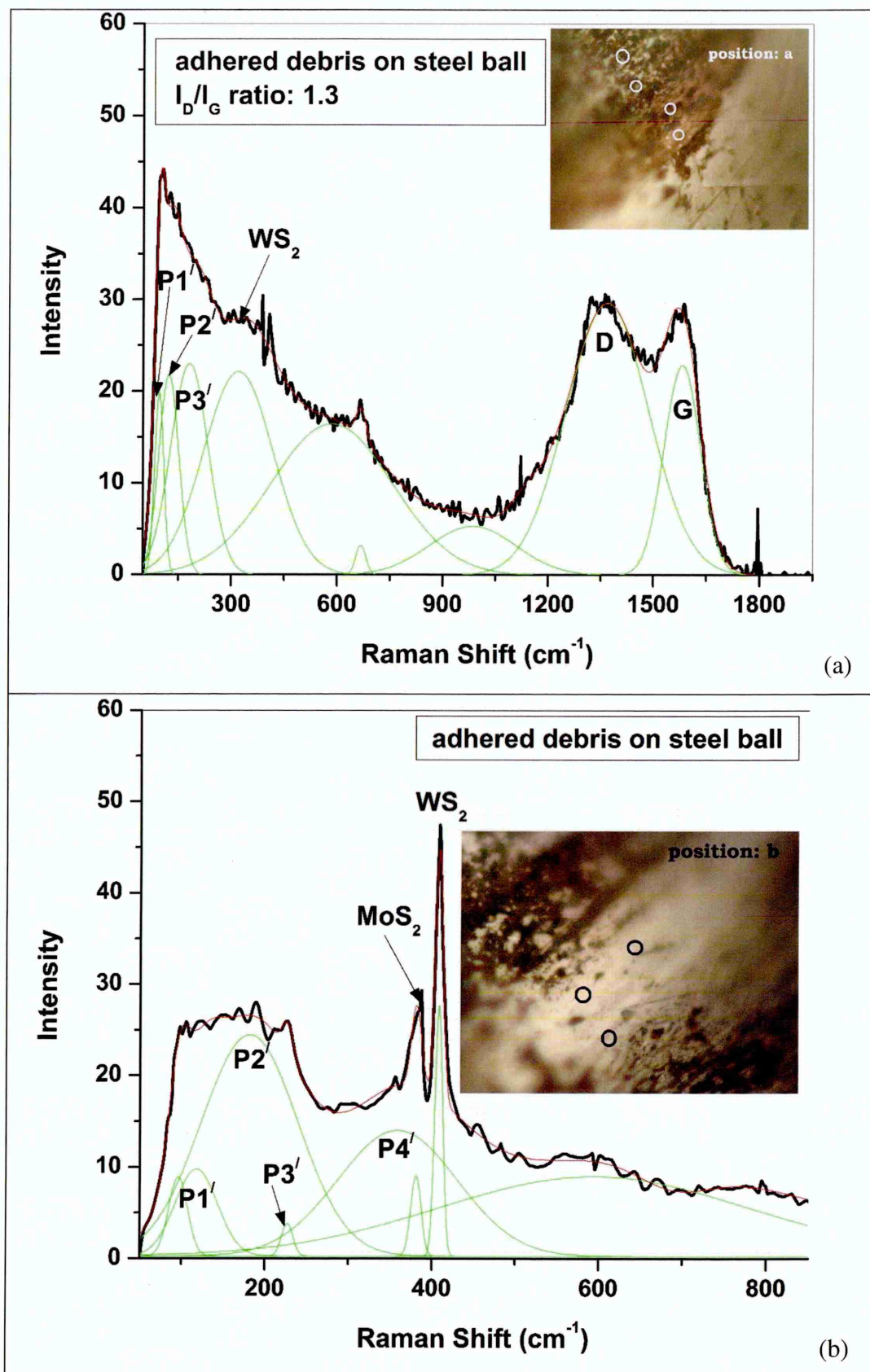


Figure 4.4-20: Raman spectra collected from the debris adhered to the steel counterpart after lubricated sliding against C6 at 200°C

IV. Wear behaviour of Mo–W–C coatings during lubricated sliding

Figure 4.4-21 shows SEM images of $\sim 219 - 283 \mu\text{m}$ wide wear tracks of Mo–W–C coatings after lubricated sliding against steel balls at 200°C . The EDX spectra collected within the wear tracks indicate strong presence of Mo, W and C similar to the as-deposited coatings. Thus the coatings are retained intact within the wear tracks after tracks. Further, the wear track of C2 contains no metal sulphides (see figure 4.4-21a), whereas the presence of metal sulphides (MoS_2 and WS_2) are observed in the wear tracks of C4 and C6 (see figures 4.4-21b and 4.4-21c).

Figure 4.4-22 shows the wear track profiles of Mo–W–C coatings after lubricated sliding. The average depth of wear tracks is found as $\sim 1.37 \mu\text{m}$, $\sim 1.72 \mu\text{m}$ and $\sim 1.88 \mu\text{m}$ for C2, C4 and C6 respectively, which is less than the respective coating thickness ($\sim 1.9 - 2.8 \mu\text{m}$ as shown in figure 4.1-1). This further confirms that the Mo–W–C coatings are retained intact within the wear track after lubricated sliding at 200°C . The wear coefficients are observed in the range of $\sim 0.92 - 1.11 \times 10^{-15} \text{ m}^3\text{N}^{-1}\text{m}^{-1}$.

Figure 4.4-23 shows the Raman spectra collected from the wear tracks of Mo–W–C coatings after lubricated sliding at 200°C . The wear track of C2 contains amorphous carbon particles and metal carbides similar to as-deposited surface. The disordered peaks (D1 and D2) and G peak are observed at $\sim 1141.05 \text{ cm}^{-1}$, $\sim 1383.31 \text{ cm}^{-1}$ and $\sim 1585.52 \text{ cm}^{-1}$ respectively and the I_D/I_G ratio is found as 1.36 (see figure 4.4-23a). The carbon particles adhered to the ball show a higher degree of graphitisation ($I_D/I_G = 2.14$ as shown in figure 4.4-18b) rather than the wear track indicating severe deformation of the debris adhered to the wear track during sliding. Unlike C2, metal sulphide peaks are observed in the wear tracks of C4 and C6 respectively and the deconvoluted peaks are listed in table A-20 (see appendix A). MoS_2 peak is observed in the wear track of C4 at $\sim 372 \text{ cm}^{-1}$ and WS_2 peak is observed in the wear track of C6 at $\sim 136.5 \text{ cm}^{-1}$. The I_D/I_G ratio of the graphitic carbon particles found in the wear tracks of C4 and C6 is observed as 1.55 and 1.49 respectively, which shows similar degree of graphitisation of the debris adhered to the ball (see figures 4.4-19a and 4.4-20a).

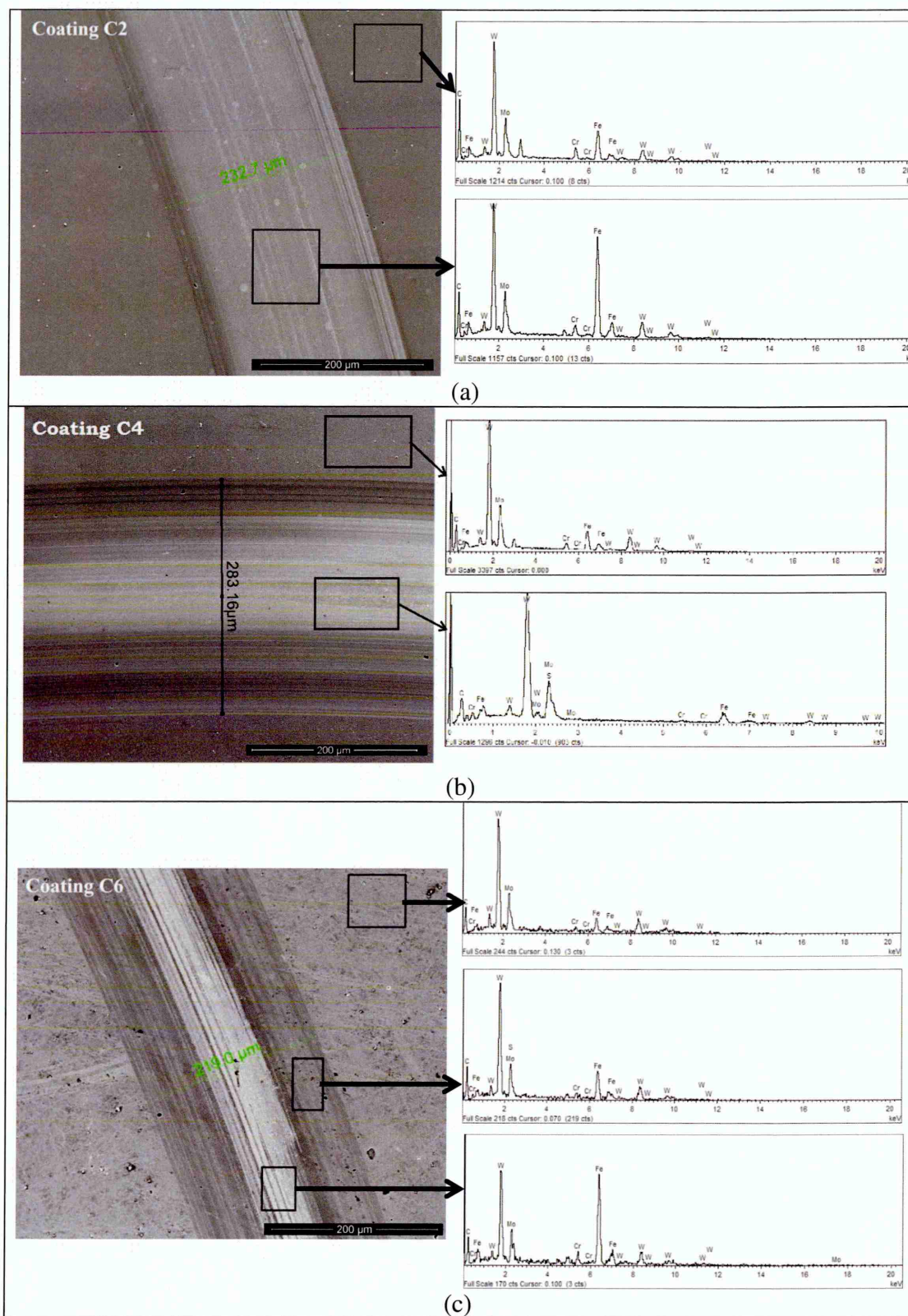


Figure 4.4-21: (a – c) SEM images of the wear tracks of Mo–W–C coatings after lubricated sliding against steel balls at 200°C

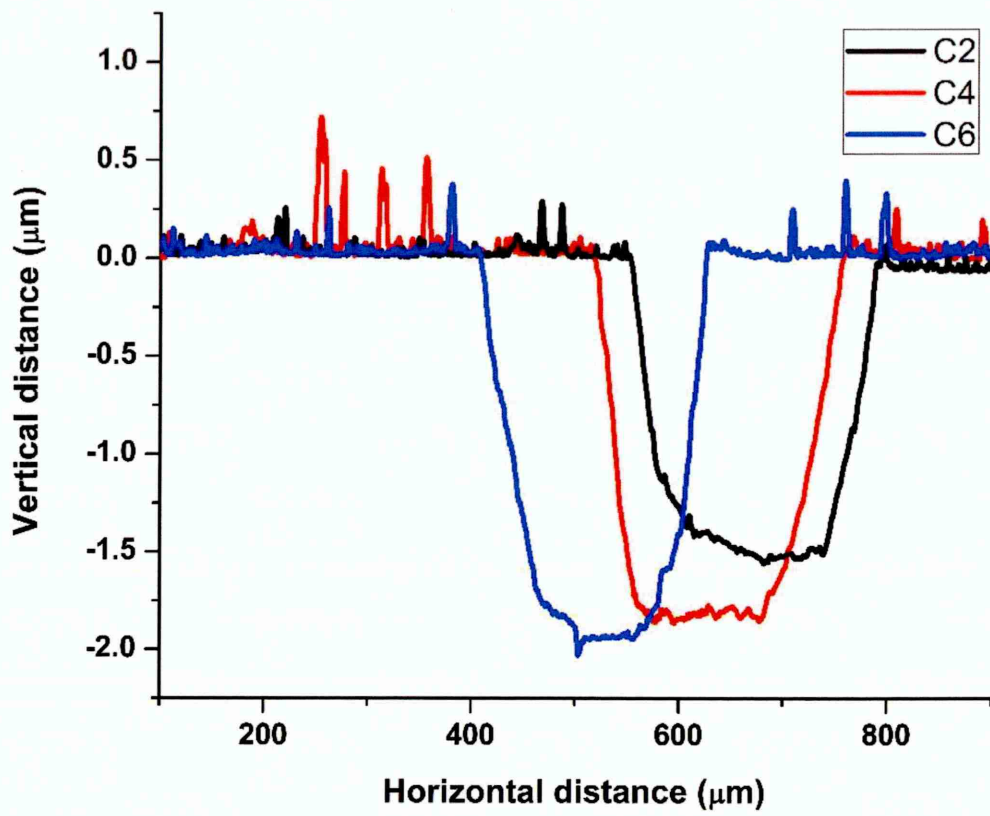


Figure 4.4-22: Wear track profile of Mo–W–C coatings after lubricated sliding against steel balls at 200°C

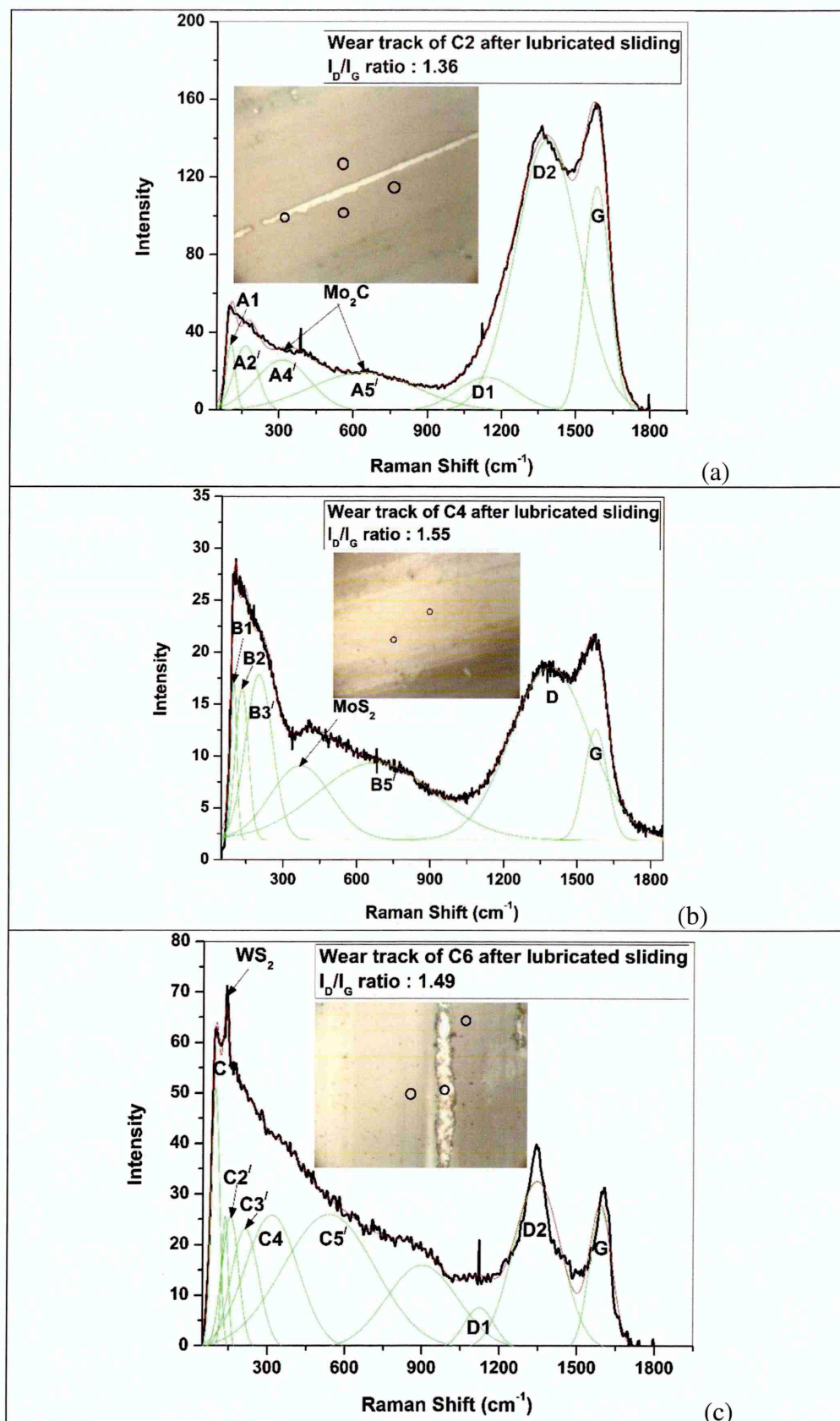


Figure 4.4-23: (a – c) Raman spectra collected within the wear track of Mo–W–C coatings after lubricated sliding against steel balls at 200°C

V. Tribo-chemically reactive wear mechanism during lubricated sliding at elevated temperature

The *tribochemically reactive* wear mechanism is observed for Mo–W–C coatings in boundary lubricated condition at ambient temperature. The continuous sliding between Mo–W–C coatings and the counterparts increases the flash temperature up to $\sim 800^{\circ}\text{C}$ at the asperity contacts. The chemical reactions occurred between Mo–W–C coatings and the sulphur-based EP additives of the engine oil produce metal sulphides at that high temperature. When the test temperature increases from ambient to 200°C , the chemical reactions are promoted and more amounts of metal sulphides are formed. The metal sulphide particles have stronger affinity towards the steel counterparts rather than the coatings, thus they adhere to the ball surfaces by forming a thick tribolayer (see figures 4.4-17 – 4.4-20).

The analytical techniques confirm the presence of graphitic carbon particles and metal sulphides such as WS_2 and MoS_2 phases in the debris adhered to the counterpart surfaces as well as within the wear tracks. Both WS_2 and MoS_2 promote sliding because of their layered structures and graphite-like lubricating properties [185]. The friction is further benefitted by the presence of amorphous carbon particles in the tribolayer. As a result, Mo–W–C coatings provide same low friction coefficient at ambient temperature ($\mu \sim 0.04 - 0.064$) and at 200°C ($\mu \sim 0.04 - 0.072$). Relatively higher wear coefficient is observed at 200°C ($K_c \sim 10^{-15} \text{ m}^3\text{N}^{-1}\text{m}^{-1}$) compared to ambient temperature (negligible wear), however the coatings are retained intact within the wear tracks in both the temperatures. It should be noted that the friction curves of Mo–W–C coatings show a steady decreasing trend with increase in sliding distance at 200°C . This indicates further reduction in the mean friction coefficient of Mo–W–C coatings for larger sliding distances. Hence, it is concluded that the *tribochemically reactive* wear mechanism of Mo–W–C coatings during lubricated sliding maintains its improved tribological properties at elevated temperature similar to ambient condition.

4.4.4. Comparison of tribological performance of C4 and DLC (Cr/Cr-WC/W:C-H/a:C-H) coatings at elevated temperature

A. Dry sliding against Al_2O_3 counterparts

Figure 4.4-24 shows the friction curves of $DLC(Cr/Cr-WC/W:C-H/a:C-H)$ coating at ambient and elevated temperature against Al_2O_3 balls under 5 N normal load. The mean friction coefficient is observed as ~ 0.083 at ambient condition, which decreases to ~ 0.044 at $200^\circ C$. Both the friction curves show dominant stick-slip motion due to present of moisture in the test environment. At $400^\circ C$, the friction curve becomes smooth through-out the steady-state period but the mean friction coefficient increases to ~ 0.075 . At $500^\circ C$, the friction curve becomes very smooth for first ~ 450 m distance with a mean friction coefficient of ~ 0.025 . Then dominant stick-slip motion is observed for rest of the sliding distance leading to a rapid increase in the mean friction coefficient to ~ 0.066 . It should be noted that at ambient condition both C4 and DLC coatings show almost similar friction coefficient (~ 0.116 and ~ 0.083 respectively), but then the friction coefficient of C4 increases to $\sim 6 - 16$ times depending on the rise in test temperature (see figure 4.4-1). Thus DLC coating performs better than C4 at elevated temperature during dry sliding.

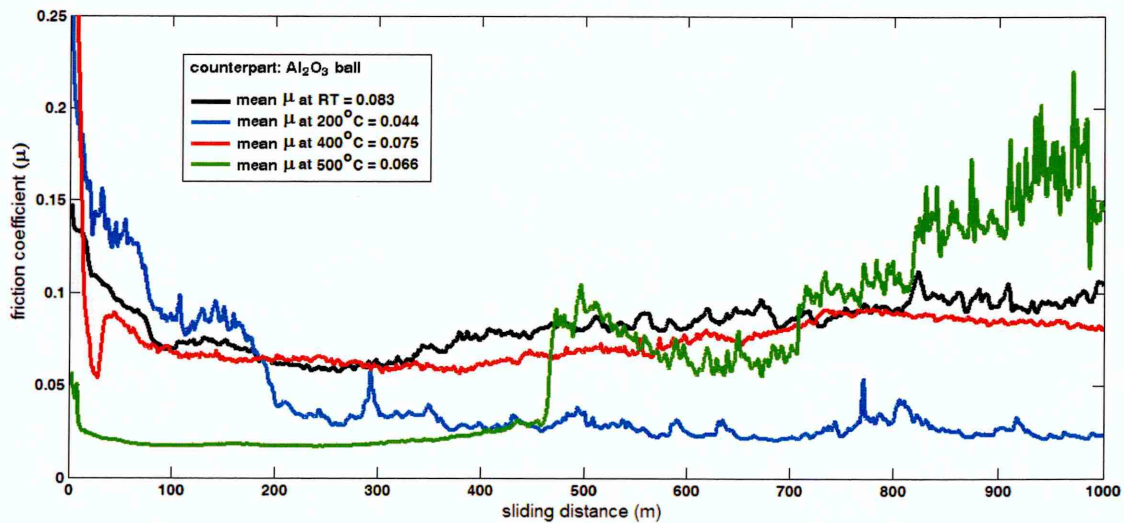


Figure 4.4-24: Friction behaviour of $DLC(Cr/Cr-WC/W:C-H/a:C-H)$ coating after dry sliding against Al_2O_3 balls at ambient and elevated temperature

Figure 4.4-25 shows the wear track profiles of DLC coating after sliding at ambient and elevated temperature (200°C – 500°C) and the SEM images of the respective track profiles are provided in the inset. The width of wear track is found as ~78 µm at ambient temperature, which increases to ~96 µm, ~146 µm and ~187 µm as the test temperature reaches to 200°C, 400°C and 500°C respectively. Lots of grooves are observed in the wear track at 500°C and the highest depth of wear track is found as ~2.2 µm, which is less than the coating thickness. Thus no substrate exposure is observed for DLC coating unlike C4. The wear coefficients of DLC coating is observed in the range of $\sim 1 - 3.6 \times 10^{-16} \text{ m}^3 \text{N}^{-1} \text{m}^{-1}$ up to 400°C, however it rapidly increases to $1.34 \times 10^{-15} \text{ m}^3 \text{N}^{-1} \text{m}^{-1}$ with local delamination of the coating at 500°C (image provided below the respective wear track). The wear coefficient of C4 is found $\sim 10^{-14} \text{ m}^3 \text{N}^{-1} \text{m}^{-1}$ after same sliding distance indicating lower wear resistance compared to DLC coating during dry sliding at elevated temperature.

Figure 4.4-26 shows the Raman spectra collected from the wear track of DLC coating after sliding at ambient and elevated temperature. At ambient condition, the disordered (D1 and D2) and G peaks are observed at $\sim 1283.97 \text{ cm}^{-1}$, $\sim 1450.52 \text{ cm}^{-1}$ and $\sim 1560.79 \text{ cm}^{-1}$ respectively and the I_D/I_G ratio is found ~ 1 (see figure 4.4-26a). When spectrum is collected from the wear track after sliding at 200°C and 400°C, the I_D/I_G ratio slightly decreases to 0.97 and 0.98 respectively (see figures 4.4-26b and 4.4-26c). The adhered debris is observed within the wear track at 500°C. The spectra collected from two different position of the adhered debris show presence of amorphous carbon particles along with different tungsten oxide phases (W_xO_y) as shown in figure 4.4-26d. The I_D/I_G ratio of the carbon particles is observed in the range of $\sim 0.87 - 1.16$. This indicates that the amorphous structure of as-deposited DLC coating (I_D/I_G ratio = 0.59) is graphitised after sliding. The presence of sharp W_xO_y peaks indicates exposure of tungsten-containing intermediate layer during sliding. The Raman spectra further confirms no exposure of substrate after sliding unlike C4.

Both C4 and DLC show *oxidative* wear mechanism during sliding at elevated temperature. However the difference in coating hardness plays an important role during dry sliding. DLC coating shows almost three times higher hardness than C4, which results in low friction and no substrate exposure within the wear track unlike C4. Thus DLC coating provides lower friction and wear coefficients than C4 during dry sliding at elevated temperature.

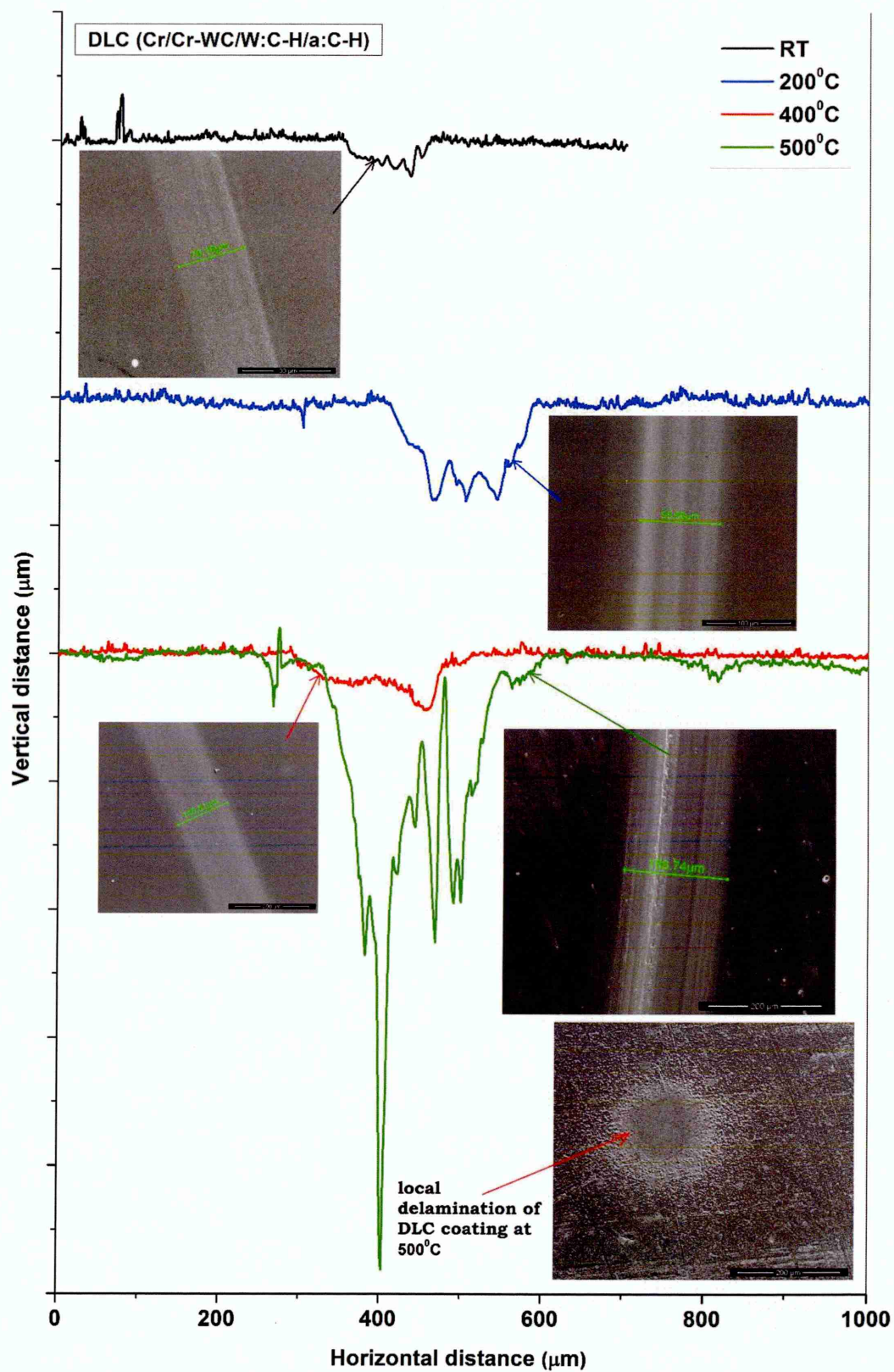


Figure 4.4-25: Wear track profile of $DLC(Cr/Cr-WC/W:C-H/a:C-H)$ coating after dry sliding against Al_2O_3 balls at ambient and elevated temperature

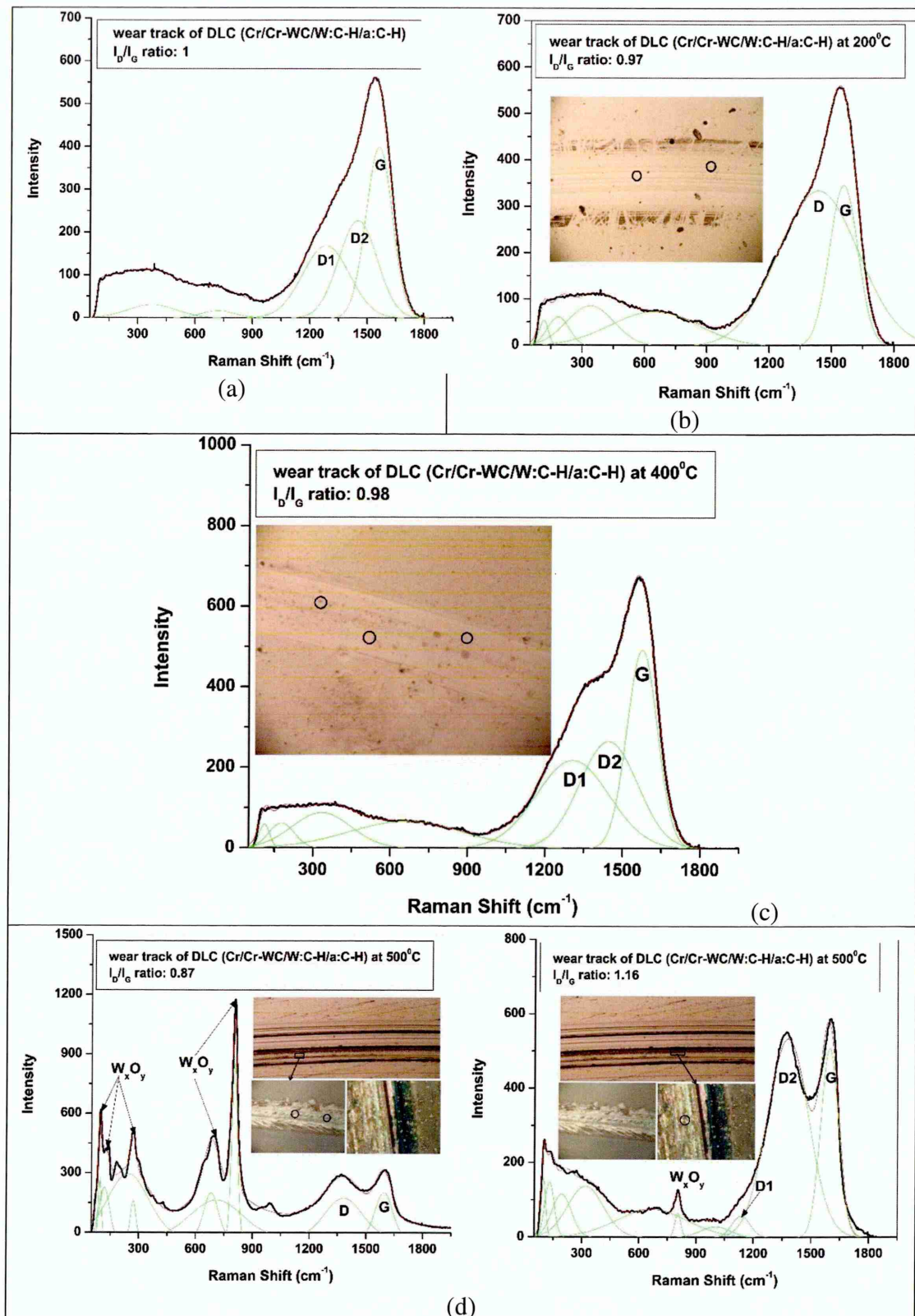


Figure 4.4-26: Raman spectra collected from the wear track of $\text{DLC}(\text{Cr}/\text{Cr}-\text{WC}/\text{W}:\text{C}-\text{H}/\text{a}:\text{C}-\text{H})$ coating (a) ambient temperature, (b) 200°C , (c) 400°C and (d) 500°C

B. Lubricated sliding against Al_2O_3 counterparts

Figure 4.4-27 shows the friction curves of $\text{DLC}(\text{Cr/Cr-WC/W:C-H/a:C-H})$ and C4 after lubricated sliding against Al_2O_3 counterparts at 200°C . A smooth friction curve with a mean friction coefficient of ~ 0.079 is observed for DLC coating. The friction coefficient of C4 is observed in the range of $\sim 0.08 - 0.09$ during run-in period of ~ 100 m, which is followed by a rapid decrease in friction coefficient ($\mu < 0.04$) for rest of the sliding distance. Overall the mean friction coefficient of C4 is found ~ 0.051 . Figure 4.4-28 shows the wear track profiles of both the coatings. DLC coating shows a shallow wear track with a wear coefficient of $6.07 \times 10^{-18} \text{ m}^3\text{N}^{-1}\text{m}^{-1}$, whereas negligible wear is observed for C4 after same sliding distance. Thus unlike dry sliding, C4 performs better than DLC coating during lubricated sliding at 200°C .

Figure 4.4-29 shows the Raman spectra collected from the wear track of C4 after lubricated sliding at 200°C . Details of the deconvoluted peaks are listed in table A-21 (see appendix A). Position 1 shows the spectrum collected from a random position within the wear track (figure 4.4-29a), which contains peaks similar to as-deposited coating (such as B1 – B6/ and Mo_2C) and graphitic carbon particles. The D and G peaks are observed $\sim 1388.77 \text{ cm}^{-1}$ and $\sim 1572.15 \text{ cm}^{-1}$ respectively and the I_D/I_G ratio is found ~ 2.67 . Another spectrum is collected from the groove within the wear track (position 2) as shown in figure 4.4-29b. The spectrum shows strong presence of MoS_2 phases along with graphitic carbon particles within the groove. Peaks B1 – B6 belong to as-deposited C4 whereas sharp MoS_2 peaks are observed centred at $\sim 371 \text{ cm}^{-1}$ and $\sim 405 \text{ cm}^{-1}$ respectively. The D and G peaks are observed $\sim 1394.32 \text{ cm}^{-1}$ and $\sim 1569.51 \text{ cm}^{-1}$ respectively and the I_D/I_G ratio is found ~ 2.77 . The formation of MoS_2 reduces the friction between sliding surfaces and minimises the wear significantly.

Figure 4.4-30 shows the Raman spectrum collected from the wear track of DLC coating after lubricated sliding at 200°C . The disordered (D1 and D2) and G peaks are observed at $\sim 1309.02 \text{ cm}^{-1}$, $\sim 1443.95 \text{ cm}^{-1}$ and $\sim 1552.96 \text{ cm}^{-1}$ respectively and the I_D/I_G ratio is found ~ 0.71 . It should be noted that the high hardness of DLC coating leads to low friction and wear coefficients during lubricated sliding whereas tribochemically reactive wear mechanism of C4 forms solid lubricants (such as MoS_2), which further decrease

friction and improve wear resistance. This confirms that unlike dry sliding, C4 performs better than DLC coating during lubricated sliding at 200°C.

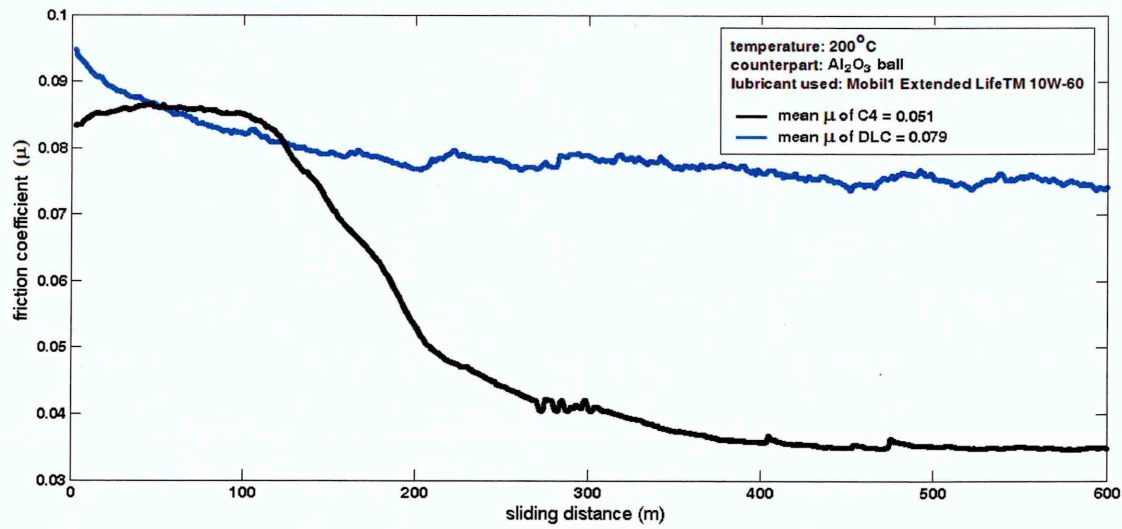


Figure 4.4-27: Friction behaviour of C4 and $DLC(Cr/Cr-WC/W:C-H/a:C-H)$ coatings after lubricated sliding against Al_2O_3 counterparts at 200°C

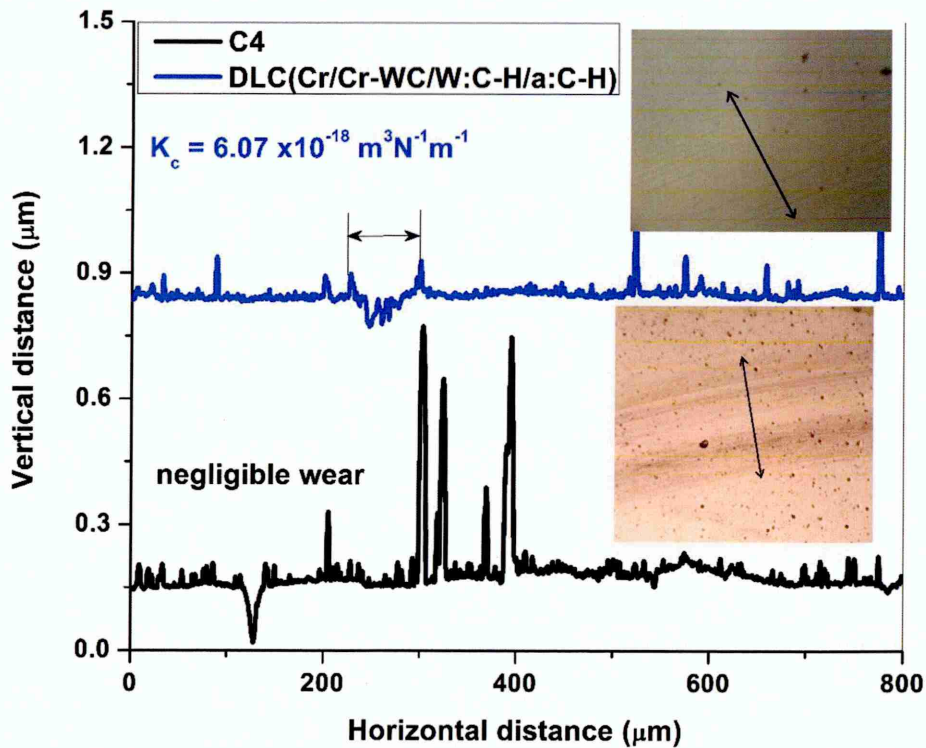


Figure 4.4-28: Wear track profiles of $DLC(Cr/Cr-WC/W:C-H/a:C-H)$ and C4 after lubricated sliding against Al_2O_3 counterparts at 200°C

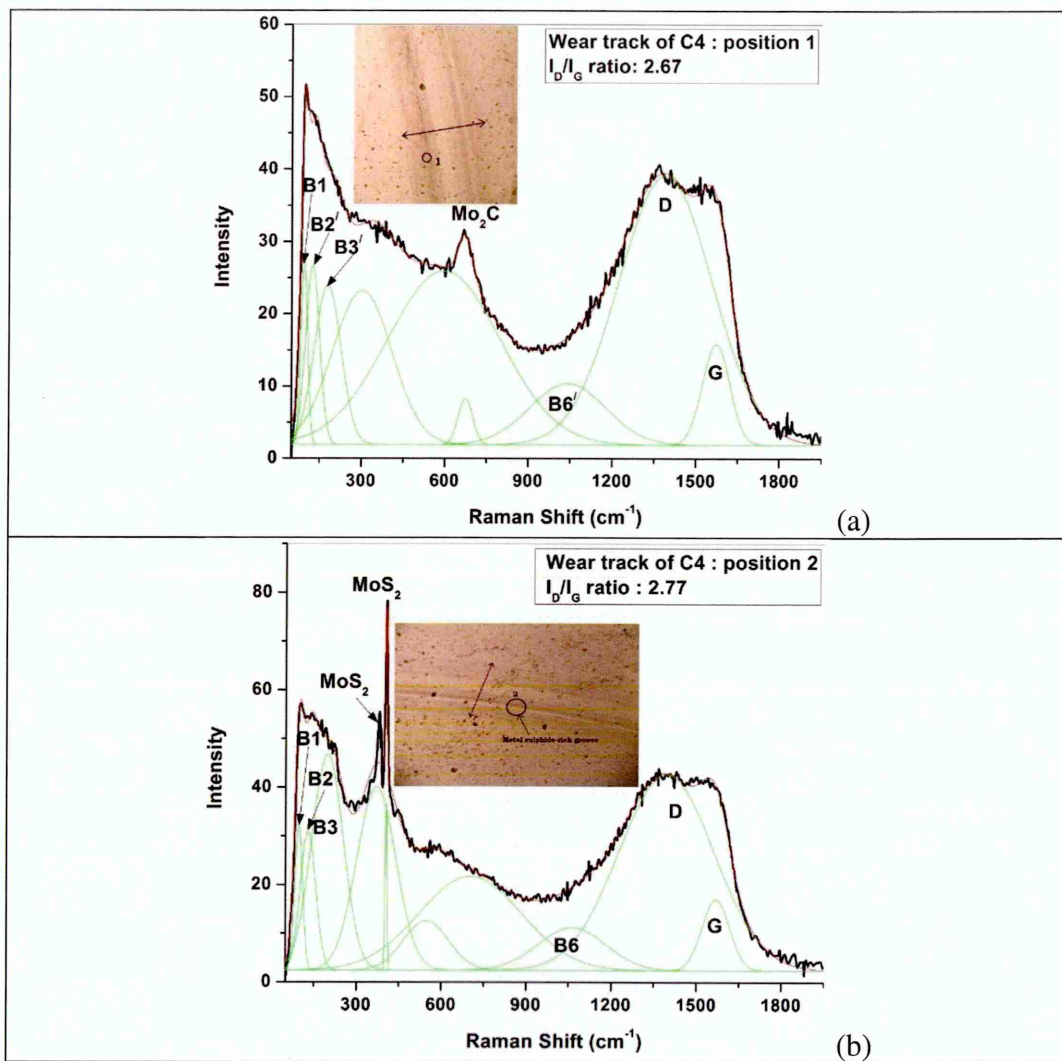


Figure 4.4-29: Raman spectra collected from the wear track of C4 after lubricated sliding against Al_2O_3 balls at 200°C

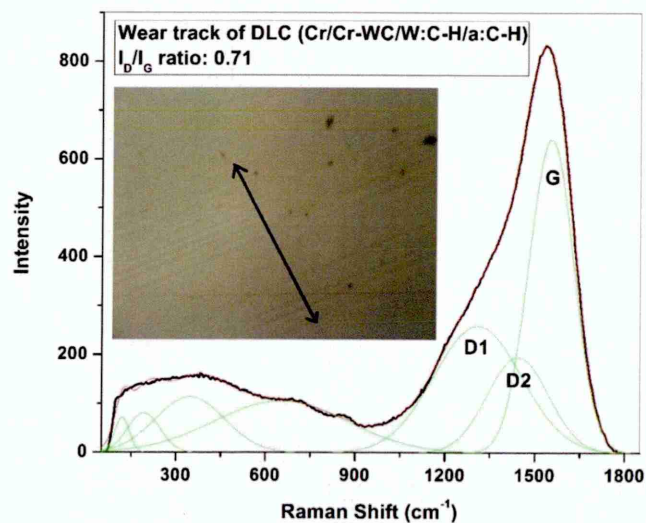


Figure 4.4-30: Raman spectrum collected from the wear track of DLC coating after lubricated sliding against Al_2O_3 balls at 200°C

C. Lubricated sliding against steel counterparts

Figure 4.4-31 shows the friction curves of $DLC(Cr/Cr-WC/W:C-H/a:C-H)$ and C4 against steel counterparts at 200°C. The friction curve of DLC shows a rapid decrease in friction in "run-in" period (segment I), followed by an increase in friction from middle of the segment II to the end of segment III. The mean friction coefficient is observed ~ 0.075 in segment III. Analytical techniques confirm that the wear debris produced from the DLC coating is of graphitic nature (see figure 4.4-33), which explains the decrease in friction coefficient in "run-in" period. However degradation of coating properties at 200°C increases the friction coefficient later (see segment III). On the other hand, C4 shows a high friction coefficient in "run-in" period (segment I), followed by a slow but steady decrease for rest of the sliding distance (see segments II and III). The high friction during "run-in" period is attributed to the abrasion at metal carbide/steel contacts whereas during steady-state period the low friction coefficient is determined by the formation of the lubricious MoS_2 and WS_2 due to tribochemically reactive wear mechanism (see figures 4.4-16b, 4.4-17b and 4.4-19b) as revealed by the X-ray mapping and Raman analyses.

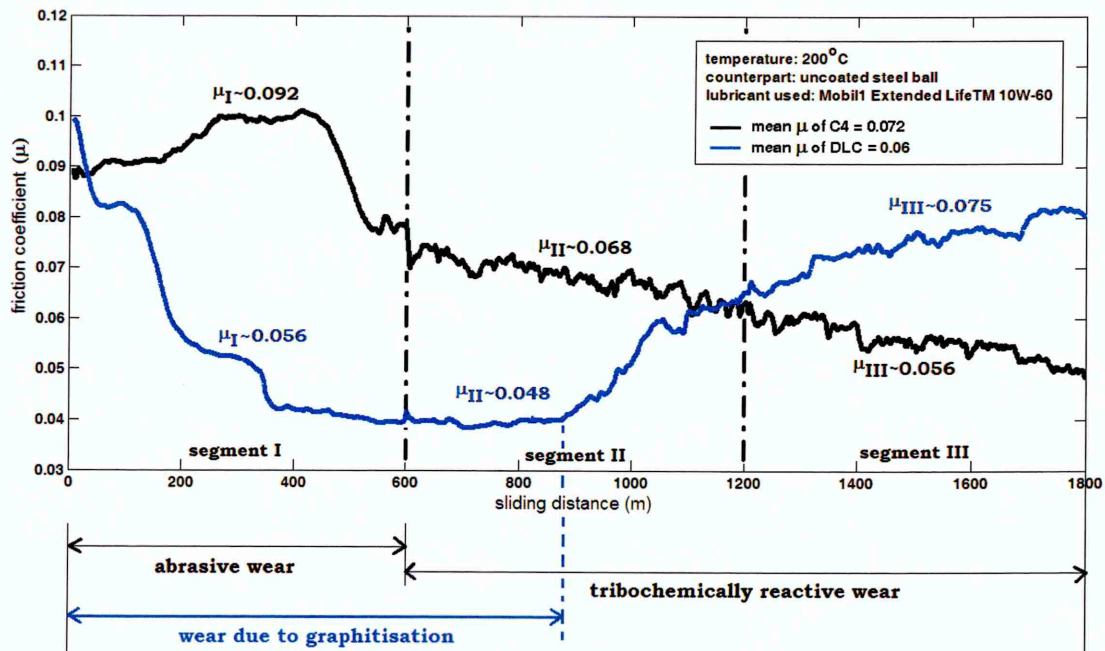


Figure 4.4-31: Friction behaviour of C4 and $DLC(Cr/Cr-WC/W:C-H/a:C-H)$ coatings after lubricated sliding against steel counterparts at 200°C

Figure 4.4-32 shows the shallow wear track of DLC coating formed during lubricated sliding. The wear coefficient is observed in the order of $\sim 10^{-18} \text{ m}^3\text{N}^{-1}\text{m}^{-1}$, which is attributed to its high hardness. On the other hand, C4 shows a deep and wide wear track with a wear coefficient in the order of $\sim 10^{-15} \text{ m}^3\text{N}^{-1}\text{m}^{-1}$ after same sliding distance (see figures 4.4-21 and 4.4-22).

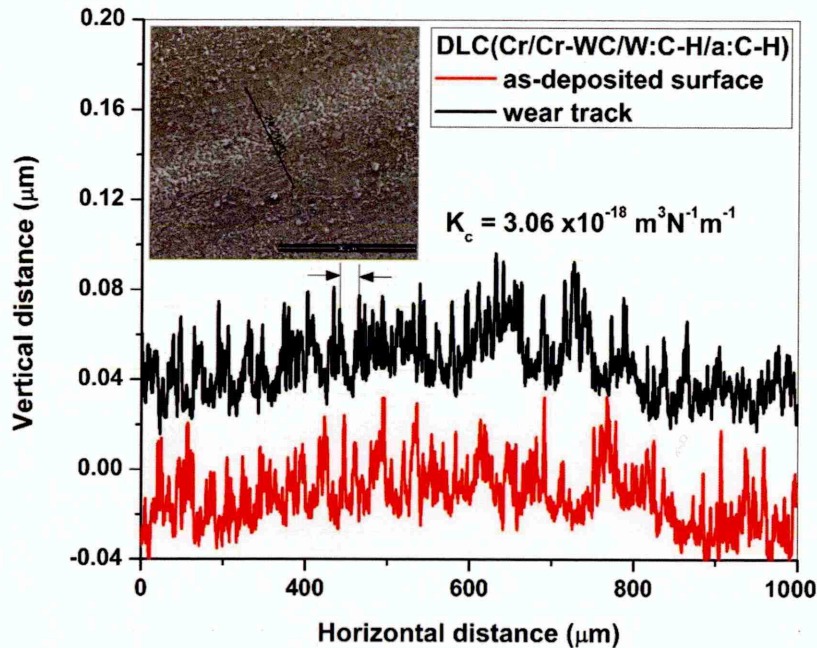


Figure 4.4-32: Wear track profile of $\text{DLC}(\text{Cr}/\text{Cr}-\text{WC}/\text{W}:\text{C}-\text{H}/\text{a}:\text{C}-\text{H})$ coating after lubricated sliding at 200°C

Figure 4.4-33a shows the Raman spectra collected from the steel ball (position 1) and the debris adhered to the steel ball (position 2) after lubricated sliding against DLC coating. The spectrum collected from position 1 is found exactly same to the spectrum collected from uncoated steel ball. But the spectrum collected from position 2 shows presence of graphitic carbon particles in the adhered debris. The dominant and distinct disordered (D1 and D2) and G peaks are observed at $\sim 1334.55 \text{ cm}^{-1}$, $\sim 1452.24 \text{ cm}^{-1}$ and $\sim 1592.15 \text{ cm}^{-1}$ respectively and the I_D/I_G ratio is found ~ 1.82 . DLC coating is amorphous, thus the presence of graphitic carbon particles in the debris indicates a structural change of debris particles due to severe deformation during sliding. Relatively little change in amorphous structure is observed when the Raman spectrum is collected from the wear track of DLC coating (figure 4.4-33b). The disordered (D1 and D2) and G peaks are observed at $\sim 1323.37 \text{ cm}^{-1}$, $\sim 1458.36 \text{ cm}^{-1}$ and $\sim 1565.07 \text{ cm}^{-1}$ respectively and the I_D/I_G ratio is found

~1.1. Similar to DLC, C4 also experiences a structural change after sliding. The graphitic carbon particles of C4 are transformed to amorphous phase after sliding due to severe deformation. Overall, C4 provides lower friction but poor wear resistance compared to DLC coating during lubricated sliding at 200°C.

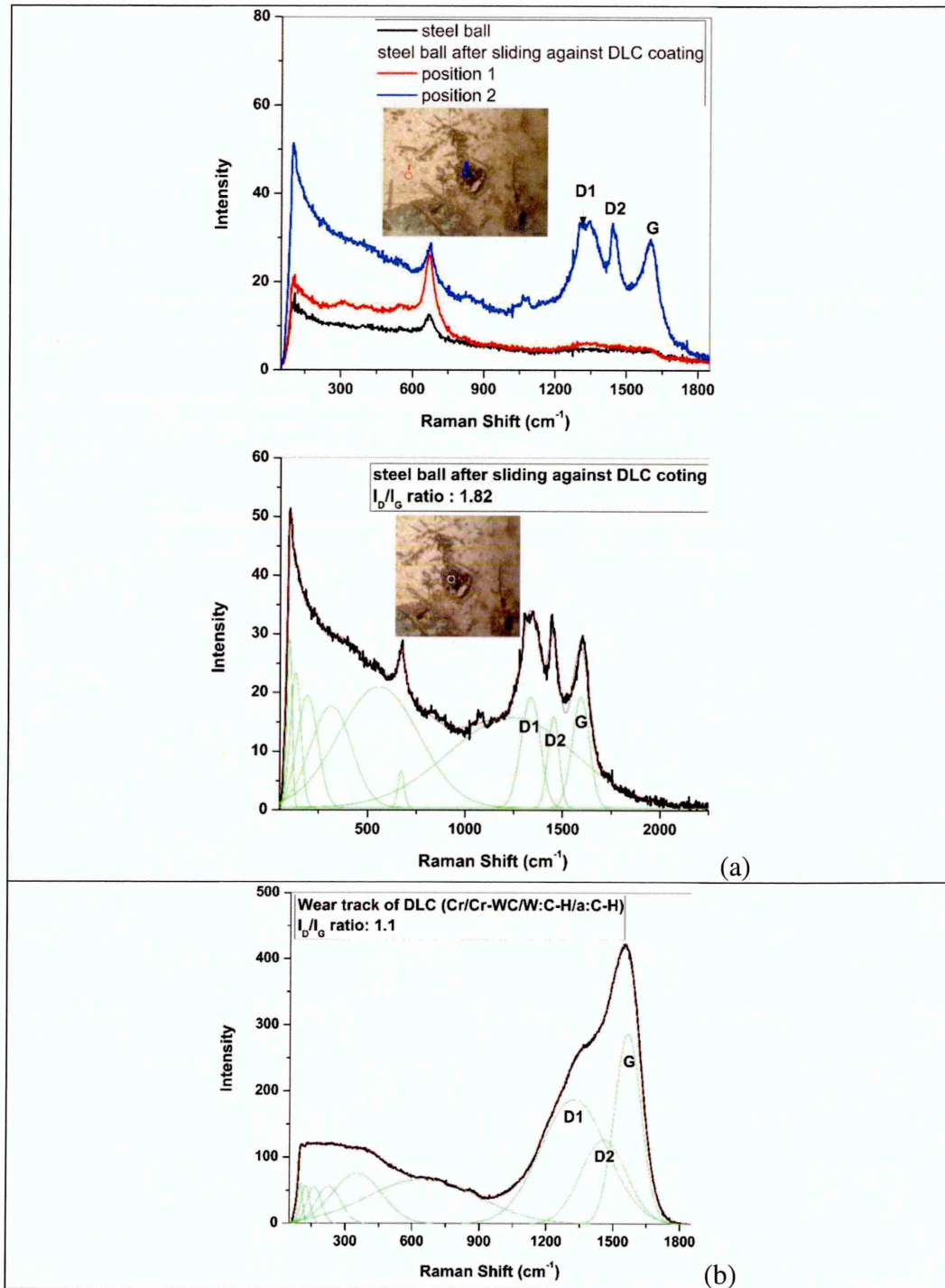


Figure 4.4-33: Raman spectra collected from (a) debris adhered to the steel ball and the (b) wear track of $DLC(Cr/Cr-WC/W:C-H/a:C-H)$ coating after lubricated sliding at 200°C

4.4.5. Concluding remarks

The tribological properties of Mo–W–C coatings in dry and lubricated sliding condition at elevated temperature are discussed in this chapter. Based on the wear debris found on the counterpart and within the wear track, *oxidative* and *tribochemically reactive* wear mechanisms are observed in dry and lubricated conditions respectively.

In dry sliding, tribological behaviour of Mo–W–C coatings is strongly influenced by the third-body abrasive wear and formation of metal oxides (mostly W_xO_y and MoO_3). With increase in temperature up to 400°C, the hardness of these metal oxides decreases leading to severe wear of the coating ($K_c \sim 10^{-14} \text{ m}^3\text{N}^{-1}\text{m}^{-1}$) and subsequent exposure of the substrate. As a result, the friction value rapidly increases to more than 0.6. At 500°C, formation of significant amount of MoO_3 decreases the friction ($\mu \sim 0.4$). In comparison, lower friction ($\mu < 0.1$) and better wear resistance ($K_c \sim 10^{-15} - 10^{-16} \text{ m}^3\text{N}^{-1}\text{m}^{-1}$) provided by state-of-the-art DLC coating at high temperature are attributed to its extremely high hardness, which is more than three times higher compared to Mo–W–C coatings.

The *tribochemically reactive* wear mechanism of Mo–W–C coatings promotes the formation of lubricious metal sulphides (WS_2 and MoS_2) at 200°C and the tribolayer containing both WS_2 and MoS_2 significantly reduces the friction coefficient in the range of $\sim 0.04 - 0.07$. It is important to note that low friction is achieved mostly due to formation of WS_2 at ambient temperature, whereas formation of both WS_2 and MoS_2 significantly decreases the friction at elevated temperature. This indicates importance of combined Mo and W doping over single-metal doping in carbon-based coatings. The transformation of graphitic carbon particles to amorphous phase further benefits the friction behaviour of Mo–W–C coating compared to the state-of-the-art DLC coating. The graphitic debris particles produces from the DLC coating cannot reduce the friction similar to the solid lubricants at 200°C. However very high hardness of DLC provides better wear resistance ($K_c \sim 10^{-18} \text{ m}^3\text{N}^{-1}\text{m}^{-1}$) compared to Mo–W–C coatings ($K_c \sim 10^{-15} \text{ m}^3\text{N}^{-1}\text{m}^{-1}$) at that temperature.

5. Conclusions

5.1. Summary

This research aims to develop a low friction and high temperature wear resistance coating, which will provide high thermal stability and maintain low friction in lubricated condition at ambient as well as at elevated temperature. Amorphous carbon coatings, especially the DLC and metal-doped DLC coatings are widely used for this purpose, however their commercial applications are limited due to low adhesion strength and poor thermal stability. Sputtered DLC (a-C), hydrogen-free DLC (ta-C), metal-free hydrogenated DLC (a:C-H), W, WC and Si doped hydrogenated DLC (W:C-H, WC:C-H and a:C-H-Si) coatings are commercially available tribological coatings to coat various engine components, which experience high mechanical loads and wear during sliding at elevated temperature. DLC coating easily survives the high temperature (150°C – 300°C) of components used in piston-cylinder and valve-train assemblies in the presence of lubricant, however the tribological behaviour depends on the counterpart material and the reactivity of lubricant with the counterfaces. A comprehensive review of currently available literatures indicates that both metal-free and metal-doped DLC coatings maintain almost similar tribological properties in lubricated condition from ambient temperature up to 110°C. In high temperature (150°C – 200°C) lubricated sliding tests, degradation of coating properties leads to significant increase in friction and wear rate. Similar tribological behaviour is observed for commercially available state-of-the-art DLC coating indicating that currently available tribological coatings are unable to maintain their excellent tribological properties in high temperature lubricated conditions. This provides the idea of developing a new generation metal-doped carbon-based coating, which will be able to withstand high operating temperature and simultaneously maintain improved tribological properties in lubricated condition at ambient and high temperature.

A good tribological performance depends on dense coating microstructure and strong coating-substrate adhesion, which are governed by the coating deposition procedure. In this research, both the transitional metals Mo and W are simultaneously introduced in a carbon-based coating (Mo–W–C) for the first time and deposited utilising the benefits of combined unbalanced magnetron sputtering (UBM) and high power impulse magnetron

sputtering (HIPIMS) techniques. Three coatings C2, C4 and C6 are deposited at 2 kW, 4 kW and 6 kW metallic target power respectively. HIPIMS technology provides high ionisation degree of the plasma particles, which leads to better adhesion and less lattice defects compared to other PVD techniques. However it suffers from lower deposition rate, which is compensated by using combined HIPIMS and UBM technique during deposition of Mo–W–C coatings.

The analyses of coating microstructure and composition were carried out using SEM, EDX, XRD and Raman spectroscopy. The adhesion and hardness of the coatings were evaluated by the scratch test, Rockwell hardness test and nanoindentation. The coatings were subjected to a series of isothermal oxidation tests and thermo-gravimetric test at elevated temperature in order to investigate the thermal stability. The tribological performance of the coatings was studied by pin-on-disc tests at ambient and elevated temperature condition. The sliding tests were carried out in dry and lubricated (non-formulated engine oil) conditions. A special attention was paid to study the friction behaviour, the formation of wear debris present in the transfer layer, the wear mechanism in dry and lubricated condition and the change in coating properties with increase in temperature. The tribological and oxidation resistance performance of the Mo–W–C coatings are compared with commercially available state-of-the-art DLC coatings (considered as benchmark).

5.2. Contributions and achievements

The contributions and achievements of this research work are discussed as follows:

- (i) ***Investigation of microstructural and mechanical properties:*** ~1.9 – 2.8 μm thick Mo–W–C coatings show nanocrystalline almost X-ray amorphous structure and the cross-sectional SEM images reveal dense columnar (C2 and C4) and completely granular (C6) microstructures. The as-deposited coatings contain graphitic carbon particles and hard metal carbide phases, which leads to hardness and elastic modulus in the range of ~1330 – 1700 HV and ~190 – 270 GPa respectively. The as-deposited coatings show good adhesion with substrate ($L_c > 80\text{N}$ as observed in C4 and C6) as well as acceptable interfacial adhesion strength (HF2 – HF4 type).

(ii) **Investigation of tribological properties at ambient temperature:** Mo–W–C coatings show *oxidative* and *tribochemically reactive* wear mechanism in dry and lubricated condition respectively. The friction behaviour during dry sliding is strongly influenced by the third-body abrasive wear and the humid test environment. A transfer layer containing fine graphitic carbon particles, MoO₃ and the Magnéli phase oxides is formed during sliding. These metal oxides act as solid lubricants due to their layered structure and together with graphitic particles, which eventually reduce friction and wear ($\mu \sim 0.22 - 0.33$ and $K_c \sim 10^{-16} \text{ m}^3 \text{ N}^{-1} \text{ m}^{-1}$). In lubricated sliding, solid lubricants such as WS₂ and MoS₂ are formed at the asperity contacts due to continuous rubbing action between the coating and the counterpart. These solid lubricants significantly decrease the friction ($\mu \sim 0.03 - 0.05$) and provide negligible wear. Thus Mo–W–C coatings show low friction and excellent wear resistance at ambient temperature.

(iii) **Investigation of oxidation resistance:** During isothermal tests, the oxidation is initiated for Mo–W–C coatings at 500°C but the as-deposited graphitic nature is still preserved. At the same temperature, DLC coating is locally delaminated due to volume expansion of metal oxides produced from both the coating and the substrate. Simultaneously the diamond-like structure is completely converted into the soft graphite-like structure indicating its poor oxidation resistance when compared to the Mo–W–C coatings. Further, the thermo-gravimetric test results show that the Mo–W–C coatings resist oxidation up to $\sim 800^\circ\text{C}$ and no coating delamination is observed during the test because of its strong metallurgical bond to the substrate. On the other hand, the evaporation and local delamination of DLC coating is observed beyond $\sim 380^\circ\text{C}$. This confirms excellent thermal stability of Mo–W–C coatings compared to DLC coating in dynamic condition.

(iv) **Investigation of tribological properties at elevated temperature:** Similar to ambient temperature, Mo–W–C coatings show *oxidative* and *tribochemically reactive* wear mechanism in dry and lubricated condition respectively. High working temperature up to 400°C promotes the formation of brittle metal oxides during dry sliding leading to an increase in both friction and wear coefficients ($\mu > 0.6$ and $K_c \sim 10^{-14} \text{ m}^3 \text{ N}^{-1} \text{ m}^{-1}$)

and subsequent exposure of the substrate. A rapid reduction in friction value ($\mu \sim 0.4$) is observed at 500°C due to formation of significant amount of lubricious MoO_3 . The *tribochemically reactive* wear mechanism promotes the formation of lubricious metal sulphides (WS_2 and MoS_2) at higher working temperature during lubricated sliding. The tribolayer containing both WS_2 and MoS_2 significantly reduces both the friction and wear coefficients ($\mu \sim 0.04 - 0.07$ and $K_c \sim 10^{-15} \text{ m}^3 \text{N}^{-1} \text{m}^{-1}$). It is observed that with increase in sliding distance, formation of more amounts of solid lubricants further decreases the friction coefficient.

- (v) ***Comparison of tribological performance with commercially available state-of-the-art DLC coatings:*** In dry sliding, very high hardness of DLC coating results in lower friction and better wear resistance compared to Mo–W–C coatings at ambient ($\mu \sim 0.17 - 0.3$ and $K_c \sim 10^{-17} \text{ m}^3 \text{N}^{-1} \text{m}^{-1}$) as well as elevated ($\mu < 0.1$ and $\sim 10^{-15} - 10^{-16} \text{ m}^3 \text{N}^{-1} \text{m}^{-1}$) temperature. In lubricated sliding at ambient temperature, DLC coating provides higher friction and lower wear resistance ($\mu \sim 0.04 - 0.09$ and $K_c \sim 10^{-19} \text{ m}^3 \text{N}^{-1} \text{m}^{-1}$) compared to Mo–W–C coatings ($\mu \sim 0.033 - 0.056$ and negligible wear). At 200°C, graphitic debris particles of DLC coating reduce friction but the degradation of coating properties eventually leads to higher friction coefficient ($\mu_{\text{III}} \sim 0.075$). On the other hand, formation of solid lubricants in the transfer layer significantly reduces the friction coefficient of Mo–W–C coatings ($\mu_{\text{III}} \sim 0.056$). Therefore Mo–W–C coatings provide better tribological performance compared to DLC coatings in lubricated condition at ambient and high temperature.
- (vi) ***Importance of combined Mo-W doping into carbon-based coating:*** The combined doping of Mo and W into the carbon-based coating increases thermal stability and significantly reduces friction in boundary lubricated condition. It is observed from the experiments that low friction is achieved mostly due to formation of WS_2 via *tribochemically reactive* wear mechanism at ambient temperature, whereas formation of both WS_2 and MoS_2 significantly decreases the friction at elevated temperature. This indicates importance of combined Mo and W doping over single-metal doping in carbon-based coatings.

5.3. Further scope

This work characterizes the capability of Mo–W–C coatings to provide low friction and improved wear resistant in lubricated condition at ambient and at elevated temperature. However, there are scopes of further studying and understanding of the coating properties as discussed below:

- Mo–W–C coatings shows excellent tribological performance when lubricated sliding tests were done in the presence of commercially available engine oil. Further investigation can be carried out on tribological behaviour of Mo–W–C coatings in the presence of fuels, such as petrol and diesel.
- The as-deposited Mo–W–C coatings have nanocrystalline almost X-ray amorphous structure and cross-sectional SEM images indicated dense columnar and complete granular microstructure. So, transmission electron microscopy (TEM) could potentially be done for better understanding of the as-deposited coating structure.
- Raman spectroscopy, X-ray mapping and EDX analyses are used for studying the friction behaviour and the wear mechanism of Mo–W–C coatings during dry and lubricated sliding. This can further be verified by carrying XPS analyses on the wear tracks and the wear scars on the counterpart.
- The counterparts were uncoated steel and Al₂O₃ balls during sliding, but no tests were carried out against Mo–W–C coated counterparts, which can be considered as a future direction of research. The performance is expected to be similar, however friction and wear coefficient values may differ.

References

- [1] X.T. Zeng, S. Zhang, X.Z. Ding and D.G. Teer, "Comparison of three types of carbon composite coatings with exceptional load-bearing capacity and high wear resistance," *Thin Solid Films*, vol. 420–421, p. 366–370, 2002.
- [2] S. Yang, D. Camino, A.H.S. Jones and D.G. Teer, "Deposition and tribological behaviour of sputtered carbon hard coatings," *Surface and Coatings Technology*, vol. 124, p. 110–116, 2000.
- [3] A. Erdemir and C. Donnet, "Tribology of diamond-like carbon films: recent progress and future prospects," *J. Phys. D: Appl. Phys.*, vol. 38, p. R301–R316, 2006.
- [4] A. Grill, "Diamond-like carbon: state of the art," *Diamond and Related Materials*, vol. 8, p. 428–434, 1999.
- [5] K.C. Walter, T. Levine, H. Kung, J. T. Tesmer, P. Kodali, B. P. Wood, D. J. Rej, M. Nastasi, J. Koskinen and J. P. Hirvonen, "Characterization and performance of diamond-like carbon films synthesized by plasma- and ion-beam-based techniques," *Surface and Coatings Technology*, vol. 74–75, p. 734–738, 1995.
- [6] A. P. Ehiasarian, J. G. Wen and I. Petrov, "Interface microstructure engineering by high power impulse magnetron sputtering for the enhancement of adhesion," *J. Appl. Phys.*, vol. 101, p. 054301, 2007.
- [7] G. Ma, S. Gong, G. Lin, L. Zhang and G. Sun, "A study of structure and properties of Ti-doped DLC film by reactive magnetron sputtering with ion implantation," vol. 258, p. 3045–3050, 2012.
- [8] D. Y. Wang, C. L. Chang and W. Y. Ho, "Oxidation behaviour of diamond-like carbon films," vol. 120–121, p. 138–144, 1999.
- [9] D. R. Tallant, J. E. Parmeter, M. P. Siegal and R. L. Simpson, "The thermal stability of diamond-like carbon," vol. 4, pp. 191–199, 1995.
- [10] Y. Liu, A. Erdemir and E.I. Meletis, "An investigation of the relationship between graphitization and frictional behavior of DLC coatings," *Surface and Coatings Technology*, Vols. 86–87, pp. 564–568, 1996.
- [11] A. Neville, A. Morina, T. Haque and M. Voong, "Compatibility between tribological surfaces and lubricant additives—How friction and wear reduction can be controlled by surface/lube synergies," *Tribology International*, vol. 40, p. 1680–1695, 2007.
- [12] H. Ronkainen, S. Varjus and K. Holmberg, "Friction and wear properties in dry, water- and oil-lubricated DLC against alumina and DLC against steel contacts," *Wear*, vol. 222, p. 120–128, 1998.
- [13] Y. Liu, A. Erdemir and E.I. Meletis, "Influence of environmental parameters on the frictional behavior of DLC coatings," *Surface & coatings technology*, Vols. 94–95, pp. 463–468, 1997.

- [14] H. Ronkainen, S. Varjus and K. Holmberg, "Tribological performance of different DLC coatings in water-lubricated conditions," *Wear*, vol. 249, p. 267–271, 2001.
- [15] A. Vanhulsel, B. Blanpain, J. P. Celis, J. Roos, E. Dekempeneer and J. Smeets, "Study of the wear behaviour of diamond-like coatings at elevated temperatures," *Surface & coatings technology*, vol. 98, no. 1-3, pp. 1047-1052, 1998.
- [16] A. Erdemir and G. R. Fenske, "Tribological performance of diamond and diamondlike carbon films at evaluated temperatures," *Tribology Transactions*, vol. 39, no. 4, pp. 787 - 794, 1996.
- [17] F. Bremond, P. Fournier and F. Platon, "Test temperature effect on the tribological behavior of DLC-coated 100C6-steel couples in dry friction," *Wear*, vol. 254, no. 7-8, pp. 774-783, 2003.
- [18] O. Wa'nstrand, M. Larsson and P. Hedenqvist, "Mechanical and tribological evaluation of PVD WC/C coatings," vol. 111, p. 247–254, 1999.
- [19] C. Corbella, G. Oncins, M.A. Gomez, M.C. Polo, E. Pascual, J. Garcia-Ce'spedes, J.L. Andujar and E. Bertran, "Structure of diamond-like carbon films containing transition metals deposited by reactive magnetron sputtering," vol. 14, p. 1103–1107, 2005.
- [20] C.W.M. Silva, J.R.T. Branco and A. Cavaleiro, "How can H content influence the tribological behaviour of W-containing DLC coatings," vol. 11, p. 1778–1782, 2009.
- [21] R. K.Y. Fu, Y.F. Mei, M. Y. Fu, X. Y. Liu and P. K. Chu, "Thermal stability of metal-doped diamond-like carbon fabricated by dual plasma deposition," *Diamond & Related Materials*, vol. 14, p. 1489 – 1493, 2005.
- [22] C. Rincón, G. Zambrano, A. Carvajal, P. Prieto, H. Galindo, E. Martínez, A. Lousa and J. Esteve, "Tungsten carbide/diamond-like carbon multilayer coatings on steel for tribological applications," *Surface & coatings technology*, vol. 148, no. 2-3, pp. 277-283, 2001.
- [23] L. Rosado, V. K. Jain and H. K. Trivedi, "The effect of diamond-like carbon coatings on the rolling fatigue and wear of M50 steel," *Wear*, vol. 212, no. 1, pp. 1-6, 1997.
- [24] B. Podgornik, "Coated machine elements — fiction or reality?," *Surface & coatings technology*, Vols. 146-147, pp. 318-323, 2001.
- [25] M. Kano, Y. Yasuda and J. P. Ye, "The effect of ZDDP and MoDTC additives in engine oil on the friction properties of DLC-coated and steel cam followers," *Lubrication Science*, vol. 17, no. 1, p. 95–103, 2004.
- [26] S. Miyake, T. Saito, Y. Yasuda, Y. Okamoto and M. Kano, "Improvement of boundary lubrication properties of diamond-like carbon (DLC) films due to metal addition," *Tribology International*, vol. 37, p. 751–761, 2004.
- [27] M. d. Barros'Bouchet, J. Martin, T. Le-Mogne and B. Vacher, "Boundary lubrication mechanisms of carbon coatings by MoDTC and ZDDP additives," *Tribology International*, vol. 38, pp. 257-264, 2005.

- [28] Y. Yamamoto and S. Gondo, "Friction and Wear Characteristics of Molybdenum Dithiocarbamate and Molybdenum Dithiophosphate," *Tribology Transactions*, vol. 32, no. 2, pp. 251-257, 1989.
- [29] S. Gondo and Y. Yamamoto, "Mechanism of the surface film formation of molybdenum dithiocarbamate (MoDTC) and effect of rubbing materials," *Jpn J Tribol*, vol. 36, no. 3, p. 323-333, 1991.
- [30] A. Morina, "Lubricant additive interactions, surface reactions and the link to tribological performance in engines (PhD thesis)," Heriot-Watt University, Edinburgh, 2005.
- [31] S. Gondo and Y. Yamamoto, "On properties of surface films formed with molybdenum dithiocarbamate (MoDTC) under different conditions," *Jpn J Tribol*, vol. 36, no. 3, pp. 309-321, 1991.
- [32] T. Haque, A. Morina and A. Neville, "Influence of friction modifier and antiwear additives on the tribological performance," *Surface & Coatings Technology*, vol. 204, p. 4001-4011, 2010.
- [33] K. Komvopoulos, S. A. Pernama, E. S. Yamaguchi and P. R. Ryason, "Friction Reduction and Anti wear Capacity of Engine Oil Blends Containing Zinc Dialkyl Dithiophosphate and Molybdenum-Complex Additives," *Tribology Transactions*, vol. 49, pp. 151-165, 2006.
- [34] G. Pereira, A. Lachenwitzer, M. Kasrai, G. M. Bancroft, P. R. Norton, M. Abrecht, P. U. P. A. Gilbert, T. Regier, R. I. R. Blyth and J. Thompson, "Chemical and mechanical analysis of tribofilms from fully formulated oils Part 1 – Films on 52100 steel," *Tribology*, vol. 1, no. 1, pp. 48-61, 2007.
- [35] "<http://www.arrowprecision.com/content/17dlccoating>," [Online].
- [36] <http://www.oerlikon.com/balzers/en/products-services/balinit-coatings/balinit-c-star/>. [Online].
- [37] <http://www.oerlikon.com/balzers/en/products-services/balinit-coatings/balinit-c/>. [Online].
- [38] <http://www.oerlikon.com/balzers/en/products-services/balinit-coatings/balinit-dlc-star/>. [Online].
- [39] "<http://www.oerlikon.com/balzers/en/products-services/balinit-coatings/balinit-dlc/>," [Online].
- [40] "<http://www.hauzertechnocoating.com/en/plasma-coating-explained/dlc-coating/>," [Online].
- [41] "<http://www.oerlikon.com/metco/en/products-services/coating-services/dlc-coatings/coatings/acarbon/>," [Online].
- [42] "<http://www.richterprecision.com/dlccoatings.html>," [Online].
- [43] M Priest and C.M Taylor, "Automobile engine tribology — approaching the surface," *Wear*, vol. 241, no. 2, pp. 193-203, 2000.

- [44] J. Stallard and D.G. Teer, "A study of the tribological behaviour of CrN, Graphit-iC and Dymon-iC coatings under oil lubrication," *Surface & coatings technology*, Vols. 188-189, pp. 525-529, 2004.
- [45] T. Haque, A. Morina, A. Neville, R. Kapadia and S. Arrowsmith, "Non-ferrous coating/lubricant interactions in tribological contacts: Assessment of tribofilms," *Tribology international*, vol. 40, no. 10-12, pp. 1603-1612, 2007.
- [46] B. Vengudusamy, J. H. Green, G. D. Lamb and H. A. Spikes, "Influence of hydrogen and tungsten concentration on the tribological properties of DLC/DLC contacts with ZDDP," *Wear*, Vols. 298-299, p. 109-119, 2013.
- [47] B. Vengudusamy, J. H. Green, G. D. Lamb and H. A. Spikes, "Tribological properties of tribofilms formed from ZDDP in DLC/DLC and DLC/steel contacts," *Tribology international*, vol. 44, no. 2, pp. 165-174, 2011.
- [48] H. Tasdemir, M. Wakayama, T. Tokoroyama, H. Kousaka, N. Umehara, Y. Mabuchi and Higuchi, T., "Wear behaviour of tetrahedral amorphous diamond-like carbon (ta-C DLC) in additive containing lubricants," *Wear*, vol. 307, no. 1-2, pp. 1-9, 2013.
- [49] S. Kosarieh, A. Morina, E. Lainé, J. Flemming and A. Neville, "Tribological performance and tribochemical processes in a DLC/steel system when lubricated in a fully formulated oil and base oil," *Surface & coatings technology*, vol. 217, pp. 1-12, 2013.
- [50] B. Vengudusamy, J. H. Green, G. D. Lamb and H. A. Spikes, "Behaviour of MoDTC in DLC/DLC and DLC/steel contacts," *Tribology international*, vol. 54, pp. 68-76, 2012.
- [51] L. Yang, A. Neville, A. Brown, P. Ransom and A. Morina, "Friction reduction mechanisms in boundary lubricated W-doped DLC coatings," *Tribology international*, vol. 70, pp. 26-33, 2014.
- [52] B. Podgornik, D. Hren, J. Vizintin, S. Jacobson, N. Stavlid and S. Hogmark, "Combination of DLC coatings and EP additives for improved tribological behaviour of boundary lubricated surfaces," *Wear*, vol. 261, no. 1, pp. 32-40, 2006.
- [53] K. Mistry, A. Morina, A. Erdemir and A. Neville, "Extreme Pressure Lubricant Additives Interacting on the Surface of Steel- and Tungsten Carbide-Doped Diamond-Like Carbon," *Tribology transactions*, vol. 56, no. 4, pp. 623-629, 2013.
- [54] T. Haque, A. Morina, A. Neville, R. Kapadia and S. Arrowsmith, "Effect of oil additives on the durability of hydrogenated DLC coating under boundary lubrication conditions," *Wear*, vol. 266, no. 1-2, pp. 147-157, 2009.
- [55] S. Kosarieh, A. Morina, E. Laine, J. Flemming and A. Neville, "The effect of MoDTC-type friction modifier on the wear performance of a hydrogenated DLC coating," *Wear*, vol. 302, no. 1-2, pp. 890-898, 2013.
- [56] C. Héau, C. Ould and P. Maurin-Perrier, "Tribological behaviour analysis of hydrogenated and nonhydrogenated DLC lubricated by oils with and without additives," *Lubrication Science*, vol. 25, no. 4, p. 275-285, 2013.

- [57] S. Yazawa, I. Minami and B. Prakash, "Reducing Friction and Wear of Tribological Systems through Hybrid Tribofilm Consisting of Coating and Lubricants," *Lubricants*, vol. 2, pp. 90-112, 2014.
- [58] M. Kalin, E. Roman and J. Vižintin, "The effect of temperature on the tribological mechanisms and reactivity of hydrogenated, amorphous diamond-like carbon coatings under oil-lubricated conditions," *Thin solid films*, vol. 515, no. 7-8, pp. 3644-3652, 2007.
- [59] B. Podgornik and J. Vižintin, "Tribological reactions between oil additives and DLC coatings for automotive applications," *Surface & coatings technology*, vol. 200, no. 5-6, pp. 1982-1989, 2005.
- [60] B. Yang, Y. Zheng, B. Zhang, L. Wei and J. Zhang, "The high-temperature tribological properties of Si-DLC films," *Surface and Interface Analysis*, vol. 44, p. 1601-1605, 2012.
- [61] W. J. Wu and M. H. Hon, "Thermal stability of diamond-like carbon films with added silicon," *Surface and Coatings Technology*, vol. 111, p. 134-140, 1999.
- [62] S.S. Camargo Jr, A. L. Baia Neto, R. A. Santos, F. L. Freire Jr, R. Carius and F. Finger, "Improved high-temperature stability of Si incorporated a-C:H films," *Diamond and Related Materials*, vol. 7, p. 1155-1162, 1998.
- [63] B. Podgornik, D. Hren and J. Vižintin, "Low-friction behaviour of boundary-lubricated diamond-like carbon coatings containing tungsten," *Thin Solid Films*, vol. 476, pp. 92-100, 2005.
- [64] B. Podgornik, S. Jacobson and S. Hogmark, "Influence of EP additive concentration on the tribological behaviour of DLC-coated steel surfaces," *Surface & Coatings Technology*, vol. 191, p. 357- 366, 2005.
- [65] A. P. Ehiasarian, P. E. Hovsepian and W. D. Munz..EP 1 260 603 A2, DE 10124749 2001 Patent US patent no. 10718435, 2005., 2005.
- [66] A. P. Ehiasarian, P. Eh. Hovsepian, L. Hultman and U. Helmersson, "Comparison of microstructure and mechanical properties of chromium nitride-based coatings deposited by high power impulse magnetron sputtering and by the combined steered cathodic arc/unbalanced magnetron technique," *Thin Solid Films*, vol. 457, p. 270-277, 2004.
- [67] J. Fontaine, C. Donnet and A. Erdemir, "Fundamentals of the Tribology of DLC coatings," in *Tribology of Diamond-Like Carbon Films*, A. E. C. Donnet, Ed., Springer, 2008.
- [68] K. Kato and K. Adachi, "Wear Mechanisms," in *Modern Tribology Handbook*, vol. 1, B. Bhushan, Ed., CRC Press, 2001.
- [69] R. Saito, G. Dresselhaus and M. S. Dresselhaus, *Physical Properties of Carbon Nanotubes*, vol. 241, World Scientific Publishing Company, 1998, p. 234-230.
- [70] R. W. G. Wyckoff, *Crystal Structures*, Interscience Publishers, 1965.
- [71] R. W. G. Wyckoff, *Crystal Structures*, Interscience Publishers, 1958.

- [72] R. H. Savage, "Graphite lubrication," *Journal of Applied Physics*, vol. 19 (1), p. 1–10, 1948.
- [73] A. Erdemir and C. Donnet, in *Modern Tribology Handbook*, B. Bhushan, Ed., CRC Press, 2000, p. 871–908.
- [74] K. Kato, N. Umehara and K. Adachi, "Friction, wear and N₂-lubrication of carbon nitride coatings: a review," *Wear*, no. 254, p. 1062–1069, 2003.
- [75] R. L. Fusaro and H. E. Sliney, "Graphite Fluoride (CF_x)_n—A New Solid Lubricant," *ASLE Transactions*, vol. 13, no. 1, pp. 56–65, 1970.
- [76] E. Rabinowicz and M. Imai, "Frictional properties of pyrolytic boron nitride and graphite," *Wear*, vol. 7, pp. 298–300, 1964.
- [77] H. Schmellenmeier, *Exp. Technik Physik*, vol. 1, p. 49, 1954.
- [78] S. Eisenberg and R. Chabot, "Ion beam deposition of thin films of diamondlike carbon," *Journal of Applied Physics*, vol. 42, no. 7, p. 2953, 1971.
- [79] C. Weissmantel, K. Bewilogua, C. Schurer, K. Breuer and H. Zscheile, "Characterization of hard carbon films by electron energy loss spectrometry," *Thin Solid Films*, vol. 61, pp. L1–L4, 1979.
- [80] J. Robertson, "Diamond-like amorphous carbon," *Materials Science and Engineering: R: Reports*, vol. 37, no. 4–6, pp. 129–281, 2002.
- [81] M.W. Moon, H.M. Jensen, J.W. Hutchinson, K.H. Oh and A.G. Evans, "The characterization of telephone cord buckling of compressed thin (lms on substrates)," *Journal of the Mechanics and Physics of Solids*, vol. 50, p. 2355 – 2377, 2002).
- [82] Y. Jeon, Y. S. Park, H. J. Kim and B. Hong, "Tribological Properties of Ultrathin DLC Films with and without Metal Interlayers," vol. 51 (3), p. 1124 – 1128, 2007.
- [83] S. Zhang, X. L. Bui and X. Li, "Thermal stability and oxidation properties of magnetron sputtered diamond-like carbon and its nanocomposite coatings," *Diamond & Related Materials*, vol. 15, p. 972–976, 2006.
- [84] M. C. Chiu, W. P. Hsieh, W.Y. Ho, D. Y. Wang and F. S. Shieu, "Thermal stability of Cr-doped diamond-like carbon films synthesized by cathodic arc evaporation," *Thin Solid Films*, vol. 476, p. 258– 263, 2005.
- [85] Y.N. Kok and P.Eh. Hovsepian, "Resistance of nanoscale multilayer C/Cr coatings against environmental attack," *Surface & Coatings Technology*, vol. 201, p. 3596–3605, 2006.
- [86] S. Zhang, D. Sun, Y. Fu and H. Du, "Toughening of hard nanostructural thin films: a critical review," *Surface & Coatings Technology*, vol. 198, p. 2 – 8, 2005.
- [87] H. W. Choi, J. H. Choi, K. R. Lee, J.P. Ahn and K. H. Oh, "Structure and mechanical properties of Ag-incorporated DLC films prepared by a hybrid ion beam deposition system," *Thin Solid Films*, vol. 516, p. 248–251, 2007.

- [88] S. Yang and D. G. Teer, "Investigation of sputtered carbon and carbon/chromium multi-layered coatings," *Surface and Coatings Technology*, vol. 131, pp. 412-416, 2000.
- [89] C. C. Chen and F. C. N. Hong, "Structure and properties of diamond-like carbon nanocomposite films containing copper nanoparticles," *Applied Surface Science*, vol. 242, p. 261-269, 2005.
- [90] W. Y. Wu and J. M. Ting, "Growth and characteristics of carbon films with nano-sized metal particles," *Thin Solid Films*, vol. 420 – 421, p. 166-171, 2002.
- [91] A. Erdemir, "Design criteria for superlubricity in carbon films and related microstructures," *Tribology International*, vol. 37, p. 577-583, 2004.
- [92] W. J. Wu, T. M. Pai and M. H. Hon, "Wear behavior of silicon-containing diamond-like carbon coatings," *Diamond and related materials*, vol. 7, no. 10, pp. 1478-1484, 1998.
- [93] O. R. Monteiro, "Synthesis, properties and applications of pure and covalently doped DLC films prepared by energetic condensation," in *33rd IUVSTA Workshop and IV Brazilian Meeting on Diamond, Diamond-Like, Nanotubes, Nitrides and Silicon Carbide*, Sao Paulo, Brazil, 2001.
- [94] F. Zhao, H. Li, L. Ji, Y. Wang, H. Zhou and J. Chen, "Ti-DLC films with superior friction performance," *Diamond & Related Materials*, vol. 19, p. 342-349, 2010.
- [95] P. C. Tsai, Y. F. Hwang, J. Y. Chiang and W. J. Chen, "The effects of deposition parameters on the structure and properties of titanium-containing DLC films synthesized by cathodic arc plasma evaporation," *Surface & Coatings Technology*, vol. 202, p. 5350-5355, 2008.
- [96] V. Derflinger, H. Brandle and H. Zimmermann, "New hard/lubricant coating for dry machining," *Surface and Coatings Technology*, vol. 113, p. 286-292, 1999.
- [97] C. L. Chang, J. Y. Jao, T. C. Chang, W. Y. Ho and D. Y. Wang, "Influences of bias voltage on properties of TiAl-doped DLC coatings synthesized by cathodic arc evaporation," *Diamond & Related Materials*, vol. 14, p. 2126 – 2131, 2005.
- [98] N.W. Khun and E. Liu, "Influence of carbon sputtering power on structure, corrosion resistance, adhesion strength and wear resistance of platinum/ruthenium/nitrogen doped diamond-like carbon thin films," *Surface & Coatings Technology*, vol. 205, p. 853-860, 2010.
- [99] C. Corbella, M. Vives, A. Pinyol, E. Bertran, C. Canal, M.C. Polo and J.L. Andujar, "Preparation of metal (W, Mo, Nb, Ti) containing a-C:H films by reactive magnetron sputtering," *Surface and Coatings Technology*, vol. 177 –178, p. 409-414, 2004.
- [100] N. Benchikh, F. Garrelie, C. Donnet, B. Bouchet-Fabre, K. Wolski, F. Rogemond, A.S Loir and J.L. Subtil, "Nickel-incorporated amorphous carbon film deposited by femtosecond pulsed laser ablation," *Thin Solid Films*, vol. 482, p. 277- 282, 2005.

- [101] N.W. Khun, E. Liu and G.C. Yang, "Structure, scratch resistance and corrosion performance of nickel doped diamond-like carbon thin films," *Surface & Coatings Technology*, vol. 204, p. 3025–3029, 2010.
- [102] O. R. Monteiro, M. P. Delplancke-Ogletree and I. G. Brown, "Tungsten-containing amorphous carbon films deposited by pulsed vacuum arc," *Thin Solid Films*, vol. 332, pp. 100-107, 1999.
- [103] C.W. Moura e Silva, J.R.T. Branco and A. Cavaleiro, "Characterization of magnetron co-sputtered W-doped C-based films," *Thin Solid Films*, vol. 515, p. 1063–1068, 2006.
- [104] A. A. Gharam, M. J. Lukitsch, M. P. Balogh, N. Irish and A. T. Alpas, "High temperature tribological behavior of W-DLC against aluminium," *Surface & Coatings Technology*, vol. 206, p. 1905–1912, 2011.
- [105] L. Ji, H. Li, F. Zhao, J. Chen and H. Zhou, "Microstructure and mechanical properties of Mo/DLC nanocomposite films," *Diamond & Related Materials*, vol. 17, p. 1949–1954, 2008.
- [106] K. Baba and R. Hatada, "Preparation and properties of metal-containing diamond-like carbon films by magnetron plasma source ion implantation," *Surface & Coatings Technology*, vol. 196, p. 207– 210, 2005.
- [107] S. Chandrasekar and B. Bhushan, "The role of environment in the friction of diamond for magnetic recording head applications," *Wear*, vol. 153, no. 1, p. 79–89, 1992.
- [108] K. Miyoshi, R. L. C. Wu, A. Garscadden, P. N. Barnes and H. E. Jackson, "Friction and wear of plasma-deposited diamond films," *Journal of Applied Physics*, vol. 74, pp. 4446-4454, 1993.
- [109] M. N. Gardosa and B. L. Soriano, "The effect of environment on the tribological properties of polycrystalline diamond films," *Journal of Materials Research*, vol. 5, no. 11, pp. 2599-2609, 1990.
- [110] D.S. Kim, T.E. Fischer and B. Gallois, "The effects of oxygen and humidity on friction and wear of diamond-like carbon films," *Surface & coatings technology*, vol. 49, no. 1-3, pp. 537-542, 1991.
- [111] A. Erdemir, C. Bindal, J. Pagan and P. Wilbur, "Characterization of transfer layers on steel surfaces sliding against diamond-like hydrocarbon films in dry nitrogen," *Surface & coatings technology*, Vols. 76-77, pp. 559-563, 1995.
- [112] A. Erdemir, C. Bindal, G.R. Fenske, C. Zuiker and P. Wilbur, "Characterization of transfer layers forming on surfaces sliding against diamond-like carbon," *Surface & coatings technology*, Vols. 86-87, pp. 692-697, 1996.
- [113] Y. Liu, A. Erdemir and E.I. Meletis, "A study of the wear mechanism of diamond-like carbon films," *Surface & coatings technology*, Vols. 1-2, pp. 48-56, 1996.
- [114] J.C. Sanchez-Lopez, A. Erdemir, C. Donnet and T.C. Rojas, "Friction-induced structural transformations of diamondlike carbon coatings under various atmospheres," *Surface & coatings technology*, Vols. 163-164, pp. 444-450, 2003.

- [115] R. Hauert, "An overview on the tribological behavior of diamond-like carbon in technical and medical applications," *Tribology international*, vol. 37, no. 11-12, pp. 991-1003, 2004.
- [116] J. Andersson, R.A. Erck and A. Erdemir, "Frictional behavior of diamondlike carbon films in vacuum and under varying water vapor pressure," *Surface & coatings technology*, Vols. 163-164, pp. 535-540, 2003.
- [117] J. Andersson, R.A. Erck and A. Erdemir, "Friction of diamond-like carbon films in different atmospheres," *Wear*, vol. 254, no. 11, pp. 1070-1075, 2003.
- [118] A. Erdemir, O. L. Eryilmaz and G. Fenske, "Synthesis of diamondlike carbon films with superlow friction and wear properties," *Journal of Vacuum Science and Technology A*, vol. 18, p. 1987, 2000.
- [119] C. Donnet, M. Belin, J.C. Augé, J.M. Martin, A. Grill and V. Patel, "Tribochemistry of diamond-like carbon coatings in various environments," *Surface & coatings technology*, Vols. 68-69, pp. 626-631, 1994.
- [120] C. Donnet, T. Le Mogne, L. Ponsonnet, M. Belin, A. Grill, V. Patel and C. Jahnes, "The respective role of oxygen and water vapor on the tribology of hydrogenated diamond-like carbon coatings," *Tribology letters*, vol. 4, no. 3-4, pp. 259-265, 1998.
- [121] M. Kano, Y. Yasuda, Y. Okamoto, Y. Mabuchi, T. Hamada, T. Ueno, J. Ye, S. Konishi, S. Takeshima, J. M. Martin, M. I. De Barros Bouchet and T. Le Mognee, "Ultralow friction of DLC in presence of glycerol mono-oleate (GNO)," *Tribology letters*, vol. 18, no. 2, pp. 245-251, 2005.
- [122] K. Oguri and T. Arai, "Tribological properties and characterization of diamond-like carbon coatings with silicon prepared by plasma-assisted chemical vapour deposition," *Surface & coatings technology*, vol. 47, no. 1-3, pp. 710-721, 1991.
- [123] A.K. Gangopadhyay, P.A. Willermet, M.A. Tamor and W.C. Vassell, "Amorphous hydrogenated carbon films for tribological applications I. Development of moisture insensitive films having reduced compressive stress," *Tribology international*, vol. 30, no. 1, pp. 9-18, 1997.
- [124] R. Gilmore and R. Hauert, "Control of the tribological moisture sensitivity of diamond-like carbon films by alloying with F, Ti or Si," *Thin solid films*, Vols. 398-399, pp. 199-204, 2001.
- [125] N. P. C. Services, Handbook on Automobile & Allied Products (2nd Revised Edition), 1 Oct 2013.
- [126] G. N. Nehme, "The effect of FeF₃/TiF₃ catalysts on the thermal and tribological performance of plain oil ZDDP under extreme pressure loading," *Wear*, Vols. 278-279, pp. 9-17, 2012.
- [127] S. Yang, X. Li, N. M. Renevier and D.G. Teer, "Tribological properties and wear mechanism of sputtered C/Cr coating," *Surface and Coatings Technology*, vol. 142-144, p. 85-93, 2001.

- [128] S. K. Pal, J. Jiang and E. I. Meletis , “Effects of N-doping on the microstructure, mechanical and tribological behavior of Cr-DLC films,” *Surface & Coatings Technology*, vol. 201, p. 7917–7923, 2007.
- [129] W. Dai and A. Wang, “Synthesis, characterization and properties of the DLC films with low Cr concentration doping by a hybrid linear ion beam system,” *Surface and Coatings Technology*, vol. 205, pp. 2882-2886, 2011.
- [130] V. Singh, J. C. Jiang and E. I. Meletis , “Cr-diamond like carbon nanocomposite films: Synthesis, characterization and properties,” *Thin Solid Films*, vol. 489, p. 150 – 158, 2005.
- [131] W. Dai, P. Ke and A. Wang, “Microstructure and property evolution of Cr-DLC films with different Cr content deposited by a hybrid beam technique,” *Vacuum*, vol. 85, pp. 792-797, 2011.
- [132] P. Eh. Hovsepian, Y. N. Kok, A. P. Ehiasarian , A. Erdemir, J. G. Wen and I. Petrov, “Structure and tribological behaviour of nanoscale multilayer C / Cr coatings deposited by the combined steered cathodic arc/unbalanced magnetron sputtering technique,” *Thin Solid Films*, vol. 447 – 448, p. 7–13, 2004.
- [133] A. Czyzniewski, “Mechanical and Tribological Properties of Cr-DLC Coatings Deposited by ARC-MAG-RF PACVD Hybrid Method,” *Plasma Process. Polym.*, vol. 4, p. S225–S230, 2007.
- [134] J. Sun, Z. Fu, W. Zhang, C. Wang, W. Yue, S. Lin and M. Dai, “Friction and wear of Cr-doped DLC films under different lubrication conditions,” *Vacuum*, vol. 94, pp. 1-5, 2013.
- [135] M. G. Kim, K. R. Lee and K. Y. Eun, “Tribological behaviour of silicon-incorporated diamond-like carbon films,” *Surface and Coatings Technology*, vol. 112, p. 204–209, 1999.
- [136] P.J. Kelly and R.D. Arnell, “Magnetron sputtering: a review of recent developments and applications,” *Vacuum*, vol. 56, pp. 159-172, 2000.
- [137] V. Kouznetsov, K. Maca’k, J. M. Schneider, U. Helmersson and I. Petrov, “A novel pulsed magnetron sputter technique utilizing very high target power densities,” *Surface & coatings technology*, vol. 122, no. 2-3, pp. 290-293, 1999.
- [138] U. Helmersson, M. Lattemann, J. Bohlmark, A.P. Ehiasarian and J.T. Gudmundsson, “Ionized physical vapor deposition (IPVD): A review of technology and applications,” *Thin solid films*, vol. 513, no. 1-2, pp. 1-24, 2006.
- [139] K. Sarakinos, J. Alami and S. Konstantinidis, “High power pulsed magnetron sputtering: A review on scientific and engineering state of the art,” *Surface & coatings technology*, vol. 204, no. 11, pp. 1661-1684, 2010.
- [140] J. W. Bradley, S. Thompson and Y. Aranda Gonzalvo, “Measurement of the plasma potential in a magnetron discharge and the prediction of the electron drift speeds,” *Plasma sources science & technology*, vol. 10, no. 3, pp. 490-501, 2001.
- [141] C. Christou and Z. H. Barber, “Ionization of sputtered material in a planar magnetron discharge,” *J. Vac. Sci. Technol. A*, vol. 18, no. 6, p. 2897, 2000.

- [142] A. Anders, "Discharge physics of high power impulse magnetron sputtering," *Surface & Coatings Technology*, vol. 205, p. S1–S9, 2011.
- [143] M. Lattemann, A.P. Ehasarian, J. Bohlmark, P.Å.O. Persson and U. Helmersson, "Investigation of high power impulse magnetron sputtering pretreated interfaces for adhesion enhancement of hard coatings on steel," *Surface & Coatings Technology*, vol. 200, p. 6495–6499, 2006.
- [144] W. D. Münz, "HIPIMS: The New PVD Technology," *Vakuum in Forschung und Praxis*, vol. 20, no. s1, pp. 27-32, 2008.
- [145] A.P. Ehasarian, R. New, W. D. Munz, L. Hultman, U. Helmersson and V. Kouznetsov, "Influence of high power densities on the composition of pulsed magnetron plasmas," *Vacuum*, vol. 65, no. 2, pp. 147-154, 2002.
- [146] A. P. Ehasarian, G. Kamath and P. Eh. Hovsepian, "Properties of TiAlCN/VCN nanoscale multilayer coatings deposited by mixed high-power impulse magnetron sputtering (HiPIMS) and unbalanced magnetron sputtering processes—impact of HiPIMS during coating," *IEEE transactions on plasma science*, vol. 38, no. 11, p. 3062, 2010.
- [147] W. D. Münz, M Schenkel, S Kunkel, J Paulitsch and K Bewilogua, "Industrial applications of hipims," *Journal of Physics:Conference Series*, vol. 100, p. 1–6, 2008.
- [148] G. Greczynski, J. Jensen, J. Böhlmark and L. Hultman, "Microstructure control of CrNx films during high power impulse magnetron sputtering," *Surface & coatings technology*, vol. 205, no. 1, pp. 118-130, 2010.
- [149] A. E. Ross, R. Sangines, B. Treverrow, M. M. M. McKenzie and D. R. Bilek, "Optimizing efficiency of Ti ionized deposition in HIPIMS," *Plasma sources science & technology*, vol. 20, no. 3, p. 035021, 2011.
- [150] B.A. Movchan and A.V. Demchishin, "Structure and properties of thick condensates of nickel, titanium, tungsten, aluminum oxides, and zirconium dioxide in vacuum," *Physics of Metals and Metallography*, vol. 28, p. 653, 1969.
- [151] J.A. Thornton, "Influence of apparatus geometry and deposition conditions on the structure and topography of thick sputtered coatings," *Journal of Vacuum Science Technology*, vol. 11, no. 4, p. 666, 1974.
- [152] R. Messier, A.P. Giri and R.A. Roy, "Revised structure zone model for thin film physical structure," *Journal of Vacuum Science Technology A*, vol. 2, no. 2, p. 500, 1984.
- [153] A. Y. Wang, K. R. Lee, J. P. Ahn and J. H. Han, "Structure and mechanical properties of W incorporated diamond-like carbon films prepared by a hybrid ion beam deposition technique," *Carbon*, vol. 44, p. 1826–1832, 2006.
- [154] H. Miki, T. Takeno and T. Takagi, "Tribological properties of multilayer DLC/W-DLC films on Si," *Thin solid films*, vol. 516, no. 16, pp. 5414-5418, 2008.

- [155] T. Takeno, T. Sugawara, H. Miki and T. Takagi, "Deposition of DLC film with adhesive W-DLC layer on stainless steel and its tribological properties," *Diamond and related materials*, vol. 18, no. 5-8, pp. 1023-1027, 2009.
- [156] N.J.M. Carvalho and J.Th.M. DeHosson, "Microstructure investigation of magnetron sputtered WC/C coatings deposited on steel substrates," *Thin solid films*, vol. 388, no. 1-2, pp. 150-159, 2001.
- [157] N. Vidakis, A. Antoniadis and N. Bilalis, "The VDI 3198 indentation test evaluation of a reliable qualitative control for layered compounds," *Journal of Materials Processing Technology*, vol. 143-144, p. 481-485, 2003.
- [158] A.A. Ogwu, R.W. Lamberton, S. Morley, P. Maguire and J. McLaughlin, "Characterisation of thermally annealed diamond like carbon (DLC) and silicon modified DLC films by Raman spectroscopy," *Physica B*, vol. 269, pp. 335-344, 1999.
- [159] M. S. Leu, S.Y. Chen, J.J. Chang, L.G. Chao and W. Lin, "Diamond-like coatings prepared by the filtered cathodic arc technique for minting application," *Surface and Coatings Technology*, vol. 177 -178, p. 566-572, 2004.
- [160] W.G. Cui, Q.B. Lai, L. Zhang and F.M. Wang, "Quantitative measurements of sp³ content in DLC films with Raman spectroscopy," *Surface & Coatings Technology*, vol. 205, p. 1995-1999, 2010.
- [161] J. F. Zhao, P. Lemoine, Z. H. Liu, J. P. Quinn and J. A. McLaughlin, "The effects of Si incorporation on the microstructure and nanomechanical properties of DLC thin films," *Journal of Physics: Condensed Matter*, vol. 12, p. 9201-9213, 2000.
- [162] D. Sheeja, B.K. Tay, S.P. Lau, X. Shi and X. Ding, "Structural and tribological characterization of multilayer ta-C films prepared by filtered cathodic vacuum arc with substrate pulse biasing," *Surface and Coatings Technology*, vol. 132, pp. 228-232, 2000.
- [163] M. A. Tamor and W. C. Vassell, "Raman "fingerprinting" of amorphous carbon films," *Journal of applied physics*, vol. 76, no. 6, p. 3823, 1994.
- [164] L. X. Liu and E. Liu, "Nitrogenated diamond-like carbon films for metal tracing," *Surface & coatings technology*, vol. 198, no. 1-3, pp. 189-193, 2005.
- [165] N. K. Cuong, M. Tahara, N. Yamauchi and T. Sone, "Diamond-like carbon films deposited on polymers by plasma-enhanced chemical vapor deposition," *Surface & coatings technology*, Vols. 174-175, pp. 1024-1028, 2003.
- [166] M. Yoshikawa, G. Katagiri, H. Ishida, A. Ishitani and T. Akamatsu, "Raman spectra of diamondlike amorphous carbon films," *Journal of applied physics*, vol. 64, no. 11, p. 6464, 1988.
- [167] D. Pradhan and M. Sharon, "Opto-electrical properties of amorphous carbon thin film deposited from natural precursor camphor," *Applied surface science*, vol. 253, no. 17, pp. 7004-7010, 2007.
- [168] C. Ziebert, M. Rinke, M. Stqber, S. Ulrich and H. Holleck, "Interfaces and temperature stability of stepwise graded DLC films studied by nanoindentation

- and Raman spectroscopy,” *Surface & coatings technology*, vol. 200, no. 1-4, pp. 1127-1131, 2005.
- [169] Q. Wang, D. D. Allred and L. V. Knight, “Deconvolution of the Raman spectrum of amorphous carbon,” *Journal of Raman Spectroscopy*, vol. 26, pp. 1039-1043, 1995.
- [170] B. Oral, R. Hauert, U. Muller and K. H. Ernst, “Structural changes in doped a-C:H films during annealing,” *Diamond and related materials*, vol. 4, no. 4, pp. 482-487, 1995.
- [171] F. C. Tai, S. C. Lee, J. Chen, C. Wei and S. H. Chang, “Multipeak fitting analysis of Raman spectra on DLCH film,” *Journal of Raman Spectroscopy*, vol. 40, p. 1055–1059, 2009.
- [172] A. C. Ferrari and J. Robertson, “Interpretation of Raman spectra of disordered and amorphous carbon,” *Physical Review B*, vol. 61, no. 20, pp. 95-107, 2000.
- [173] F. Tuinstra and J. L. Koenig, “Raman Spectrum of Graphite,” *The Journal of Chemical Physics*, vol. 53, no. 3, pp. 1126-1130, 1970.
- [174] M. L. Frauwallner , F. López-Linares, J. Lara-Romero, C. E. Scott, V. Ali, E. Hernández and P. Pereira-Almao, “Toluene hydrogenation at low temperature using a molybdenum carbide catalyst,” *Applied Catalysis A: General*, vol. 394, p. 62–70, 2011.
- [175] I. M. Hutchings, *Tribology - Friction and Wear of Engineering Materials*, Hodder Headline PLC., 1992.
- [176] S. J. Oh, D. C. Cook and H. E. Townsend, “Characterization of Iron Oxides Commonly Formed as Corrosion Products on Steel,” *Hyperfine Interactions*, vol. 112, no. 1-4, pp. 59-66, 1998.
- [177] J. E. Maslar, W. S. Hurst, W. J. Bowers Jr., J. H. Hendricks, M. I. Aquino and I. Levin, “In situ Raman spectroscopic investigation of chromium surfaces under hydrothermal condition,” *Applied Surface Science*, vol. 180, pp. 102-118, 2001.
- [178] J. Chen, D. Lu, W. Zhang, F. Xie, J. Zhou, L. Gong, X. Liu , S. Deng and N. Xu, “Synthesis and Raman spectroscopic study of W20O58 nanowires,” *Journal of Physics D: Applied Physics*, vol. 41, p. 115305, 2008.
- [179] H. Knozinger and H. Jeziorowski, “Raman Spectra of Molybdenum Oxide Supported on the Surface of Aluminas,” *The Journal of Physical Chemistry*, vol. 18, p. 82, 1978.
- [180] M. Dieterle and G. Mestl, “Raman spectroscopy of molybdenum oxides Part II. Resonance Raman spectroscopic characterization of the molybdenum oxides Mo4O11 and MoO2,” *Physical Chemistry Chemical Physics*, vol. 4, p. 822–826, 2002.
- [181] M. Mihalev, C. Hardalov, C. Christov, M. Michailov, B. Rangelov and H. Leiste, “Structural and adhesional properties of thin MoO3 films prepared by laser coating,” *Journal of Physics: Conference Series*, vol. 514, p. 012022, 2014.

- [182] M. Dieterle, G. Mestl, J. Jäger, Y. Uchida, H. Hibst and R. Schlögl, "Mixed molybdenum oxide based partial oxidation catalyst 2. Combined X-ray diffraction, electron microscopy and Raman investigation of the phase stability of (MoVW)5O14-type oxides," *Journal of Molecular Catalysis A: Chemical*, vol. 174, no. 1-2, pp. 169-185, 2001.
- [183] R. K. Sharma and G. B. Reddy, "Influence of O₂ – plasma ambience and growth temperature on the oxidation of Mo-metal and volatilization of oxides," *AIP Advances*, vol. 3, p. 092112, 2013.
- [184] X. Chen, Z. Peng, Z. Fu, S. Wu, W. Yue and C. Wang, "Microstructural, mechanical and tribological properties of tungsten-gradually doped diamond-like carbon films with functionally graded interlayers," *Surface & Coatings Technology*, vol. 205, p. 3631–3638, 2011.
- [185] N. N. Greenwood and A. Earnshaw, "Chapter 23," in *Chemistry of the Elements - 2nd edition*, Butterworth-Heinemann, 1997.
- [186] "Standard Test Method for Sulfated Ash from Lubricating Oils and Additives, Designation: D 874 – 00".
- [187] "http://www.mobil.co.uk/UK-English-LCW/carengineoils_products_mobil-1-extended-life-10w60.aspx#," [Online].
- [188] W.D. Münz, D. Schulze and F.J.M. Hauzer, "A new method for hard coatings: ABS TM (arc bond sputtering)," *Surface and Coatings Technology*, vol. 50, pp. 169-178, 1992.
- [189] P. Eh. Hovsepian, Y. N. Kok, A.P. Ehiasarian, R. Haasch, J. G. Wen and I. Petrov, "Phase separation and formation of the self-organised nanostructure in C/Cr coatings in conditions of high ion irradiation," *Surface & Coatings Technology*, vol. 200, pp. 1572-1579, 2005.
- [190] Y. N. Kok, P. Eh. Hovsepian, Q. Luo, D.B. Lewis, J. G. Wen and I. Petrov, "Influence of the bias voltage on the structure and the tribological performance of nanoscale multilayer C/Cr PVD coatings," *Thin Solid Films*, vol. 475, p. 219– 226, 2005.
- [191] A. Barata, L. Cunha and C. Moura, "Characterisation of chromium nitride films produced by PVD techniques," *Thin Solid Films*, vol. 398 –399, p. 501–506, 2001.
- [192] Q. Wei, Z. Li, Z. Zhang and Q. Zhou, "Facile Synthesis of α -Fe₂O₃ Nanostructured Films with Controlled Morphology," *Materials Transactions*, vol. 50, no. 6, pp. 1351-1354, 2009.
- [193] D. L. A. Faria, S. V. Silva and M. T. Oliveira, "Raman Microspectroscopy of Some Iron Oxides and Oxyhydroxides," *Journal of Raman Spectroscopy*, vol. 28, pp. 873-878, 1997.
- [194] Z. Zhou, I. M. Ross, L. Ma, W. M. Rainforth, A. P. Ehiasarian and P. Hovsepian, "Wear of hydrogen free C/Cr PVD coating against Al₂O₃ at room temperature," *Wear*, vol. 271, pp. 2150-2156, 2011.

- [195] R.E. Sowden, J.M. Orza and S. Nontero , “Vibrational spectra of anhydrous chromium(III) chloride,” *Polyhedron*, vol. 1, no. 5, pp. 475-477, 1982.
- [196] Y. Zhu, L. Wang, W. Yao and L. Cao, “The interface diffusion and reaction between Cr layer and diamond particle during metallization,” *Applied Surface Science*, vol. 171, pp. 143-150, 2001.
- [197] A. Boughriet, B. Ouddane , C. Cordier and J. Laureyns, “Thermodynamic, spectroscopic and magnetic studies on anoxic sediments from the Seine river estuary,” *Journal of Chemical Society Faraday Transactions*, vol. 94, pp. 3677-3683, 1998.
- [198] “[http://en.wikipedia.org/wiki/File:Chromium\(III\)-chloride-sheet-from-monoclinic-xtal-3D-balls.png](http://en.wikipedia.org/wiki/File:Chromium(III)-chloride-sheet-from-monoclinic-xtal-3D-balls.png),” [Online].
- [199] “[http://en.wikipedia.org/wiki/File:Chromium\(III\)-chloride-layers-stacking-from-monoclinic-xtal-3D-balls.png](http://en.wikipedia.org/wiki/File:Chromium(III)-chloride-layers-stacking-from-monoclinic-xtal-3D-balls.png),” [Online].
- [200] E. A. Gulbransen, K. F. Andrew and F. A. Brassart, “Studies On The High Temperature Oxidation Of Molybdenum, Tungsten, Niobium, Tantalum, Titanium, And Zirconium,” Project Number: ARG-D-I96, Westinghouse Electric Corporation Research Laboratories, Pittsburgh, Pennsylvania 15235, April 18, 1967.
- [201] E. Lassner and W. D. Schubert, “Chapter 3,” in *Tungsten: Properties, Chemistry, Technology of the Elements, Alloys, and Chemical Compounds*, Springer Science & Business Media, 1999, p. 86.
- [202] M. Lee and D. G. Flom, “Hardness of Polycrystalline Tungsten and Molybdenum Oxides at Elevated Temperatures,” *Journal of American Ceramic Society*, vol. 73, no. 7, pp. 2117-18, 1990.
- [203] “http://www.engineeringtoolbox.com/linear-expansion-coefficients-d_95.html,” [Online].
- [204] A. Warren, A. Nylund and I. Olefjord, “Oxidation of tungsten and tungsten carbide in dry and humid atmospheres,” *International Journal of Refractory Metals and Hard Materials*, vol. 14, no. 5-6, p. 345–353, 1996.
- [205] E. A. Gulbransen, K. F. Andrew and F. A. Brassart, “Oxidation of Molybdenum 550° to 1700°C,” *J. Electrochem. Soc.*, vol. 110, no. 9, pp. 952-959, 1963.
- [206] D. Y. Lu , J. Chen , J. Zhou, S. Z. Deng, N. S. Xu and J. B. Xu , “Raman spectroscopic study of oxidation and phase transition in W18O49 nanowires,” *Journal of Raman Spectroscopy*, vol. 38, p. 176–180, 2007.
- [207] P.M. Sousa, A.J. Silvestre, N. Popovici and O. Conde, “Morphological and structural characterization of CrO₂/Cr₂O₃ films grown by Laser-CVD,” *Applied Surface Science*, vol. 247, p. 423–428, 2005.
- [208] P.G. Li, M. Lei and W.H. Tang, “Raman and photoluminescence properties of α -Al₂O₃ microcones with hierarchical and repetitive superstructure,” *Materials Letters*, vol. 64, p. 161–163, 2010.

APPENDIX - A

Table A-1: Raman peaks of the spectra collected from as-deposited Mo–W–C coatings

Raman peaks assigned to		Raman peaks (this work)	Raman peaks (literature)
(a) as-deposited coating C2			
A1		~ 100 cm ⁻¹ with a width of ~ 25 cm ⁻¹	–
A2		~ 132 cm ⁻¹ with a width of ~ 57 cm ⁻¹	
A3		~ 193 cm ⁻¹ with a width of ~ 106 cm ⁻¹	
A4	Mo ₂ C	~ 353 cm ⁻¹ with a width of ~ 216 cm ⁻¹	~334 cm ⁻¹ , ~376 cm ⁻¹ [174]
A5		~ 634 cm ⁻¹ with a width of ~ 271 cm ⁻¹	~666 cm ⁻¹ [174]
(b) as-deposited coating C4			
B1		~ 100 cm ⁻¹ with a width of ~ 27 cm ⁻¹	–
B2		~ 131.5 cm ⁻¹ with a width of ~ 54 cm ⁻¹	
B3		~ 190 cm ⁻¹ with a width of ~ 103 cm ⁻¹	
B4	Mo ₂ C	~ 342 cm ⁻¹ with a width of ~ 213 cm ⁻¹	~334 cm ⁻¹ [174]
B5		~ 652 cm ⁻¹ with a width of ~ 330 cm ⁻¹	~666 cm ⁻¹ [174]
B6		~ 1065 cm ⁻¹ with a width of ~ 302 cm ⁻¹	–
(c) as-deposited coating C6			
C1		~ 100 cm ⁻¹ with a width of ~ 24 cm ⁻¹	–
C2		~ 127 cm ⁻¹ with a width of ~ 56 cm ⁻¹	
C3		~ 181 cm ⁻¹ with a width of ~ 105 cm ⁻¹	
C4		~ 318 cm ⁻¹ with a width of ~ 225 cm ⁻¹	
C5		~ 582 cm ⁻¹ with a width of ~ 440 cm ⁻¹	
C6		~ 1057 cm ⁻¹ with a width of ~ 723 cm ⁻¹	

Table A-2: Raman peaks of the spectra collected from the uncoated steel ball and the wear scar on the steel balls after dry sliding against Mo–W–C coatings

Raman peaks assigned to		Raman peaks (this work)	Raman peaks (literature)
(a) uncoated steel ball			
P1		~ 100 cm ⁻¹ with a width of ~ 28 cm ⁻¹	—
P2		~ 141 cm ⁻¹ with a width of ~ 65 cm ⁻¹	
P3		~ 218.5 cm ⁻¹ with a width of ~ 128 cm ⁻¹	
P4		~ 375 cm ⁻¹ with a width of ~ 253 cm ⁻¹	
P5		~ 787 cm ⁻¹ with a width of ~ 384 cm ⁻¹	
(b) steel ball after sliding against C2			
P1'		~ 97 cm ⁻¹ with a width of ~ 24 cm ⁻¹	—
P2'		~ 128 cm ⁻¹ with a width of ~ 51 cm ⁻¹	
P3'		~ 202 cm ⁻¹ with a width of ~ 120 cm ⁻¹	
P4'		~ 385 cm ⁻¹ with a width of ~ 266 cm ⁻¹	
P5'		~ 797 cm ⁻¹ with a width of ~ 359 cm ⁻¹	
(c) steel ball after sliding against C4			
P1'		~ 94 cm ⁻¹ with a width of ~ 18 cm ⁻¹	—
P2'		~ 111 cm ⁻¹ with a width of ~ 51 cm ⁻¹	
P3'		~ 177 cm ⁻¹ with a width of ~ 122.5 cm ⁻¹	
P4'	Fe ₂ O ₃	~ 328 cm ⁻¹	~293 – 298 cm ⁻¹ [176]
	Cr ₂ O ₃	with a width of ~ 311 cm ⁻¹	~300 cm ⁻¹ and ~350 cm ⁻¹ [177]
P5'		~ 792 cm ⁻¹ with a width of ~ 328 cm ⁻¹	—
(d) steel ball after sliding against C6			
P1'		~ 93 cm ⁻¹ with a width of ~ 18 cm ⁻¹	—
P2'		~ 110 cm ⁻¹ with a width of ~ 51 cm ⁻¹	
P3'		~ 178 cm ⁻¹ with a width of ~ 118 cm ⁻¹	
P4'	Fe ₂ O ₃	~ 323 cm ⁻¹	~293 – 298 cm ⁻¹ [176]
	Cr ₂ O ₃	with a width of ~ 301 cm ⁻¹	~300 cm ⁻¹ and ~350 cm ⁻¹ [177]
P5'		~ 794 cm ⁻¹ with a width of ~ 347 cm ⁻¹	—

Table A-3: Raman peaks of the spectra collected from the debris adhered to the steel counterpart after dry sliding against Mo–W–C coatings

Raman peaks assigned to		Raman peaks (this work)	Raman peaks (literature)
(a) adhered debris on steel ball after sliding against C2			
A1 (from coating)		~ 96 cm ⁻¹ with a width of ~ 26 cm ⁻¹	—
A2 (from coating)		~ 126.5 cm ⁻¹ with a width of ~ 54 cm ⁻¹	
A3 (from coating)		~ 190 cm ⁻¹ with a width of ~ 97 cm ⁻¹	
Mo _x O _y + W _x O _y	W ₂₀ O ₅₈	~303 cm ⁻¹ with a width of ~ 115.5 cm ⁻¹	~298 cm ⁻¹ and ~319 cm ⁻¹ [178]
	MoO ₃		~292 cm ⁻¹ [179]
	Mo ₄ O ₁₁		~306 cm ⁻¹ [180]
	Mo ₄ O ₁₁	~ 438 cm ⁻¹	~431 cm ⁻¹ [180]
	WO ₃	with a width of ~ 208 cm ⁻¹	~417 cm ⁻¹ and ~437 cm ⁻¹ [178]
WO ₃		~ 720 cm ⁻¹ with a width of ~ 271 cm ⁻¹	~717 cm ⁻¹ [178]
Mo _x O _y	Mo ₄ O ₁₁	~ 920 cm ⁻¹ with a width of ~ 165 cm ⁻¹	~907 cm ⁻¹ [181]
	Mo ₅ O ₁₄		~902 cm ⁻¹ [182]
	Mo ₈ O ₂₃		~902 cm ⁻¹ and ~958 cm ⁻¹ [183]
(b) adhered debris on steel ball after sliding against C4			
B1 (from coating)		~ 100 cm ⁻¹ with a width of ~ 25 cm ⁻¹	—
B2 (from coating)		~ 137 cm ⁻¹ with a width of ~ 59 cm ⁻¹	
B3 (from coating)		~ 211 cm ⁻¹ with a width of ~ 121.5 cm ⁻¹	
Mo _x O _y + W _x O _y	MoO ₂	~ 335 cm ⁻¹ with a width of ~ 215 cm ⁻¹	~357 cm ⁻¹ [174]
	MoO ₃		~337 cm ⁻¹ [179]
	WO ₃		~331 cm ⁻¹ and ~348 cm ⁻¹ [178]
	Mo ₄ O ₁₁		~340 cm ⁻¹ [180]
	W ₂₀ O ₅₈		~319 cm ⁻¹ and ~341 cm ⁻¹ [178]
Mo _x O _y	Mo ₄ O ₁₁	~ 929 cm ⁻¹ with a width of ~ 108 cm ⁻¹	~907 cm ⁻¹ [181]
	Mo ₅ O ₁₄		~902 cm ⁻¹ [182]
	Mo ₈ O ₂₃		~902 cm ⁻¹ and ~958 cm ⁻¹ [183]
(c) adhered debris on steel ball after sliding against C6			
C1 (from coating)		~ 95 cm ⁻¹ with a width of ~ 25 cm ⁻¹	—
C2 (from coating)		~ 125 cm ⁻¹ with a width of ~ 49.5 cm ⁻¹	
C3 (from coating)		~ 178 cm ⁻¹ with a width of ~ 87 cm ⁻¹	
Mo ₂ C + Mo _x O _y	Mo ₂ C	~280 cm ⁻¹ with a width of ~ 149cm ⁻¹	~280 cm ⁻¹ [174]
	W ₂₀ O ₅₈		~281 cm ⁻¹ and ~298 cm ⁻¹ [178]
	MoO ₃		~284 cm ⁻¹ and ~292 cm ⁻¹ [179]
	Mo ₄ O ₁₁		~264 cm ⁻¹ [180]
Mo _x O _y + W _x O _y	Mo ₄ O ₁₁	~ 433.5 cm ⁻¹	~431 cm ⁻¹ [180]
	WO ₃	with a width of ~ 248.5 cm ⁻¹	~417 cm ⁻¹ and ~437 cm ⁻¹ [178]
	Mo ₄ O ₁₁	~ 787 cm ⁻¹	~744 cm ⁻¹ and ~790 cm ⁻¹ [180]
	WO ₃	with a width of ~ 368 cm ⁻¹	~807 cm ⁻¹ [178]

Table A-4: Raman peaks of the spectra collected within the wear track of Mo–W–C coatings after dry sliding against steel balls

Raman peaks assigned to		Raman peaks (this work)	Raman peaks (literature)
(a) wear track of C2 after sliding			
A1		~ 100 cm ⁻¹ with a width of ~ 27 cm ⁻¹	—
A2		~ 133 cm ⁻¹ with a width of ~ 58 cm ⁻¹	
A3		~ 194 cm ⁻¹ with a width of ~ 107 cm ⁻¹	
A4	Mo ₂ C	~ 358 cm ⁻¹ with a width of ~ 216 cm ⁻¹	~334 cm ⁻¹ and ~376 cm ⁻¹ [174]
A5		~ 636 cm ⁻¹ with a width of ~ 248 cm ⁻¹	~666 cm ⁻¹ [174]
A6		~ 900 cm ⁻¹ with a width of ~ 369 cm ⁻¹	—
(b) wear track of C4 after sliding			
B3'		~ 173 cm ⁻¹ with a width of ~ 100 cm ⁻¹	—
B4'	Mo ₂ C	~ 320 cm ⁻¹ with a width of ~ 226 cm ⁻¹	~334 cm ⁻¹ [174]
	WO ₃		~326 cm ⁻¹ and ~331 cm ⁻¹ [178]
	W ₂₀ O ₅₈		~319 cm ⁻¹ and ~341 cm ⁻¹ [178]
B5'	Mo ₂ C	~ 644 cm ⁻¹ with a width of ~ 383 cm ⁻¹	~666 cm ⁻¹ [174]
	MoO ₂		~640 cm ⁻¹ and ~666 cm ⁻¹ [174]
	MoO ₃		~667 cm ⁻¹ [179]
	Mo ₈ O ₂₃		~658 cm ⁻¹ [183]
WC		~ 942 cm ⁻¹ with a width of ~150 cm ⁻¹	~960 cm ⁻¹ [184]
(c) wear track of C6 after sliding			
C1		~ 105 cm ⁻¹ with a width of ~ 35 cm ⁻¹	—
C3'	MoO ₃	~ 159 cm ⁻¹ with a width of ~ 94 cm ⁻¹	~158 cm ⁻¹ [179]
C4'	MoO ₃	~ 290 cm ⁻¹ with a width of ~ 211 cm ⁻¹	~284 cm ⁻¹ and ~292 cm ⁻¹ [179]
	W ₂₀ O ₅₈		~298 cm ⁻¹ [178]
C5'		~ 531 cm ⁻¹ with a width of ~ 357 cm ⁻¹	—
C6'		~ 866 cm ⁻¹ with a width of ~ 563 cm ⁻¹	

Table A-5: Raman peaks of the spectra collected within the wear track of Mo–W–C coatings after lubricated sliding against steel balls

Raman peaks assigned to		Raman peaks (this work)	Raman peaks (literature)
(a) wear track of C2 after lubricated sliding			
A1		~ 100 cm ⁻¹ with a width of ~ 30.5 cm ⁻¹	–
WS ₂		~ 136.5 cm ⁻¹ with a width of ~ 33 cm ⁻¹	~128 cm ⁻¹ [figure 4.2-14a]
A3'		~ 168 cm ⁻¹ with a width of ~ 69 cm ⁻¹	–
Mo ₂ C		~ 235 cm ⁻¹ with a width of ~ 111 cm ⁻¹	~234 cm ⁻¹ [174]
A4'	Mo ₂ C	~ 368.5 cm ⁻¹ with a width of ~ 187.5 cm ⁻¹	~334 cm ⁻¹ , ~376 cm ⁻¹ [174]
A5'		~ 626 cm ⁻¹ with a width of ~ 322 cm ⁻¹	~666 cm ⁻¹ [174]
WC		~ 955 cm ⁻¹ with a width of ~ 237.5 cm ⁻¹	~ 960 cm ⁻¹ [184]
(b) wear track of C4 after lubricated sliding			
B1		~ 97 cm ⁻¹ with a width of ~ 26 cm ⁻¹	–
WS ₂		~ 133 cm ⁻¹ with a width of ~ 51 cm ⁻¹	~128 cm ⁻¹ [figure 4.2-14a]
B3		~ 199 cm ⁻¹ with a width of ~ 111 cm ⁻¹	–
B4	Mo ₂ C	~ 341 cm ⁻¹ with a width of ~ 210 cm ⁻¹	~334 cm ⁻¹ [174]
B5'		~ 623 cm ⁻¹ with a width of ~ 346 cm ⁻¹	~666 cm ⁻¹ [174]
Mo ₂ C		~ 993 cm ⁻¹	~995 cm ⁻¹ [174]
WC		with a width of ~ 278 cm ⁻¹	~ 960 cm ⁻¹ [184]
(c) wear track of C6 after lubricated sliding			
C1		~ 98 cm ⁻¹ with a width of ~ 25 cm ⁻¹	–
WS ₂		~ 135 cm ⁻¹ with a width of ~ 50 cm ⁻¹	~128 cm ⁻¹ [figure 4.2-14a]
C3'		~ 199 cm ⁻¹ with a width of ~ 109 cm ⁻¹	–
C4'		~ 341 cm ⁻¹ with a width of ~ 199 cm ⁻¹	
C5'		~ 609 cm ⁻¹ with a width of ~ 352 cm ⁻¹	
Mo ₂ C		~ 968 cm ⁻¹	~995 cm ⁻¹ [174]
WC		with a width of ~ 304 cm ⁻¹	~ 960 cm ⁻¹ [184]

Table A-6: Raman peaks of the spectrum collected within the wear track of C4 after lubricated sliding against Al₂O₃ ball

Raman peaks assigned to		Raman peaks (this work)	Raman peaks (literature)
B1		~ 97 cm ⁻¹ with a width of ~ 19 cm ⁻¹	-
B2'		~ 108 cm ⁻¹ with a width of ~ 50 cm ⁻¹	
B3'		~ 159 cm ⁻¹ with a width of ~ 102 cm ⁻¹	
WS ₂		~ 253 cm ⁻¹ with a width of ~ 88 cm ⁻¹	~254 cm ⁻¹ [figure 4.2-14a]
B4'	Mo ₂ C	~ 360 cm ⁻¹ with a width of ~ 210 cm ⁻¹	~334 cm ⁻¹ [174]
B5'		~ 637 cm ⁻¹ with a width of ~ 300 cm ⁻¹	~666 cm ⁻¹ [174]
WC		~ 949 cm ⁻¹	~ 960 cm ⁻¹ [184]
Mo ₂ C		with a width of ~ 244 cm ⁻¹	~995 cm ⁻¹ [174]

Table A-7: Raman peaks of the spectra collected from the (a) as-deposited Cr/C coating and the wear track after (b) dry and (c) lubricated sliding against steel balls

Raman peaks assigned to	Raman peaks (this work)	Raman peaks (literature)
<i>(a) as-deposited Cr/C coating</i>		
P1	~ 98 cm ⁻¹ with a width of ~ 24 cm ⁻¹	—
P2	~ 134 cm ⁻¹ with a width of ~ 55 cm ⁻¹	
P3	~ 207 cm ⁻¹ with a width of ~ 113 cm ⁻¹	
P4	~ 348 cm ⁻¹ with a width of ~195 cm ⁻¹	
P5	~ 637 cm ⁻¹ with a width of ~ 344 cm ⁻¹	
P6	~ 1015 cm ⁻¹ with a width of ~ 209 cm ⁻¹	
<i>(b) wear track after dry sliding</i>		
P1	~ 97 cm ⁻¹ with a width of ~ 26 cm ⁻¹	—
P2	~ 128 cm ⁻¹ with a width of ~ 45 cm ⁻¹	
P3'	~ 169 cm ⁻¹ with a width of ~ 69 cm ⁻¹	
P4'	~ 237 cm ⁻¹ with a width of ~ 112 cm ⁻¹	
Cr ₂ N	~ 384 cm ⁻¹ with a width of ~ 189 cm ⁻¹	~ 385 cm ⁻¹ [191]

Cr ₂ O ₃	~ 536 cm ⁻¹ with a width of ~ 115 cm ⁻¹	~ 527 – 530 cm ⁻¹ [177]
Cr ₂ O ₃	~679 cm ⁻¹ with a width of ~ 194 cm ⁻¹	~552 cm ⁻¹ and ~613 cm ⁻¹ [177]
Fe ₂ O ₃		~611– 613 cm ⁻¹ [192], [193]
Fe ₃ O ₄		~661– 663 cm ⁻¹ [192], [193]
P6'	~ 967 cm ⁻¹ with a width of ~ 320 cm ⁻¹	–
<i>(c) wear track after lubricated sliding</i>		
P1	~ 97 cm ⁻¹ with a width of ~ 25 cm ⁻¹	–
P2	~ 132 cm ⁻¹ with a width of ~ 56 cm ⁻¹	
CrCl ₃	~ 205 cm ⁻¹ with a width of ~ 116 cm ⁻¹	~ 207.5±2 cm ⁻¹ [195]
Cr ₂ C	~ 349 cm ⁻¹ with a width of ~ 200 cm ⁻¹	~344 cm ⁻¹ [196]
CrCl ₃		~342±2 cm ⁻¹ [195]
Cr ₂ S ₃		~536 cm ⁻¹ [figure 4.2-19]
FeS ₂		~341 cm ⁻¹ [197]
Cr ₂ C	~653 cm ⁻¹ with a width of ~388 cm ⁻¹	~544 cm ⁻¹ , ~601 cm ⁻¹ and ~695 cm ⁻¹ [196]
Cr ₂ N		~586 cm ⁻¹ , ~667 cm ⁻¹ and ~760 cm ⁻¹ [191]
CrN		~660 cm ⁻¹ [191]
Cr ₂ S ₃		~536 cm ⁻¹ [figure 4.2-19]
P6'	~ 1052 cm ⁻¹ with a width of ~ 211 cm ⁻¹	–

Table A-8: Raman peaks of the metal carbides present in C4 after heat-treated to 400°C

Raman peaks assigned to	Raman peaks (this work)	Raman peaks (literature)
Mo ₂ C	~ 342 cm ⁻¹ with a width of ~ 239 cm ⁻¹	~ 334 cm ⁻¹ [174]
WC	~ 943 cm ⁻¹ with a width of ~ 76 cm ⁻¹	~ 960 cm ⁻¹ [184]

Table A-9: Raman peaks of the metal carbides and metal oxides present in C4 after heat-treated to 500°C

Raman peaks assigned to	Raman peaks (this work)	Raman peaks (literature)
WO ₃	~ 320 cm ⁻¹ with a width of ~ 213 cm ⁻¹	~ 326 cm ⁻¹ [178]
W ₁₈ O ₄₉		~ 100–400 cm ⁻¹ [206]
W ₂₀ O ₅₈		~ 319 cm ⁻¹ [178]
Mo ₂ C	~ 462 cm ⁻¹ with a width of ~ 64 cm ⁻¹	~ 470 cm ⁻¹ [174]
MoO ₃		~ 474 cm ⁻¹ [179]
Mo ₄ O ₁₁		~ 452 cm ⁻¹ [180]
W ₂₀ O ₅₈		~ 463 cm ⁻¹ [179]
WO ₃	~ 707 cm ⁻¹ with a width of ~ 112 cm ⁻¹	~ 717 cm ⁻¹ [178]
W ₁₈ O ₄₉		~ 600–800 cm ⁻¹ [206]
W ₂₀ O ₅₈		~ 700 cm ⁻¹ [178]
Mo ₂ C	~ 817 cm ⁻¹ with a width of ~ 81 cm ⁻¹	~ 819 cm ⁻¹ [174]
MoO ₃		~ 820 cm ⁻¹ [179]
WO ₃		~ 717 cm ⁻¹ [178]
WC		~ 960 cm ⁻¹ [184]
Mo ₄ O ₁₁	~ 944 cm ⁻¹ with a width of ~ 119 cm ⁻¹	~ 907 cm ⁻¹ and ~ 985 cm ⁻¹ [180]
Mo ₅ O ₁₄		~ 902 cm ⁻¹ [182]
Mo ₈ O ₂₃		~ 902 cm ⁻¹ and ~ 958 cm ⁻¹ [183]

Table A-10: Raman peaks of the metal oxides present in C4 after heat-treated to 600°C

Raman peaks assigned to	Raman peaks (this work)	Raman peaks (literature)
WO ₃	~ 99 cm ⁻¹ with a width of ~ 29.5 cm ⁻¹	~ 95 cm ⁻¹ [178]
WO ₃	~ 140 cm ⁻¹ with a width of ~ 27 cm ⁻¹	~ 134 cm ⁻¹ [178]
W ₁₈ O ₄₉		~ 100–400 cm ⁻¹ [206]
WO ₃	~ 274 cm ⁻¹ with a width of ~ 34 cm ⁻¹	~ 273 cm ⁻¹ [178]
W ₁₈ O ₄₉		~ 100–400 cm ⁻¹ [206]
WO ₃	~ 353 cm ⁻¹ with a width of ~ 73 cm ⁻¹	~ 348 cm ⁻¹ [178]
MoO ₃		~ 337 cm ⁻¹ and ~ 367 cm ⁻¹ [179]
Mo ₄ O ₁₁		~ 340 cm ⁻¹ [180]
WO ₃	~ 704 cm ⁻¹ with a width of ~ 77 cm ⁻¹	~ 717 cm ⁻¹ [178]
W ₁₈ O ₄₉		~ 600–800 cm ⁻¹ [206]
W ₂₀ O ₅₈		~ 700 cm ⁻¹ [178]
Mo ₄ O ₁₁	~ 789 cm ⁻¹ with a width of ~ 29 cm ⁻¹	~ 790 cm ⁻¹ [180]
MoO ₃	~ 842 cm ⁻¹ with a width of ~ 74 cm ⁻¹	~ 820 cm ⁻¹ [179]
Mo ₄ O ₁₁		~ 843 cm ⁻¹ [180]
Mo ₅ O ₁₄		~ 845 cm ⁻¹ and ~ 860 cm ⁻¹ [182]
Mo ₈ O ₂₃	~ 958 cm ⁻¹ with a width of ~ 52 cm ⁻¹	~ 958 cm ⁻¹ [183]
WC		~ 960 cm ⁻¹ [184]

Table A-11: Raman peaks of the metal oxides present in C4 after heat-treated to 700°C

Raman peaks assigned to	Raman peaks (this work)	Raman peaks (literature)
WO ₃	~ 99 cm ⁻¹ with a width of ~ 27 cm ⁻¹	~ 95 cm ⁻¹ [178]
WO ₃	~ 138 cm ⁻¹ with a width of ~ 23.5 cm ⁻¹	~ 134 cm ⁻¹ [178]
W ₁₈ O ₄₉		~ 100–400 cm ⁻¹ [206]
WO ₃	~ 271 cm ⁻¹ with a width of ~ 23.5 cm ⁻¹	~ 273 cm ⁻¹ [178]
W ₁₈ O ₄₉		~ 100–400 cm ⁻¹ [206]
WO ₃	~ 345 cm ⁻¹ with a width of ~ 96 cm ⁻¹	~ 348 cm ⁻¹ [178]
MoO ₃		~ 337 cm ⁻¹ and ~ 367 cm ⁻¹ [179]
Mo ₄ O ₁₁		~ 340 cm ⁻¹ [180]
Fe ₂ O ₃	~ 495 cm ⁻¹	~ 497 cm ⁻¹ [176]
WO ₃	~ 707.5 cm ⁻¹ with a width of ~ 46 cm ⁻¹	~ 717 cm ⁻¹ [178]
W ₁₈ O ₄₉		~ 600–800 cm ⁻¹ [206]
W ₂₀ O ₅₈		~ 700 cm ⁻¹ [178]
CrO ₂		~ 700 cm ⁻¹ [207]
MoO ₃	~ 837 cm ⁻¹ with a width of ~ 90 cm ⁻¹	~ 820 cm ⁻¹ [179]
Mo ₄ O ₁₁		~ 835 cm ⁻¹ and ~ 843 cm ⁻¹ [180]
Mo ₅ O ₁₄		~ 845 cm ⁻¹ and ~ 860 cm ⁻¹ [182]
Mo ₈ O ₂₃		~ 958 cm ⁻¹ [183]
WC	~ 950 cm ⁻¹ with a width of ~ 32 cm ⁻¹	~ 960 cm ⁻¹ [184]

Table A-12: Raman peaks of the metal oxides present in C4 after heat-treated to 800°C

Raman peaks assigned to	Raman peaks (this work)	Raman peaks (literature)
WO ₃	~ 93 cm ⁻¹	~ 95 cm ⁻¹ [178]
WO ₃	~ 135 cm ⁻¹	~ 134 cm ⁻¹ [178]
W ₁₈ O ₄₉		~ 100–400 cm ⁻¹ [206]
WO ₃	~ 202 cm ⁻¹	~ 205 cm ⁻¹ [178]
MoO ₃		~ 199 cm ⁻¹ [179]
Mo ₄ O ₁₁		~ 206 cm ⁻¹ [180]
W ₂₀ O ₅₈	~ 360 cm ⁻¹	~ 359 cm ⁻¹ [178]
MoO ₃		~ 367 cm ⁻¹ [179]
MoO ₂		~ 357 cm ⁻¹ [174]
Fe ₂ O ₃	~ 497 cm ⁻¹	~ 497 cm ⁻¹ [176]
MoO ₂	~ 552 cm ⁻¹	~ 566 cm ⁻¹ [174]
Mo ₄ O ₁₁		~ 568 cm ⁻¹ [180]
Cr ₂ O ₃		~ 554 cm ⁻¹ [207] ~ 552 cm ⁻¹ [177]
Cr ₂ C	~ 688 cm ⁻¹	~ 695 cm ⁻¹ [196]
WO ₃	~ 729 cm ⁻¹	~ 717 cm ⁻¹ [178]
MoO ₂		~ 732 cm ⁻¹ [174]
Mo ₅ O ₁₄		~ 720 cm ⁻¹ [182]
CrO ₂		~ 700 cm ⁻¹ [207]

W ₂₀ O ₅₈	~ 836 cm ⁻¹	~ 830 cm ⁻¹ [178]
MoO ₃		~ 820 cm ⁻¹ [179]
Mo ₄ O ₁₁		~ 835 cm ⁻¹ and ~ 843 cm ⁻¹ [180]
Mo ₈ O ₂₃	~ 945 cm ⁻¹	~ 958 cm ⁻¹ [183]
WC		~ 960 cm ⁻¹ [184]

Table A-13: Raman peaks of the metal carbides and metal oxides present in Mo–W–C coatings after dynamic oxidation

Raman peaks assigned to	Raman peaks (this work)	Raman peaks (literature)
(a) coating C2		
WO ₃	~ 100 cm ⁻¹	~ 95 cm ⁻¹ [178]
W ₂₀ O ₅₈	~ 213 cm ⁻¹	~ 216 cm ⁻¹ [178]
WO ₃	~ 334 cm ⁻¹	~ 331 cm ⁻¹ [178]
W ₂₀ O ₅₈	~ 488 cm ⁻¹	~ 483 cm ⁻¹ [178]
WO ₃	~ 580 cm ⁻¹	~ 576 cm ⁻¹ [178]
WO ₃	~ 678 cm ⁻¹	~ 639 cm ⁻¹ [178]
W ₂₀ O ₅₈		~ 648 cm ⁻¹ [178]
Cr ₂ C	~ 700 cm ⁻¹	~ 695 cm ⁻¹ [196]
W ₂₀ O ₅₈		~ 700 cm ⁻¹ [178]
Fe ₂ O ₃	~ 1330 cm ⁻¹	~ 1320 cm ⁻¹ [176]
(b) coating C4		
WO ₃	~ 234 cm ⁻¹	~ 240 cm ⁻¹ [178]
W ₂₀ O ₅₈		~ 240 cm ⁻¹ [178]
WO ₃	~ 296 cm ⁻¹	~ 294 cm ⁻¹ [178]
Fe ₂ O ₃		~ 292 cm ⁻¹ [176]
Cr ₂ O ₃		~ 300 cm ⁻¹ [177]
Fe ₂ O ₃	~ 418 cm ⁻¹	~ 411 cm ⁻¹ [176]
Fe ₂ O ₃	~ 509 cm ⁻¹	~ 497 cm ⁻¹ [176]
Fe ₂ O ₃	~ 614 cm ⁻¹	~ 612 cm ⁻¹ [176]
Cr ₂ O ₃		~ 613 cm ⁻¹ [177]
Fe ₂ O ₃	~ 665 cm ⁻¹	~ 670 cm ⁻¹ [176]
Fe ₃ O ₄		~ 667 cm ⁻¹ [176]
Fe ₂ O ₃	~ 1327 cm ⁻¹	~ 1320 cm ⁻¹ [176]
(c) coating C6		
WO ₃	~ 226 cm ⁻¹	~ 220 cm ⁻¹ [178]
Fe ₂ O ₃		~ 226 cm ⁻¹ [176]
WO ₃	~ 293 cm ⁻¹	~ 294 cm ⁻¹ [178]
Fe ₂ O ₃		~ 292 cm ⁻¹ [176]
Cr ₂ O ₃		~ 300 cm ⁻¹ [177]
Fe ₂ O ₃	~ 412 cm ⁻¹	~ 411 cm ⁻¹ [176]
Fe ₂ O ₃	~ 503 cm ⁻¹	~ 497 cm ⁻¹ [176]
Fe ₂ O ₃	~ 614 cm ⁻¹	~ 612 cm ⁻¹ [176]
Cr ₂ O ₃		~ 613 cm ⁻¹ [177]
Fe ₂ O ₃	~ 665 cm ⁻¹	~ 670 cm ⁻¹ [176]
Fe ₃ O ₄		~ 667 cm ⁻¹ [176]
Fe ₂ O ₃	~ 1330 cm ⁻¹	~ 1320 cm ⁻¹ [176]

Table A-14: Raman peaks of the debris adhered to the Al_2O_3 balls after sliding against C2 at elevated temperature

Raman peaks assigned to	Raman peaks (this work)	Raman peaks (literature)
<i>(a) debris adhered to Al₂O₃ ball at 200°C</i>		
WO ₃	~ 180 cm ⁻¹	~ 178 cm ⁻¹ [178]
W ₂₀ O ₅₈	with a width of ~ 119 cm ⁻¹	~ 179 cm ⁻¹ [178]
WO ₃	~ 293 cm ⁻¹	~ 294 cm ⁻¹ [178]
W ₂₀ O ₅₈	with a width of ~ 45 cm ⁻¹	~ 298 cm ⁻¹ [178]
Al ₂ O ₃	~ 386 cm ⁻¹	~ 378 cm ⁻¹ [208]
Al ₂ O ₃	~ 660 cm ⁻¹ with a width of ~ 149 cm ⁻¹	~ 648 cm ⁻¹ [208]
WO ₃		~ 639 cm ⁻¹ [178]
W ₂₀ O ₅₈		~ 648 cm ⁻¹ [178]
<i>(b) debris adhered to Al₂O₃ ball at 400°C</i>		
WO ₃	~ 186 cm ⁻¹	~ 178 cm ⁻¹ [178]
W ₂₀ O ₅₈	with a width of ~ 115 cm ⁻¹	~ 179 cm ⁻¹ [178]
WO ₃	~ 295.5 cm ⁻¹	~ 294 cm ⁻¹ [178]
W ₂₀ O ₅₈	with a width of ~ 40 cm ⁻¹	~ 298 cm ⁻¹ [178]
W ₂₀ O ₅₈	~ 358 cm ⁻¹	~ 359 cm ⁻¹ [178]
Al ₂ O ₃	~ 652 cm ⁻¹ with a width of ~ 95 cm ⁻¹	~ 648 cm ⁻¹ [208]
WO ₃		~ 639 cm ⁻¹ [178]
W ₂₀ O ₅₈		~ 648 cm ⁻¹ [178]
<i>(c) debris adhered to Al₂O₃ ball at 600°C</i>		
WO ₃	~ 219 cm ⁻¹	~ 216 cm ⁻¹ [178]
W ₂₀ O ₅₈	with a width of ~ 141 cm ⁻¹	~ 220 cm ⁻¹ [178]
Al ₂ O ₃	~ 380 cm ⁻¹	~ 378 cm ⁻¹ [208]
MoO ₃	with a width of ~ 261 cm ⁻¹	~ 380 cm ⁻¹ [179]
Al ₂ O ₃	~ 651 cm ⁻¹	~ 648 cm ⁻¹ [208]
MoO ₃	with a width of ~ 71 cm ⁻¹	~667 cm ⁻¹ [179]

Table A-15: Raman peaks of the spectra collected within the wear track of Mo–W–C coatings after sliding against Al_2O_3 balls at ambient temperature

Raman peaks assigned to	Raman peaks (this work)	Raman peaks (literature)
<i>(a) wear track of C2 after sliding</i>		
A1'	$\sim 96 \text{ cm}^{-1}$ with a width of $\sim 24.5 \text{ cm}^{-1}$	—
A2'	$\sim 124 \text{ cm}^{-1}$ with a width of $\sim 53 \text{ cm}^{-1}$	

A3'		~ 182.5 cm ⁻¹ with a width of ~ 109 cm ⁻¹	
A4'	Mo ₂ C	~ 339 cm ⁻¹ with a width of ~ 220 cm ⁻¹	~334 cm ⁻¹ and ~376 cm ⁻¹ [174]
A5'		~ 660.5 cm ⁻¹ with a width of ~ 351 cm ⁻¹	~666 cm ⁻¹ [174]
(b) debris adhered to the wear track of C2 after sliding			
A1'		~ 94 cm ⁻¹ with a width of ~ 24 cm ⁻¹	–
W _x O _y + MoO ₃	WO ₃	~ 127 cm ⁻¹ with a width of ~ 40 cm ⁻¹	~134 cm ⁻¹ [178]
	W ₂₀ O ₅₈		~121 cm ⁻¹ and ~131 cm ⁻¹ [178]
	MoO ₃		~129 cm ⁻¹ [179]
W _x O _y	WO ₃	~ 190 cm ⁻¹	~187 cm ⁻¹ [178]
	W ₂₀ O ₅₈	with a width of ~ 112 cm ⁻¹	~191 cm ⁻¹ [178]
W _x O _y + MoO ₃	W ₂₀ O ₅₈	~ 283 cm ⁻¹	~281 cm ⁻¹ [178]
	MoO ₃	with a width of ~ 33 cm ⁻¹	~284 cm ⁻¹ [179]
W _x O _y + MoO ₃	WO ₃	~ 331.5 cm ⁻¹	~331 cm ⁻¹ [178]
	MoO ₃	with a width of ~ 174 cm ⁻¹	~337 cm ⁻¹ [179]
W ₂₀ O ₅₈		~ 506 cm ⁻¹ with a width of ~ 143 cm ⁻¹	~500 cm ⁻¹ [178]
W _x O _y + MoO ₃	W ₂₀ O ₅₈	~ 656 cm ⁻¹	~648 cm ⁻¹ [178]
	MoO ₃	with a width of ~ 128 cm ⁻¹	~667 cm ⁻¹ [179]
W _x O _y + MoO ₃	W ₂₀ O ₅₈	~ 855 cm ⁻¹	~830 cm ⁻¹ and ~873 cm ⁻¹ [178]
	MoO ₃	with a width of ~ 160 cm ⁻¹	~820 cm ⁻¹ [179]
(c) wear track of C4 after sliding			
B1		~ 98 cm ⁻¹ with a width of ~ 29 cm ⁻¹	–
B2		~ 131.5 cm ⁻¹ with a width of ~ 57 cm ⁻¹	
B3		~ 190 cm ⁻¹ with a width of ~ 102 cm ⁻¹	
B4	Mo ₂ C	~ 334 cm ⁻¹ with a width of ~ 202 cm ⁻¹	~334 cm ⁻¹ and ~376 cm ⁻¹ [174]
B5'		~ 625 cm ⁻¹ with a width of ~ 100 cm ⁻¹	~666 cm ⁻¹ [174]
(d) debris adhered to the wear track of C4 after sliding			
B1		~ 95 cm ⁻¹ with a width of ~ 21 cm ⁻¹	–
W _x O _y + MoO ₃	WO ₃	~ 125 cm ⁻¹ with a width of ~ 36 cm ⁻¹	~134 cm ⁻¹ [178]
	W ₂₀ O ₅₈		~121 cm ⁻¹ and ~131 cm ⁻¹ [178]
	MoO ₃		~129 cm ⁻¹ [179]
B3'		~174.5 cm ⁻¹ with a width of ~ 78 cm ⁻¹	–
W _x O _y + MoO ₃	WO ₃	~274 cm ⁻¹ with a width of ~ 147 cm ⁻¹	~273 cm ⁻¹ [178]
	W ₂₀ O ₅₈		~281 cm ⁻¹ [178]
	MoO ₃		~284 cm ⁻¹ [179]
W _x O _y	WO ₃	~415 cm ⁻¹	~417 cm ⁻¹ [178]
	W ₂₀ O ₅₈	with a width of ~ 243 cm ⁻¹	~408 cm ⁻¹ [178]
W ₂₀ O ₅₈		~872 cm ⁻¹ with a width of ~ 33 cm ⁻¹	~873 cm ⁻¹ [178]

<i>(e) wear track of C6 after sliding</i>		
C1'	~ 97 cm ⁻¹ with a width of ~ 24 cm ⁻¹	—
C2'	~124 cm ⁻¹ with a width of ~ 49 cm ⁻¹	
C3'	~177 cm ⁻¹ with a width of ~ 99 cm ⁻¹	
C4'	~316 cm ⁻¹ with a width of ~ 222 cm ⁻¹	
C5'	~618.5 cm ⁻¹ with a width of ~ 429 cm ⁻¹	

Table A-16: Raman peaks of the spectra collected within the wear track of Mo–W–C coatings after sliding against Al₂O₃ balls at 200°C

Raman peaks assigned to		Raman peaks (this work)	Raman peaks (literature)
(a) wear track of C2 : position 1			
W _x O _y + MoO ₃	WO ₃	~ 135 cm ⁻¹ with a width of ~ 97.5 cm ⁻¹	~134 cm ⁻¹ [178]
	W ₂₀ O ₅₈		~131 cm ⁻¹ [178]
	MoO ₃		~129 cm ⁻¹ [179]
W _x O _y + MoO ₃	WO ₃	~ 216 cm ⁻¹ with a width of ~ 35.5 cm ⁻¹	~220 cm ⁻¹ [178]
	W ₂₀ O ₅₈		~216 cm ⁻¹ [178]
	MoO ₃		~218 cm ⁻¹ [179]
WO ₃		~ 275 cm ⁻¹ with a width of ~ 47 cm ⁻¹	~273 cm ⁻¹ [178]
W _x O _y + Fe ₂ O ₃	WO ₃	~ 372 cm ⁻¹ with a width of ~ 147 cm ⁻¹	~378 cm ⁻¹ [178]
	W ₂₀ O ₅₈		~376 cm ⁻¹ [178]
	Fe ₂ O ₃		~ 381 cm ⁻¹ [176]
W ₂₀ O ₅₈		~ 489.5 cm ⁻¹ with a width of ~ 47 cm ⁻¹	~483 cm ⁻¹ [178]
W ₂₀ O ₅₈		~ 602 cm ⁻¹ with a width of ~ 174 cm ⁻¹	~603 cm ⁻¹ [178]
Fe ₂ O ₃		~ 1290 cm ⁻¹ with a width of ~ 100.5 cm ⁻¹	~1320 cm ⁻¹ [176]
(b) wear track of C2 : position 2			
A1		~ 105.5 cm ⁻¹ with a width of ~ 38 cm ⁻¹	—
W _x O _y	WO ₃	~ 165 cm ⁻¹	~167 cm ⁻¹ [178]
	W ₂₀ O ₅₈	with a width of ~ 97 cm ⁻¹	~167 cm ⁻¹ [178]
A4'	Mo ₂ C	~ 320 cm ⁻¹ with a width of ~ 224.5 cm ⁻¹	~334 cm ⁻¹ [174]
A5'		~ 656 cm ⁻¹ with a width of ~ 371 cm ⁻¹	~666 cm ⁻¹ [174]
(c) wear track of C4 : position 1			
W _x O _y + MoO ₃	WO ₃	~ 133 cm ⁻¹ with a width of ~ 79 cm ⁻¹	~134 cm ⁻¹ [178]
	W ₂₀ O ₅₈		~131 cm ⁻¹ [178]
	MoO ₃		~129 cm ⁻¹ [179]

$W_xO_y + MoO_3$	WO_3	$\sim 217\text{ cm}^{-1}$ with a width of $\sim 43\text{ cm}^{-1}$	$\sim 220\text{ cm}^{-1}$ [178]
	$W_{20}O_{58}$		$\sim 216\text{ cm}^{-1}$ [178]
	MoO_3		$\sim 218\text{ cm}^{-1}$ [179]
W_xO_y	WO_3	$\sim 280\text{ cm}^{-1}$ with a width of $\sim 43.5\text{ cm}^{-1}$	$\sim 273\text{ cm}^{-1}$ [178]
	$W_{20}O_{58}$		$\sim 281\text{ cm}^{-1}$ [178]
$W_xO_y + Fe_2O_3$	WO_3	$\sim 377\text{ cm}^{-1}$ with a width of $\sim 132.5\text{ cm}^{-1}$	$\sim 378\text{ cm}^{-1}$ [178]
	$W_{20}O_{58}$		$\sim 376\text{ cm}^{-1}$ [178]
	Fe_2O_3		$\sim 381\text{ cm}^{-1}$ [176]
Fe_2O_3		$\sim 495\text{ cm}^{-1}$ with a width of $\sim 52\text{ cm}^{-1}$	$\sim 497\text{ cm}^{-1}$ [176]
Fe_2O_3		$\sim 612\text{ cm}^{-1}$ with a width of $\sim 129\text{ cm}^{-1}$	$\sim 612\text{ cm}^{-1}$ [176]
(d) wear track of C4 : position 2			
B1		$\sim 97\text{ cm}^{-1}$ with a width of $\sim 23\text{ cm}^{-1}$	—
B2		$\sim 123\text{ cm}^{-1}$ with a width of $\sim 61\text{ cm}^{-1}$	
B3		$\sim 185\text{ cm}^{-1}$ with a width of $\sim 115\text{ cm}^{-1}$	
B4	Mo_2C	$\sim 339\text{ cm}^{-1}$ with a width of $\sim 208\text{ cm}^{-1}$	$\sim 334\text{ cm}^{-1}$ and $\sim 376\text{ cm}^{-1}$ [174]
W_xO_y	WO_3	$\sim 619.5\text{ cm}^{-1}$ with a width of $\sim 368\text{ cm}^{-1}$	$\sim 639\text{ cm}^{-1}$ [178]
	$W_{20}O_{58}$		$\sim 603\text{ cm}^{-1}$ and $\sim 648\text{ cm}^{-1}$ [178]
(e) wear track of C6 : position 1			
$W_xO_y + MoO_3$	$W_{20}O_{58}$	$\sim 113\text{ cm}^{-1}$ with a width of $\sim 49\text{ cm}^{-1}$	$\sim 113\text{ cm}^{-1}$ [178]
	MoO_3		$\sim 117\text{ cm}^{-1}$ [179]
$W_xO_y + MoO_3$	WO_3	$\sim 209\text{ cm}^{-1}$ with a width of $\sim 107\text{ cm}^{-1}$	$\sim 205\text{ cm}^{-1}$ [178]
	MoO_3		$\sim 218\text{ cm}^{-1}$ [179]
$W_xO_y + MoO_3$	WO_3	$\sim 293.5\text{ cm}^{-1}$ with a width of $\sim 37\text{ cm}^{-1}$	$\sim 294\text{ cm}^{-1}$ [178]
	$W_{20}O_{58}$		$\sim 298\text{ cm}^{-1}$ [178]
	MoO_3		$\sim 292\text{ cm}^{-1}$ [179]
$W_xO_y + Fe_2O_3$	WO_3	$\sim 383\text{ cm}^{-1}$ with a width of $\sim 127\text{ cm}^{-1}$	$\sim 378\text{ cm}^{-1}$ [178]
	$W_{20}O_{58}$		$\sim 376\text{ cm}^{-1}$ [178]
	Fe_2O_3		$\sim 381\text{ cm}^{-1}$ [176]
W_xO_y	WO_3	$\sim 640.5\text{ cm}^{-1}$ with a width of $\sim 103\text{ cm}^{-1}$	$\sim 639\text{ cm}^{-1}$ [178]
	$W_{20}O_{58}$		$\sim 648\text{ cm}^{-1}$ [178]
(f) wear track of C6 : position 2			
C1		$\sim 97\text{ cm}^{-1}$ with a width of $\sim 23\text{ cm}^{-1}$	—
C2		$\sim 123.5\text{ cm}^{-1}$ with a width of $\sim 58\text{ cm}^{-1}$	
C3		$\sim 181\text{ cm}^{-1}$ with a width of $\sim 109\text{ cm}^{-1}$	
C4		$\sim 319\text{ cm}^{-1}$ with a width of $\sim 221\text{ cm}^{-1}$	
C5'		$\sim 573\text{ cm}^{-1}$ with a width of $\sim 346\text{ cm}^{-1}$	

Table A-17: Raman peaks of the spectra collected within the wear track of Mo–W–C coatings after sliding against Al₂O₃ balls at 400°C

Raman peaks assigned to		Raman peaks (this work)	Raman peaks (literature)
(a) wear track of C2 : position 1			
Fe ₂ O ₃		~ 226 cm ⁻¹ with a width of ~ 8 cm ⁻¹	~226 cm ⁻¹ [176]
W _x O _y + MoO ₃	WO ₃	~ 294.5 cm ⁻¹ with a width of ~ 17 cm ⁻¹	~294 cm ⁻¹ [178]
	W ₂₀ O ₅₈		~298 cm ⁻¹ [178]
	MoO ₃		~292 cm ⁻¹ [179]
Fe ₂ O ₃		~ 412 cm ⁻¹ with a width of ~ 13 cm ⁻¹	~411 cm ⁻¹ [176]
W ₂₀ O ₅₈		~ 503 cm ⁻¹ with a width of ~ 13 cm ⁻¹	~500 cm ⁻¹ [178]
Fe ₂ O ₃		~ 615 cm ⁻¹ with a width of ~ 26 cm ⁻¹	~612 cm ⁻¹ [176]
Fe _x O _y + MoO ₃	Fe ₂ O ₃	~ 663.5 cm ⁻¹ with a width of ~ 33 cm ⁻¹	~670 cm ⁻¹ [176]
	Fe ₃ O ₄		~667 cm ⁻¹ [176]
	MoO ₃		~667 cm ⁻¹ [179]
Fe ₂ O ₃		~ 1323 cm ⁻¹ with a width of ~ 60 cm ⁻¹	~1320 cm ⁻¹ [176]
(b) wear track of C2 : position 2			
A1		~ 97 cm ⁻¹ with a width of ~ 325 cm ⁻¹	—
A2		~ 123.5 cm ⁻¹ with a width of ~ 53 cm ⁻¹	
A3		~ 180 cm ⁻¹ with a width of ~ 109 cm ⁻¹	
A4'	Mo ₂ C	~ 326.5 cm ⁻¹ with a width of ~ 223 cm ⁻¹	~334 cm ⁻¹ [174]
A5'		~ 672 cm ⁻¹ with a width of ~ 500 cm ⁻¹	~666 cm ⁻¹ [174]
(c) wear track of C4 : position 1			
W _x O _y	WO ₃	~ 135 cm ⁻¹ with a width of ~ 63 cm ⁻¹	~131 cm ⁻¹ [178]
	W ₂₀ O ₅₈		~134 cm ⁻¹ [178]
Fe ₂ O ₃		~ 226 cm ⁻¹ with a width of ~ 8 cm ⁻¹	~226 cm ⁻¹ [176]
W _x O _y + MoO ₃	WO ₃	~ 294 cm ⁻¹ with a width of ~ 20 cm ⁻¹	~294 cm ⁻¹ [178]
	W ₂₀ O ₅₈		~298 cm ⁻¹ [178]
	MoO ₃		~292 cm ⁻¹ [179]
Fe ₂ O ₃		~ 412 cm ⁻¹ with a width of ~ 14 cm ⁻¹	~411 cm ⁻¹ [176]
W _x O _y + MoO ₃	WO ₃	~ 656 cm ⁻¹ with a width of ~ 64 cm ⁻¹	~639 cm ⁻¹ [178]
	W ₂₀ O ₅₈		~648 cm ⁻¹ [178]
	MoO ₃		~557 cm ⁻¹ [179]
W ₂₀ O ₅₈		~ 844 cm ⁻¹ with a width of ~ 121 cm ⁻¹	~830 cm ⁻¹ [178]
Fe ₂ O ₃		~ 1322 cm ⁻¹	~1320 cm ⁻¹ [176]

		with a width of $\sim 64 \text{ cm}^{-1}$	
(d) wear track of C4 : position 2			
B1		$\sim 105 \text{ cm}^{-1}$ with a width of $\sim 37 \text{ cm}^{-1}$	–
W_xO_y	WO_3	$\sim 163 \text{ cm}^{-1}$	$\sim 167 \text{ cm}^{-1}$ [178]
	$\text{W}_{20}\text{O}_{58}$	with a width of $\sim 93.5 \text{ cm}^{-1}$	$\sim 167 \text{ cm}^{-1}$ [178]
W_xO_y	WO_3	$\sim 304.5 \text{ cm}^{-1}$	$\sim 298 \text{ cm}^{-1}$ [178]
	$\text{W}_{20}\text{O}_{58}$	with a width of $\sim 226 \text{ cm}^{-1}$	$\sim 294 \text{ cm}^{-1}$ [178]
$\text{W}_{20}\text{O}_{58}$		$\sim 642 \text{ cm}^{-1}$ with a width of $\sim 467 \text{ cm}^{-1}$	$\sim 603 \text{ cm}^{-1}$ and $\sim 648 \text{ cm}^{-1}$ [178]
(e) wear track of C6 : position 1			
Fe_2O_3		$\sim 226 \text{ cm}^{-1}$ with a width of $\sim 8.5 \text{ cm}^{-1}$	$\sim 226 \text{ cm}^{-1}$ [176]
$\text{W}_x\text{O}_y + \text{MoO}_3$	WO_3	$\sim 295 \text{ cm}^{-1}$ with a width of $\sim 18 \text{ cm}^{-1}$	$\sim 294 \text{ cm}^{-1}$ [178]
	$\text{W}_{20}\text{O}_{58}$		$\sim 298 \text{ cm}^{-1}$ [178]
	MoO_3		$\sim 292 \text{ cm}^{-1}$ [179]
Fe_2O_3		$\sim 412 \text{ cm}^{-1}$ with a width of $\sim 13 \text{ cm}^{-1}$	$\sim 411 \text{ cm}^{-1}$ [176]
$\text{W}_x\text{O}_y + \text{MoO}_3$	WO_3	$\sim 658 \text{ cm}^{-1}$ with a width of $\sim 57 \text{ cm}^{-1}$	$\sim 639 \text{ cm}^{-1}$ [178]
	$\text{W}_{20}\text{O}_{58}$		$\sim 648 \text{ cm}^{-1}$ [178]
	MoO_3		$\sim 667 \text{ cm}^{-1}$ [179]
$\text{W}_x\text{O}_y + \text{MoO}_3$	$\text{W}_{20}\text{O}_{58}$	$\sim 830 \text{ cm}^{-1}$ with a width of $\sim 52 \text{ cm}^{-1}$	$\sim 830 \text{ cm}^{-1}$ [178]
	MoO_3		$\sim 820 \text{ cm}^{-1}$ [179]
Fe_2O_3		$\sim 1323 \text{ cm}^{-1}$ with a width of $\sim 63 \text{ cm}^{-1}$	$\sim 1320 \text{ cm}^{-1}$ [176]
(f) wear track of C6 : position 2			
C1		$\sim 98 \text{ cm}^{-1}$ with a width of $\sim 26 \text{ cm}^{-1}$	–
C2		$\sim 130 \text{ cm}^{-1}$ with a width of $\sim 52 \text{ cm}^{-1}$	
C3		$\sim 186 \text{ cm}^{-1}$ with a width of $\sim 100.5 \text{ cm}^{-1}$	
C4		$\sim 326 \text{ cm}^{-1}$ with a width of $\sim 232.5 \text{ cm}^{-1}$	
$\text{W}_x\text{O}_y + \text{MoO}_3$	WO_3	$\sim 662 \text{ cm}^{-1}$ with a width of $\sim 446 \text{ cm}^{-1}$	$\sim 639 \text{ cm}^{-1}$ [178]
	$\text{W}_{20}\text{O}_{58}$		$\sim 648 \text{ cm}^{-1}$ [178]
	MoO_3		$\sim 667 \text{ cm}^{-1}$ [179]

Table A-18: Raman peaks of the spectra collected within the wear track of Mo–W–C coatings after sliding against Al_2O_3 balls at 500°C

Raman peaks assigned to	Raman peaks (this work)	Raman peaks (literature)
(a) wear track of C2 after sliding		
$\text{W}_{20}\text{O}_{58}$	$\sim 143 \text{ cm}^{-1}$ with a width of $\sim 87 \text{ cm}^{-1}$	$\sim 151 \text{ cm}^{-1}$ [178]
Fe_2O_3	$\sim 231 \text{ cm}^{-1}$	$\sim 226 \text{ cm}^{-1}$ [176]

		with a width of $\sim 33 \text{ cm}^{-1}$	
$W_xO_y +$ $Fe_2O_3 +$ MoO_3	Fe_2O_3	$\sim 297 \text{ cm}^{-1}$ with a width of $\sim 46 \text{ cm}^{-1}$	$\sim 292 \text{ cm}^{-1}$ [176]
	WO_3		$\sim 294 \text{ cm}^{-1}$ [178]
	$W_{20}O_{58}$		$\sim 298 \text{ cm}^{-1}$ [178]
	MoO_3		$\sim 292 \text{ cm}^{-1}$ [179]
Fe_2O_3		$\sim 405 \text{ cm}^{-1}$ with a width of $\sim 63 \text{ cm}^{-1}$	$\sim 411 \text{ cm}^{-1}$ [176]
$W_xO_y +$ MoO_3	$W_{20}O_{58}$	$\sim 653 \text{ cm}^{-1}$	$\sim 648 \text{ cm}^{-1}$ [178]
	MoO_3	with a width of $\sim 86 \text{ cm}^{-1}$	$\sim 667 \text{ cm}^{-1}$ [179]
MoO_3		$\sim 820 \text{ cm}^{-1}$ with a width of $\sim 97 \text{ cm}^{-1}$	$\sim 820 \text{ cm}^{-1}$ [179]
Mo_8O_{23}		$\sim 944 \text{ cm}^{-1}$ with a width of $\sim 83 \text{ cm}^{-1}$	$\sim 958 \text{ cm}^{-1}$ [183]
Fe_2O_3		$\sim 1321.5 \text{ cm}^{-1}$ with a width of $\sim 62 \text{ cm}^{-1}$	$\sim 1320 \text{ cm}^{-1}$ [176]
(b) wear track of C4 after sliding			
W_xO_y	WO_3	$\sim 140 \text{ cm}^{-1}$	$\sim 131 \text{ cm}^{-1}$ [178]
	$W_{20}O_{58}$	with a width of $\sim 75 \text{ cm}^{-1}$	$\sim 134 \text{ cm}^{-1}$ [178]
Fe_2O_3		$\sim 228 \text{ cm}^{-1}$ with a width of $\sim 31 \text{ cm}^{-1}$	$\sim 226 \text{ cm}^{-1}$ [176]
$W_xO_y +$ $Fe_2O_3 +$ MoO_3	Fe_2O_3	$\sim 295 \text{ cm}^{-1}$ with a width of $\sim 29 \text{ cm}^{-1}$	$\sim 292 \text{ cm}^{-1}$ [176]
	WO_3		$\sim 294 \text{ cm}^{-1}$ [178]
	$W_{20}O_{58}$		$\sim 298 \text{ cm}^{-1}$ [178]
	MoO_3		$\sim 292 \text{ cm}^{-1}$ [179]
Fe_2O_3		$\sim 411 \text{ cm}^{-1}$ with a width of $\sim 17 \text{ cm}^{-1}$	$\sim 411 \text{ cm}^{-1}$ [176]
$W_xO_y +$ MoO_3	$W_{20}O_{58}$	$\sim 658 \text{ cm}^{-1}$	$\sim 648 \text{ cm}^{-1}$ [178]
	MoO_3	with a width of $\sim 68 \text{ cm}^{-1}$	$\sim 667 \text{ cm}^{-1}$ [179]
MoO_3		$\sim 828 \text{ cm}^{-1}$ with a width of $\sim 167 \text{ cm}^{-1}$	$\sim 820 \text{ cm}^{-1}$ [179]
Fe_2O_3		$\sim 1319 \text{ cm}^{-1}$ with a width of $\sim 73 \text{ cm}^{-1}$	$\sim 1320 \text{ cm}^{-1}$ [176]
(c) wear track of C6 after sliding			
Fe_2O_3		$\sim 228 \text{ cm}^{-1}$ with a width of $\sim 7 \text{ cm}^{-1}$	$\sim 226 \text{ cm}^{-1}$ [176]
$W_xO_y +$ $Fe_2O_3 +$ MoO_3	Fe_2O_3	$\sim 296 \text{ cm}^{-1}$ with a width of $\sim 16 \text{ cm}^{-1}$	$\sim 292 \text{ cm}^{-1}$ [176]
	WO_3		$\sim 294 \text{ cm}^{-1}$ [178]
	$W_{20}O_{58}$		$\sim 298 \text{ cm}^{-1}$ [178]
	MoO_3		$\sim 292 \text{ cm}^{-1}$ [179]
Fe_2O_3		$\sim 414 \text{ cm}^{-1}$ with a width of $\sim 13 \text{ cm}^{-1}$	$\sim 411 \text{ cm}^{-1}$ [176]
$W_xO_y +$ MoO_3	$W_{20}O_{58}$	$\sim 656 \text{ cm}^{-1}$	$\sim 648 \text{ cm}^{-1}$ [178]
	MoO_3	with a width of $\sim 70 \text{ cm}^{-1}$	$\sim 667 \text{ cm}^{-1}$ [179]
MoO_3		$\sim 827 \text{ cm}^{-1}$ with a width of $\sim 122 \text{ cm}^{-1}$	$\sim 820 \text{ cm}^{-1}$ [179]
Fe_2O_3		$\sim 1323 \text{ cm}^{-1}$ with a width of $\sim 60 \text{ cm}^{-1}$	$\sim 1320 \text{ cm}^{-1}$ [176]

Table A-19: Raman peaks of the spectra collected from the adhered debris on the steel ball after lubricated sliding against Mo–W–C coatings at 200°C

Raman peaks assigned to	Raman peaks (this work)	Raman peaks (literature)
<i>(a) Adhered debris on C2 : position a</i>		
P1	~ 97 cm ⁻¹ with a width of ~ 27 cm ⁻¹	-
P2'	~ 130 cm ⁻¹ with a width of ~ 62 cm ⁻¹	
P3'	~ 204 cm ⁻¹ with a width of ~ 101 cm ⁻¹	
P4'	~ 366 cm ⁻¹ with a width of ~ 122 cm ⁻¹	
MoS ₂	~ 382.5 cm ⁻¹ with a width of ~ 11 cm ⁻¹	~376 cm ⁻¹ [figure 4.2-14b]
MoS ₂	~ 408 cm ⁻¹	~402 cm ⁻¹ [figure 4.2-14b]
WS ₂	with a width of ~ 10 cm ⁻¹	~412 cm ⁻¹ [figure 4.2-14a]
<i>(b) Adhered debris on C2 : position b</i>		
P1'	~ 111 cm ⁻¹ with a width of ~ 49 cm ⁻¹	-
P3'	~ 199 cm ⁻¹ with a width of ~ 114 cm ⁻¹	
MoS ₂	~ 364.5 cm ⁻¹ with a width of ~ 92 cm ⁻¹	~376 cm ⁻¹ [figure 4.2-14b]
WS ₂	~ 412 cm ⁻¹ with a width of ~ 10 cm ⁻¹	~412 cm ⁻¹ [figure 4.2-14a]
<i>(c) Adhered debris on C4: position a</i>		
P1	~ 98 cm ⁻¹ with a width of ~ 25 cm ⁻¹	-
P2'	~ 128 cm ⁻¹ with a width of ~ 49 cm ⁻¹	
P3'	~ 192 cm ⁻¹ with a width of ~ 93 cm ⁻¹	
WS ₂	~ 323 cm ⁻¹ with a width of ~ 153 cm ⁻¹	~322 cm ⁻¹ [figure 4.2-14a]
<i>(d) Adhered debris on C4 : position b</i>		
P1	~ 99 cm ⁻¹ with a width of ~ 25 cm ⁻¹	-
P2	~ 141 cm ⁻¹ with a width of ~ 71 cm ⁻¹	
P3	~ 216 cm ⁻¹ with a width of ~ 68 cm ⁻¹	
P4	~ 376 cm ⁻¹ with a width of ~ 159 cm ⁻¹	
MoS ₂	~ 379 cm ⁻¹ with a width of ~ 12 cm ⁻¹	~376 cm ⁻¹ [figure 4.2-14b]
MoS ₂	~ 406.5 cm ⁻¹	~402 cm ⁻¹ [figure 4.2-14b]
WS ₂	with a width of ~ 9 cm ⁻¹	~412 cm ⁻¹ [figure 4.2-14a]
<i>(e) Adhered debris on C6 : position a</i>		

P1'	~ 95 cm ⁻¹ with a width of ~ 26 cm ⁻¹	-
P2'	~ 122 cm ⁻¹ with a width of ~ 57 cm ⁻¹	
P3'	~ 180 cm ⁻¹ with a width of ~ 106 cm ⁻¹	
WS ₂	~ 319 cm ⁻¹ with a width of ~ 197.5 cm ⁻¹	~322 cm ⁻¹ [figure 4.2-14a]
(f) Adhered debris on C6 : position b		
P1'	~ 118 cm ⁻¹ with a width of ~ 51 cm ⁻¹	-
P2'	~ 181 cm ⁻¹ with a width of ~ 116 cm ⁻¹	
P3'	~ 227 cm ⁻¹ with a width of ~ 14 cm ⁻¹	
P4'	~ 359 cm ⁻¹ with a width of ~ 143 cm ⁻¹	
MoS ₂	~ 381 cm ⁻¹ with a width of ~ 12 cm ⁻¹	~376 cm ⁻¹ [figure 4.2-14b]
WS ₂	~ 408 cm ⁻¹ with a width of ~ 9 cm ⁻¹	~412 cm ⁻¹ [figure 4.2-14a]

Table A-20: Raman peaks of the spectra collected from the wear track of the Mo–W–C coatings after lubricated sliding against steel balls at 200°C

Raman peaks assigned to		Raman peaks (this work)	Raman peaks (literature)
(a) wear track of C2 after lubricated sliding			
A1		~ 106 cm ⁻¹ with a width of ~ 36 cm ⁻¹	—
A2'		~ 165.5 cm ⁻¹ with a width of ~ 95 cm ⁻¹	
A4'	Mo ₂ C	~ 313 cm ⁻¹ with a width of ~ 219.5 cm ⁻¹	~334 cm ⁻¹ , ~376 cm ⁻¹ [174]
A5'		~ 641 cm ⁻¹ with a width of ~ 429 cm ⁻¹	~666 cm ⁻¹ [174]
(b) wear track of C4 after lubricated sliding			
B1		~ 100 cm ⁻¹ with a width of ~ 25 cm ⁻¹	—
B2		~ 132 cm ⁻¹ with a width of ~ 53 cm ⁻¹	
B3'		~ 202 cm ⁻¹ with a width of ~ 109 cm ⁻¹	
MoS ₂		~ 372 cm ⁻¹ with a width of ~ 245 cm ⁻¹	~376 cm ⁻¹ [figure 4.2-14b]
B5'		~ 677 cm ⁻¹ with a width of ~ 473 cm ⁻¹	~666 cm ⁻¹ [174]

<i>(c) wear track of C6 after lubricated sliding</i>		
C1	~ 99 cm ⁻¹ with a width of ~ 32.5 cm ⁻¹	–
WS ₂	~ 136.5 cm ⁻¹ with a width of ~ 25 cm ⁻¹	~128 cm ⁻¹ [figure 4.2-14a]
C2'	~ 157 cm ⁻¹ with a width of ~ 65 cm ⁻¹	–
C3'	~ 214 cm ⁻¹ with a width of ~ 107 cm ⁻¹	
C4	~ 316 cm ⁻¹ with a width of ~ 206 cm ⁻¹	
C5'	~ 539 cm ⁻¹ with a width of ~ 357 cm ⁻¹	

Table A-21: Raman peaks of the spectra collected from the wear track of C4 after lubricated sliding against Al₂O₃ ball at 200°C

Raman peaks assigned to	Raman peaks (this work)	Raman peaks (literature)
<i>(a) wear track of C4 : position 1</i>		
B1	~ 95 cm ⁻¹ with a width of ~ 24 cm ⁻¹	–
B2'	~ 124.5 cm ⁻¹ with a width of ~ 50 cm ⁻¹	
B3'	~ 178 cm ⁻¹ with a width of ~ 96 cm ⁻¹	
Mo ₂ C	~ 674.5 cm ⁻¹ with a width of ~ 52 cm ⁻¹	~666 cm ⁻¹ [174]
B6'	~ 1041 cm ⁻¹ with a width of ~ 272 cm ⁻¹	–
<i>(b) wear track of C4 : position 2</i>		
B1	~ 97 cm ⁻¹ with a width of ~ 27 cm ⁻¹	–
B2	~ 129 cm ⁻¹ with a width of ~ 55 cm ⁻¹	
B3	~ 198 cm ⁻¹ with a width of ~ 112 cm ⁻¹	
MoS ₂	~ 371 cm ⁻¹ with a width of ~ 139 cm ⁻¹	~376 cm ⁻¹ [figure 4.2-14b]
MoS ₂	~ 405 cm ⁻¹ with a width of ~ 7.5 cm ⁻¹	~402 cm ⁻¹ [figure 4.2-14b]
B6	~ 1062 cm ⁻¹ with a width of ~ 239 cm ⁻¹	–